UNIVERSITY OF SOUTHAMPTON

FACULTY OF NATURAL AND ENVIRONMENTAL SCIENCES

Ocean and Earth Sciences

ANALYSIS OF FAULT NETWORKS AND CONJUGATE SYSTEMS

by

Casey William Nixon

Thesis for the degree of Doctor of Philosophy

January 2013

UNIVERSITY OF SOUTHAMPTON

ABSTRACT

FACULTY OF NATURAL AND ENVIRONMENTAL SCIENCES

Ocean and Earth Sciences

Doctor of Philosophy

ANALYSIS OF FAULT NETWORKS AND CONJUGATE SYSTEMS

By Casey William Nixon

Faults networks exist over a range of scales and are important for understanding the brittle deformation and fluid transport processes within the Earth's crust. Analysing fault networks by characterizing the organization of faulting within them; the distribution of numerous attributes (i.e. displacement, density, strain etc.); and assessing their connectivity is essential, as these provide information about a fault networks behaviour, growth and development. This thesis presents an analysis of various strike-slip and normal fault networks from north Devon, New Zealand and Alaska. The fault networks are interpreted using an array of datasets such as field observation, aerial photography, multibeam bathymetry, high resolution seismic profiles and 3-D seismic volumes. These are integrated with ArcGIS and robust methodologies are used to analyse each network.

Spatial mapping of various attributes indicates that there is much heterogeneity in the organization of faulting within fault networks. Different domains, defined by their deformation style and/or their kinematic behaviour, can develop within a fault network. Domino domains have a dominant fault set with larger displacements, which controls systematic rotation of faults and bedding. Conjugate domains form when there are equal sizes and proportions of each fault set and show little or no rotation of bedding. Domains interact with one another and can form large damage zones to accommodate changes in strain. Strain accommodated by each domain can vary within a network and is either distributed across numerous faults or localized to a few large faults, however, the network will preserve strain compatibility between domains.

Fault interactions including splays, abutments and cross-cutting relationships are characterized by different displacement profiles. These can be divided into two groups based on their kinematics: antithetic interactions and synthetic interactions, which involve faults with the opposite and same motion senses, respectively. Fault development can be influenced by interactions with pre-existing structures. When earlier fault generations are reactivated they affect the orientation, displacement and distribution of new fault generations.

A topological analysis is developed to characterize fault networks and assess connectivity. This considers a network to comprise of nodes (I, Y and X) and branches (I-I, I-C and C-C) between nodes. The number and proportion of each topological component can be used to produce parameters that relate to the connectivity of a network, such as the number of connections per line or per branch. They can also provide information about the clustering and compartmentalization within a network.

Contents

1. Introduction……. 1

1.1. Definition of a fault network ……..... 1
1.2. Importance of fault networks …… 2
1.3. Background ……... 2
1.4. Project aims and methods ……. 4
1.5. Thesis outline ……... 7
1.6. References ……. 8

2. Deformation within a strike-slip fault network at Westward Ho!, Devon U.K.: Domino vs conjugate faulting……..... 15

2.1. Abstract …….. 15
2.2. Introduction ……... 16
2.3. Geological Setting ……... 18
2.4. Methodology ……. 22
2.4.1. Mapping …… 22
2.4.2. Displacement analysis …… 22
2.4.3. Strain determination …… 23
2.5. Fault Network Characteristics ……. 24
2.5.1. Spatial distribution and magnitude variation of fault sets…….. 24
2.5.2. Displacement profiles and interaction of fault sets ……..... 26
2.5.3. Strain …… 29
2.6. Domino vs conjugate faulting …….. 32
2.6.1. Conjugate Area …… 32
2.6.2. Domino Area ……..... 33
2.6.3. Damage Area …… 34
2.7. Discussion ……. 35
2.8. Conclusions …….. 37
2.9. References ……..... 39

3. Analysis of a strike-slip fault network using high resolution multibeam bathymetry, offshore NW Devon U.K. ……..... 43

3.1. Abstract ……. 43
3.2. Introduction …….. 44
3.3. Geological Setting …….. 45
3.4. Mapping Methods ……..... 46
3.5. Mapping Results …….. 50
3.5.1. Folds and bedding attitudes …….. 50
3.5.2. Relationship between faults and folding ……..... 50
3.5.3. Spatial distribution and relative proportions of fault sets …….. 52
3.6. Displacement and Scaling ……..... 55
3.6.1. Effects of scale on the spatial arrangement of the fault network.. 55
3.6.2. Strain distribution ……... 56
3.7. Topology ……..... 60
3.8. Discussion and Comparison with Westward Ho! …… 62
3.8.1. Westward Ho! …….. 63
3.8.2. Strain ……. 65
3.8.3. Connectivity …….. 67
3.9. Summary and Conclusions ……... 69
3.10. References ……..... 70

4. A topological analysis of 2-D fault networks and its use in assessing connectivity ……..... 75

4.1. Abstract …….. 75
4.2. Introduction ……... 76
4.2.1. Topology of fault networks ……. 77
4.3. Methodology ……. 81
4.3.1. Topological measures …… 81
4.3.2. Maps and contour plots …….. 86
4.4. Case studies – Hartland Point and Westward Ho! …….. 87
4.4.1. Spatial distribution of trace-length and displacement …… 90
4.5. Topological analysis …….. 90
4.5.1. Node analysis …….. 90
4.5.2. Branch analysis …… 94
4.6. Characteristic properties of topological components …….. 96
4.6.1. Synthetic Y-nodes vs antithetic Y-nodes …… 96
4.6.2. Branch length distribution …….. 97
4.6.3. Isolated branches vs connected branches …….. 98
4.7. Discussion – Assessing connectivity …… 101

4.7.1. Characterizing connectivity in fault networks 102
4.7.2. Clustering 105
4.7.3. Influences on connectivity 106
4.8. Conclusions 107
4.9. References..... 108

5. Mesoscale faulting on the Kaikoura Peninsula, South Island, NZ 113

5.1. Abstract 113
5.2. Introduction 114
5.2.1. Stratigraphy and structure 115
5.3. Methodology 118
5.3.1. Mapping 118
5.3.2. Line sampling 118
5.3.3. Strain determination 118
5.4. Fault systems on the Kaikoura Peninsula 120
5.4.1. Evidence of strike-slip deformation 120
5.4.2. South Bay 122
5.4.3. Point Kean 125
5.4.4. Spaniards Bay 128
5.5. Local variations in fault network behaviour 131
5.5.1. Damage zones 131
5.5.2. Lithology 133
5.6. Discussion 134
5.7. Conclusions 138
5.8. References 140

6. The organization of faulting and distribution of strain around a large magnitude fault in the Whakatane Graben, New Zealand 143

6.1. Abstract 143
6.2. Introduction 144
6.3. Tectonic Setting 145
6.4. Methodology 148
6.4.1. Seismic data and interpretation 148
6.4.2. Displacement measurements and analysis 149
6.5. Results 151

6.5.1. Geometry and spatial variation in faulting …….. 151
6.5.2. Distribution and accumulation of displacement ……. 152
6.5.3. Displacement rates ……. 154
6.5.4. Strain analysis ……. 157
6.6. Discussion …… 161
6.7. Conclusions …… 163
6.8. References ……..... 165

7. Analysis of a normal fault network with multiple fault sets at Milne Point, Alaska ……. 169

7.1. Abstract ……. 169
7.2. Introduction …….. 170
7.3. Geological setting ……... 171
7.4. Methods ……..... 173
7.4.1. Data acquisition and interpretation …….. 173
7.4.2. Network analysis ……. 175
7.5. Fault network characteristics …….. 177
7.5.1. General structural trends and relationships …… 177
7.5.2. Organization of faulting and displacement distribution ……. 179
7.5.3. Strain analysis …… 182
7.6. Fault interactions ……..... 183
7.6.1. Isolated faults, abutments and splays ……. 183
7.6.2. Fault segments linked at depth ……. 191
7.6.3. Trailing faults …… 194
7.7. Topology ……..... 198
7.7.1. Nodes and branches …….. 198
7.7.2. Compartments ……. 198
7.8. Discussion ……. 204
7.8.1. Fault chronology …….. 204
7.8.2. Network development ……. 205
7.8.3. Compartmentalization ……... 208
7.9. Conclusions …….. 209
7.10. References ……..... 211

8. Summary and conclusions …… 215

8.1. Fault organization, interaction and the role of pre-existing structures……..……. 215
8.2. Distribution and localization of strain within fault ……. 217

8.3. Topological variation in fault networks, connectivity and compartmentalization ……..... 219

9. Appendix…….. 221

9.1. ArcGIS Workflow 1 – Analysis from field observation and digital air photographs at Westward Ho! …… 222

9.2. ArcGIS Workflow 2 – Structural analysis of multibeam bathymetry data offshore Hartland ……. 225

9.3. ArcGIS Workflow 3 – Analysis from high resolution seismic data and 3D seismic data ……. 226

9.4. ArcGIS Workflow 4 – Extraction and analysis of data from ArcGIS ……. 227

9.5. ArcGIS Workflow 5 – Analysis of network topology …….. 229

List of Figures

Figure 1.1 Chart of the work flow from the analysis and interpretation of each data type to the extraction of data from ArcGIS for the network analysis. 6

Figure 2.1 Interpreted aerial photograph of the wave-cut platform at Westward Ho!. 17

Figure 2.2 a) Length-weighted rose diagram of faults at Westward Ho! b) Equal-area stereographic projection of fault data. 19

Figure 2.3 Fault maps of the northern area in Figure 2.1. 20

Figure 2.4 Fault maps of the central area in Figure 2.1. 21

Figure 2.5 Length-weighted and (length x displacement)weighted rose diagrams for Westward Ho!. 25

Figure 2.6 Plots of displacement against azimuth for: a) the northern area; b) the north central area. 26

Figure 2.7 Plots of displacement against distance for different fault interactions. 27

Figure 2.8 a) Diagram showing the orientations of the principal horizontal extensions for different sub areas. b) Graph of % extension plotted against distance. 31

Figure 2.9 Strain restoration diagrams a) the conjugate area and b) the domino area. 31

Figure 2.10 Schematic diagram illustrating typical fault geometries for a conjugate network and domino network. 33

Figure 3.1 Location map with the main geological units. 46

Figure 3.2 Interpreted multibeam bathymetry image with applied hillshade effect from offshore Hartland Point. 48

Figure 3.3 Multibeam bathymetry images with applied hillshade effect showing the quality of the imagery and the onshore-offshore correlation. 49

Figure 3.4 Fault map of a wave-cut platform at Hartland Quay. 51

Figure 3.5 Equal-area stereographic projections of fault and bedding data. 52

Figure 3.6 Interpretation of field photographs from Hartland Quay showing folds cut by strike-slip faults. 53

Figure 3.7 A plot of displacement against azimuth for the fault segment data offshore from Hartland Point. 54

Figure 3.8 Displacement maps of fault segments offshore Hartland Point. Each map has a different displacement cut-off representing different resolutions. 54

Figure 3.9 Linear-log plots of fault data from offshore Hartland Point showing the distribution of trace-length and % extension vs displacement cut-off. 58

Figure 3.10 a) A multibeam bathymetry image with applied hillshade effect illustrating a system with fault branches and nodes. b) A ternary plot of I-, Y-, and X-node proportions. 61

Figure 3.11 Linear-log plot of connecting node % vs displacement cut-off. 62

Figure 3.12 Fault map of the wave-cut platform at Westward Ho! showing the localities of the left-lateral, damage and right-lateral areas. 64

Figure 3.13 Linear-log plots of fault data from the left-lateral, damage and right-lateral areas. 65

Figure 3.14 Ternary diagram of I-, Y- and X-Node percentages showing the connectivity pathways from 50 m resolution to full resolution of the fault networks from offshore Hartland Point and onshore Westward Ho!. 67

Figure 4.1 A schematic diagram showing a fault trace 'AB' divided into nodes and branches. 78

Figure 4.2 Schematic diagram showing the different topological geometries and interactions between faults. 79

Figure 4.3 Schematic diagram illustrating different topological arrangements and clusters within a fault network. 80

Figure 4.4 Ternary plots of nodes and branches illustrating the contours of the number of connections per line and per branch. 82

Figure 4.5 An example of sampling the nodes and branches from a subarea. 86

Figure 4.6 a) A fault trace map of displacement for i) Hartland and ii) Westward Ho! indicating the location of each subarea; b) Contour plots of fault trace-length density showing the distribution of fault trace-length; c) Contour plots of connecting node frequency. 89

Figure 4.7 a) log-log plot of connecting node frequency vs fault density. b) log-log plot of connecting node frequency vs fault length. c) log-normal plot of connecting node frequency vs fault set proportion where 50% represents equal proportions of each fault set. 91

Figure 4.8 a) A ternary plot of the proportions of I-, Y- and X- nodes. b) A ternary plot of the proportions of I-I, I-C and C-C branches for Westward Ho! and Hartland. 93

Figure 4.9 Fault maps of each network displaying the distribution of each branch type (I-I, I-C and C-C) within the fault networks at i) Hartland and ii) Westward Ho!. 95

Figure 4.10 a) Histogram illustrating the acute angles of intersection for synthetic and antithetic Y-node interactions. b) Log-normal plot of connecting node frequency vs fault set proportion for synthetic Y(s)-nodes and antithetic Y(a)-nodes. 96

Figure 4.11 Histograms showing the frequency of different branch lengths for a) Hartland and b) Westward Ho!. 97

Figure 4.12 Fault maps and contour plots of fault trace-length for the fault network offshore Hartland showing the distribution of connected and isolated branches. 100

Figure 4.13 Plot of branch length (log) against azimuth for a) isolated branches from Hartland and b) connected branches from Hartland. 101

Figure 4.14 a) A ternary branch diagram showing the estimated path of increasing connectivity. b) A plot showing the linear relationship between the proportion of I-C and C-C branches and values of $n_{C/B.}$ 104

Figure 5.1 Location map of Kaikoura Peninsula showing the main structures that surround the peninsula. 115

Figure 5.2 Geological map of Kaikoura Peninsula showing the main lithologies of the wave-cut platforms, NE-trending fold structures and the three study areas. 116

Figure 5.3 a) Equal angle stereographic projection of bedding showing the main trend of folding; b) field photograph of parasitic folding within the Spyglass Formation at Spaniards Bay. 117

Figure 5.4 a) Equal angle stereographic projection of fault planes and associated slickensides taken from fault and fractures across the area; b) Length x displacement weighted rose diagram of faults from all three study areas; c) Length x displacement weighted histogram showing the distribution of faults with right-lateral and left-lateral separations. 117

Figure 5.5 a) Field photograph from Spaniards Bay of steeply dipping fractures being offset laterally by left-lateral faults; b) field photograph from South Bay showing the axial trace of a parasitic fold being offset laterally offset by a fault. 120

Figure 5.6. a) Small scale pull apart associated with a step-over between two small left-lateral faults; b) a releasing bend with an anastomosing damage zone between to left- 121

lateral faults; c) field photograph from Point Kean showing a dilational jog between right-lateral shear fractures (blue lines) within a lens structure.

Figure 5.7 a) Fault map of the South Bay. b) Trace-length weighted rose diagram and histogram for the mapped South Bay fault network; c) trace-length x displacement weighted rose diagram and histogram for the mapped South Bay area. 123

Figure 5.8 a) Fault map of the Point Kean. b) Trace-length weighted rose diagram and histogram for the mapped Point Kean fault network; c) trace-length x displacement weighted rose diagram and histogram for the mapped Point Kean area. 124

Figure 5.9 a) Field photograph illustrating vertical movement and drag of a siltstone bed at Point Kean indicating transpression; b) a more competent ridge along a fault line indicative of transpression. 126

Figure 5.10 A schematic illustration of right-lateral reactivation of a left-lateral fault. Displacement profiles represent the fault before (a) and after (b) reactivation. 127

Figure 5.11 a) Fault map of the Spaniards Bay. b) Trace-length weighted rose diagram and histogram for the mapped Point Kean fault network; c) trace-length x displacement weighted rose diagram and histogram for the mapped Spaniards Bay area. 130

Figure 5.12 Cliff top photograph of the mapped wave-cut platform at Spaniards Bay showing the location of two line samples and a damage zone between them. 132

Figure 5.13 Cliff top photograph of the wave-cut platform at South Bay showing the location of line samples 3, 4 and 5 with proximity to the Spyglass/Waima boundary. 134

Figure 5.14 A schematic diagram showing the main structures and their associated regional stress directions. 136

Figure 6.1 a) Location map of the Whakatane Graben showing the position of the Rangitaiki Fault and the study area. The position of boomer lines 104, 124 and 137 are also shown. b) A fault map of the study area showing the segments of the Rangitaiki Fault. The hanging wall and footwall fault groups are NW and SE of the Rangitaiki Fault, respectively. c) Length-weighted rose diagrams showing the fault trends within each fault group. 147

Figure 6.2 Interpreted seismic profiles for boomer lines 104, 124 and 137 indicating the positions of four horizons H1-H4. 149

Figure 6.3 Fault displacement profiles of cumulative displacement along strike of the Rangitaiki fault network for horizons H1- H4. 153

Figure 6.4 Fault displacement profiles of cumulative displacement along strike of the fault network for H4. Showing the contribution to the overall displacement of individual groups of faults, introduced at locations 1- 5, within the hanging wall and footwall fault blocks of the Rangitaiki Fault. 154

Figure 6.5 Fault maps showing the displacement rates of each fault within the fault network for different time intervals over the last 17 kyr. 156

Figure 6.6 Displacement Rate variations along strike of the fault network for different time intervals, comparing the displacement rates of the Rangitaiki Fault to the hanging wall and footwall faults. Location 1 marks the change from localized faulting to distributed faulting. 157

Figure 6.7 Strain Profile for H4 indicating the variations in the % extension of each boom line along strike of the fault network showing the strain accommodated by the Rangitaiki Fault (black) and the hanging wall and footwall faults (grey). Shows the contribution of each fault to the overall extension of boom lines 104, 124 and 137. 158

Figure 7.1 Location map showing the key structural features of the Alaska North Slope (ANS) and the position of Milne Point. 171

Figure 7.2 Summary of the ages of the stratigraphic sequences and the formation lithologies that were seismically imaged. The KUP and SAG horizons are also indicated. 172

Figure 7.3 Seismic reflection images of a) a NW-SE trending crossline and b) a NE-SW trending inline. 174

Figure 7.4 Fault maps of the KUP horizon on the left and the SAG horizon on the right: a) Surface horizon maps showing the topography of the horizons; b) Fault map colour-coded by azimuth; c) Fault map colour-coded by throw. 176

Figure 7.5 Length-weighted rose diagrams and an equal angle stereographic projection of poles to fault segments for each fault set in the KUP horizon and SAG horizon. 177

Figure 7.6 Interpreted seismic sections showing the stratigraphic thickness in relation to a) the NNE-trending faults and b) the WNW-trending faults. c) An isochore map showing the variation in stratigraphic thickness between the KUP and SAG horizon. 178

Figure 7.7 Logarithmic plots of fault length vs maximum throw for a) all the faults; b) the KUP Horizon and c) the SAG horizon. 180

Figure 7.8 Equal angle stereographic projection of poles to fault segments showing the principal strain orientations. 181

Figure 7.9 Normalized fault profiles for isolated faults from both the KUP and SAG horizons. 185

Figure 7.10 3D diagrams of fault planes that form abutting interactions. 186

Figure 7.11 Normalized fault profiles for single tip abutting faults taken from both the KUP and SAG horizons. 187

Figure 7.12 Normalized fault profiles for double tip abutting faults taken from both the KUP and SAG horizons. 188

Figure 7.13 The fault profiles of a main fault and a splay fault showing their fault plane geometries and variations in throw. 189

Figure 7.14 Fault throw profiles of long individual faults (>2000m length) which have intersecting and abutting faults. 191

Figure 7.15 Fault throw profiles from the a) the SAG horizon and b) the KUP horizon of four large WNW-trending faults (Faults i, ii, iii and iv) that share relay ramps and interact with each other with some associated splay faults. 193

Figure 7.16 3D diagram of NNE trending fault planes that abut and locally reactivate WNW trending fault planes and form a trailing fault segment that links two abutting faults. 194

Figure 7.17 Fault throw profiles showing an example of a synthetic trailing fault interaction where two faults abut and reactivate a portion of another fault that shares the same motion sense. 195

Figure 7.18 Fault throw profiles showing an example of an antithetic trailing fault where faults abut and reactivate a portion of another fault which has the opposite motion sense. 196

Figure 7.19 Ternary triangles showing the proportions of a) I, Y and X nodes and b) I-I, I-C and C-C branches within the network. 199

Figure 7.20 Fault map showing the topologies and spatial distribution of each branch type at Milne Point. The coloured areas represent the different closed compartments within the network. 201

Figure 7.21 Fault maps for the KUP horizon and SAG horizon showing the compartments of the fault network after extending the tips of faults 203

Figure 7.22 Schematic diagram of throw profiles for abutting faults at different stages of development. 206

List of Tables

Table 1.1 List of localities used for the project indicating the type of fault network and the data sources used 5

Table 2.1 Structural characteristics of mapped areas (Figure 2.2) at Westward Ho!. 30

Table 2.2 Characteristics of conjugate and domino regions. 36

Table 3.1 Structural characteristics and distribution of strain and trace-length within the fault networks offshore Hartland Point and onshore Westward Ho!. 59

Table 3.2 Nodal percentages of the fault networks from offshore Hartland Point and onshore Westward Ho!. 60

Table 4.1 Different physical attributes for both Westward Ho! and Hartland. The subareas (located in Figure 4.6) for each fault network are in ascending order of fault density with dark grey representing subareas that have >80% of one fault set. 88

Table 4.2 Proportions of each node type within the fault networks at Hartland and Westward Ho!. 92

Table 4.3 Statistical analysis of branch and line lengths 98

Table 5.1 Strain values and orientations within the horizontal plane for each mapped fault network on Kaikoura Peninsula. 125

Table 5.2 Physical Attributes of Line samples taken from Spaniards Bay an South Bay. 133

Table 6.1 A table showing the estimated ages of horizons H1- H4, from Bull et al. (2006). 148

Table 6.2 A table of displacement rates for different time intervals over the last 17 kyr calculated from the throws each fault at each and the estimated ages of each horizon. 155

Table 6.3 3D strain values of the fault network at H4. Comparing the strain distribution within the area of localized faulting and the area of distributed faulting. 159

Table 7.1 Fault trace-length and throw statistics at Milne Point. 179

Table 7.2 3-Dimensional strain values and orientations for the KUP and SAG horizons. 183

Table 7.3 Proportions of each topological component with the number of connections per line ($N_{C/L}$) and per branch ($N_{C/B}$) for both horizons and from selected subareas. 200

Table 7.4 Compartment statistics showing their number and sizes at each horizon for different fault tip extensions. 202

DECLARATION OF AUTHORSHIP

I, **Casey William Nixon** declare that the thesis entitled

'**Analysis of fault networks and conjugate systems**'

and the work presented in the thesis are both my own, and have been generated by me as the result of my own original research. I confirm that:

- This work was done wholly or mainly while in candidature for a research degree at this University;
- Where any part of this thesis has previously been submitted for a degree or any other qualification at this University or any other institution, this has been clearly stated;
- Where I have consulted the published work of others, this is always clearly attributed;
- Where I have quoted from the work of others, the source is always given. With the exception of such quotations, this thesis is entirely my own work;
- I have acknowledged all main sources of help;
- Where the thesis is based on work done by myself jointly with others, I have made clear exactly what was done by others and what I have contributed myself;
- Parts of this work have been published as:

Nixon, C.W., Sanderson, D.J., Bull J.M., 2011. Deformation within a strike-slip fault network at Westward Ho!, Devon U.K. : Domino vs conjugate faulting. Journal of Structural Geology 33. 833-843. doi.org/10.1016/j.jsg.2011.03.009

Nixon, C.W., Sanderson, D.J., Bull, J.M., 2012. Analysis of a strike-slip fault network using high resolution multibeam bathymetry, offshore NW Devon U.K.. Tectonophysics 541-543, 69-80. doi.org/10.1016/j.tecto.2012.03.021

Signed: ……..

Date:…….

Acknowledgements

First and foremost I would like to thank my official supervisors Professor Jon Bull and Professor Dave Sanderson for their guidance and support during the course of my PhD. Their advice and feedback has been invaluable and will always be well received. I would also like to thank Steve Dee and Robert Humphreys of BP for their help in acquiring access to the Milne Point dataset and the technical support they provided whilst I was using the facilities at BP Sunbury. Thanks also go to Professor Jarg Pettinga, Dr Mark Quigley and Jack van Berkel for their friendly welcome to the Edward Percival Field Station in Kaikoura and for showing me around the field area. The technical support I received at the National Oceanography Centre was always much appreciated and I would like to thank Gawen Trathen and Dr Pierre Cazenave for their help over the past few years. I would also like to say a special thank you to my office mates, past and present, who have always been encouraging and supportive, as well as the coffee crew regulars who brightened up most weeks of writing with numerous intellectual and witty coffee breaks.

Throughout this PhD I have used numerous data sets and material which I would like to acknowledge including: the aerial photography that images the north Devon coastline courtesy of the Channel Coast Observatory; the UKHO for providing the high resolution multibeam bathymetry offshore north Devon; NIWA for their involvement in the acquisition of the high resolution seismic data in the Bay of Plenty; and BP for providing the 3-D seismic volume from Milne Point. I would also like to acknowledge the financial support from my NERC case-studentship with BP.

Outside of work I would like to say a big thank you to my family for their endless support and for being incredibly understanding of my PhD commitment. Their enthusiasm and interest has always helped to motivate and encourage me to do my best at all times. I would also like to mention Rosanna, my girlfriend, who has never given me a chance to doubt myself and always helped to sternly push me forwards through the challenges of PhD life. Finally I would like to say thanks to all of my friends within the NOC post-graduate community who have made the last few years of PhD life so enjoyable.

1. Introduction

1.1. Definition of a fault network

Faults are discontinuities within the Earth's crust that form planes of brittle deformation across which the surrounding rock mass has been displaced. Faulting is the main deformation mechanism in the upper crust and is often associated with earthquakes (e.g. Scholz, 1990). Faults grow and develop over long time periods, 10^4-10^6 yrs, by the accumulation of displacement from incremental slip events (Cowie and Scholz, 1992; Manzocchi et al., 2006; Mouslopoulou et al., 2009) and show significant displacement variations over their surfaces (e.g. Walsh and Watterson, 1989; Nicol et al., 1996).

A fault network is an organization of numerous faults that generally display a range of lengths, sizes and orientations. Faults within a network may link geometrically and/or kinematically interact with each other by the transfer of displacement through wall-rock deformation (e.g. Peacock and Sanderson, 1991; Soliva and Benedicto, 2004; Bull et al., 2006; Nicol et al., 2010). Furthermore, whilst an individual planar fault surface can only accommodate a plane strain, the network as a whole will generally accommodate triaxial strains that vary spatially (e.g. Reches, 1978; Nieto-Samaniego, 1999).

In its simplest form, a fault network can be a pair of conjugate faults (e.g. Nicol et al., 1995; Ferrill et al., 2009), but more generally fault networks involve interaction between multiple faults belonging to different sets (e.g. Krantz, 1988; Nieto-Samaniego and Alaniz-Alvarez, 1997; Maerten et al., 1999). The faults comprising a network may form in response to a single deformation event under the same overall stress field. In this case, their displacements will be related to the different traction vectors acting on the differently oriented surfaces (Pollard and Fletcher, 2005), modified by local stresses produced by their interaction with each other (Zhang and Sanderson, 1996; Aksari et al., 2010). Alternatively fault networks may result from the superposition of two or more stress systems, producing sets of differently oriented faults. Slip may occur on each set at different times, but more commonly involves reactivation of existing faults, with complex cross-cutting relationships (e.g. Kim et al., 2001; Bailey et al., 2005;

Henza et al., 2011; Giba et al., 2012). In all cases, the linkage and interaction of movement on different faults will result in wall-rock deformation, producing folding and areas of damage around faults (Shipton and Cowie, 2003; Kim et al., 2004; Faulkner et al., 2010, 2011).

1.2. Importance of fault networks

Faults rarely occur individually or without associated deformation and the resulting fault networks can affect both local and regional geology and are of high importance for understanding the brittle deformation of the Earth's crust. Networks are also important as interconnected faults can provide pathways for fluid flow allowing migration, entrapment and escape of resources such as hydrocarbons and groundwater (Aydin, 2000). It has also been well documented that sealing faults can stop lateral and vertical migration of hydrocarbons producing traps and compartmentalization of reservoirs (Smith, 1980; Spencer and Larsen, 1990; Leveille et al., 1997; Jolley et al., 2007). Furthermore, fault propagation, interaction and associated damage zones are areas of increased stress and connectivity, producing sites of preferential hydrothermal fluid flow (Curewitz and Karson, 1997; Zhang and Sanderson, 1998). These sites act as fluid conduits, but also active fault slip and rupturing can control localization and mixing of fluids (Sibson, 1987; Micklethwaite and Cox, 2004). Hence, it has long been recognised that fault zones and fracture arrays are very important for localizing and depositing minerals and metal ores (Norton and Knapp, 1977; Kerrich, 1986). Also, kinematic evidence shows that faults interact with one another on timescales of individual earthquakes to millions of years (e.g. Bull et al., 2006; Nicol et al., 2010). Therefore, a better understanding of fault networks will improve understanding of hazardous seismogenic faults and development of earthquake risk assessments (King, 1986; Sibson, 1989; Nicol et al., 2010; Quigley et al., 2012).

1.3. Background

Faults can be characterized using numerous attributes such as orientation, length, displacement, thickness, etc. There have been many studies describing

the spatial distribution and relationships of such attributes within individual faults and fault populations (Walsh and Watterson, 1988; Marrett and Allmendinger, 1992; Dawers et al., 1993; Cartwright et al., 1995; Cowie et al., 1995; Peacock and Sanderson, 1996; Manighetti et al., 2001; Walsh et al., 2003; Soliva and Benedicto, 2004; Kim and Sanderson, 2005; Schultz et al., 2008; Xu et al., 2010; Faulkner et al., 2011; Kolyukhin and Torabi, 2012). Most of these studies have investigated the scaling relationships of attributes and describe power-law distributions (e.g. Cowie et al., 1995; Pickering et al., 1995; Schultz et al., 2008; Brogi, 2011), although some studies have also noted log normal and negative exponential distributions as well (e.g. Ackermann et al., 2001; Soliva and Schultz, 2008). These have been useful for describing the size distributions of faults and the relationship between displacement and length within a fault population (Kakimi, 1980; Heffer and Bevan, 1990; Walsh et al., 1991; Pickering et al., 1997; Kim and Sanderson, 2005; Schultz et al., 2008).

Fault attributes are particularly useful for the geometric and kinematic characterization of fault populations and are a basis for determining the formation, movement and interactions of faults. These studies have added to our knowledge of fault growth, including processes of fault propagation (Nicol et al., 1996; Peacock and Sanderson, 1996; Sharp et al., 2000; Childs et al., 2003), the development of relay zones (Peacock and Sanderson, 1994, 1995; Huggins et al., 1995; Imber et al., 2004; Kristensen et al., 2008), linkage between fault segments (Taylor, 2004; Bull et al., 2006; Soliva et al., 2008; Long and Imber, 2012) and the formation of damage structures around faults (Kim et al., 2003; Mitchell and Faulkner, 2009; Faulkner et al., 2011).

Other studies have shown that faults increase in both length and displacement becoming more linked with increasing finite strain (Walsh and Watterson, 1991; Dawers et al., 1993; Anders and Schlische, 1994; Cowie et al., 1995; Dawers and Anders, 1995; Cowie, 1998; Gupta et al., 1998; Gupta and Scholz, 2000). Such studies have been further applied to characterize the evolution of fault systems. In general it is thought that the basic fault pattern initiates in the early stages of a fault system and evolves from a distributed array of faulting to a system where strain is localized onto a few larger better connected faults with smaller isolated faults preferentially dying (Meyer et al., 2002; Walsh et al.,

2003; Taylor, 2004; Cowie et al., 2005; Soliva and Schultz, 2008). The progressive localization of deformation has also been supported by physical modelling (Ackermann et al., 2001; Mansfield and Cartwright, 2001) and agrees with geomechanical modelling (e.g. Sanderson and Zhang, 1999, 2004).

Processes of fault growth, fault interactions and the relationships between different fault attributes are all important for understanding the organization and development of faulting within fault networks (Schwarz and Kilfitt, 2008; Schlische and Withjack, 2009) as well as fault network connectivity (e.g. Bour and Davy, 1997; Berkowitz et al., 2000; Cherpeau et al., 2010).

1.4. Project aims and methods

The major aim of this thesis is to better understand the behaviour of fault networks, as opposed to that of individual faults. This is achieved by investigating the geometry, topology, strain, kinematics and interactions of faults within networks and conjugate systems. The thesis addresses the following problems:

1. The distribution of displacement and other attributes within fault networks;
2. The distribution and localization of strain;
3. The spatial, temporal and kinematic organization within a network; e.g. domino and conjugate fault systems, interaction of faults and fault systems, etc.;
4. The assessment of connectivity within fault networks;

Overall these will characterize the deformation observed within fault networks and improve methods of fault network analysis. The thesis also develops a topological analysis that describes the relationships between geometrical elements of the network. This is of particular importance as it can be related to fault network properties, such as connectivity, but could also provide a link between geometry and the behaviour of the network.

The project uses five case studies from various localities (i.e. New Zealand, north Devon and Alaska) where there are exceptional examples of strike-slip

and normal fault systems. These are summarized in Table 1.1 and are based on the mapping of faults from field observations, aerial photography, or geophysical data (i.e. seismic reflection and multibeam data).

Table 1.1 List of localities used for the project indicating the type of fault network and the data sources used.

Locality	Fault type	Data type
Westward Ho!, N. Devon	Strike-slip	Field Observation, Aerial Photography
Hartland, N. Devon	Strike-slip	Field, High Resolution Multibeam Bathymetry
Kaikoura Penisnula, NZ	Strike-slip	Field Observation, Aerial Photography
Whakatane Graben, NZ	Normal	High Resolution 2D Seismic Reflection
Milne Point, Alaska	Normal	3D Seismic Reflection

Westward Ho!, Hartland and Kaikoura Peninsula were used for the analysis of strike-slip fault networks. These localities have well exposed wave-cut platforms with definitive, moderately steeply dipping stratigraphy that allowed accurate mapping from aerial photography. At Hartland, onshore mapping could be correlated with offshore multibeam bathymetry data. These strike-slip fault networks are exposed in plan view and provide networks that are geometrically simple with conjugate fault sets. Furthermore, the main geometrical elements and displacements occur in a horizontal plane producing a simple plane strain at the same level in the Earth's crust.

Normal fault systems allow the lateral and vertical variations in deformation to be studied. These form the second part of the thesis and provide examples of networks with a more complex triaxial strain. Whakatane Graben and Milne Point were used for the analysis of normal fault networks from 2D and 3D seismic reflection data with excellent horizon correlations, which were essential for interpreting faults and measuring dip-slip separation/throw. The offshore Whakatane Graben was chosen as it is an example of a normal fault network with one sub-parallel conjugate fault set, formed under a single stress system, producing a simple network where spatial variations along strike of the network

could be easily investigated. Furthermore, a known syn-rift stratigraphy gives the opportunity to investigate any temporal variations as well. Milne Point was chosen as an example of a normal fault network that formed under more than one stress system and has multiple fault sets, which are well connected. The 3D seismic reflection data was of high quality and suitable for structurally interpreting and analysing the network.

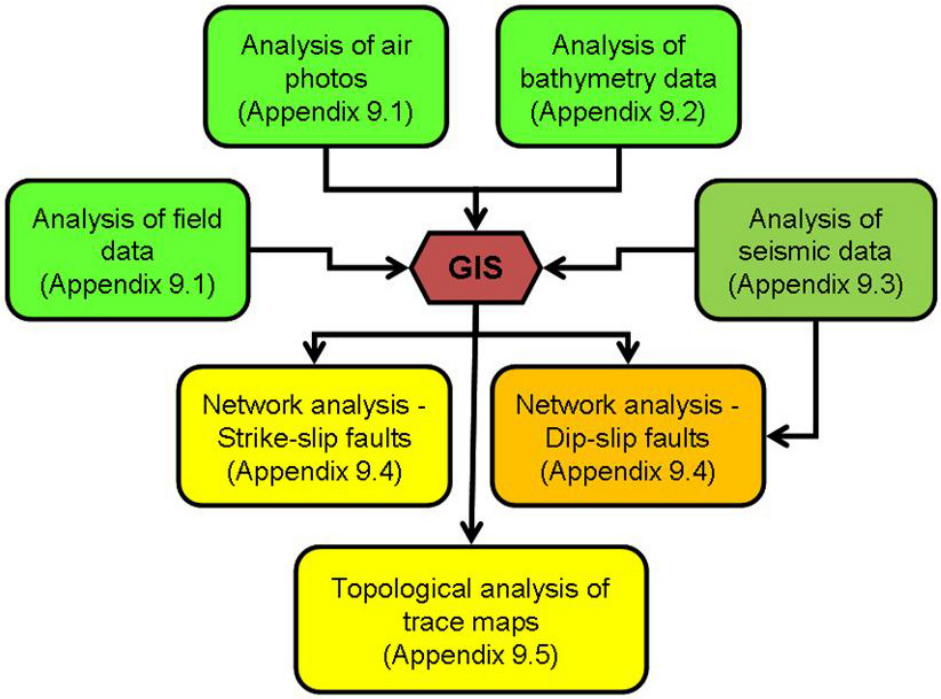

Figure 1.1 Chart of the work flow from the analysis and interpretation of each data type to the extraction of data from ArcGIS for the network analysis.

The fault networks were systematically mapped using different methods, depending on the data source (Table 1.1). Faults were then digitized and analysed in ArcGIS to produce fault maps and extract geometrical and topological information. In order to understand the spatial and kinematic organization of the fault networks, all faults were grouped either by dip direction, strike or kinematic motion sense and multiple measurements of throw/displacement were taken along each fault length. These data could then be extracted from ArcGIS and used in spreadsheets to analyse the fault trends, displacement, strain and topology of each fault network and subareas within (Figure 1.1; see Appendix for more detail).

1.5. Thesis outline

The thesis is presented as a series of chapters in journal article format, two of which have been published, the others represent early drafts of potential papers. Together they tackle the overall aims and problems proposed within this project. The first part of the thesis is on strike-slip faults, whereas the second part concentrates on the localities that are characterized by normal faults.

Chapter 2 investigates the spatial variation of strain, geometry, displacement and other physical attributes within the strike-slip fault network at Westward Ho! to define and characterize the kinematic behaviour of fault networks. It describes different interactions between individual faults as well as areas of faulting and produces a classification system to characterize domino and conjugate faulting (Nixon et al., 2011).

In **Chapter 3** a methodology is developed to analyse fault networks from high resolution multibeam bathymetry imagery from offshore Hartland. It looks at the distribution of physical attributes through a scaling analysis, assessing the role of small and large faults within a fault network, with particular reference to strain localization and connectivity (Nixon et al., 2012).

The two datasets from north Devon are used in **Chapter 4** to develop a detailed topological analysis to characterize fault networks. It explores the spatial distribution, characteristics and proportions of different topological components within fault networks and discusses their use for assessing connectivity.

Chapter 5 describes the strike-slip fault network exposed on Kaikoura Peninsula and its relationship to the regional geological setting. It also provides some description of the spatial effects of lithology and damage on faulting and the distribution of strain within the fault network.

Chapter 6 investigates the along strike variations in displacement and strain of the fault network associated with the Rangitaiki Fault in the Whakatane Graben. It describes spatial changes in the character of the fault network from distributed faulting to localized faulting with particular reference to strain localization onto the Rangitaiki Fault.

Chapter 7 explores the relationships between different fault sets at Milne Point. It describes variations with depth in fault trend, density, displacement, strain and topology of the fault network and discusses the effects of pre-existing structures on the development of fault sets within a fault network.

Chapter 8 provides a synopsis that draws together the findings and main themes of the thesis and provides some overall conclusions on the characterization of fault networks and conjugate systems.

1.6. References

Ackermann, R.V., Schlische, R.W., Withjack, M.O., 2001. The geometric and statistical evolution of normal fault systems: an experimental study of the effects of mechanical layer thickness on scaling laws. Journal of Structural Geology 23, 1803–1819.

Aksari, D., Karabulut, H., Özalaybey, S., 2010. Stress interactions of three moderate size earthquakes in Afyon, southwestern Turkey. Tectonophysics 485, 141–153.

Anders, M.H., Schlische, R.W., 1994. , 1994. Overlapping faults, intrabasin highs, and the growth of normal faults. Journal of Geology 102, 165–180.

Aydin, A., 2000. Fractures, faults, and hydrocarbon entrapment, migration and flow. Marine and Petroleum Geology 17, 797–814.

Bailey, W.R., Walsh, J.J., Manzocchi, T., 2005. Fault populations, strain distribution and basement fault reactivation in the East Pennines Coalfield, UK. Journal of Structural Geology 27, 913–928.

Berkowitz, B., Bour, O., Davy, P., Odling, N., 2000. Scaling of fracture connectivity in geological formations. Geophysical research letters 27, 2061–2064.

Bour, O., Davy, P., 1997. Connectivity of random fault networks following a power law fault length distribution. Water Resources Research 33, 1567–1583.

Brogi, A., 2011. Variation in fracture patterns in damage zones related to strike-slip faults interfering with pre-existing fractures in sandstone (Calcione area, southern Tuscany, Italy). Journal of Structural Geology 33, 644–661.

Bull, J.M., Barnes, P.M., Lamarche, G., Sanderson, D.J., Cowie, P. A., Taylor, S.K., Dix, J.K., 2006. High-resolution record of displacement accumulation on an active normal fault: implications for models of slip accumulation during repeated earthquakes. Journal of Structural Geology 28, 1146–1166.

Cartwright, J., Trudgill, B., Mansfield, C., 1995. Fault growth by segment linkage: an explanation for scatter in maximum displacement and trace length data from the Canyonlands Grabens of SE Utah. Journal of Structural Geology 17, 1319–1326.

Cherpeau, N., Caumon, G., Lévy, B., 2010. Stochastic simulations of fault networks in 3D structural modeling. Comptes Rendus Geoscience 342, 687–694.

Childs, C., Nicol, A., Walsh, J.J., Watterson, J., 2003. The growth and propagation of synsedimentary faults. Journal of Structural Geology 25, 633–648.

Cowie, P., Underhill, J., Behn, M., Lin, J., Gill, C., 2005. Spatio-temporal evolution of strain accumulation derived from multi-scale observations of Late Jurassic rifting

in the northern North Sea: A critical test of models for lithospheric extension. Earth and Planetary Science Letters 234, 401–419.

Cowie, P. A., Sornette, D., Vanneste, C., 1995. Multifractal scaling properties of a growing fault population. Geophysical Journal International 122, 457–469.

Cowie, P.A., 1998. A healing – reloading feedback control on the growth of seismogenic faults. Journal of Structural Geology 20, 1075–1087.

Cowie, P.A., Scholz, C.H., 1992. Growth of faults by accumulation of seismic slip. Journal of Geophysical Research 97, 11085–11095.

Curewitz, D., Karson, J.A., 1997. Structural settings of hydrothermal outflow: Fracture permeability maintained by fault propagation and interaction. Journal of Volcanology and Geothermal Research 79, 149–168.

Dawers, N.H., Anders, M.H., 1995. Displacement – length scaling and fault linkage. Journal of Structural Geology 17, 607–614.

Dawers, N.H., Anders, M.H., Scholz, C.H., 1993. Growth of normal faults: displacment-length scaling. Geology 21, 1107–1110.

Faulkner, D.R., Jackson, C. A. L., Lunn, R.J., Schlische, R.W., Shipton, Z.K., Wibberley, C. A. J., Withjack, M.O., 2010. A review of recent developments concerning the structure, mechanics and fluid flow properties of fault zones. Journal of Structural Geology 32, 1557–1575.

Faulkner, D.R., Mitchell, T.M., Jensen, E., Cembrano, J., 2011. Scaling of fault damage zones with displacement and the implications for fault growth processes. Journal of Geophysical Research 116, 1–11.

Ferrill, D. A., Morris, A.P., McGinnis, R.N., 2009. Crossing conjugate normal faults in field exposures and seismic data. AAPG Bulletin 93, 1471–1488.

Giba, M., Walsh, J.J., Nicol, A., 2012. Segmentation and growth of an obliquely reactivated normal fault. Journal of Structural Geology 39, 253–267.

Gupta, A., Scholz, C.H., 2000. A model of normal fault interaction based on observations and theory. Journal of Structural Geology 22, 865–879.

Gupta, S., Cowie, P.A., Dawers, N.H., Underhill, J.R.A., 1998. Mechanism to explain rift basin subsidence and stratigraphic patterns through fault array evolution. Geology 26, 595–598.

Heffer, K.J., Bevan, T.G., 1990. Scaling relationships in natural fractures – data, theory and applications. Proc. Eur. Petrol. Conf. 2, 367–376 (SPE Pap, 20981).

Henza, A. A., Withjack, M.O., Schlische, R.W., 2011. How do the properties of a pre-existing normal-fault population influence fault development during a subsequent phase of extension? Journal of Structural Geology 33, 1312–1324.

Huggins, P., Watterson, J., Walsh, J.J., Childs, C., 1995. Relay zone geometry and displacement transfer between normal faults recorded in coal-mine plans. Journal of Structural Geology 17, 1741–1755.

Imber, J., Tuckwell, G.W., Childs, C., Walsh, J.J., Manzocchi, T., Heath, A. E., Bonson, C.G., Strand, J., 2004. Three-dimensional distinct element modelling of relay growth and breaching along normal faults. Journal of Structural Geology 26, 1897–1911.

Jolley, S.J., Barr, D., Walsh, J.J., Knipe, R.J., 2007. Structurally complex reservoirs: an introduction. Geological Society, London, Special Publications 292, 1–24.

Kakimi, T., 1980. Magnitude-frequency relation for displacement of minor faults and its significance in crustal deformation. Bull. Geol. Surv. Jpn 31, 467–487.

Kerrich, R., 1986. Fluid infiltration into fault zones: Chemical, isotopic, and mechanical effects. Pure and Applied Geophysics 124, 225–268.

Kim, Y-S., Andrews, J.R., Sanderson, D.J., 2001. Reactivated strike–slip faults: examples from north Cornwall, UK. Tectonophysics 340, 173–194.

Kim, Y-S., Peacock, D.C.., Sanderson, D.J., 2003. Mesoscale strike-slip faults and damage zones at Marsalforn, Gozo Island, Malta. Journal of Structural Geology 25, 793–812.

Kim, Y-S., Peacock, D.C.., Sanderson, D.J., 2004. Fault damage zones. Journal of Structural Geology 26, 503–517.

Kim, Y-S., Sanderson, D.J., 2005. The relationship between displacement and length of faults: a review. Earth-Science Reviews 68, 317–334.

King, G., 1986. Speculations on the geometry of the initiation and termination processes of earthquake rupture and its relation to morphology and geological structure. Pure and Applied Geophysics 124, 567–585.

Kolyukhin, D., Torabi, A., 2012. Statistical analysis of the relationships between faults attributes. Journal of Geophysical Research 117, 1–14.

Krantz, R.W., 1988. Multiple fault sets and three-dimensional strain: Theory and application. Journal of Structural Geology 10, 225–237.

Kristensen, M.B., Childs, C.J., Korstgård, J. A., 2008. The 3D geometry of small-scale relay zones between normal faults in soft sediments. Journal of Structural Geology 30, 257–272.

Leveille, G., Knipe, R., More, C., Ellis, D., Dudley, G., Jones, G., Fisher, Q.J., Allinson, G., 1997. Compartmentalization of Rotliegendes gas reservoirs by sealing faults, Jupiter Fields area, southern North Sea. Geological Society, London, Special Publications 123, 87–104.

Long, J.J., Imber, J., 2012. Strain compatibility and fault linkage in relay zones on normal faults. Journal of Structural Geology 36, 16–26.

Maerten, L., Willemse, E.J.M., Pollard, D.D., Rawnsley, K., 1999. Slip distributions on intersecting normal faults. Journal of Structural Geology 21, 259–272.

Manighetti, I., King, G., Gaudemer, Y., Scholz, C., 2001. Slip accumulation and lateral propagation of active normal faults in Afar. Journal of Geophysical Research 106, 13667–13696.

Mansfield, C., Cartwright, J., 2001. Fault growth by linkage: observations and implications from analogue models. Journal of Structural Geology 23, 745–763.

Manzocchi, T., Walsh, J.J., Nicol, A., 2006. Displacement accumulation from earthquakes on isolated normal faults. Journal of Structural Geology 28, 1685–1693.

Marrett, R., Allmendinger, R.W., 1992. Amount of extension on " small " faults: An example from the Viking graben.

Meyer, V., Nicol, A., Childs, C., Walsh, J.J., Watterson, J., 2002. Progressive localisation of strain during the evolution of a normal fault population. Journal of Structural Geology 24, 1215–1231.

Micklethwaite, S., Cox, S.F., 2004. Fault-segment rupture, aftershock-zone fluid flow, and mineralization. Geology 32, 813.

Mitchell, T.M., Faulkner, D.R., 2009. The nature and origin of off-fault damage surrounding strike-slip fault zones with a wide range of displacements: A field study from the Atacama fault system, northern Chile. Journal of Structural Geology 31, 802–816.

Mouslopoulou, V., Walsh, J.J., Nicol, A., 2009. Fault displacement rates on a range of timescales. Earth and Planetary Science Letters 278, 186–197.

Nicol, A., Walsh, J.J., Villamor, P., Seebeck, H., Berryman, K.R., 2010. Normal fault interactions, paleoearthquakes and growth in an active rift. Journal of Structural Geology 32, 1101–1113.

Nicol, A., Walsh, J.J., Watterson, J., Bretan, P., 1995. Three-dimensional geometry and growth of conjugate normal faults. Journal of Structural Geology 17, 847–862.

Nicol, A., Watterson, J., Walsh, J., Childs, C., 1996. The shapes, major axis orientations and displacement patterns of fault surfaces. Journal of Structural Geology 18, 235–248.

Nieto-Samaniego, Á. F., Alaniz-Alvarez, S. A., 1997. Origin and tectonic interpretation of multiple fault patterns. Tectonophysics 270, 197–206.

Nieto-Samaniego, Á.F., 1999. Stress, strain and fault patterns. Journal of Structural Geology 21, 1065–1070.

Nixon, C.W., Sanderson, D.J., Bull, J.M., 2011. Deformation within a strike-slip fault network at Westward Ho!, Devon U.K.: Domino vs conjugate faulting. Journal of Structural Geology 33, 833–843.

Nixon, C.W., Sanderson, D.J., Bull, J.M., 2012. Analysis of a strike-slip fault network using high resolution multibeam bathymetry, offshore NW Devon U.K. Tectonophysics 541-543, 69–80.

Norton, D., Knapp, R., 1977. Transport phenomena in hydrothermal systems: the nature of porosity. Am. J. Sci.;(United States) 277, 913–936.

Peacock, D.C.P, Sanderson, D.J, 1991. Displacements, segment linkage and relay ramps in normal fault zones. Journal of Structural Geology 13, 721–733.

Peacock, D.C.P., Sanderson, D.J., 1994. Geometry and development of relay ramps in normal fault systems. AAPG Bulletin 78, 147–165.

Peacock, D.C.P., Sanderson, D.J., 1995. Strike-slip relay ramps. Journal of Structural Geology 17, 1351–1360.

Peacock, D.C.P., Sanderson, D.J., 1996. Effects of propagation rate on displacement variations along faults. Journal of Structural Geology 18, 311–320.

Pickering, G., Bull, J.M., Sanderson, D.J., 1995. Sampling power-law distributions. Tectonophysics 248, 1–20.

Pickering, G., Peacock, D.C.P., Sanderson, D.J., Bull, J.M., 1997. Modeling Tip Zones to Predict the Throw and Length Characteristics of Faults. AAPG Bulletin 81, 82–99.

Pollard, D.D., Fletcher, R.C., 2005. Fundamentals of Structural Geology. Cambridge University Press, Cambridge.

Quigley, M., Van Dissen, R., Litchfield, N., Villamor, P., Duffy, B., Barrell, D., Furlong, K., Stahl, T., Bilderback, E., Noble, D., 2012. Surface rupture during the 2010 Mw 7.1 Darfield (Canterbury) earthquake: Implications for fault rupture dynamics and seismic-hazard analysis. Geology 40, 55–58.

Reches, Z., 1978. Analysis of faulting in three-dimensional strain field. Tectonophysics 47, 109–129.

Sanderson, D.J., Zhang, X., 1999. Critical stress localization of flow associated with deformation of well-fractured rock masses, with implications for mineral deposits. Geological Society, London, Special Publications 155, 69–81.

Sanderson, D.J., Zhang, X., 2004. Stress-controlled localization of deformation and fluid flow in fractured rocks. Geological Society, London, Special Publications 231, 299–314.

Schlische, R.W., Withjack, M.O., 2009. Origin of fault domains and fault-domain boundaries (transfer zones and accommodation zones) in extensional provinces: Result of random nucleation and self-organized fault growth. Journal of Structural Geology 31, 910–925.

Scholz, C.H., 1990. Mechanics of Faults and Earthquakes. Cambridge University Press, New York.

Schultz, R. A., Soliva, R., Fossen, H., Okubo, C.H., Reeves, D.M., 2008. Dependence of displacement–length scaling relations for fractures and deformation bands on the volumetric changes across them. Journal of Structural Geology 30, 1405–1411.

Schwarz, H.-U., Kilfitt, F.-W., 2008. Confluence and intersection of interacting conjugate faults: A new concept based on analogue experiments. Journal of Structural Geology 30, 1126–1137.

Sharp, I.R., Gawthorpe, R.L., Underhill, J.R., Gupta, S., 2000. Fault-propagation folding in extensional settings: Examples of structural style and synrift sedimentary response from the Suez rift, Sinai, Egypt. Geological Society of America Bulletin 112, 1877–1899.

Shipton, Z.K., Cowie, P. A., 2003. A conceptual model for the origin of fault damage zone structures in high-porosity sandstone. Journal of Structural Geology 25, 333–344.

Sibson, R.H., 1987. Earthquake rupturing as a mineralizing agent in hydrothermal systems.

Sibson, R.H., 1989. Earthquake faulting as a structural process. Journal of Structural Geology 11, 1–14.

Smith, D.R., 1980. Sealing and nonsealing faults in Louisiana Gulf Coast Salt Basin. AAPG Bulletin 64, 145–172.

Soliva, R., Benedicto, a., Schultz, R. A., Maerten, L., Micarelli, L., 2008. Displacement and interaction of normal fault segments branched at depth: Implications for fault growth and potential earthquake rupture size. Journal of Structural Geology 30, 1288–1299.

Soliva, R., Benedicto, A., 2004. A linkage criterion for segmented normal faults. Journal of Structural Geology 26, 2251–2267.

Soliva, R., Schultz, R. A., 2008. Distributed and localized faulting in extensional settings: Insight from the North Ethiopian Rift–Afar transition area. Tectonics 27, TC2003.

Spencer, A.M., Larsen, V.B., 1990. Fault traps in the northern North Sea. Geological Society, London, Special Publications 55, 281–298.

Taylor, S.K., Bull, J.M., Lamarche, G., Barnes, P.M., 2004. Normal fault growth and linkage in the Whakatane Graben, New Zealand, during the last 1.3 Myr. Journal of Geophysical Research 109, B02408.

Walsh, J., Watterson, J., 1989. Displacement gradients on fault surfaces. Journal of Structural Geology 11, 307–316.

Walsh, J., Watterson, J., Yielding, G., 1991. The importance of small-scale faulting in regional extension. Nature 351, 391–393.

Walsh, J.J., Childs, C., Imber, J., Manzocchi, T., Watterson, J., Nell, P. A. R., 2003. Strain localisation and population changes during fault system growth within the Inner Moray Firth, Northern North Sea. Journal of Structural Geology 25, 307–315.

Walsh, J.J., Watterson, J., 1988. Analysis of the relationship between displacements and dimensions of faults. Journal of Structural Geology 10, 239–247.

Walsh, J.J., Watterson, J., 1991. Geometric and kinematic coherence and scale effects in normal fault systems. Geological Society, London, Special Publications 59, 193–203.

Xu, S., Nieto-Samaniego, a. F., Alaniz-Álvarez, S. a., Velasquillo-Martínez, L.G., Grajales-Nishimura, J.M., García-Hernández, J., Murillo-Muñetón, G., 2010. Changes in fault length distributions due to fault linkage. Journal of Geodynamics 49, 24–30.

Zhang, X., Sanderson, D.J., 1996. Numerical modelling of the effects of fault slip on fluid flow around extensional faults. Journal of Structural Geology 18, 109–119.

Zhang, X., Sanderson, D.J., 1998. Numerical study of critical behaviour of deformation and permeability of fractured rock masses. Marine and Petroleum Geology 15, 535–548.

2. Deformation within a strike-slip fault network at Westward Ho!, Devon U.K.: Domino vs conjugate faulting

Casey W. Nixon, David J. Sanderson, Jonathan M. Bull

2.1. Abstract

A system of NE-trending left-lateral faults and NW-trending right-lateral faults at Westward Ho! (north Devon, U.K.) cut steeply dipping (~60°) strata. Faults were accurately mapped in the field and from aerial photography, and lateral separations of marker beds measured along the fault traces. These data are used to examine the displacements within the network of interacting faults and to calculate variations in the density and relative proportions of the fault sets. The displacements are also used in a tensor analysis of the strain and, together with block rotations, used to restore the deformation.

The results show a range of heterogeneity within the fault network, both in terms of the fault patterns and strain. Some sub-areas show a dominance of one fault set, with regularly spaced larger displacements, separating relatively weakly deformed blocks with smaller antithetic faults. Within these areas up to 20º rotation of the faults and bedding produces a domino style deformation that accommodates up to ~15% extension. The domino regions are separated by areas of conjugate faulting, in which both sets of faults are equally developed and have similar displacement ranges. Conjugate areas have little or no rotation of the bedding and generally lower strains than domino regions.

2.2. Introduction

The major aim of this paper is to characterize the deformation and kinematic behaviour within a strike-slip fault network and demonstrate the applicability to other fault networks. The geometry, connectivity, displacement distribution, role of different fault sets and strain distribution are important to understanding fault networks. These features are important for controlling the behaviour of the rock mass. For example, fault networks provide pathways for fluid flow that are important in the generation, exploration and production of hydrocarbons, groundwater and mineral deposits, and in understanding the distribution of displacement and earthquakes in active systems (e.g. King, 1986; Sibson, 1989; Taylor et al., 2004).

Much work has been done to determine the movement and formation of individual faults (Muraoka and Kamata, 1983; Barnett et al., 1987; Walsh and Watterson 1988; Nicol et al., 1996; Kim et al., 2001) and interacting fault segments (Peacock, 1991; Peacock and Sanderson, 1994, 1995; Cartwright et al., 1995; Childs et al., 1995; Huggins et al., 1995; Taylor et al., 2004). Such studies have increased our understanding of the growth and evolution of individual fault zones (Cox and Scholz, 1988), particularly for strike-slip faults (Aydin and Schultz, 1990; Peacock, 1991; Peacock and Sanderson,1995; Du and Aydin, 1995; Kim et al., 2003). Single sets of faults may become organized to accommodate crustal deformation, as in the case of domino faulting and associated block rotations (Luyendyk et al., 1980; Nur et al., 1986; Axen, 1988; Peacock et al., 1998) or more commonly two or more fault sets may interact to produce a fault network. The simplest example of this is a pair of conjugate faults (e.g. Freund, 1974; Nicol et al., 1995; Zhao and Johnson, 1991; Kelly et al., 1998).

This paper seeks to extend and develop such studies to large fault networks, within which deformation may be distributed with varying degrees of heterogeneity as a result of the interaction and localization of displacement and strain (e.g. Zhang & Sanderson 2001). It describes and identifies the characteristics and behaviour on a mesoscale strike-slip fault network at Westward Ho!, north Devon, Furthermore, it assesses the variation in geometry and kinematics that exist within the network, focussing on the way that the faults

interact with one another, the spatial variations in their geometry and the strain that is produced.

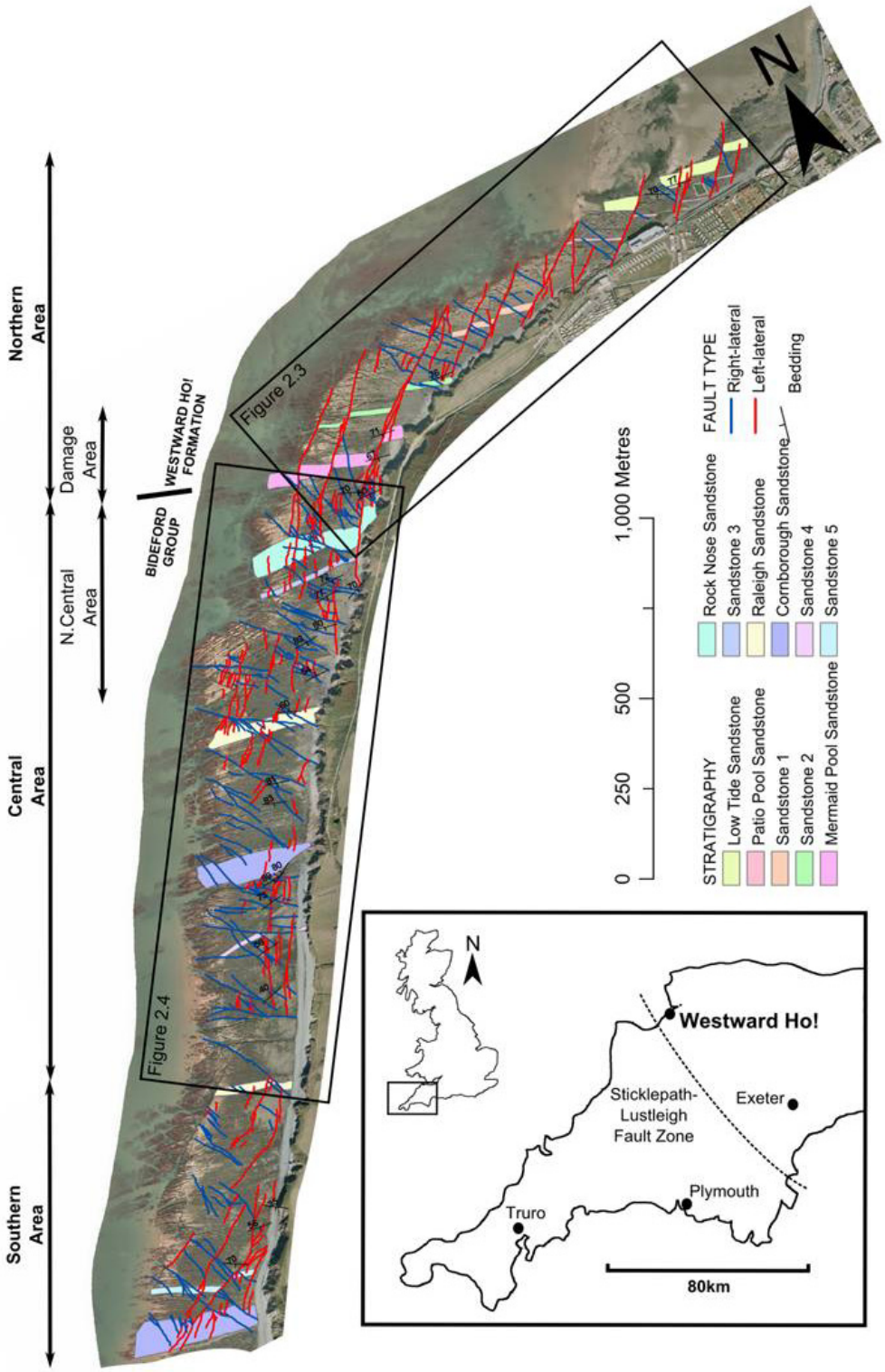

Figure 2.1 Interpreted aerial photograph of the wave-cut platform at Westward Ho! showing the main sandstone units. The northern area corresponds to Figure 2.3 and the central area to Figure 2.4. Inset is a location map of the area. Image/Data courtesy of the Channel Coastal Observatory.

Strike-slip systems are very suitable for such analysis since most of the significant variation is presented in map-view. Hence, the requirements for this study were a well exposed surface with many faults and a detailed (and steeply dipping) stratigraphy that would allow accurate determination of fault displacement throughout the network. The wave-cut platform at Westward Ho!, north Devon, provides such conditions.

2.3. Geological Setting

The strike-slip faults at Westward Ho! cut Upper Carboniferous stratigraphy comprising repeated, coarsening upwards cycles of mudstones, siltstones and sandstones, originally deposited in a deltaic environment (Elliot, 1976). These cycles are divided into two units (Figure 2.1): the Westward Ho! Formation (~400 m) and the Bideford Group (~800 m) (Walker, 1970; Elliot, 1976; Higgs et al., 1990). This detailed stratigraphy provides a basis for the accurate determination of displacement along the faults.

WNW-trending upright folds are observed in the Bideford Group and formed during Variscan deformation (Sanderson, 1984) that inverted the basin at the end of the Carboniferous period. The strike-slip faults are divided into NE-trending left-lateral faults and NW-trending right-lateral faults, implying a N-S directed maximum horizontal principal stress during deformation.

Much of SW Britain was affected by late Variscan NW-SE strike-slip faulting (Dearman, 1963) that cross-cuts earlier folds and thrusts. This deformation was part of a late Variscan right-lateral shear zone that transected southern Europe during the Late Palaeozoic (Arthaud and Matte, 1977; Badham, 1982), as a result of right-lateral transpression due to oblique NW-SE convergence between the African and European plates (Coward and McClay, 1983; Sanderson, 1984; Barnes and Andrews, 1986; Holdsworth, 1989).

The strike-slip faults at Westward Ho! clearly post-date the Variscan folds and, hence, are either related to this late Variscan event or to later Cretaceous-Tertiary N-S shortening (Lake and Karner, 1987; Chadwick, 1993; Peacock and Sanderson, 1998). The precise age or cause of the faults in the area is not required for this study, because the faults do not appear to show signs of

multiphase movement or reactivation. What is important is that the faults are strike-slip in nature and, hence, their displacement can be characterized by measuring the mapped offsets of the known stratigraphy.

The map (Figure 2.1) shows two dominant sets of faults cutting steeply dipping (>60º) beds. The faults are interpreted as forming a strike-slip fault network on the basis of:

1. In map view, they form two sets with relatively straight traces at about 60-70º to each other (Figure 2.2);
2. The NW-SE trending set consistently produces right-lateral separations of marker beds, whereas the NE-SW trending set has consistent left-lateral separations (Figures 2.3 and 2.4);
3. Both sets of faults are sub-vertical and their intersection is steeply plunging (Figure 2.2b);
4. Both sets have sub-horizontal slickenside lineations (Figure 2.2b);
5. Occasional fold hinges are offset laterally by the faults and have both limbs offset with the same separation.

Both fault sets extend layering sub-parallel to bedding strike (~E-W). The possibility that they could have developed as normal faults prior to the steepening of the beds can be dismissed because the faults cross-cut the folds and have similar geometry and separations on opposite limbs (point 5 above).

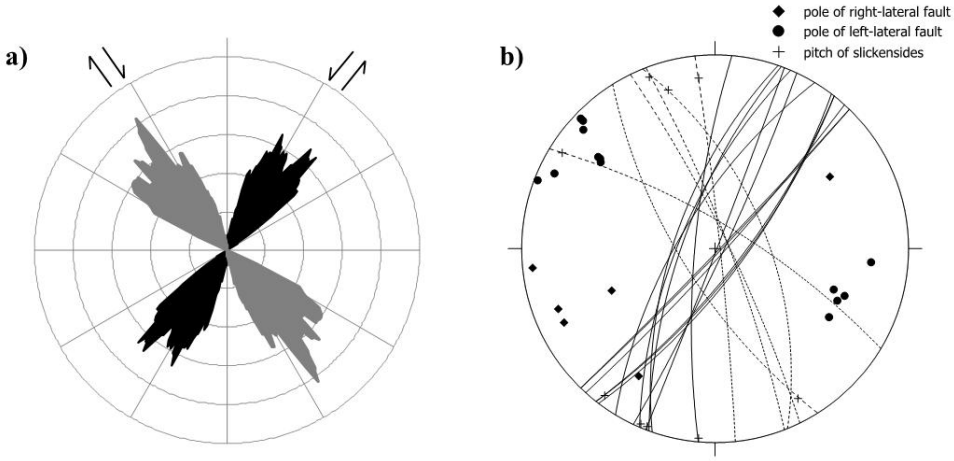

Figure 2.2 a) Length-weighted rose diagram of the study area with grey representing right-lateral faults and black for left-lateral faults. b) Equal-area stereographic projection of fault data throughout the area. Dotted lines represent right-lateral faults and solid lines represent left-lateral faults.

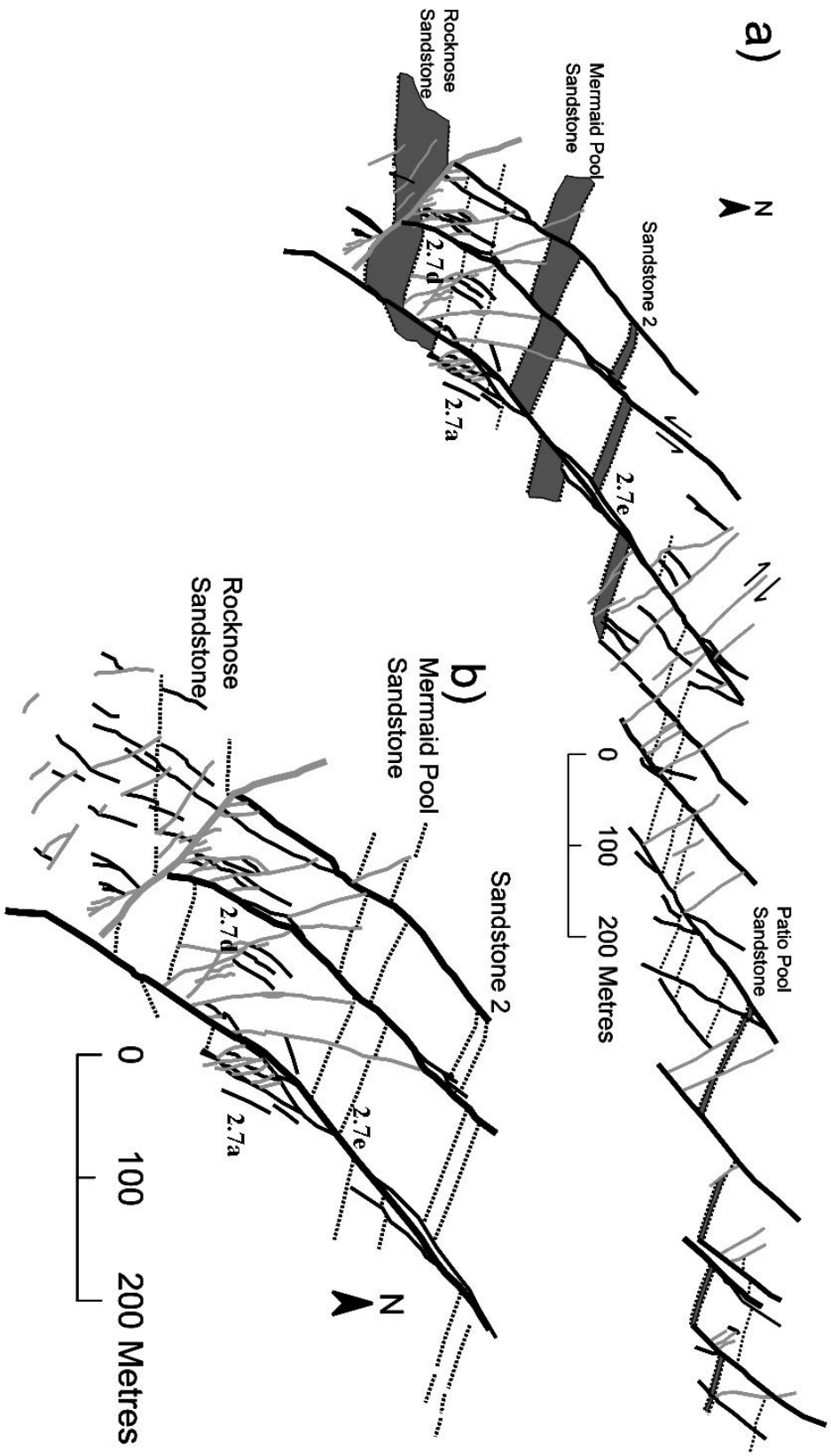

Figure 2.3 a) Map of the northern area in Figure 2.1, which shows the dominance and slight rotation of left-lateral faults. b) An enlarged fault map of a damage zone at the southern limits of the northern area (Figure 2.3a). The location of the D-X plots in Figures 2.7a, d and e are indicated. Solid lines represent faults with grey and black for right- and left-lateral faults, respectively.

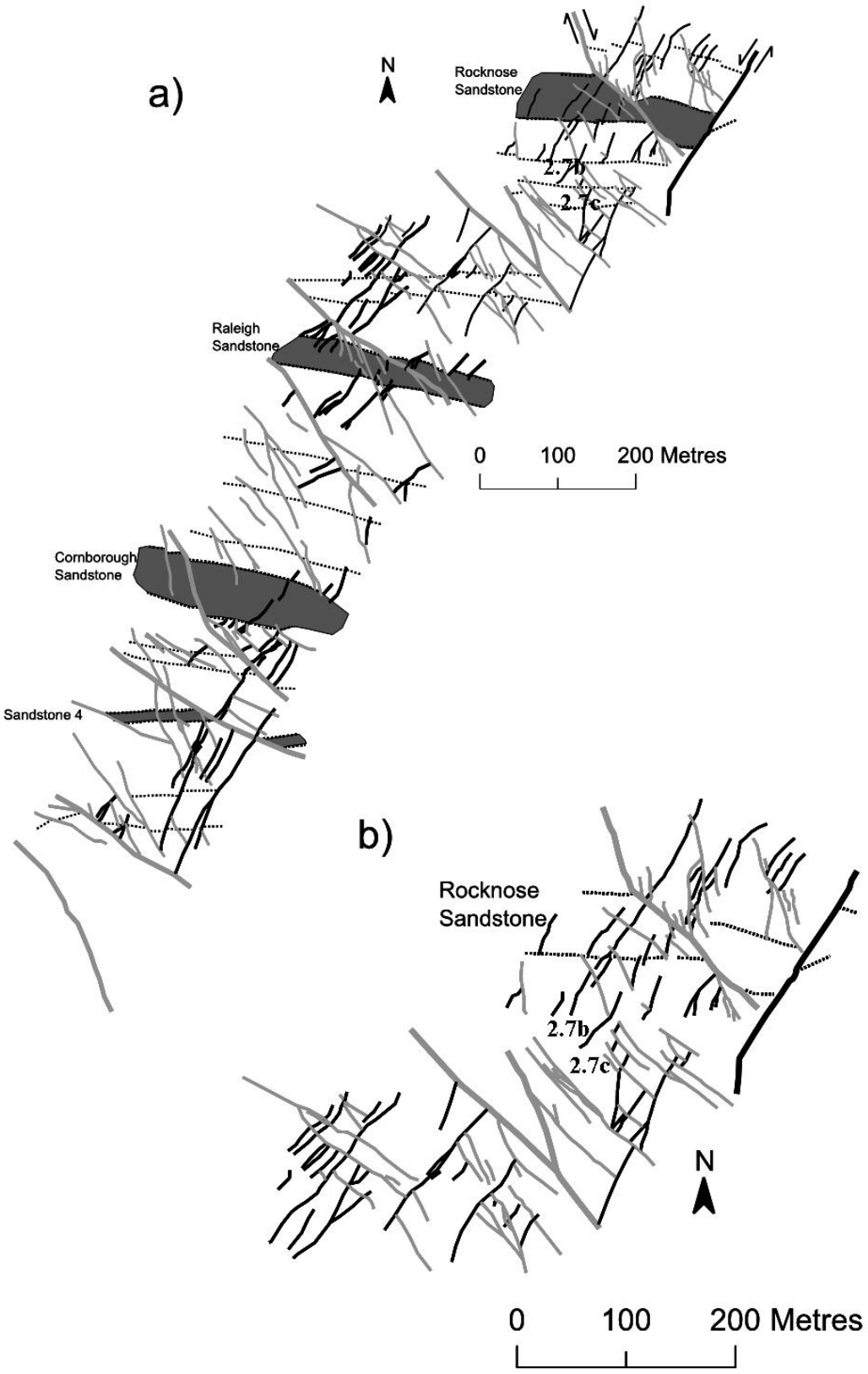

Figure 2.4 a) Map of the central area in Figure 2.1, which shows the dominance of right-lateral faults. b) An enlarged fault map of the north central area showing a greater concentration of smaller magnitude faults of both fault sets. The location of the D-X plots in Figures 2.7b and c are indicated. Solid lines represent faults with grey and black as right- and left-lateral faults, respectively.

2.4. Methodology

2.4.1. Mapping

The fault network at Westward Ho! is continuously exposed along a 4 km-long wave-cut platform, with a width of 200-400 m (Figure 2.1). Digital aerial photography of the wave-cut platform was acquired at low tide in 2006 and made available courtesy of the Channel Coast Observatory. The images have a pixel resolution of 0.1 m (equivalent to a 1:5000 scale film) and are orthorectified. These aerial images were used to provide excellent base maps for detailed mapping, and to expand the field mapping to cover the entire coastal strip.

Marker beds on either side of faults were correlated and their lateral separations measured. The maps were integrated with previous mapping by Walker (1970) and Higgs et al. (1990). Structural data were also collected, including bedding and fault orientations, as well as slickenside measurements where possible.

2.4.2. Displacement analysis

The orthorectified aerial images were imported into ArcGIS with all the field data and interpreted marker beds. The cut-offs of marker beds were digitized along most faults, allowing the calculation of separations at locations along fault traces. Data from ArcGIS were exported to spreadsheets for further analysis and display (d-x plots, rose diagrams, etc.).

Lateral separations of beds on the sub-horizontal wave-cut platform approximate the strike-slip displacement of the faults. In the field, direct measurement of separation was done using a 30 m tape. Measurements of lateral separations also used the measuring tool in ArcGIS. Comparison of these two approaches showed excellent agreement and separations are considered to have errors of < 0.5 m for large faults, with direct field measurement of separations on small faults being accurate to ~10 mm.

Given displacement and fault orientation are available for many positions along faults, we displayed the information in four ways:

1. **Displacement-distance (d-x) plots** were produced for selected faults, where the distance (x) may be the length along the fault trace or the

projection of this length along some chosen direction. The latter type of plot is mainly used to look at the interactions of NW and NE-trending faults and, hence, the N-S direction is a convenient common reference. Where faults intersect each other, displacement profiles were produced for each interacting fault branch and extrapolated to the intersection point. Consequently, no displacement was allocated to the intersection point because it represents an abrupt change in displacement from one fault branch to another.

2. **Displacement-orientation plots**, which are simply scatter-plots of displacement against fault strike for each fault segment, are used to indicate differences in the displacement characteristics for the different fault sets.

3. **Length-weighted rose diagrams** were obtained by calculating the total trace-length within varying orientation bins. In general a 15º class interval was used centred on a 1º step around the circle. These plots are mainly to examine the variation in frequency and orientation of the fault sets in different subareas.

4. **(Length x displacement) weighted rose diagrams** are similar to length-weighted rose diagrams, except that the distribution of the product of trace-length x displacement is plotted against orientation. These plots therefore indicate the dominant displacements on the different fault sets throughout the network.

2.4.3. Strain determination

Strain analysis was conducted using a technique based on the method developed by Peacock and Sanderson (1993). This approach involves the calculation of a displacement tensor $\mathbf{D_{ij}}$, that is formed from the cross-product of the unit vector normal to the fault plane, (**n**) and the displacement direction within the fault plane, (*s* **u**), where u is a unit vector in the slip direction and s is the displacement on the fault. Peacock and Sanderson (1993) applied this approach to *n* faults sampled along a line of length *L*, using a weighting factor (*w*) to correct for the orientation bias of such samples, where $\mathbf{D_{ij}} = ws$ (**n** x **u**). The Lagrangian strain tensor is $\mathbf{E_{ij}}$, given by:

$$\mathbf{E_{ij}} = n/L \sum [(\mathbf{D_{ij}} + \mathbf{D_{ji}})/2] \quad (2.1)$$

The same approach is valid for sampling on a plane. The weight (w) is determined from the angle between the fault normal and the plane. As the strike-slip faults are sub-vertical, both the fault normal and displacement vector are sub-horizontal and, hence, the weighting factor can be ignored (i.e. $w \rightarrow 1$). If the fault trace strikes at an angle θ to north then:

$$\mathbf{n} = (-\sin\theta,\ \cos\theta) \quad \text{and} \quad \mathbf{u} = (\cos\theta,\ \sin\theta) \quad (2.2)$$

and

$$D_{ij} = \sum s \begin{pmatrix} n_1 u_1 & n_1 u_2 \\ n_2 u_1 & n_2 u_2 \end{pmatrix} = \sum s \begin{pmatrix} -\sin\theta\cos\theta & -\sin^2\theta \\ \cos^2\theta & \cos\theta\sin\theta \end{pmatrix} \quad (2.3)$$

where *s* is +ve for left-lateral and –ve for right-lateral faults. The term *n/L* in equation 2.1 represents the fault density and is replaced in the planar sample by Σ(*tracelength*)/*area* ($\Sigma t/A$) , the 2-D equivalent of the fault density. Thus the Lagrangian strain tensor is given by:

$$\mathbf{E_{ij}} = 1/A \sum t\ (\mathbf{D_{ij}} + \mathbf{D_{ji}})/2] \quad (2.4)$$

The eigenvectors and eigenvalues of the strain tensor provide estimates of the orientation and magnitude of the principal strains.

2.5. Fault Network Characteristics

2.5.1. Spatial distribution and magnitude variation of fault sets

The two sets of strike-slip faults vary in their relative abundance throughout the Westward Ho! area (Figures 2.1, 2.3, 2.4). The northern area (Figure 2.3) is dominated by a series of long left-lateral faults, whereas the adjacent region to the south (Figure 2.4b) has approximately equal distributions of left- and right-lateral faults. By contrast, in the central part of the study area (Figure 2.4a) large right-lateral faults are dominant. This variation is clearly seen in the rose diagrams of the trace-length distributions that show a dominance of left-lateral

faults in the northern area (Figure 2.5a) and right-lateral faults in the south-central area (Figure 2.5c) with a region of more equal representation of both sets in the centre (Figure 2.5b).

Fault displacements may be as large as 80 m, but 79% of the overall fault trace-length has displacements less than 10 m. The distribution of fault displacements varies (Figure 2.6). In the left-lateral dominated area in the north, faults with displacements >10 m form about half the mapped trace-length and all are left-lateral (Figure 2.6a). In contrast, in the north central area (Figure 2.4b) only 10% of the trace length is formed from large (>10 m) displacement faults, which include both left- and right-lateral sets.

The (length x displacement) weighted rose diagrams (Figure 2.5) further emphasize that the dominant fault set changes across the area. The north central area still has equal proportions of both fault sets (Figure 2.5e), whereas the areas to the north and south have a dominance of left- (Figure 2.5d) and right- (Figure 2.5f) lateral displacement, respectively.

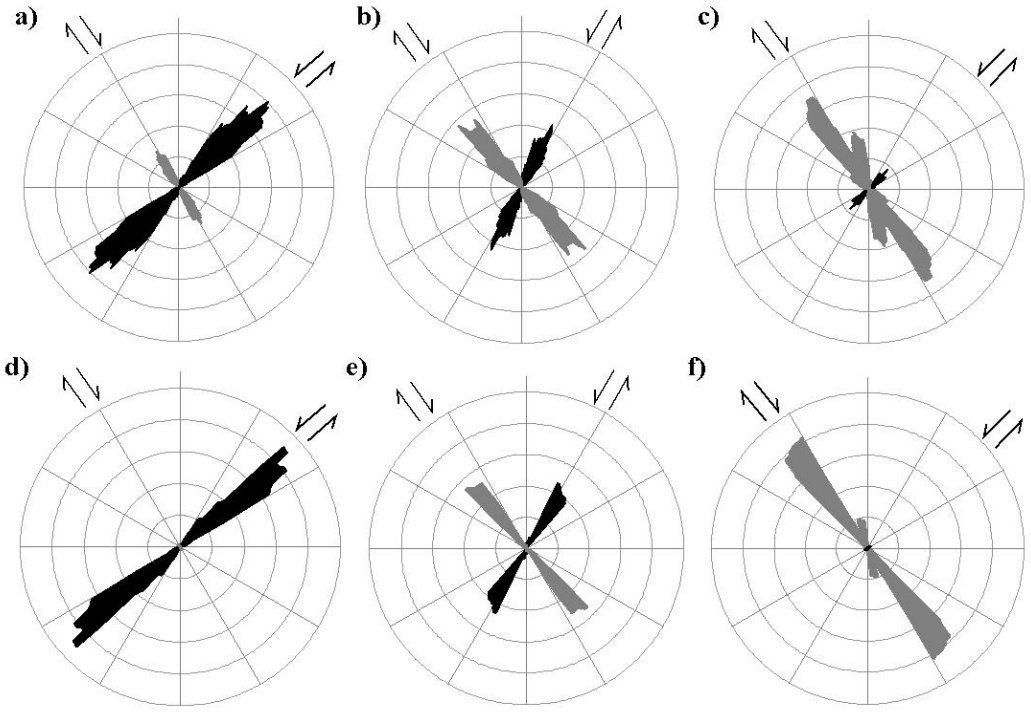

Figure 2.5 Length-weighted rose diagrams for: a) the northern area; b) the north central area; c) the central area. (Length x displacement) weighted rose diagrams for: d) the northern area; e) the north central area; f) the central area with a dominance of right-lateral faults. Note the change in dominance from north to south. Grey represents right-lateral faults and black represents left-lateral faults.

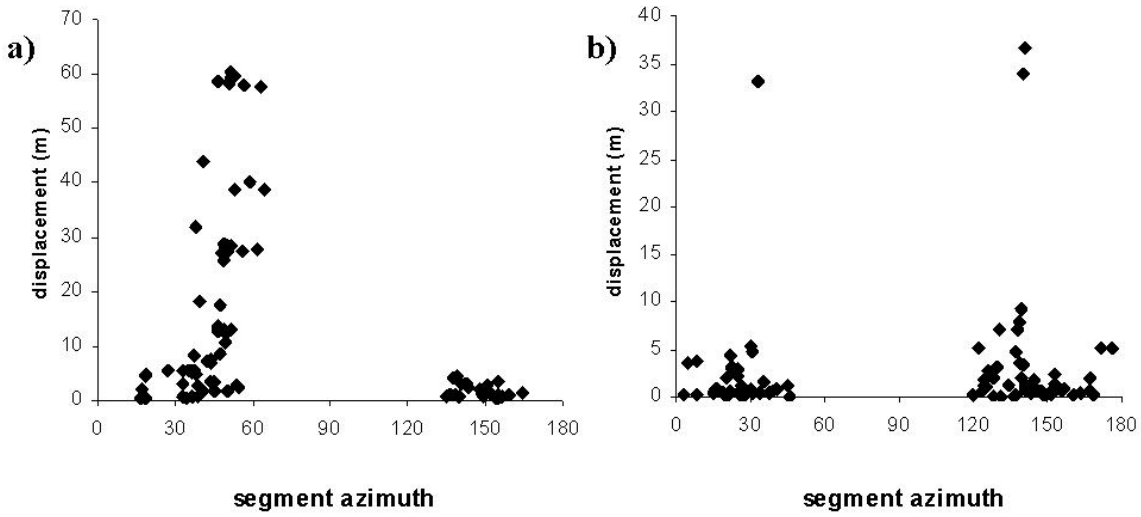

Figure 2.6 Plot of displacement against azimuth for: a) the northern area; b) the north central area.

The left-lateral dominated areas in the north (Figure 2.3) and at the southern limits of the study area are characterized by large magnitude (10-80 m) left-lateral faults, and large magnitude right-lateral faults characterize the right-lateral dominated central area (Figure 2.4a). The large left-lateral faults are more closely spaced (75-100 m) than their right-lateral counterparts (100-200 m) and have smaller displacements than the largest right-lateral faults.

2.5.2. Displacement profiles and interaction of fault sets

Isolated faults are relatively uncommon and tend to be small faults with a simple pattern of displacement that increases from zero at the tips to a maximum value, usually near the centre of the fault trace (Figure 2.7a). This pattern has been widely described before (e.g. Barnett et al., 1987).

Y- or T- shaped intersections are where a fault abuts against a fault of the other set (e.g. Figure 2.7b). Displacement changes abruptly on AB at the intersection (C), which corresponds to a similar change on CD. Thus, both faults show similar displacement patterns as they approach their intersection point, such that the displacements on both faults almost cancel out one another. Another important feature of many Y-shaped intersections is that the displacement on the abutting fault (CD) increases away from the intersection (cf. splays discussed below).

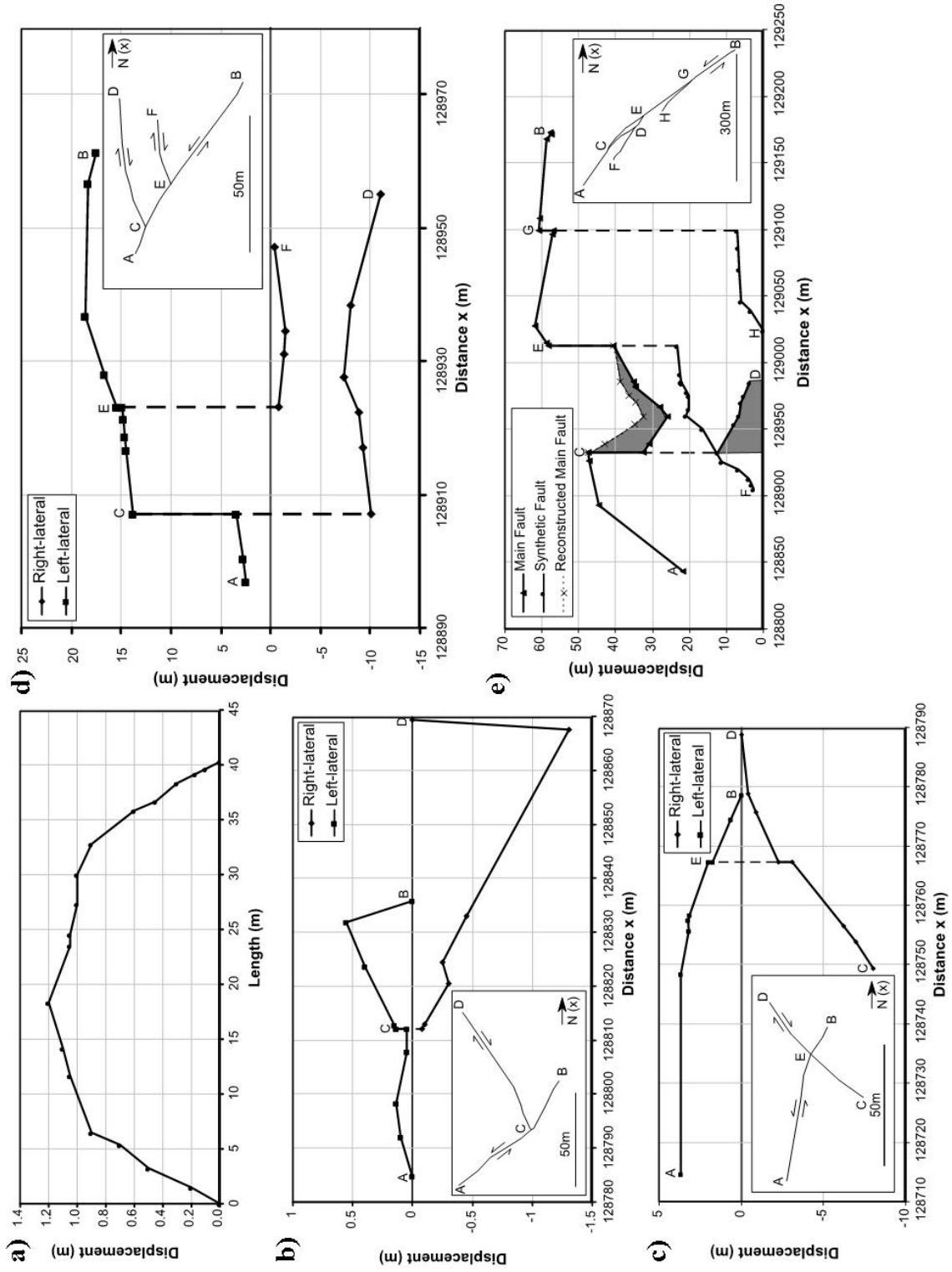

Figure 2.7 Plots of displacement against distance for different fault interactions in which left- and right-lateral displacements are plotted as +ve and –ve, respectively: a) an isolated fault; b) Y- shaped intersection; c) X-shaped intersection; d) antithetic fault interactions; e) synthetic fault interaction with a damage lens, and a reconstructed profile for the main fault without the lens is also plotted. For each d-x plot an inset shows the plan-view geometry of the fault intersection.

X-shaped intersections result when two faults cross-cut one another. They are much less frequent than Y-intersections, and are commonly small displacement (<10 m) faults (e.g. Figure 2.7c). For example, a left-lateral fault (AB) and a right-lateral fault (CD) have displacements of 4 m and 8 m at points A and C, respectively, with tips at B and D (Figure 2.7c). At the intersection point, the displacements decrease to about 2 m on both faults at steps of ~1 m. Assuming that these faults were propagating towards their tips, much of the displacement was possibly achieved prior to their intersection. The similarity in the stepping of the displacement and the lack of offset suggests that one fault is not simply displacing the other. Such intersections cannot be reconstructed by the movement of rigid blocks and must involve significant internal deformation of the fault blocks. They may form due to sequential movement of the fault sets (Freund, 1974; Ramsay and Huber, 1987; Zhao and Johnson, 1991) or simultaneous movement of the two fault sets (Horsfield, 1980; Nicol et al., 1995). At Westward Ho!, these X-intersections are usually developed in mud-rich parts of the sequence.

All faults that abut or cross-cut each other produce Y- or X- shaped intersections, respectively. Still, two additional intersection geometries are:

Antithetic fault interactions result when smaller displacement faults abut (or occasionally cross-cut) larger displacement faults with the opposite motion sense, producing a series of Y- *(*and occasionally X-) shaped intersections along the major fault. They generally produce small steps in the d-x profiles of the dominant faults. For example, the left-lateral fault (AB) in Figure 2.7d has a displacement (18 m) with two interacting antithetic faults (CD - 10 m and EF - 2 m). Both antithetic faults maintain a near constant displacement approaching the main fault and at the intersection. At the intersections, the 10 m and 1 m displacements on CD and EF produce corresponding changes in the displacement on fault AB. Hence, a series of antithetic faults on the same wall of the dominant fault create stepped displacement changes and characteristically is a geometry by which faults reduce displacement towards their tip (e.g. Figure 2.7d).

Synthetic faults interactions are where a major fault branches, producing a series of Y- shaped intersections and lenses. The splays generally have

smaller displacements with the same sense of motion, and occur at a small angle (generally < 30º) to the major fault. Splays that rejoin the main fault produce lenses.

Figure 2.7e shows a left-lateral fault with a displacement of ~60 m that has a series of splays (at E and G) and lenses (between C and D). The total displacement on the main fault is determined by combining the displacements C to D with that on the main trace between C and E. This determination produces a displacement profile with two main steps at E and G. A simple splay occurs at G with a ~6 m step in displacement onto the splay, that branches from the main fault and extends for ~75 m to a tip at H. Another splay occurs at E with a ~20 m step in displacement onto the splay, that branches from the main fault and extends for ~200 m to a tip at F. Note that in both cases, the maximum displacement for the splay is at the intersection (E and G) with the main fault.

The development and spatial distribution of these different interactions varies throughout the study area. The north central area (Figure 2.4b) has many Y- and X-shaped intersections of small-magnitude faults in areas between large magnitude faults. In contrast, the northern area (Figure 2.3a) has a more organized arrangement of large left-lateral faults that have intersections with smaller interacting antithetic faults (and some synthetic faults). These synthetic and antithetic faults are more concentrated in the damage area (Figure 2.3b) between these two regions.

2.5.3. Strain

The Lagrangian strain tensor, determined from the fault displacements, shows a variation in the maximum extension from < 5% to > 15% (Figure 2.8; Table 2.1). The largest extension (15.5%) is in the northern area, with 10.4% in the damage area and 5.3% in the north central area. The strains increase to the south (Figure 2.8b). The strain in the northern area is accommodated by the block rotation and larger displacement along the left-lateral faults. It is about three times greater than in the north central region, which has approximately equal numbers of left- and right-lateral faults with negligible block rotation.

An overall E-W (N093ºE) extension is present in the north central area of conjugate faults (Figure 2.4b), changing to ENE-WSW (N068ºE) in the northern

area. In the central area, the trend is WNW-ESE (N114ºE) where right-lateral faults dominate (Figure 2.4a). Furthermore, the changes in extension direction coincide with changes in percentage extension (Figure 2.8). This change supports the idea that greater rotational strains are developed where one fault set dominates in different areas of the fault network.

Table 2.1 Structural characteristics of mapped areas (Figure 2.2) at Westward Ho!.

	Northern Area	Damage Area	N. Central Area	Central Area
	Domino (left-lateral)		Conjugate	Domino (right-lateral)
Fault density (km^{-1})	11	39	28	19
% extension	15.5	10.4	5.3	6.3
Direction of maximum extension (θ)	N068ºE	N073ºE	N093ºE	N114°E

A graph of the % maximum extension against N-S distance (Figure 2.8b) illustrates a progressive change in strain between the northern, central and southern areas. The extension in an E-W direction is ~5% in the northern area and is, hence, compatible with the E-W extensions in the conjugate region to the south such that no discontinuities are required at subarea boundaries.

Strain restoration (Figure 2.9) was performed by dividing a region into blocks of stratigraphy bounded by the main faults. The blocks were rotated until the stratigraphic bedding was orientated approximately E-W with fault displacements removed. This procedure produced a restoration with only minor gaps and overlaps (Figure 2.9). The north-central area was restored by removing the displacements on the two sets of faults without rotation (Figure 2.9a). In contrast, the northern area, which is dominated by left-lateral faults, shows a pronounced left-lateral shear accompanied by N-S shortening or left-lateral transpression that is accommodated by large displacements on the left-lateral faults and clockwise rotation of the intervening blocks (Figure 2.9b). This is consistent with the compatibility of deformation between the regions. Thus, the larger strains in the northern area are accommodated by the increased rotation.

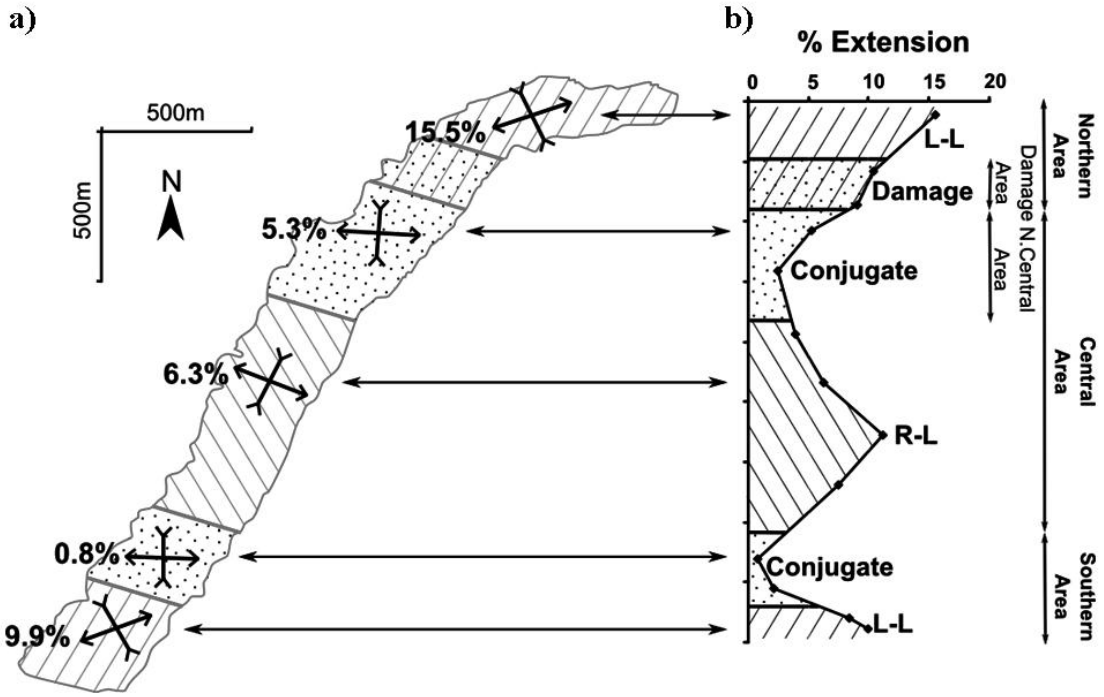

Figure 2.8 a) Diagram showing the orientations of the principal horizontal extensions for different sub areas. b) Graph of % extension plotted against distance.

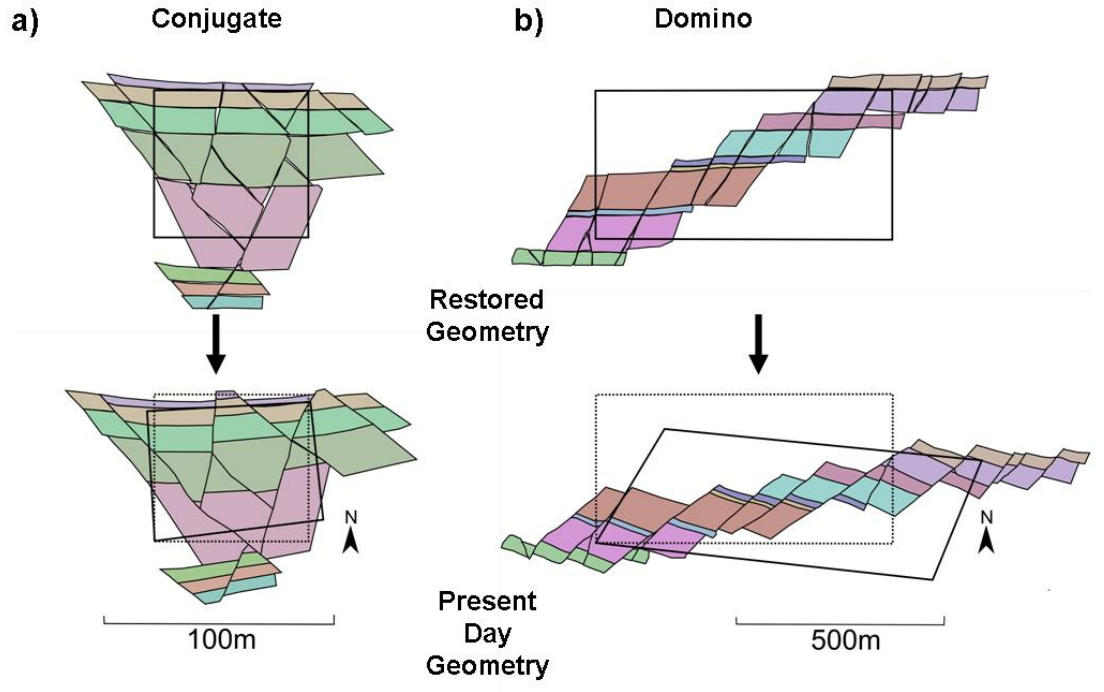

Figure 2.9 Strain restoration diagrams a) the conjugate area (Figure 2.4b) and b) the domino area (Figure 2.3a).

The fault densities of the four sub areas were also calculated (Table 2.1), where a density of 25 km^{-1} means that 25 km of fault trace-length is present in each square km of wave-cut platform. Again, fault densities vary between areas and even between right-lateral and left-lateral dominated areas.

2.6. Domino vs conjugate faulting

Variation in fault style on the wave-cut platform at Westward Ho! can be interpreted with reference to conjugate and domino models. Conjugate systems comprise similar numbers of the two intersecting sets of faults with their opposite displacement senses, which accommodate pure shear bulk deformation with little rotation of bedding. The maximum and minimum principal stress directions (σ_1 and σ_3) bisect the angle between the two fault sets, with σ_1 as the acute angle (~60°) bisector (Figure 2.10). Domino faulting, on the other hand, consists of mainly one fault set, producing fault bounded blocks which rotated during deformation (e.g. Axen, 1988) (Figure 2.10). Fault blocks may have internal deformation due to the presence of smaller magnitude faults. The distribution and arrangement of small faults within a fault block can sometimes counteract the rotation of the fault block (Peacock et al., 1998).

2.6.1. Conjugate Area

An area of conjugate faults is found in the north-central area and separates the right-lateral and left-lateral dominant areas (Figure 2.8). In this area, both left-lateral and right-lateral faults are developed to a more-or-less equal degree (Figures 2.5b and 2.5e). The maximum weighted azimuth for the fault sets are N320°E for right-lateral faults and N030°E for left-lateral faults with a bisector at N355°E, which is assumed to approximate the maximum horizontal compressive stress direction during deformation. The area consists dominantly of small-displacement (< 10 m) faults that compose 90% of the fault trace-length (Figure 2.6b). The fault density is 28 km^{-1} and the faults produce 5.3% extension in an E-W direction (Table 2.1).

Small-displacement faults typically form conjugate Y- and X-shaped intersections, which have similar displacements and experience related

changes in displacement at intersection points (Figure 2.7b and 2.7c). Within this region, the overall strike of bedding is approximately E-W, and is only locally deflected adjacent to both sets of faults. Restoration of the fault blocks does not require rotation and produces small gaps and overlaps (Figure 2.9). These characteristics attest to an approximately pure shear deformation.

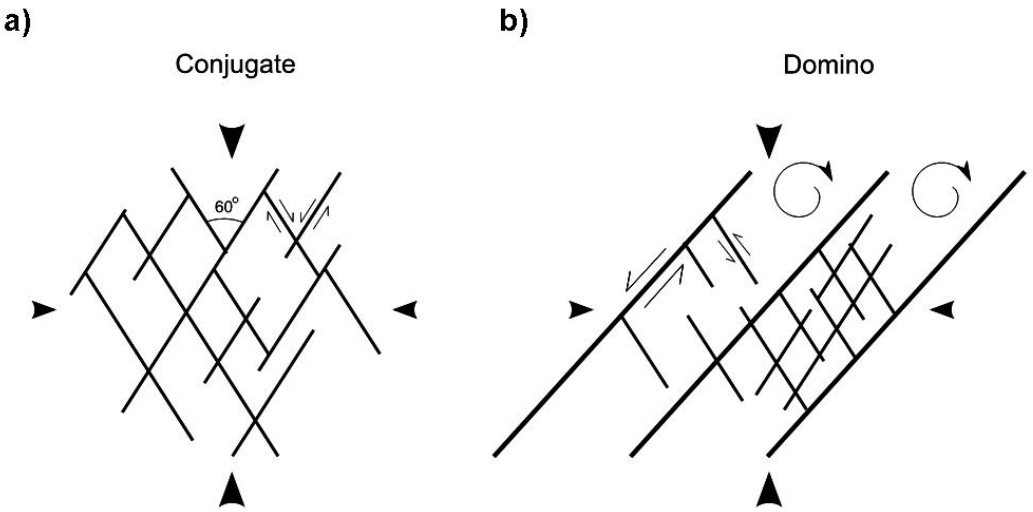

Figure 2.10 Schematic diagram illustrating typical fault geometries: a) Conjugate fault network where faults have similar magnitudes and the maximum stress direction bisects the acute angle of intersection; b) Domino fault network with a dominant fault set and rotation of fault blocks. Arrows indicate far-field loading.

2.6.2. Domino Area

The domino areas are much larger than the conjugate areas. The northern area (Figure 2.3) best exemplifies this style of deformation, having an abundance of large left-lateral faults (Figures 2.5a and 2.5d). The central area (Figure 2.4a) has some characteristics of a right-lateral domino domain.

2.6.2.1. *Northern area*

Left-lateral faults have a modal orientation of N050°E, which is a 20° clockwise rotation when compared with the modal orientation of left-lateral faults in the conjugate area. They have displacements of 10-80 m and compose 49% of the total trace-length for all faults in the subarea (Figure 2.9b; Table 2.1) accounting for most of the displacement (Figure 2.5d).

The northern domino area has approximately half the fault density ($11km^{-1}$) of the conjugate area, but has about three times the extension (15.5%). The orientation of maximum extension is N068°E. The strike of bedding between

the dominant faults is N110°E, which agrees well with the 20° clockwise rotation inferred from the fault rotation. The strain restoration illustrates the importance of block rotation of stratigraphy in the domino area, which accounts for the rotation of faults and bedding (Figure 2.9).

2.6.2.2. *Central area*

Many features in the central (Figure 2.4a) area fit a right-lateral domino model: trace-length (Figure 2.5c) and displacement (Figure 2.5f) predominantly related to right-lateral faults. The right-lateral area has both antithetic and synthetic faults, compared to the well developed antithetic faults between the main faults in the northern area. The fault density (19 km^{-1}) is intermediate between the northern domino area and the north-central conjugate area, mainly due to the greater development of both sets of faults between the larger faults. This geometry shows that the internal fault-block deformation of the right-lateral dominated areas is greater with conjugate sets, forming small-displacement Y- and X-shaped fault intersections between large, widely spaced, right-lateral faults. The lack of rotation in the right-lateral domains could be due to greater internal deformation and the distance between large faults (Axen, 1988).

2.6.3. Damage Area

The southern limit of the northern domino area occurs in the region surrounding the outcrop of the Rocknose Sandstone (Figure 2.3b). This area is dominated by several large-displacement left-lateral faults with orientations of about N030°E. Displacement along the main left-lateral faults is small where they curve with many small antithetic and synthetic faults, forming damage lenses, producing a large fault density of 39 km^{-1}. The complexity of the fault geometry in this area is enhanced by the development of synthetic splay faults and transfer faults across the lenses.

This damage area is situated between the well-developed conjugate and domino areas. It inherits some damage features related to the transition from domino to conjugate and the change from left-lateral to right-lateral dominant areas, and is related to the change in fault dominance and kinematic behaviour (i.e. simple shear to pure shear).

2.7. Discussion

Displacement distribution profiles across individual faults within the network can be broadly categorised into two types:

a) Conjugate interactions involving Y- and X-shaped intersections between faults with similar magnitudes. Similar kinematic characteristics have been found in other areas. Peacock (1991) described conjugate interactions between faults in Scotland where displacements on one fault are related to the other as the intersection point was approached. He also noted that conjugate intersections were associated with rapid loss of displacement at fault tips, much like examples in Figure 2.7b and 2.7c.

b) Antithetic and synthetic interactions, where large faults are linked to sets of smaller displacement faults with opposite and similar displacement senses, respectively. The smaller faults produce a series of systematic steps in the displacement profile of the larger fault. Kim et al. (2000) also found this change in displacement magnitudes for numerous antithetic fault interactions at Crackington Haven in North Cornwall, where small step-like decreases in displacement occurred like the main left-lateral fault in Figure 2.7d.

The fault geometries, displacement distribution and the strain variation in the study area are heterogeneously developed throughout the whole strike-slip network. In general, the network has conjugate areas that form between domino areas. This relationship has been observed in other types of fault systems where the dominant fault sets change. For example, McClay et al. (2002) described conjugate areas of normal faults in the East African Rift system between areas dominated by east-dipping normal faults and west-dipping normal faults. Similarly, Fossen and Hesthammer (1998) described adjacent domino and conjugate (horst and graben) regions in the Gullfaks field in the Northern North Sea.

The strain distribution throughout the fault network at Westward Ho! indicates a more organized system with greater strains being accommodated by the development of domino regions that interact with each other. These domino regions have displacement and strain localized onto one of the fault sets with

slip and rotation creating a change in orientation for the maximum extension. Where two domino regions with opposite dominant fault sets, interact with each other, a conjugate region forms. The existence of distinct conjugate and domino regions within the fault network allows a comparison between the two (summarized in Table 2.2).

Table 2.2 Characteristics of conjugate and domino regions.

	CONJUGATE	DOMINO
One fault set dominant	no	yes
Symmetrical fault trend (displacement Weighted)	yes	no
Equal displacement on both sets	yes	no
Rotation of stratigraphy and faults	no	yes

The conjugate area has symmetrical fault trends with similar trace-lengths and displacements on opposing fault sets. Evidence for significant rotation of either the faults or the stratigraphy is absent. Similar characteristics are found in other conjugate networks, for example the strike-slip fault networks in the Yilgarn Craton of western Australia (Vearncombe, 1998) and Nash Point in south Wales (Bourne and Willemse, 2001). The fault network map for Nash Point is very similar to that for the conjugate area at Westward Ho! (i.e. Figure 2.10a and Figure 2.4b), showing faults cross-cutting each other, forming conjugate fault intersections. Similar characteristics were also seen for conjugate normal faults (Nicol et al..1995; Ferrill et al., 2000, 2009).

In contrast, the domino area contains a dominant fault set, with asymmetrical trace-length and displacement weighted rose diagrams. Both the faults and bedding show a systematic rotation. Strike-slip movement in southern California also exhibits these domino characteristics with regions rotated clockwise and anti-clockwise depending on the dominant fault set. For example, the Mojave Desert Block has rotated anti-clockwise due to a dominance of right-lateral fault movement (Dokka and Travis, 1990), whereas the NE area of the Mojave Desert Block has accumulated a clockwise rotation due to the dominance of left-lateral faults (Luyendyk et al., 1980; Dokka and

Travis 1990). Furthermore, the original domino models observed by Wernicke and Burchfiel (1982) and Proffett (1977) in the Basin and Range region of the USA show similar characteristics for a normal fault system.

The applicability of these characteristics from the study area to other fault networks means that we can use them to identify whether a fault network is behaving in a domino or conjugate fashion (i.e. simple shear or pure shear, respectively) and whether it is kinematically homogeneous or heterogeneous. For the cases discussed here, the fault sets are at a high angle to layering which has a minimal affect on the resulting geometries. This means that the observations and characteristics are easily related to strike-slip and normal fault networks. However, this study cannot be as easily related to thrust regimes where layer-parallel detachment is usually more dominant and strongly influences fault geometry.

In this study, methods and observations, which have previously been used for individual faults, have been developed and applied to describe the geometry, kinematics and deformation of a fault network. This is an important step forward in fault analysis as faults rarely occur individually and without associated deformation. Hence, analysing faults on a network scale is vital to understanding the brittle deformation of the crust.

2.8. Conclusions

Detailed mapping on a well exposed wave-cut platform at Westward Ho!, north Devon is used to characterize a strike-slip fault network. The fault network comprises NW-trending right-lateral faults and NE-trending left-lateral faults. Geometric interactions between faults involve conjugate, antithetic and synthetic arrangements and include Y- and X-shaped intersection points, the former being most common.

Changes in the size and proportion of the fault sets within the fault network can be related to variations in bulk strain and kinematic behaviour, whilst preserving strain compatibility between different domains. Areas with domino-fault geometries have:

a) A dominant fault set with an asymmetry in (length x displacement) weighted rose diagrams.

b) A distinction between larger displacement, regularly spaced, faults of the dominant set and smaller antithetic faults in the intervening blocks. The smaller faults interact with the larger faults to produce changes in displacement along their lengths.

c) Systematic rotation of both the dominant faults and bedding.

In contrast, areas with overall conjugate-fault geometry have:

a) Equal development of both sets of faults, and each have similar ranges of displacement.

b) The interactions between faults typically produce abutting or cross-cutting relationships with displacement changes affecting both intersecting faults.

c) Little or no rotation of the bedding.

Domino areas accumulated greater strains, with extensions of ~15% compared with <5% in conjugate areas. The higher strains are usually accommodated by a greater proportion of large-displacement faults and rotation of the maximum horizontal extension.

Restoration of fault displacement shows rotational strains in the domino areas and irrotational (pure shear) strain in the conjugate areas. Boundaries between these deformation domains are difficult to determine due to the limits of the exposures, but appear to be sub-parallel to bedding strike (i.e. E-W). Both the domino and conjugate areas have similar E-W extensions of ~ 5% and, hence, there is compatibility of strain across their boundaries. Damage zones can also be found between domains with lenses at fault bends and complex zones where faults die out against a large conjugate fault.

The techniques developed for the study area to analyse the fault patterns, interactions and resulting strains should be applicable to other fault networks. They can be used to analyse the deformation style, heterogeneity and strain/displacement localization within fault networks.

2.9. References

Arthaud, F., Matte, P., 1977. Late Paleozoic strike-slip faulting in southern Europe and northern Africa: Result of a right-lateral shear-zone between the Appalachians and the Urals. Geological Society of America Bulletin 88, 1305-1320.

Axen, G.J., 1988. The geometry of planar domino-style normal faults above a dipping basal detachment. Journal of Structural Geology 10, 405-411.

Aydin, A., Schultz, R.A., 1990. Effect of mechanical interaction on the development of strike-slip faults with echelon patterns. Journal of Structural Geology 12, 123-129.

Badham, J.P.N., 1982. Strike-slip orogens – an explanation for the Hercynides. Journal of the Geological Society 139, 493-504.

Barnes, R.P., Andrews, J.R., 1986. Upper Palaeozoic ophiolite generation and obduction in south Cornwall. Journal of the Geological Society 143, 117-124.

Barnett, J.A.M., Mortimer, J., Rippon, J., Walsh, J.J., Watterson, J., 1987. Displacement geometry in the volume containing a single normal fault. AAPG Bulletin 71, 925–937.

Bourne, S.J., Willemse, E.J.M, 2001. Elastic stress control on the pattern of tensile fracturing around a small fault network at Nash Point, UK. Journal of Structural Geology 23, 1753-1770.

Cartwright, J.A., Trudgill, B.D., Mansfield, C.B., 1995. Fault growth by segment linkage: an explanation for scatter in maximum displacement and trace length data from the Canyonlands Grabens of SE Utah. Journal of Structural geology 17, 1319-1326.

Chadwick, R.A., 1993. Aspects of basin inversion in southern Britain. Journal of the Geological Society 150, 311-322.

Childs, C., Watterson, J., Walsh, J.J., 1995. Fault overlap zones within developing normal fault systems. Journal of the Geological Society 152, 535–549.

Coward, M.P., McClay, K.R., 1983. Thrust tectonics of S.Devon. Journal of the Geological Society 140, 215-228.

Cox, S.J.D., Scholz, C.H., 1988. On the formation and growth of faults: an experimental study. Journal of Structural Geology 10, 413-430

Dearman, W.R., 1963. Wrench faulting in Cornwall and south Devon. Proceedings Geological Association 74, 265-287.

Dokka, R.K., Travis, C.J., 1990. Late Cenozoic strike-slip faulting in the Mojave Desert, California. Tectonics 9, 311-340.

Du, Y., Aydin, A., 1995. Shear fracture patterns and connectivity at geometric complexities along strike-slip faults. Journal of Geophysical Research 100, 18093-18102.

Elliott, T., 1976. Upper Carboniferous sedimentary cycles produced by river dominated, elongate deltas. Journal of the Geological Society 132, 199-208.

Ferrill, D.A, Morris,, A.P., Stamatakos, J.A., Sims, D.W. 2000. Crossing conjugate normal fault. AAPG Bulletin 84, 1543–1559.

Ferrill, D.A., Morris, A.P., McGinnis, R.N., 2009. Crossing conjugate normal faults in field exposures and seismic data. AAPG Bulletin 93, 1471-1488

Fossen, H., and J. Hesthammer, 1998, Structural geology of the Gullfaks field, northern North Sea. Geological Society, London, Special Publication 127, 231–261.

Freund, R., 1974. Kinematics of transform and transcurrent faults. Tectonophysics 21, 93-134

Higgs, R., Reading, H.G., Li, X., 1990. Upper Carboniferous lacustrine and deltaic sedimentology, SW England: Westward Ho! and Bude. British Sedimetological Research Group.

Holdsworth, R.E., 1989. The Start-Perranporth line: a Devonian terrane boundary in the Variscan orogen on SW England. Journal of the Geological Society 146, 419-421.

Horsfield, W. T., 1980. Contemporaneous movement along crossing conjugate normal faults. Journal of Structural Geology 5, 305-310.

Huggins, P., Watterson, J., Walsh, J.J., Childs, C., 1995. Relay zone geometry and displacement transfer between normal faults recorded in coal-mine plans. Journal of Structural Geology 17, 1741–1755.

Kelly, P.G., Sanderson, D.J., Peacock, D.C.P., 1998. Linkage and evolution of conjugate strike-slip fault zones in limestones of Somerset, Northumbria. Journal of Structural Geology 20, 1477-1493.

Kim, Y-S., Andrews, J.R., Sanderson, D.J., 2000. Damage zones around strike-slip fault systems and strike-slip evolution, Crackington Haven, southwest England. Geoscience Journal 4, 53-72.

Kim, Y-S., Andrews, J.R., Sanderson, D.J., 2001. Reactivated strike-slip faults: examples from north Cornwall. Tectonphysics 340, 173-194.

Kim, Y-S., Peacock, D.C.P., Sanderson, D.J., 2003. Strike-slip faults and damage zones at Marsalforn, Gozo Island, Malta. Journal of Structural Geology 25, 793-812.

King, G.C.P., 1986. Speculations on the geometry of the initiation and termination processes of earthquake rupture and its relation tomorphology and geological structure. Pure and Applied Geophysics 124, 567-585.

Lake, S.D., Karner, G.D., 1987. The structure and evolution of the Wessex Basin, southern England: an example of inversion tectonics. Tectonophysics 137, 347-378.

Luyendyk, B.P., Kamerling, M.J., Terres, R., 1980. Geometric model for Neogene crustal rotations in southern California. Geological Society of America Bulletin 91, 211-217.

McClay, K.R., Dooley, T., Whitehouse, P., Mills, M., 2002. 4-D evolution of rift systems: insights from scaled physical models. AAPG Bulletin 86, 935-959.

Muraoka, H., Kamata, H., 1983. Displacement distribution along minor fault traces. Journal of Structural Geology 5, 483-495.

Nicol, A., Walsh, J. J., Watterson, J., Bretan, P. G., 1995. Three-dimensional geometry and growth of conjugate normal faults. Journal of Structural Geology 17, 847-862.

Nicol, A., Watterson, J., Walsh, J.J., Childs, C., 1996. The shapes, major axis orientations and displacement patterns of fault surfaces. Journal of Structural Geology 18, 235–248.

Nur, A., Ron, H., Scotti, O., 1986. Fault mechanics and kinematics of block rotations. Geology 14, 746-749.

Peacock, D.C.P., 1991. Displacements and segment linkage in strike-slip fault zones. Journal of Structural Geology 13, 1025-1035.

Peacock, D.C.P., Sanderson, D.J., 1993. Estimating strain from fault slip using a line sample. Journal of Structural Geology 15, 1513-1516.

Peacock, D.C.P., Sanderson, D.J., 1994. Geometry and development of relay ramps in normal fault systems. AAPG Bulletin 78, 147-165.

Peacock, D.C.P., Sanderson, D.J., 1995. Strike-slip relay ramps. Journal of Structural Geology 17, 1351-1360.

Peacock, D.C.P., Sanderson, D.J., 1998. Deformation history and basin-controlling faults in the Mesozoic sedimentary rocks of the Somerset coast. Proceedings Geological Association 110, 41-52.

Peacock, D.C.P., Anderson, M.W., Morris, A., Randall, D.E., 1998. Evidence for the importance of 'small' faults on block rotation. Tectonophysics 299, 1-13.

Proffett, J.M., 1977. Cenozoic geology of the Yerington district, Nevada, and implications for the nature and origin of Basin and Range faulting. Geological Society of America Bulletin 88, 247-266.

Ramsay, J.G., Huber, M. I., 1987. Techniques of modern structural geology volume 2: folds and fractures. Academic Press, London.

Sanderson, D.J., 1984. Structural variation across the northern margin of the Variscides in NW Europe. Geological Society, London, Special Publications 14, 149-165.

Sibson, R.H., 1989. Earthquake faulting as a structural process. Journal of Structural geology 11, 1-14.

Taylor, S.K., Bull, J.M., Lamarche, G., Barnes, P.M., 2004. Normal fault growth and linkage in the Whakatane Graben, New Zealand, during the last 1.3 Myr. Journal of Geophysical Research 109, B02408

Vearncombe, J.R., 1998. Shear zones, fault networks, Archean gold. Geology 26, 855-858.

Walker, T.G., 1970. Deposition of turbidites and agitated water siltstones: a study of the Upper Carboniferous Westward Ho! Formation, North Devon. Proceedings Geological Association 18, 43-67.

Walsh, J.J., Watterson, J., 1987. Distributions of cumulative displacement and seismic slip on a single normal fault. Journal of Structural Geology 9, 1039-1046.

Walsh, J.J,, Watterson, J., 1988. Analysis and relationship between displacements and dimensions of faults. Journal of Structural Geology 10, 239-247.

Wernicke, B., Burchfiel, B.C., 1982. Modes of extensional tectonics. Journal of Structural Geology 4, 105-115.

Zhang X., Sanderson D.J. 2001. Evaluation of instability in fractured rock masses using numerical analysis methods: effects of fracture geometry and loading direction. Journal of Geophysical Research. 106, 26671-26687.

Zhao, G., Johnson, A.M., 1991. Sequential and incremental formation of conjugate sets of faults. Journal of Structural Geology 13, 887-895.

3. Analysis of a strike-slip fault network using high resolution multibeam bathymetry, offshore NW Devon U.K.

Casey W. Nixon, David J. Sanderson, Jonathan M. Bull

3.1. Abstract

Imaging of the sea floor offshore from Hartland Point (north Devon, U.K.), using high resolution multibeam bathymetry, reveals a strike-slip fault network. This consists of NE-trending left-lateral faults and NW-trending right-lateral faults that cut folded and steeply dipping strata (~60°). Faults were accurately mapped using the multibeam imagery, and lateral separations of marker beds measured along fault traces. These data are used to examine the spatial arrangement, fault displacement, and strain distribution within the network at different displacement cut-offs.

At high displacement cut-offs, the fault network is dominated by a few long isolated right-lateral fault segments that bound fault blocks, but at lower displacement cut-offs shorter left-lateral and right-lateral fault segments make up fault tips and infill fault blocks. The majority (70%) of fault trace-length is taken up by small fault segments that have <10 m displacement whereas 84% of strain is localised onto large fault segments with >10 m displacement. The topology and relative connectivity of the network is analyzed in terms of a system of fault branches between tips (I-nodes) or intersections (X or Y-nodes), the relative proportions of which reflect the connectivity of the network. Although the kinematic behaviour of the fault network is controlled by large fault segments, connectivity is very dependant on the small fault segments.

A comparison with a similar, nearby, strike-slip fault network at Westward Ho! (north Devon) shows many similarities and indicates that fault networks are better connected with increasing strain and that the network becomes better connected when strain is localised within damage zones rather than on individual faults.

3.2. Introduction

The analysis of fault networks is vital to understanding the brittle deformation of the Earth's crust as faults rarely occur individually and without associated deformation. Therefore, the major aim of this paper is to assess the changes in geometry, fault displacement and topology within a strike-slip fault network at different scales, hence, investigating the role of small and large faults. It will also demonstrate the use of high resolution multibeam bathymetry data as a tool to map and analyse an offshore strike-slip fault network.

Initial work on fault populations includes the application of power-law distributions to fault populations. This has been particularly useful for describing fault growth by looking at the distribution of fault displacement and fault trace-lengths (Cartwright et al., 1995; Gupta and Scholz, 2000; Soliva and Schultz, 2008; Xu et al., 2010). Geometric and kinematic studies of fault populations have also contributed to the understanding of fault segmentation, growth and propagation (e.g. Peacock & Sanderson 1991, 1994; Cartwright et al., 1995; Childs et al., 2003; Taylor et al., 2004; Bull et al., 2006; Baudon and Cartwright, 2008). Other work has investigated the importance and contribution of small scale faulting to the overall extension of an area (e.g. Walsh et al., 1991; Marrett and Allmendinger, 1992, Putz-Perrier and Sanderson 2008a, 2010) and their role in block rotations (e.g. Peacock et al., 1998).

This work suggests that fault systems evolve by individual faults increasing in both length and displacement, and that they become more linked with increasing finite strain (Ferrill et al., 1999; Walsh et al., 2001). This has been further supported by studies which show that fault populations evolve into longer and simpler systems with strain becoming localized within a fault system (e.g. Cowie et al., 1995; Nicol et al., 1997; Cowie et al., 2005; Moriya et al., 2005; Soliva and Schultz, 2008).

The use of high resolution reflection seismology has helped investigate displacement rate patterns within fault networks, both temporally and spatially, adding further to our understanding of fault movement, interaction and linkage within fault networks (Taylor et al., 2004; Mouslopoulou et al., 2009; Nicol et al., 2010). More recently Nixon et al. (2011) use aerial photography combined with

field data to map a strike-slip fault network at Westward Ho!, north Devon. This demonstrated a spatial variation in fault pattern, displacement distribution and kinematic behaviour, hence, illustrating the heterogeneity of deformation within a fault network.

This paper seeks to further this study by combining the techniques used in Nixon et al. (2011) with multibeam bathymetry data to map and describe a strike-slip fault network offshore Hartland Point, north Devon (Figure 3.1). It will determine the overall fault trends and kinematic behaviour of the network, investigating the possible affects of changing resolution on the geometry, topology, connectivity, and strain distribution within the network. This is then compared and correlated with onshore strike-slip networks at Hartland Quay and Westward Ho!.

3.3. Geological Setting

The strike-slip faults in north Devon cut Upper Carboniferous mudstones, siltstones and sandstones of the Crackington, Westward Ho!, Bideford and Bude Formations (Figure 3.1) (Higgs et al., 1990). These form part of the Culm Basin that was later inverted at the end of the Carboniferous period during Variscan deformation, which produced ~E-W trending upright folds throughout the region (Sanderson, 1979, 1984).

The strike-slip faults comprise NE-trending left-lateral faults and NW-trending right-lateral faults that are related to approximately N-S compression. The precise age of the strike-slip faults may not be determined stratigraphically, but field evidence shows that they do post-date the late Variscan folding (Higgs et al., 1990). Hence, it is thought that these faults formed in either: **1)** a late Variscan right-lateral shear zone that occured during the Late Paleozoic (Arthaud and Matte, 1977; Badham, 1982) caused by oblique NW-SE convergence between the African and European plates (Coward and McClay, 1983; Sanderson, 1984; Barnes and Andrews, 1986; Holdsworth, 1989); or **2)** during late Cretaceous-Tertiary N-S shortening (Lake and Karner, 1987; Chadwick, 1993; Peacock and Sanderson, 1998) caused by the northward collision of the African plate into the Eurasian plate and/or Atlantic ridge-push

forces as Britain drifted from the American plate (Underhill and Patterson, 1998).

Some strike-slip faults in north Cornwall and Devon are known to be reactivated (Kim et al., 2001). For example, the Sticklepath-Lustleigh fault zone (Figure 3.1) is thought to have formed in the late Variscan event as a NW-trending right-lateral fault zone before undergoing left-lateral reactivation in the late Cretaceous-Tertiary (Holloway and Chadwick, 1986). The faults at Hartland do not show signs of multiphase movement or reactivation and, hence, their precise age is not important for this study. What is important is that the upright folding, steeply dipping bedding and strike-slip nature of the faults allow accurate measurements of displacements from mapped offsets of folds and stratigraphy.

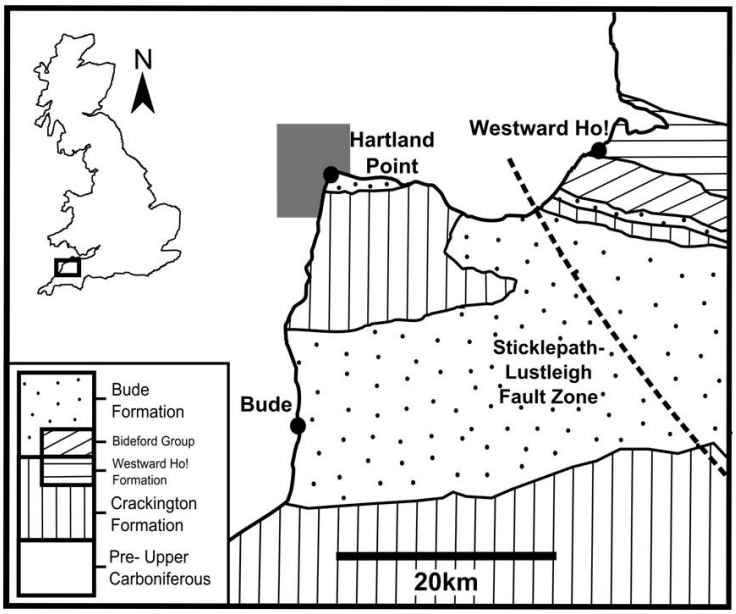

Figure 3.1 Location map with the main geological units. The grey area represents the interpreted offshore region.

3.4. Mapping Methods

The strike-slip fault network was mapped from high resolution multibeam bathymetry data of the offshore region to the north and west of Hartland Point (Figure 3.1). These data were collected as part of the UK Civil Hydrography Programme with the data being collected in 2007 and 2008 by two vessels: MV Meridian using a Reson 7125 400 kHz multibeam, and MV Jetstream using a Kongsberg Maritime EM3002D multibeam. The data are of high quality and

image features at the coast in water depths of only -1.0 m chart datum. This coverage was achieved by surveying at high tide and utilising the large tidal range in the Bristol Channel.

The multibeam bathymetry data were imported into ArcGIS for analysis and interpretation, and a geo-referenced 3D image with a pixel resolution of 0.5 m was created. Interpretation was completed using Hillshade images which accentuated bedding and fault traces. An illumination source azimuth of 315° with an altitude of 45° was used for the Hillshade, which was chosen to enhance bed structure for identifying offsets of marker beds and measuring displacements. The degree of slope was also calculated from the multibeam data, and this combined with measurement of the strike of identified bedding planes, allowed determination of the strike and dip of bedding.

The multibeam bathymetry (Figure 3.2) revealed a submerged platform of bedrock extending ~2.5 km from the shore line that provides a much more extensive area (~16 km^2), than that exposed at low tide on the wave-cut platforms. The high quality of the multibeam data allowed direct correlation of bedding and faults with features mapped onshore on wave-cut platforms (Figure 3.3). However there are localized sand pockets offshore which prevents correlation in some of the more sheltered coves such as the areas between Dyers Lookout and Damehole Point and adjacent to Upright Cliff.

The faults were digitized manually from the bathymetry imagery. The cut-offs of marker beds with faults were identified and these then used to calculate a series of lateral separations along each fault trace. Thus, the trace of each fault comprises a number of segments separated by points with a measured separation. The average separation was determined for each fault segment. Separations are difficult to measure at intersections between two faults, hence, fault segments that share an intersection point with another fault were assigned the same separation value as that measured at the other end of the segment. This means that all the faults comprising the network are divided into segments and that each is associated with a value of separation or displacement. The extracted fault segments were the primary structural data used for further analysis.

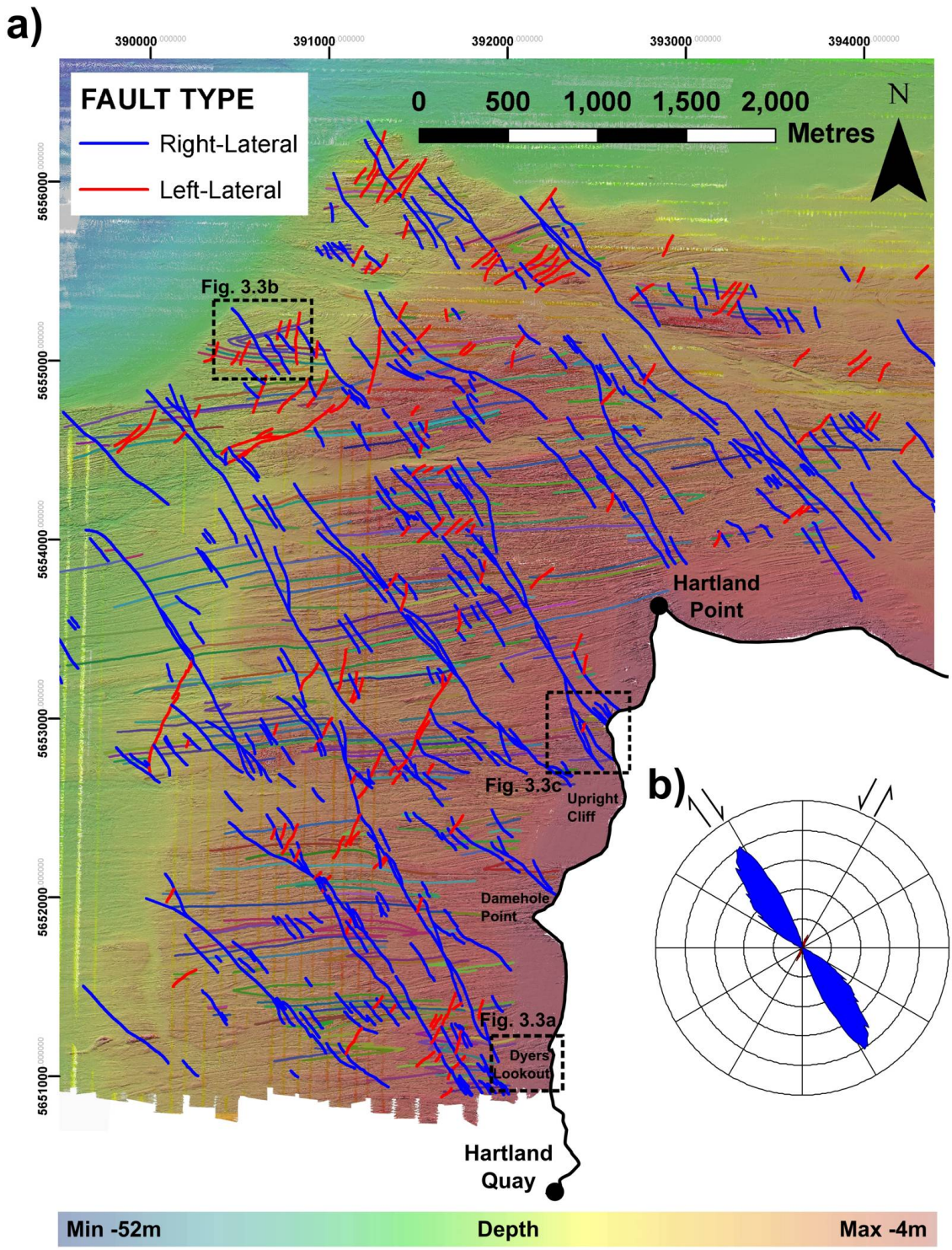

Figure 3.2 a) Interpreted multibeam bathymetry image with applied hillshade effect from offshore Hartland Point showing the extent of the mapped fault network. Inset are the locations of the images in Figure 3.3. b) Length-weighted rose diagram indicating the main fault trends.

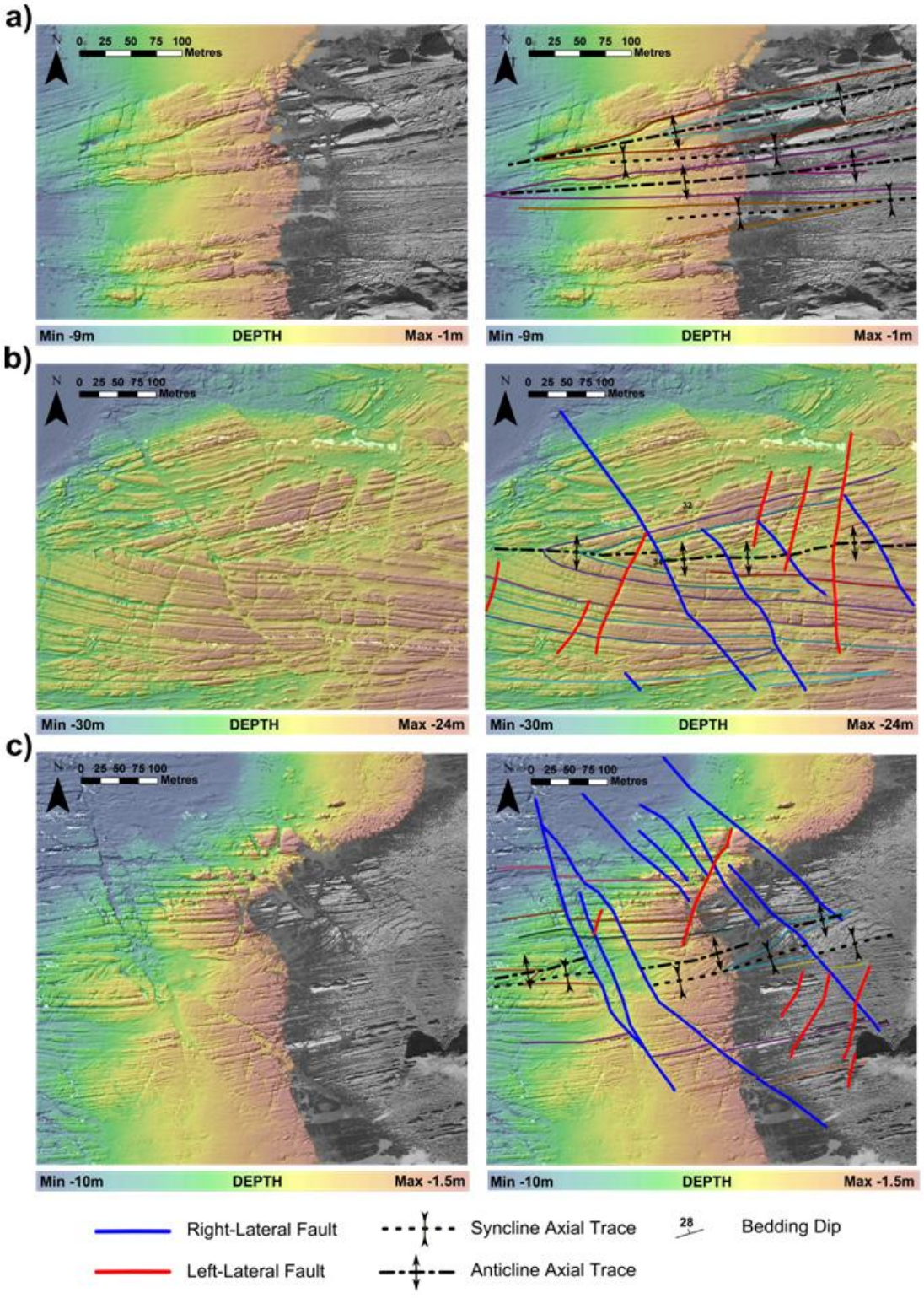

Figure 3.3 Multibeam bathymetry images with applied hillshade effect showing the quality of the imagery and the onshore-offshore correlation: a) An aerial photograph image (onshore) of strata and fold structures (grey) that can be traced into the offshore bathymetry survey (colour); b) An image of the sea-bed c. 2.5 km offshore showing an anticline that is cut by right- and left-lateral faults showing offsets in the same direction on both limbs; c) An offshore bathymetry image (colour) with faults, strata and fold structures which can be traced onto an onshore aerial photograph (grey). Aerial photography courtesy of the Channel Coastal Observatory.

The mapped fault network was correlated with onshore field mapping at Hartland Quay (a well studied and easily accessible part of the coastline with numerous and well exposed fold hinge lines and faults), where further 3D structural data was collected including bedding, fault orientations and slickenside measurements where possible.

3.5. Mapping Results

3.5.1. Folds and bedding attitudes

The multibeam bathymetry images an extensive submerged platform of bedrock with a general E-W trend of moderately to steeply dipping and folded bedding. This matches the attitude of bedding seen in onshore cliffs and wave cut platforms (Figure 3.3a). Onshore mapping from Hartland Quay shows that the bedding has been intensively folded, with chevron folds varying in wave-lengths from 15-80 m (Figure 3.4). This folding has been studied in detail from the cliff outcrops (e.g. Tanner, 1992; Davison et al., 2004) and can also be seen offshore. Throughout the submerged platform many marker beds can be identified and traced around fold hinges (Figure 3.3). Stereographic projections of poles to bedding show that the folds trend approximately E-W, related to N-S compression (Figure 3.5). The profile planes from both onshore and offshore bedding data correlate with each other (Figure 3.5) indicating the strike and dip measurements of bedding taken from the multibeam bathymetry data are accurate. However, there is a bias in the dip data from offshore due to the more limited availability of exposed bedding surfaces needed for slope calculations as the dip increases.

3.5.2. Relationship between faults and folding

Mapping from the multibeam bathymetry indicates two distinct sets of faults, based on their trend and lateral separation. The NW-trending faults have consistent right-lateral separations and NE-trending faults have left-lateral separations (Figure 3.2). The relationship between the mapped faults and folding indicates that the faults post-date the folding, as the faults cut and offset both layering and fold axial traces (Figure 3.3b).

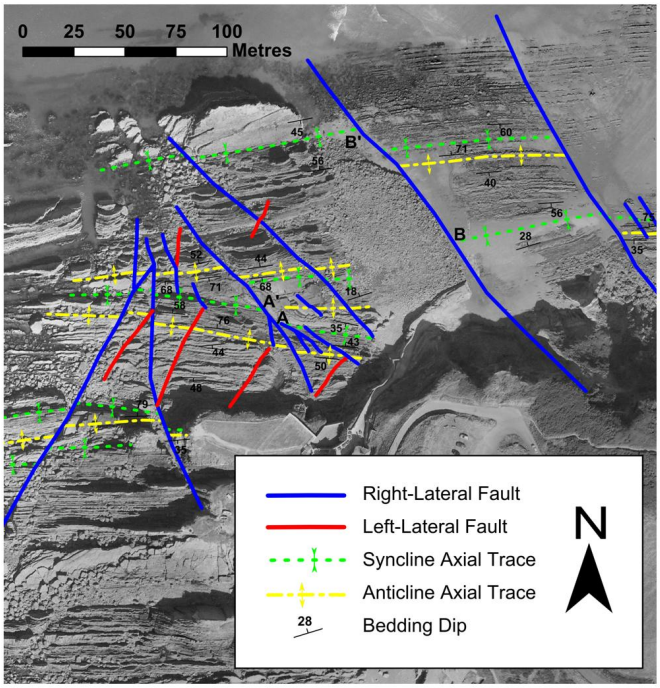

Figure 3.4 Fault map of a wave-cut platform at Hartland Quay showing lateral offsets of fold axial traces. Points A-A' and B-B' represent the piercement points shown in the field photographs in Figure 3.6a and 3.6b, respectively. Aerial photography courtesy of the Channel Coastal Observatory.

The fault sets mapped from the bathymetry can be traced onshore (Figure 3.3c) and correlate with onshore observations at Hartland Quay, where there are many examples of NW-trending right-lateral faults and NE-trending left-lateral faults (Figure 3.4). Folds at Hartland Quay are also cross-cut by the faults, with fold hinges defining piercement points on both fault sets that show a dominant component of strike-slip offset (Figures 3.4 and 3.6). Furthermore, structural measurements taken from Hartland Quay show that the fault planes are sub-vertical and have sub-horizontal slickensides (Figure 3.5a).

Thus, the mapped offshore and onshore faults are strike-slip based on the fact that:

1. They form two separate fault sets in map view that have consistent and opposite lateral separations, forming NW-trending right-lateral faults and NE-trending left-lateral faults (Figure 3.2);
2. Both sets are steeply dipping with shallowly plunging slickensides (Figure 3.5a);

3. They laterally offset fold hinges and limbs in the same direction (Figures 3.3b and 3.4);
4. Fold hinge lines form piercement points with a dominant strike-slip displacement (Figure 3.6a).

3.5.3. Spatial distribution and relative proportions of fault sets

The strike-slip fault network is dominated by NW-trending right-lateral faults as seen in the (length x displacement) weighted rose diagram (Figure 3.2b). These make up 80% of the overall trace-length with the largest right-lateral faults showing displacements of up to 146 m. Left-lateral faults are less numerous and much smaller, forming conjugate intersections with right-lateral faults (Figure 3.7).

The larger right-lateral faults have long traces (up to 2.6 km) that approximately divide the stratigraphy into elongated NW-trending blocks. Within these blocks are many smaller right-lateral and left-lateral faults. Many of these are isolated, but some are connected to each other by small left-lateral faults. Within the fault blocks there is a slight anticlockwise rotation of stratigraphy and, combined with the right-lateral dominance, this suggests that the strike-slip fault network is acting in a domino fashion controlled by the larger right-lateral faults as defined by Nixon et al., 2011 (Figure 3.8f).

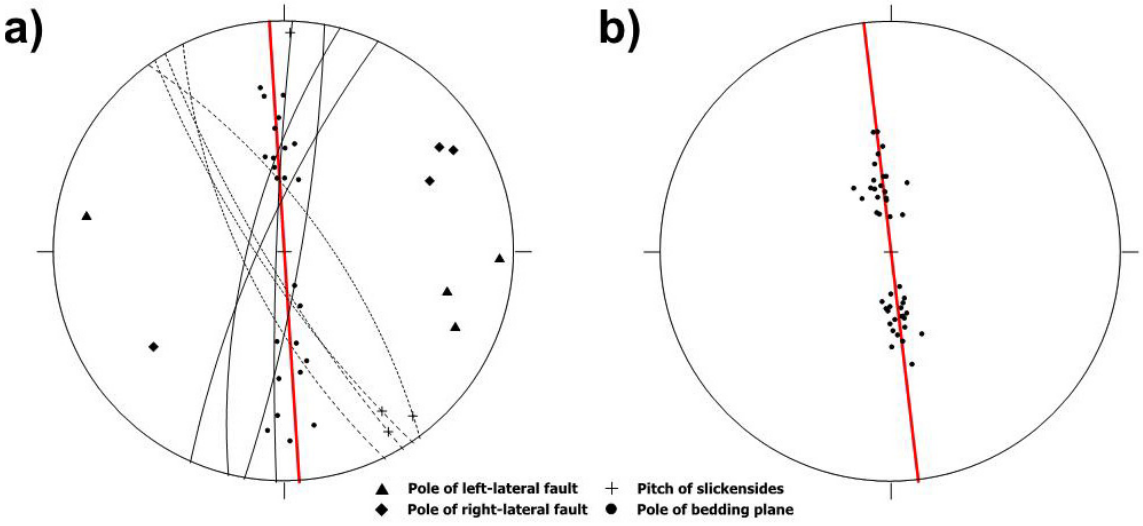

Figure 3.5 Equal-area stereographic projections: a) fault and bed data from Hartland Quay, the dotted lines represent right-lateral faults and solid lines represent left-lateral faults; b) offshore bedding data measured from the multibeam bathymetry.

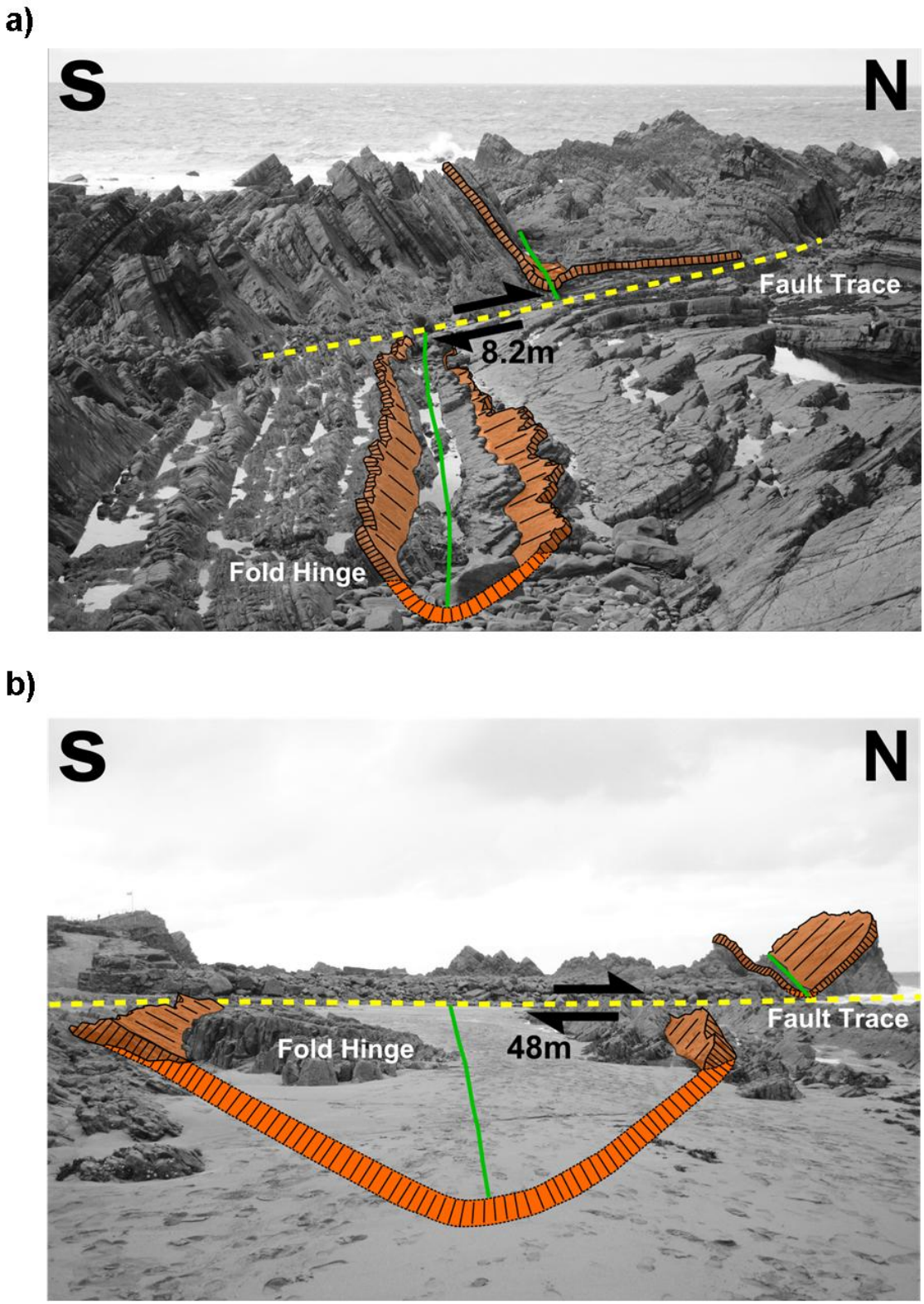

Figure 3.6 Interpretation of field photographs from Hartland Quay showing folds cut by strike-slip faults, a) Small fold with steeper N-dipping and shallower S-dipping limb, with hinge in same bed forming a piercement offset of 8.4 m right-laterally (A-A'). b) Large fold with hinge in same bed offset ~48 m right-laterally (B-B').

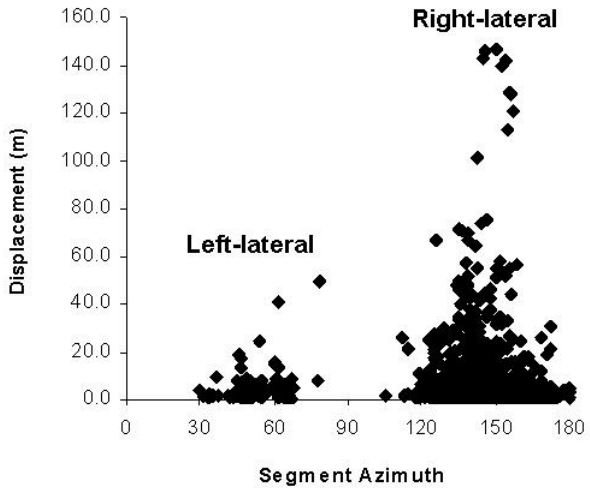

Figure 3.7 A plot of displacement against azimuth for the fault segment data offshore from Hartland Point.

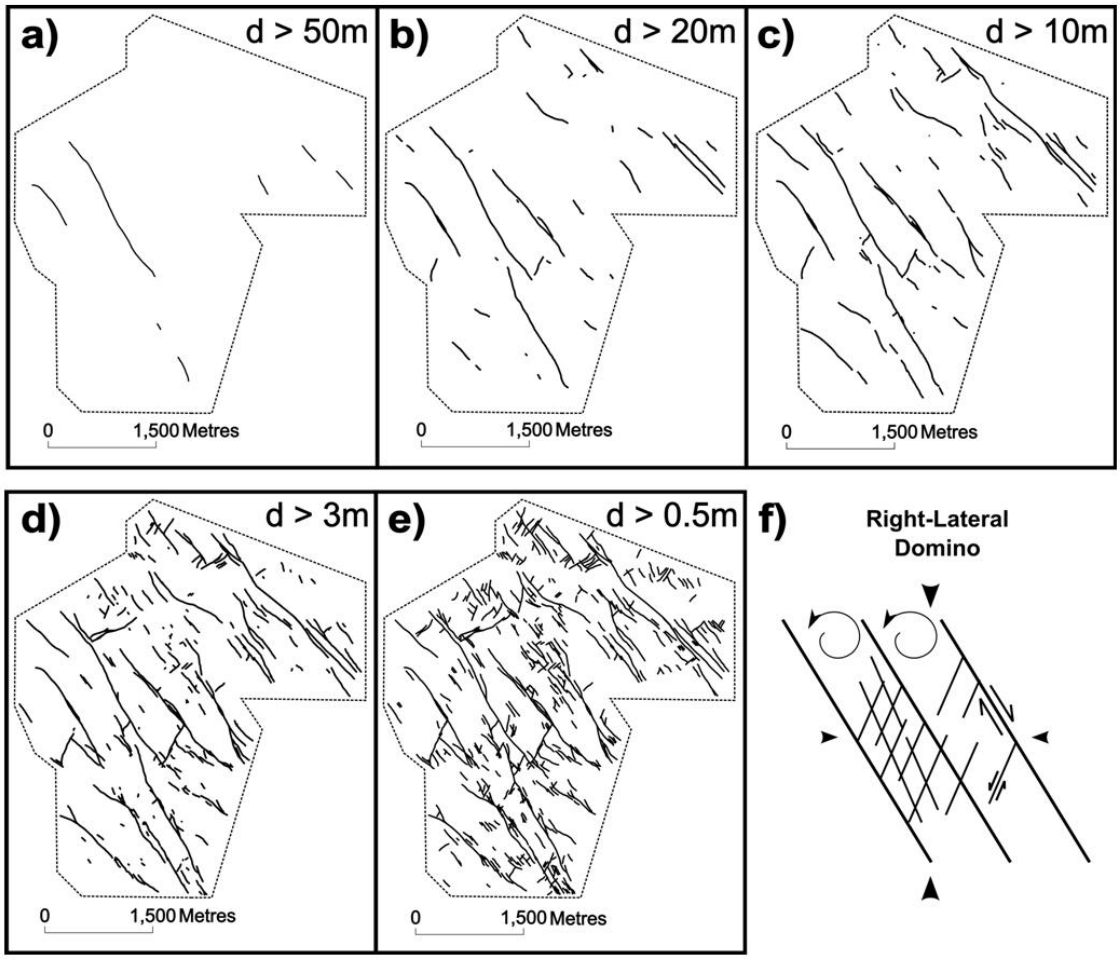

Figure 3.8 Displacement maps of fault segments offshore Hartland Point. Each map has a different displacement cut-off representing different resolutions: a) 50 m, b) 20 m, c) 10 m, d) 3 m and e) 0.5 m. f) Schematic diagram of a domino fault network with a dominant right-lateral fault set and anticlockwise rotation of fault blocks between large faults, modified from Nixon et al. (2011). Arrows indicate far-field loading.

3.6. Displacement and Scaling

The ability to segment and display the fault traces by measured offset points means that the fault network can be displayed at different scales by removing the fault segments with average displacements below a specified value. For example, Figure 3.8 shows a series of maps of the network produced by clipping the fault segments at different displacements, ranging from 0.5-50 m. This is referred to as a 'displacement cut-off' and is similar to the approach used by Watterson et al. (1996) to analyse the scaling properties of faults in the South Yorkshire coalfield. Rather than giving a maximum displacement/throw to a whole fault trace this technique is applied to each fault segment, which provides a more accurate representation of resolution as it preserves the spatial location of the faults and clips trace-lengths by removal of the low displacement segments at fault tips (cf. Pickering et al. 1997).

Different attributes can be measured at each resolution clipping (i.e. trace-length, fault density, fault set percentages, strain etc.), which is particularly useful for analysing the distribution of each attribute across different sizes of fault within the network. Using 10 m as a displacement cut-off value allows a direct comparison of small and large fault segments and helps assess their role within the fault network, with small fault segments and large fault segments having <10 m displacement and ≥10 m displacement, respectively. The value of 10 m is used as it corresponds with the approximate limit of resolution in many 3-D seismic reflection surveys.

3.6.1. Effects of scale on the spatial arrangement of the fault network

At high displacement cut-offs (i.e. Figures 3.8a and 3.8b) the network is dominated by a few, long, isolated right-lateral faults, but at lower cut-offs the system appears more connected with smaller conjugate left-lateral faults connecting the larger right-lateral faults (Figures 3.8c, d, and e). This is reflected in the trace-length percentages for each fault set with left-lateral faults increasing from 7% to 20% with the inclusion of faults with less than 10 m displacement (Figure 3.9c).

The larger fault segments form boundaries to NW-trending elongated blocks of stratigraphy with small fault segments infilling the spaces in between, increasing

fault density from 1.8 to 5.9 km^{-1} (1 km^{-1} represents 1 km of fault trace per square km). Consequently, at high displacement cut-offs coherent and 'unfaulted' regions appear between a series of widely spaced right-lateral faults when in reality there is deformation at a smaller scale within the blocks.

It is apparent that the small fault segments are either infilling faults, small left-lateral faults, or tips of larger faults. These are responsible for the increase in fault density and have a significant effect on the distribution of trace-length. A plot of trace-length density vs displacement cut-off (Figure 3.9a) shows the majority of trace-length is taken up by smaller fault segments with the larger-displacement (>10 m) fault segments only making up 30% of the trace-length. This is a further reflection of the increased deformation within the fault blocks with the inclusion of smaller fault segments.

There are few conjugate intersections between fault segments with >10 m displacement, with the formation of strike-slip relays (Peacock & Sanderson, 1995) being the main source of fault interaction, whereas splays and abutting faults become more frequent with the inclusion of smaller fault segments. Hence, the fault network appears less connected at high displacement cut-offs.

This analysis shows that the spatial arrangement of the fault network varies with scale, with the appearance of left-lateral faults at higher resolutions. Watterson et al. (1996) observe a somewhat similar pattern for multiple sets of normal faults in the southern Yorkshire coal fields, with one fault set being cut out at high-throw cut-offs. This suggests that this variation with scale is common where one fault set is dominant.

3.6.2. Strain distribution

The displacements calculated for each fault segment were used in a tensor analysis of strain, which provides an estimate of the maximum extension and its orientation. This involves the calculation of a Lagrangian strain tensor from the cross-product of the unit normal and displacement vectors of each fault segment. Peacock and Sanderson (1993) apply this to faults sampled along a line, using a weighting factor to correct for the orientation bias of such samples. The same approach is valid for sampling on a plane, where *(displacement x segment length)* / *unit area* replace the *displacement* / *unit length* in a line

sample. The weight (w) is determined from the angle between the fault normal and the plane. As we are dealing with sub-vertical strike-slip faults, both the fault normal and displacement vector lie close to the sub-horizontal plane of the sample and the weighting factor can be ignored (i.e. $w \rightarrow 1$). The eigenvectors and eigenvalues of the strain tensor provide estimates of the orientation and magnitude of the principal strains. For a more detailed methodology see Nixon et al. (2011).

The strain analysis shows that the area has an overall maximum extension of ~4.2% in a WNW-ESE orientation, with the large fault segments and small fault segments accommodating extensions of 3.5% and 0.7%, respectively (Table 3.1). The plot of percentage extension vs displacement cut-off shows the distribution of strain for different fault sizes within the network (Figure 3.9b). Even though most of the fault trace-length is taken up by smaller fault segments, 86% of the overall extension is accumulated on fault segments with ≥10 m displacement and ~45% by fault segments with >40 m displacement.

There is a small variation in maximum horizontal extension direction from N113°E for large faults to N107°E for small faults (Table 3.1). Although small, and undoubtedly within the errors of the determination of the principal strain axes, this sense of rotation is consistent with the domino behaviour of the system. The overall orientation of maximum extension is N112°E (see Table 3.1) which is weighted more towards the large fault segments of the fault network. This indicates that the kinematic behaviour of the fault network is mainly controlled by the larger fault segments within the network.

Overall, the majority of strain within the strike-slip network is accommodated by the large fault segments. Putz-Perrier and Sanderson (2008) show similar distributions of strain for normal faults at Kimmeridge Bay with large faults accommodating 65% of the overall strain, suggesting localization of strain onto the larger faults. This has also been seen in numerical and physical modelling (Cowie et al., 1995; Ackermann et al., 2001; Mansfield and Cartwright, 2001).

Although strain is localized onto the larger fault segments, the smaller fault segments are still significant, accommodating 14% of the overall extension. This is due to the high trace-length of small fault segments. Therefore, our work on

strike-slip faults systems (this paper; Nixon et al., 2011) supports similar work by Putz-Perrier & Sanderson (2008a, b, 2010) on normal faults, and establishes by direct measurement the relative contribution to deformation made by faults with different displacements. This is an important factor when producing extension estimates from seismic reflection data as the faults that are too small to be resolved seismically may contribute significantly to the total strain, as was originally suggested by extrapolation assuming power-law scaling (e.g. Walsh et al., 1991, Marrett and Allmindinger, 1992, Jackson and Sanderson 1992; Pickering et al., 1996).

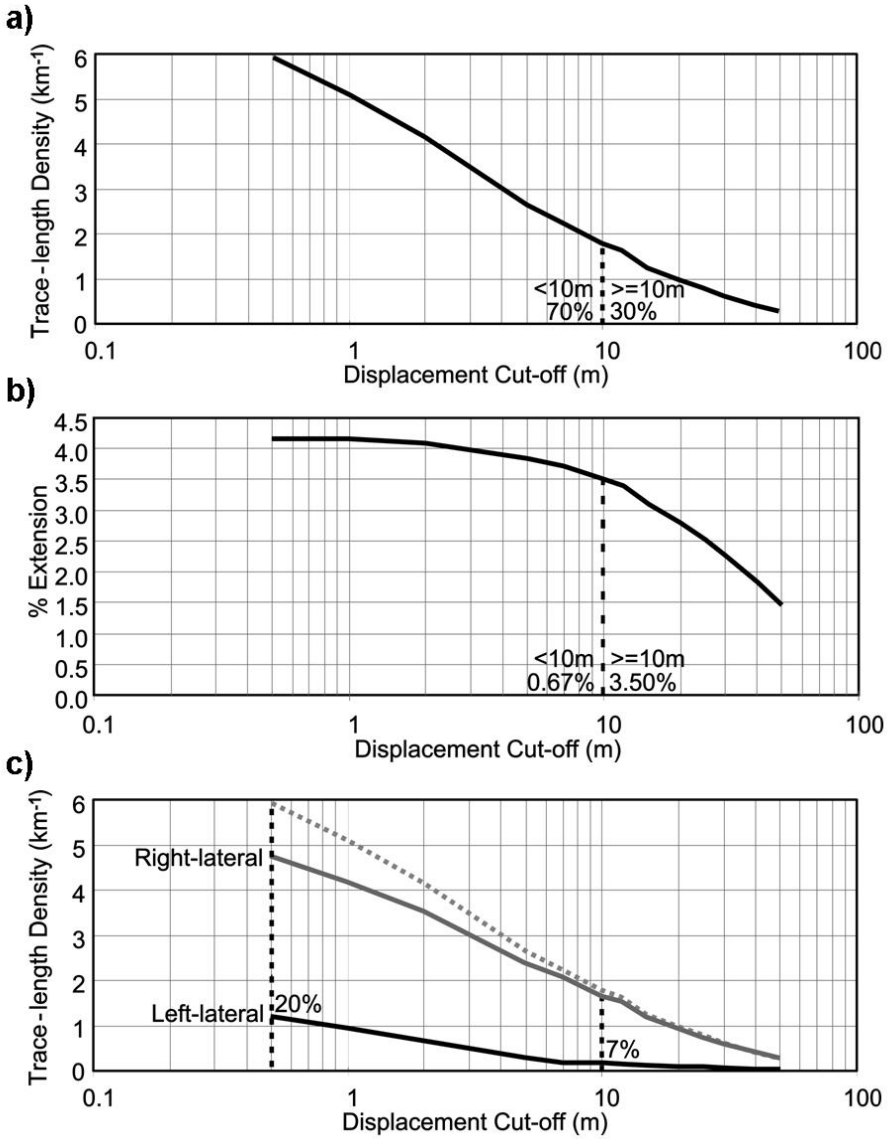

Figure 3.9 Linear-log plots of fault data from offshore Hartland Point showing the distribution of trace-length (a) and % extension (b) vs displacement cut-off. c) Indicates the proportion of trace-length taken up by left-lateral (black) and right-lateral (grey) faults.

Table 3.1 Structural characteristics and distribution of strain and trace-length within the fault networks offshore Hartland Point and onshore Westward Ho!.

	Offshore Hartland Point			Left-lateral - Westward Ho!			Damage - Westward Ho!			Right-lateral - Westward Ho!		
	Large fault segments (>=10 m)	Small fault segments (<10 m)	Overall	Large fault segments (>=10 m)	Small fault segments (<10 m)	Overall	Large fault segments (>=10 m)	Small fault segments (<10 m)	Overall	Large fault segments (>=10 m)	Small fault segments (<10 m)	Overall
Trace-length	30%	70%	-	29%	71%	-	21%	79%	-	12%	88%	-
% extension	3.5	0.7	4.2	25.2	1.6	26.8	20.8	3.4	24.3	12.2	3.5	15.7
Proportion of Strain	86%	14%	-	94%	6%	-	86%	14%	-	77%	23%	-
Orientation of maximum extension (θ)	N113°E	N107°E	N112°E	N067°E	N089°E	N068°E	N074°E	N093°E	N077°E	N114°E	N107°E	N112°E
Fault Density (km^{-1})	-	-	5.9	-	-	39.5	-	-	80.4	-	-	45.1

Pickering et al. (1997) recognise that fault lengths and throws of normal fault tips are often not seismically resolved. Therefore, estimates of sub-seismic strain using displacement scaling of fault populations will still underestimate sub-seismic strain as they do not take into account any additional contribution from fault tips, linkage zones and associated damage. By using fault segments rather than individual faults, this study incorporates the effects of fault tips and linkage zones, with that of small faults, in evaluating their role in accommodating extension within a basin.

3.7. Topology

The fault network was analysed in terms of a system of fault branches between tips (I-nodes) or intersections (X- or Y-nodes) (Figure 3.10). Manzocchi (2002) uses this system to estimate connectivity by looking at the relative proportions of I-, Y- and X-nodes within a fracture network. Like fracture networks, fault networks become connected through a combination of crossing fault intersections (X-nodes), and abutments and splays of fault tips (Y-nodes). Hence, for this study the combined percentage of X- and the Y-nodes was used to represent the connectivity of the fault network. This is then taken further by analysing how the percentage and nature of connecting nodes within the fault network changes with resolution.

Table 3.2 Nodal percentages of the fault networks from offshore Hartland Point and onshore Westward Ho!.

	I-Node %	Y-Node %		X-Node %
		Synthetic	Antithetic	
Offshore Hartland Point	78.8	6.5	11.5	3.2
Left-lateral - Westward Ho!	54.5	6.4	25.7	13.4
Damage - Westward Ho!	26.5	18.8	42.7	12.0
Right-lateral - Westward Ho!	63.5	15.2	19.2	2.1

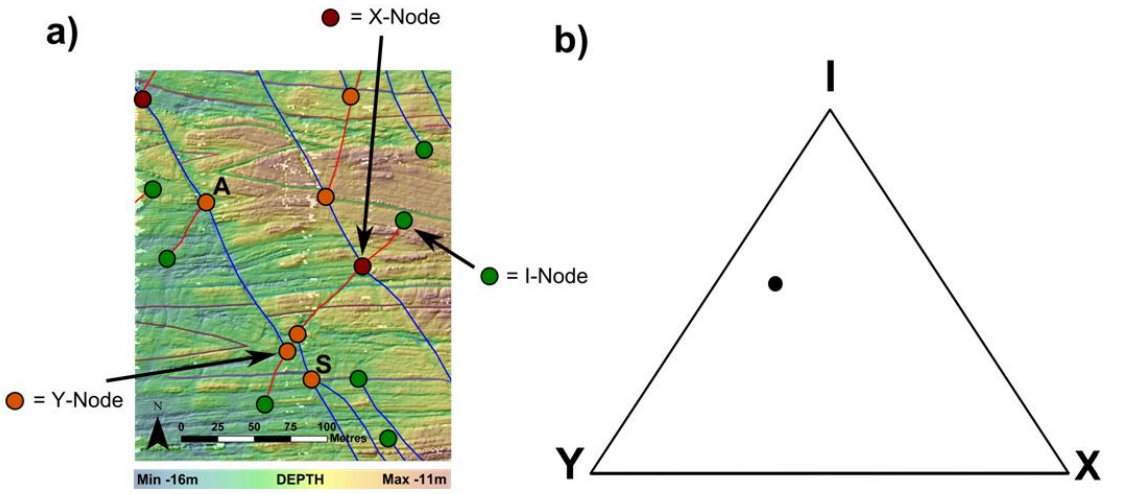

Figure 3.10 a) A multibeam bathymetry image with applied hillshade effect illustrating a system with fault branches and nodes. Nodes A and S represent an antithetic Y-node and a synthetic Y-node, respectively. b) A ternary plot of I-, Y-, and X-node proportions illustrating the connectivity of the fault network example in Figure 3.10a. Where the network plots within the ternary diagram illustrates the I:Y:X node ratio which is 7:6:2 for this example. In general, fault networks become better connected away from the I-node corner of the triangle, see Manzocchi (2002) for a more detailed discussion of this in terms of percolation theory.

The percentages of different node (Table 3.2) show that the fault network offshore Hartland Point is dominated by I-nodes (isolated tips). Connecting nodes make up just 21.2% of all nodes with the majority being Y-nodes. Two different types of Y-node can be identified (Figure 3.10a): **1)** Synthetic Y-nodes where two faults with the same motion sense intersect resulting from a fault linkage or splay; and **2)** Antithetic Y-nodes where two faults with the opposite motion sense intersect as a result of one fault abutting another. The latter make up over 50% of all connecting nodes which emphasizes the importance of conjugate fault sets when considering the connectivity of a fault network.

The plot of connecting node % vs displacement cut-off shows that the percentage of fault branches ending at Y-shaped or X-shaped nodes approximately halves with the exclusion of the small fault segments (Figure 3.11). This is quite significant considering that there are no connecting nodes present for fault segments at displacement cut-offs of greater than 25 m, resulting in the network appearing very unconnected at low resolutions. Furthermore, the nature of interacting Y- and X- nodes varies with scale. Synthetic Y-nodes (or splays) are dominant for faults with >5 m displacement, whereas for faults with <5 m displacement, antithetic Y-nodes dominate and

crossing X-nodes are occasionally developed. This pattern suggests that larger faults are more likely to form linkage and splays, due to fault growth, and that low displacements are usually needed for crossing X-shaped fault intersections to be preserved.

Overall the offshore network at Hartland is poorly connected, but the connectivity of the strike-slip network increases with increasing resolution, particularly with the inclusion of faults smaller than the seismic resolution cut-off. This, combined with an increase in fault density from 1.8 to 5.9 km^{-1}, indicates that the connectivity of the fault network is very dependant on small fault segments. Pickering et al. (1997) found similar results when modeling the connectivity of normal fault tips, highlighting that the connectivity of fault networks is often underestimated due to the limited resolution of seismic data.

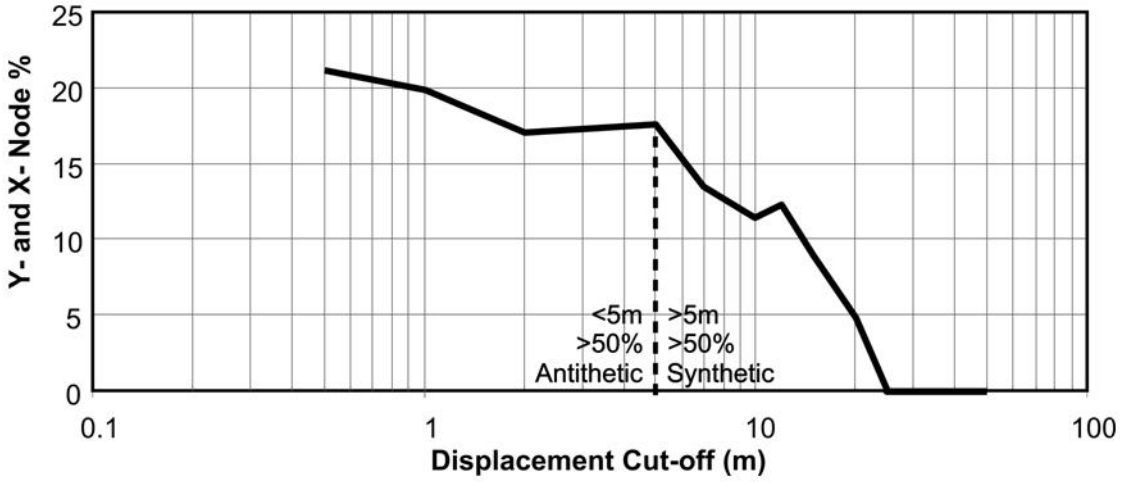

Figure 3.11 Linear-log plot of connecting node % vs displacement cut-off.

3.8. Discussion and Comparison with Westward Ho!

Analysis of the offshore strike-slip fault network at Hartland shows that the distribution of different attributes varies with displacement. This has highlighted three main points: **1)** small faults, fault tips and linkage zones contribute the majority of the overall trace-length; **2)** strain is localized onto individual large displacement fault segments; **3)** at low displacement cut-offs the fault network appears more connected with the inclusion of small faults, fault tips and linkage zones. To show that these observations are applicable to other fault networks,

the same scaling analysis has been applied to an onshore strike-slip fault network at Westward Ho! previously described by Nixon et al. (2011).

3.8.1. Westward Ho!

The fault sets at Westward Ho! have orientations that match those found offshore at Hartland Point (NW-trending right-lateral faults and NE-trending left-lateral faults), and they also post-date folding. The network has large faults that divide the rock-mass into elongated blocks with small faults accommodating deformation within each block, not unlike the offshore network. There is much heterogeneity within the fault network at Westward Ho!, with fault set dominance changing throughout (Nixon et al., 2011), however the geometric and lithological similarities with the offshore fault network make Westward Ho! a good comparison. Three contrasting small areas of intense deformation from within the fault network at Westward Ho! were chosen for comparison (Figure 3.12):

Left-lateral area – This has the highest strain value of the three areas with an overall maximum extension of ~26.8% and an orientation of N068°E resulting from the left-lateral dominance of the fault network (Nixon et al., 2011). The majority of the trace-length, 71%, is taken up by small fault segments (Table 3.1). However, 94% of the overall extension is accommodated by the larger fault segments, which is the largest proportion in comparison with the other two onshore areas.

Damage Area – This is a region of more internal deformation lying between large left-lateral faults (Figure 3.12) and has an overall maximum extension of ~24.3% with an orientation of N077°E. The trace-length density is almost double the trace-length density of the left lateral area (Table 3.1) and small fault segments, make up 79% of overall trace-length (Table 3.1). Hence, the small fault segments are much more significant than in the left-lateral area and accommodate 14% of the overall extension.

Right-lateral area – This has the lowest strain value of the three areas with an overall maximum extension of ~15.7% and an orientation of N112°E. Again the majority of the trace-length is taken up by the small fault segments with only 12% being taken up by the large-fault segments (Table 3.1). The distribution of

strain shows a similar pattern with 77% being localized onto the large fault segments, however, this is much less than both the left-lateral and damage areas (Table 3.1).

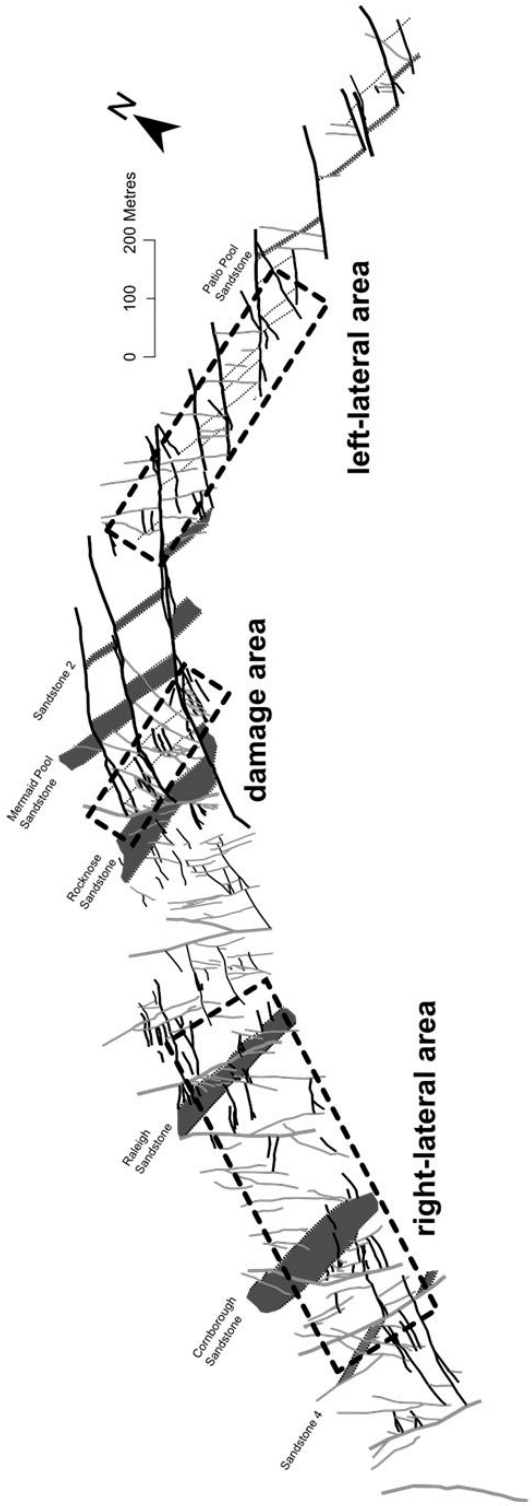

Figure 3.12 Fault map of the wave-cut platform at Westward Ho! showing the localities of the left-lateral, damage and right-lateral areas. Right-lateral and left-lateral faults are displayed as grey and black, respectively. Modified from Nixon et al. (2011).

3.8.2. Strain

Overall the three areas at Westward Ho! accommodate much higher strains and fault densities in comparison with the offshore network at Hartland (Table 3.1). This is not an effect of resolution as it is consistent for all displacement cut-offs (Figure 3.13), instead this indicates that the areas at Westward Ho! are more intensely deformed. The linear-log plots (Figure 3.13) show that the three onshore areas have a similar pattern of trace-length and strain distribution to the fault network offshore. Most of the fault trace-length is taken up by small displacement (<10 m) fault segments and the majority of the strain is still accommodated by large displacement (>=10 m) fault segments, again supporting the idea of strain localization onto larger faults.

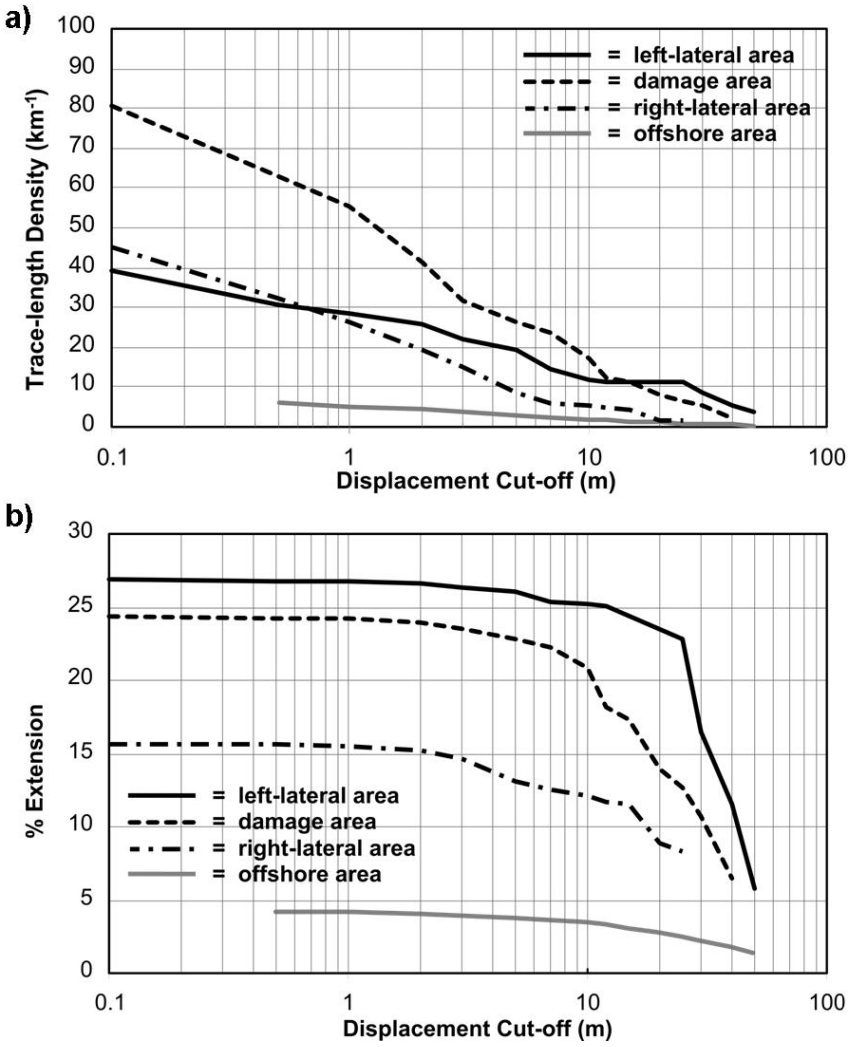

Figure 3.13 Linear-log plots of fault data from the left-lateral, damage and right-lateral areas at Westward Ho!. a) trace-length density vs displacement cut-off and b) % extension vs displacement cut-off. The data for the offshore network is also included for comparison (grey).

The strains for the three onshore areas at Westward Ho! show that more strain is localized onto the larger fault segments (Table 3.1). This is reflected in the linear-log plot of strain vs displacement cut-off (Figure 3.13b) as an increase in gradient at higher displacements and suggests that as strain increases strain becomes localized onto higher displacement fault segments. This is consistent with the observations of Nicol et al. (1997) who show that, with increasing strain, networks have faults with higher displacement rates.

Whilst strain localization appears to increase with increasing strain for the three areas at Westward Ho!, the fault network offshore from Hartland Point does not fit this observation. Even though the offshore network accommodates much lower strains than the onshore areas at Westward Ho!, 85% of the strain is localized onto the large fault segments, which is a higher proportion than the right-lateral area and similar to the damage area (Table 3.1). This is due to the increased deformation seen at Westward Ho! as indicated by the high strains and fault densities (Table 3.1; Figure 3.13). Strain is localized to areas of intense deformation, not just individual fault planes, and accommodated by internal deformation within fault blocks and associated damage zones. Hence, in areas of localized deformation less strain is localized on the larger fault segments due to increased amounts of internal deformation between large faults.

Pickering et al. (1996) found similar affects for normal faults by fitting to power-law distributions of the form:

$$N \propto (\text{displacement})^{-D}, \qquad (3.1)$$

where the D-value is termed the power-law exponent. They found that for a D-value of 0.5 almost all the extension is taken up by faults with heaves greater than 20 m, whereas for a D-value of 0.9 their contribution decreases to less than half. As an increase in the D-value of a fault population reflects a higher degree of small-scale faulting, this supports the idea that for areas with increased amounts of internal deformation less strain is localized onto the larger faults.

The significance of small faults within areas of internal deformation is also reflected in the strain orientations with the damage area accommodating less

rotation in comparison to the left-lateral area. This is opposite to the conclusions of Peacock et al. (1998) who proposed that small faults added to the overall rotation of an area. This difference is due to the nature of internal deformation, with the majority of small faults in this study being antithetic and conjugate to the bounding faults. Although the small fault segments have an increased significance in areas with increased deformation the majority of strain is still accommodated by the larger fault segments, indicating that the kinematic behaviour of the fault network is controlled by the large faults.

3.8.3. Connectivity

The connecting node percentage (X- and Y-nodes) for the left-lateral, damage and right-lateral areas at Westward Ho! are 45.5%, 73.5% and 37.5%, respectively (Table 3.2). The majority of connecting nodes are antithetic Y-nodes, which agrees with the offshore fault network and further emphasizes the importance of conjugate fault sets when considering connectivity. The percentages for all connecting nodes are much higher than the offshore network indicating that the three areas at Westward Ho! are better connected. The damage area is also the most connected, mainly due to its increased fault density.

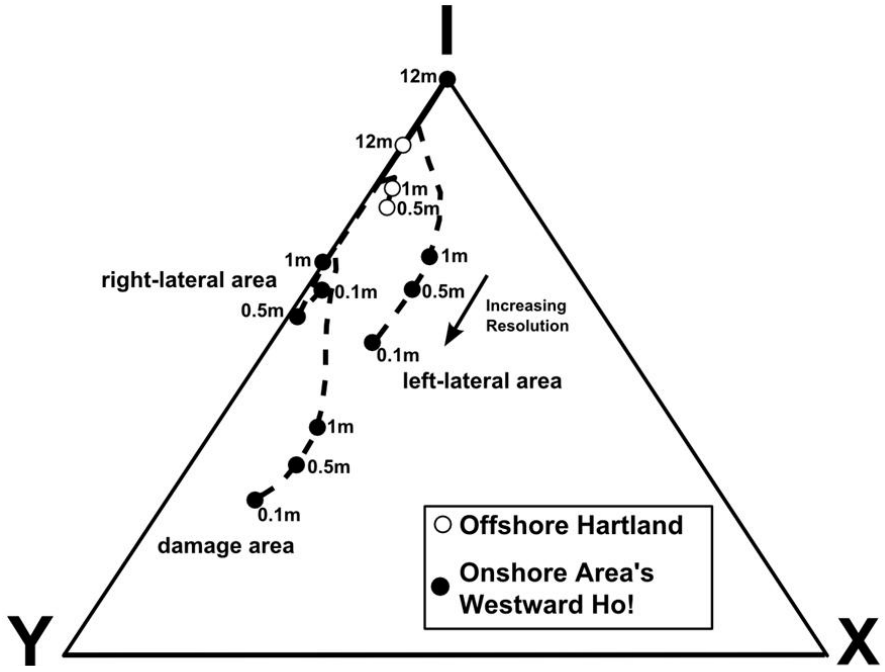

Figure 3.14 Ternary diagram of I-, Y- and X-Node percentages showing the connectivity pathways from 50 m resolution to full resolution of the fault networks from offshore Hartland Point and onshore Westward Ho!.

A ternary plot of the proportions of I-, Y-, and X-nodes illustrates that the connectivity changes in a fault network with increasing resolution. In general, the networks become better connected away from the I-node corner of the triangle (Figure 3.14), but see Manzocchi (2002) for a more detailed discussion of this in terms of percolation theory. Overall the proportion of connecting nodes within each fault network, from both Westward Ho! and Hartland Point, increases with increasing resolution. The right-lateral area has a similar connectivity pathway to the network at Hartland Point. They both follow the I-Y margin of the ternary diagram and only have a small contribution of connecting X-nodes, even at high resolutions. The left-lateral and damage areas also follow the I-Y line on the ternary diagram. However, they are influenced much more by the presence of connecting X-nodes and are more connected at higher resolutions.

All the fault networks experience a significant increase in the proportion of X- and Y- nodes once faults with less than 12 m displacement are included (Figure 3.14). The fault networks at Westward Ho! are better connected than at Hartland Point suggesting that fault networks become more connected with increasing strain (Table 3.2 and Figure 3.14). Furthermore, the damage area is much more connected than the right- and left-lateral areas, indicating that damage zones and areas with increased internal deformation are better connected. These areas often have increased numbers of smaller faults further supporting the idea that connectivity is reliant on small faults.

Even though the connectivity of fault networks is primarily dependant on the length, density and orientation of the faults and their spatial correlation (Berkowitz et al., 2000), the strain and the nature of the localization also play an important role. Fault networks appear to be better connected when strain is localized to an area, creating damage zones of intense deformation and high fault densities, rather than when strain is localized onto individual faults forming longer and simpler systems. This also suggests that connectivity increases with increased amounts of deformation. Micarelli et al. (2006) show similar results with the connectivity of fracture networks being higher in intensely deformed damage zones than in weakly deformed damage zones around normal fault planes.

3.9. Summary and Conclusions

Multibeam bathymetry has been used to identify and map an extensive area of a strike-slip fault network offshore from Hartland Point, north Devon. The fault network comprises NW-trending right-lateral faults and NE-trending left-lateral faults and behaves in a right-lateral domino fashion. The spatial arrangement, topology, and distribution of strain and trace-length of the fault network vary with resolution:

1. Small (<10 m) displacement fault segments infill fault blocks, bounded by large displacement (10-150 m) faults, and make up most of the trace-length.
2. Strain is localized onto the large-displacement fault segments with ≥10 m displacement that bound the fault blocks.
3. The kinematic behaviour of the fault network is controlled by block rotation between the large faults within the fault network.
4. Fault networks appear less connected at lower resolutions as the connectivity of the fault network is very dependant on the presence of small fault segments.

Comparison with onshore field examples from Westward Ho! confirms these points with similar distributions of strain and fault trace-length. Furthermore, combining the two datasets suggests that strain localization and connectivity are influenced by both the overall strain and amount of internal deformation:

5. More strain is localized onto the larger-displacement fault segments, however, small fault segments can make an important contribution to strain in areas with large amounts of internal deformation (damage zones).
6. The connectivity of a fault network increases with increasing strain as well as with increasing resolution.
7. Damage zones and areas with internal deformation are better connected due to increased contributions of small fault segments and high fault densities.

8. Fault networks are better connected when strain is localized to an area rather than when strain is localized onto individual faults.

The comparison with the onshore fault networks at Westward Ho! confirms that the observations from the analysis of the offshore fault network at Hartland are applicable to other fault networks. The techniques and methods developed for this study have helped to further the analysis of fault networks. The application of high resolution multibeam bathymetry imagery has allowed expansion and uncovering of an extensive fault network. This combined with analysis of fault patterns, topology and distribution of resulting strains highlights the importance of resolution when investigating crustal deformation, particularly when considering faults smaller than the seismic resolution cut-off.

3.10. References

Ackermann, R.V., Schlische, R.W., Withjack, M.O., 2001. The geometric and statistical evolution of normal fault systems: and experimental study of the effects of mechanical layer thickness on scaling laws. Journal of Structural Geology 23, 1803-1326.

Arthaud, F., Matte, P., 1977. Late Paleozoic strike-slip faulting in southern Europe and northern Africa: Result of a right-lateral shear-zone between the Appalachians and the Urals. Geological Society of America Bulletin 88, 1305-1320.

Badham, J.P.N., 1982. Strike-slip orogens – an explanation for the Hercynides. Journal of the Geological Society 139, 493-504.

Barnes, R.P., Andrews, J.R., 1986. Upper Palaeozoic ophiolite generation and obduction in south Cornwall. Journal of the Geological Society 143, 117-124.

Baudon, C., Cartwright, J., 2008. Early stage evolution of growth faults: 3D seismic insights from the Levant Basin, Eastern Mediterranean. Journal of Structural Geology 30, 888-898.

Berkowitz, B., Bour, O., Davy, P., Odling, N., 2000. Scaling of fracture connectivity in geological formations. Geophysical Research Letters 37, 2061-2064.

Bull, J.M., Barnes, P.M., Lamarche, G., Sanderson, D.J., Cowie, P.A., Taylor, S.K., Dix, D.K., 2006. High-resolution record of displacement accumulation on an active normal fault: implications for models of slip accumulation during repeated earthquakes. Journal of Structural Geology 28, 1146-1166.

Cartwright, J.A., Trudgill, B.D., Mansfield, C.B., 1995. Fault growth by segment linkage: an explanation for scatter in maximum displacement and trace-length data from the Canyonlands Grabens of SE Utah. Journal of Structural Geology 17, 1319-1326.

Chadwick, R.A., 1993. Aspects of basin inversion in southern Britain. Journal of the Geological Society 150, 311-322.

Childs, C., Nicol, A., Walsh, J.J., Watterson, J., 2003. The growth and propagation of synsedimentary faults. Journal of Structural Geology 25, 633-648.

Coward, M.P., McClay, K.R., 1983. Thrust tectonics of S.Devon. Journal of the Geological Society 140, 215-228.

Cowie, P.A., Sornette, D.C., Vanneste, C., 1995. Multifractal scaling properties of a growing fault population. Geophysical Journal International 122, 457-469.

Cowie, P.A., Underhill, J.R., Behn, M.D., Lin, J., Gill, C.E., 2005. Spatio-temporal evolution of strain accumulation derived from multi-scale observations of Late Jurassic rifting in the northern North Sea: A critical test of models for lithospheric extension. Earth and Planetary Science Letters 234, 401-419.

Davison, I., Jeffcoate, A., Qing, H., 2004. Geometry of chevron folding and shortening estimates at Hartland Quay, North Cornwall, UK, and some regional implications for Culm Basin development. Geoscience in south-west England 11, 42-50.

Ferrill, D.A., Stamatakos, J.A., Sims, D., 1999. Normal fault corrugation: implications for growth and seismicity of active normal faults. Journal of Structural Geology 21, 1107-1110.

Gupta, A., Scholz, C.H., 2000. Brittle strain regime transition in the Afar depression: Implications for fault growth and seafloor spreading. Geology 28, 1087-1090.

Higgs, R., Reading, H.G., Li, X., 1990. Upper Carboniferous lacustrine and deltaic sedimentology, SW England: Westward Ho! and Bude. British Sedimentological Research Group.

Holdsworth, R.E., 1989. The Start-Perranporth line: a Devonian terran boundary in the Variscan orogen on SW England. Journal of the Geological Society 146, 419-421.

Holloway, S., Chadwick, R.A., 1986. The Sticklepath-Lustleigh fault zone: Tertiary sinistral reactivation of a Variscan dextral strike-slip fault. Journal of the Geological Society 143, 447-452.

Jackson, P., Sanderson, D.J., 1992. Scaling of fault displacements from the Badojoz – Cordoba shear zone, SW Spain. Tectonophysics 210, 179-190.

Kim, Y-S., Andrews, J.R., Sanderson, D.J., 2001. Reactivated strike-slip faults: examples from north Cornwall. Tectonphysics 340, 173-194.

Lake, S.D., Karner, G.D., 1987. The structure and evolution of the Wessex Basin, southern England: an example of inversion tectonics. Tectonophysics 137, 347-378.

Mansfield, C., Cartwright, J., 2001. Fault growth by linkage: observations and implications from analogue models. Journal of Structural Geology 23, 745-763.

Manzocchi, T., 2002. The connectivity of two-dimensional networks of spatially correlated fractures. Water Resources Research 38, 1162.

Marrett, R., Allmendinger, R.W., 1992. Amount of extension on “small” faults: An example from the Viking graben. Geology 20, 47-50.

Micarelli, L., Benedicto, A., Wibberley, C.A.J., 2006. Structural evolution and permeability of normal fault zones in highly porous carbonate rocks. Journal of Structural Geology 28, 1214-1227.

Moriya, S., Childs, C., Manzocchi, T., Walsh, J.J., 2005. Analysis of the relationships between strain, polarity and population slope for normal fault systems. Journal of Structural Geology 27, 1113-1127.

Mouslopoulou, V., Walsh, J.J., Nicol, A., 2009. Fault displacement rates on a range of timescales. Earth and Planetary Science Letters 278, 186-197.

Nicol, A., Walsh, J.J., Watterson, J., Underhill, J.R., 1997. Displacement rates of normal faults. Nature 390, 157-159.

Nicol, A., Walsh, J.J., Villamor, P., Seebeck, H., Berryman, K.R., 2010. Normal fault interactions, paleoearthquakes and growth in an active rift. Journal of Structural Geology 32, 1101-1113.

Nixon, C.W., Sanderson, D.J., Bull, J.M., 2011. Deformation within a strike-slip fault network at Westward Ho!, Devon U.K.: Domino vs conjugate faulting. Journal of Structural Geology 33, 833-843.

Peacock, D.C.P., 1991. Displacements and segment linkage in strike-slip fault zones. Journal of Structural Geology 13, 1025-1035.

Peacock, D.C.P., Sanderson, D.J., 1993. Estimating strain from fault slip using a line sample. Journal of Structural Geology 15, 1513-1516.

Peacock, D.C.P., Sanderson, D.J., 1994. Geometry and development of relay ramps in normal fault systems. AAPG Bulletin 78, 147-165.

Peacock, D.C.P., Sanderson, D.J., 1995. Strike-slip relay ramps. Journal of Structural Geology 17, 1351-1360.

Peacock, D.C.P., Sanderson, D.J., 1998. Deformation history and basin-controlling faults in the Mesozoic sedimentary rocks of the Somerset coast. Proceedings Geological Association 110, 41-52.

Peacock, D.C.P., Anderson, M.W., Morris, A., Randall, D.E., 1998. Evidence for the importance of 'small' faults on block rotation. Tectonophysics 299, 1-13.

Pickering, G., Bull, J.M., Sanderson, D.J., 1996. Scaling of fault displacements and implications for the estimation of sub-seismic strain. Geological Society, London, Special Publications 99, 11-26.

Pickering, G., Peacock, D.C.P., Sanderson, D.J., Bull, J.M., 1997. Modeling tip zones to predict the throw and length characteristics of faults. AAPG Bulletin 81, 82-99.

Putz-Perrier, M.W., Sanderson, D.J., 2008a. The distribution of faults and fractures and their importance in accommodating extensional strain at Kimmeridge Bay, Dorset, UK. Geological Society, London, Special Publication 299, 97-111.

Putz-Perrier, M.W., Sanderson, D.J., 2008b. Spatial distribution of brittle strain in layered sequences. Journal of Structural Geology 30, 50-64.

Putz-Perrier, M.W., Sanderson, D.J., 2010. Distribution of faults and extensional strain in fractured carbonates of the North Malta Graben. AAPG Bulletin 94, 435-456.

Sanderson, D.J., 1979. The transition from upright to recumbent folding in the Variscan fold belt of southwest England: a model based on the kinematics of simple shear. Journal of Structural Geology 1, 171-180.

Sanderson, D.J., 1984. Structural variation across the northern margin of the Variscides in NW Europe. Geological Society, London, Special Publications 14, 149-165.

Soliva, R., Schultz, R.A., 2008. Distributed and localized faulting in extensional settings: Insight from the North African Rift – Afar transition area. Tectonics 27, TC2003.

Tanner, G.W.P., 1992. Morphology and geometry of duplexes formed during flexural-slip folding. Journal of Structural Geology 14, 1173-1192.

Taylor, S.K., Bull, J.M., Lamarche, G., Barnes, P.M., 2004. Normal fault growth and linkage in the Whakatane Graben, New Zealand, during the last 1.3 Myr. Journal of Geophysical Research 109, B02408.

Underhill, J.R., Paterson, S., 1998. Genesis of tectonic inversion structures: seismic evidence for the development of key structures along the Purbeck – Isle of Wright Disturbance. Journal of the Geological Society 155, 975-992.

Walsh, J.J., Watterson, J., Yielding, G., 1991. The importance of small scale faulting in regional extension. Nature 351, 391-393.

Walsh, J.J., Childs, C., Manzocchi, T., Imber, J., Nicol, A., Meyer, V., Tuckwell, G., Bailey, W.R., Bonson, C.G., Watterson, J., Nell, P.A.R., Strand, J., 2001. Geometrical controls on the evolution of normal fault systems. Geological Society, London, Special Publication 186, 157–170.

Watterson, J., Walsh, J.J., Gillespie, P.A., Easton, S., 1996. Scaling systematics of fault sizes on a large-scale range fault map. Journal of Structural Geology 18, 199-214.

Xu, S., Nieto-Samaniego, A.F., Alaniz-Alvarez, S.A., Velasquillo-Martinez, L.G., Grajales-Nishimura, J.M., Garcia-Hernandez, J., Murillo-Muneton, G., 2010. Changes in fault length distribution due to fault linkage. Journal of Geodynamics 49, 24-30.

4. A topological analysis of 2-D fault networks and its use in assessing connectivity

Casey W. Nixon, David J. Sanderson, Jonathan M. Bull

4.1. Abstract

A topological analysis is used to characterize and describe fault networks in which the network is considered to form from two topological components: nodes and branches. Nodes are divided into I-nodes (fault tips), Y-nodes (abutments and splays) and X-nodes (cross-cutting faults). Branches are divided into I-I branches (isolated faults), I-C branches (dangling ends of clusters) and C-C branches (backbone of clusters).

The characteristic properties of the topological components are described and topological measures are developed for determining the topology of fault networks. Results show that fault networks form more Y-nodes than X-nodes, and that there is much heterogeneity in the spatial distribution of connecting nodes within fault networks. In general, clusters of connecting nodes form where there are high trace-length densities such as areas of damage and linkage between faults.

A new method for assessing the clusters in a fault network is developed using a branch analysis and the number of connections per branch, which identifies whether clusters are small and isolated (dominated by I-C branches) or large clusters (dominated by C-C branches) that might span large areas. Thus, these parameters relate directly to the connectivity within fault networks. Overall there is much spatial heterogeneity in the character and degree of connectivity within fault networks and that strain is localized onto the connected faults.

4.2. Introduction

The study and characterization of fault networks is vital to our understanding of brittle deformation within the Earth's crust and many physical processes in rocks. Furthermore, as faults can act as either conduits or barriers to fluid flow, fault networks are important in exploration for resources such as water, hydrocarbons, mineral deposits from hydrothermal fluids and potential areas of CO_2 storage and other waste.

There have been many studies that investigate the distribution of different attributes within fault networks such as geometry, density, displacement, strain etc. (e.g. Schlische et al., 1996; Walsh et al., 2003; Nicol et al., 2006; Putz-Perrier and Sanderson, 2008, 2010). Investigating such attributes allows us to describe and characterize important processes within fault networks including kinematic behaviour (e.g. Nixon et al., 2011), fault interactions and associated damage zones (e.g. Kim et al., 2000; Faulkner et al., 2011), strain localization (e.g. Zhang and Sanderson, 2001; Meyer et al., 2002; Walsh et al., 2003) and connectivity (e.g. Zhang and Sanderson, 2001; Meyer et al., 2002; Walsh et al., 2003). Furthermore, the characterization of such attributes can be used to test models of fault network growth and development (Childs et al., 2003; Soliva and Schultz, 2008; Mouslopoulou et al., 2009; Nicol et al., 2010; Faulkner et al., 2011) and its role in larger scale tectonics (McClay et al., 2002; Cowie et al., 2005; Giba et al., 2010). The major aim of this chapter is to explore the concept of network topology in the characterization of fault networks.

Topology has been a tool for characterizing and describing complex network structures for a wide range of subjects in both the natural and social sciences (e.g. Latora and Marchiori, 2002; Ravasz and Barabási, 2003; Boccaletti et al., 2006). In general, topology describes the relationships between geometrical elements of a network (i.e. compartments, intersections, boundaries and blocks produced by the faults within a network) (Jing and Stephansson, 1997). Unlike geometrical attributes, such as length, thickness, and spacing that are measured by defined dimensional units, topological attributes are dimensionless (Jing and Stephansson, 1997).

Topology is important in the assessment of the connectivity of a fault network, which is essential for evaluating fluid flow and transport properties (see Adler and Thovert, 1999 for summary and background). Hence, there has been some recent work applying topological analysis to fracture network models in order to evaluate the connectivity of fracture networks (Huseby et al., 1997; Jing and Stephansson, 1997; Manzocchi, 2002; Valentini et al., 2007a, 2007b). These studies use a variety of parameters calculated from different topological components to quantitatively assess connectivity, such as the number of intersections per line (e.g. Manzocchi, 2002), the density of intersections (e.g. Jing and Stephansson, 1997) and the efficiency of connectivity, which evaluates the ability of a network to connect two different points to one another (e.g. Valentini et al., 2007a, 2007b).

Nixon et al., (2012), use a basic topological analysis to investigate the connectivity of two natural fault networks, located offshore Hartland Point and onshore at Westward Ho! in NW Devon (UK). This chapter builds on this work and aims to: **1)** define the different topological components and measures for fault networks; **2)** investigate the properties and local variability of such components; and **3)** discuss the applications of the topological analysis in assessing the connectivity of fault networks.

4.2.1. Topology of fault networks

Topological components within fault networks can be evaluated in two-dimensions and three-dimensions. In three-dimensions a network consists of fault planes, which terminate at tip lines or produce intersection lines (branch lines) and divide the rock mass into blocks. Whereas in two-dimensions a network consists of fault traces, which terminate at points (fault tips) or intersect and abut one another dividing the surface area into compartments. Some topological studies use the components which describe the space between faults, such as the blocks and compartments, to assess the connectivity of fracture networks (e.g. Huseby et al., 1997; Adler and Thovert, 1999). Other studies use the fault planes, traces, tips and intersections that describe the fault network itself (e.g. Manzocchi, 2002; Valentini et al., 2007a, 2007b).

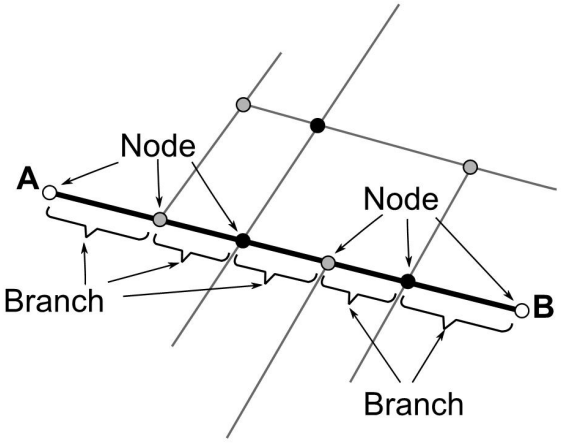

Figure 4.1 A schematic diagram showing a fault trace 'AB' divided into nodes and branches.

In this study we consider the topology of two-dimensional fault networks concentrating on the topological components that describe the faults within the network (i.e. fault traces, tips, intersections, abutments). These are of particular importance as fractures and faults are often characterized using trace maps from rock outcrops, boreholes and thin sections etc. We do not assess the space between faults (compartments) as these are often not fully closed or leave the extent of the fault map.

The terminology used for describing the topological components of a network varies between studies. Fault traces are often described as edges, boundaries, connectors or branches and form a system of line segments in 2-D. These are separated by points of intersection/fault tips which are described as vertices, connections or nodes. In this study, we consider the topology of a fault network to consist of lines, nodes and branches between nodes (Figure 4.1). Nodes can be divided into isolated (I-)nodes, representing isolated fault tips, and connecting nodes that can be described by their geometry as intersecting X-nodes and Y-nodes (Manzocchi, 2002). I-nodes do not connect any branches whereas as X-nodes and Y-nodes connect 4 and 3 branches, respectively (natural fracture systems rarely have more than four fractures intersecting at any one node). The branches themselves have a node at each end and can be topologically described by these two nodes (e.g. I-I, I-X, I-Y...etc.). As nodes can be divided into connecting (C i.e. X- or Y- nodes) and isolated (I) nodes we can further classify the branches into three main topological groups: I-I branches, I-C branches, and C-C branches.

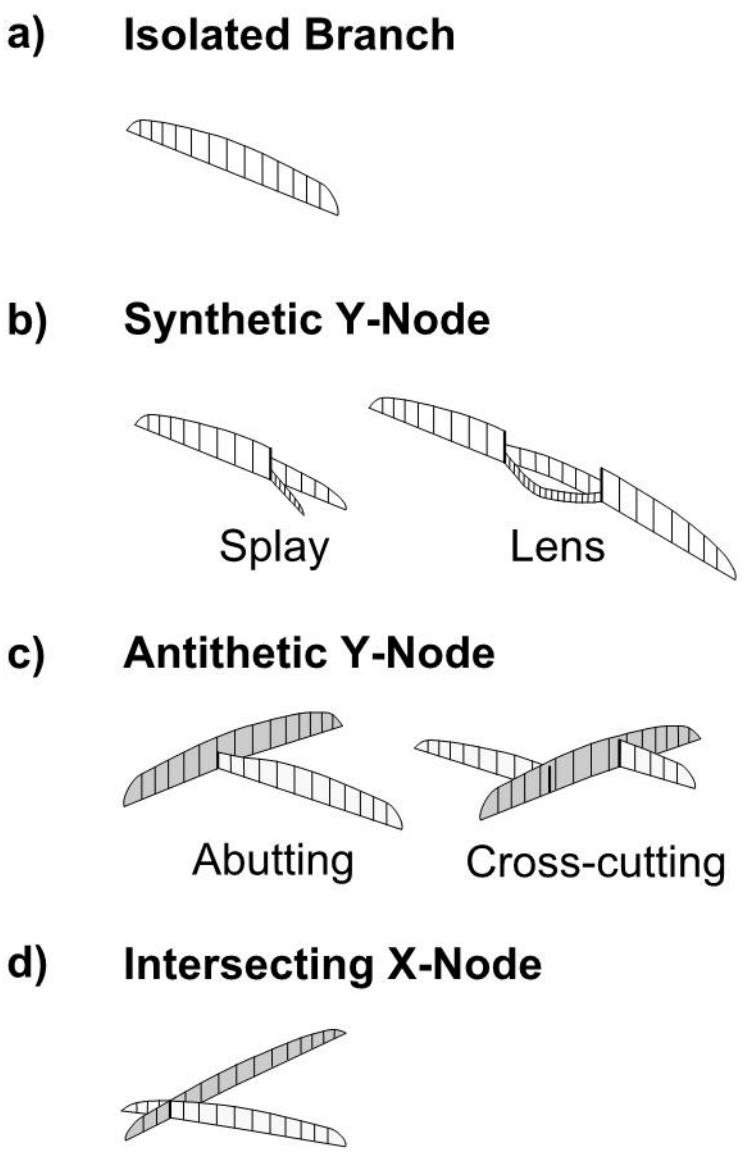

Figure 4.2 Schematic diagram showing the different topological geometries and interactions between faults. a) Isolated branch with a simple displacement profile; b) synthetic Y-node interactions including fault splays and lenses; c) antithetic Y-node interactions including abutments and cross-cutting fault sets; d) intersecting X-node. Grey and white represents different fault sets.

In natural fault systems, a variety of different geometries can form. An isolated I-I branch is the simplest geometry combining two I-nodes and one branch (Figure 4.2a). These can form in all fault networks and often have simple displacement profiles due to a lack of interaction with other faults (Walsh and Watterson, 1988; Peacock and Sanderson, 1996). However, most geometries form by fault interactions that produce connecting nodes. For example, X-nodes form by the crossing of two fractures and usually involve the tips of faults

or small faults with low displacements (Figure 4.2d) (c.f. Nixon et al., 2012). Y-nodes are produced by a variety of interactions such as fault abutments, fault splays and cross-cutting faults (Figure 4.2b and 4.2c). In fault networks, these can be grouped into synthetic and antithetic Y-nodes which involve branches with the same motion sense or branches with opposing motion senses, respectively (c.f. Nixon et al., 2011). In general, cross-cutting faults and abutting faults form antithetic Y-node geometries (Figure 4.2c) whereas fault splays and lenses form synthetic Y-node geometries (Figure 4.2b).

Fault networks can consist of both isolated faults and connected faults. As the fault network grows the interacting faults connect to form clusters of varying size and geometry (Figure 4.3). These clusters are built from two main components: I-C branches and C-C branches. The simplest cluster involves just I-C branches forming 'small isolated' clusters (Figure 4.3b). These isolated clusters can connect with each other forming larger more complicated clusters, which consist of a back-bone of C-C branches and dangling ends of I-C branches (Figure 4.3c). Large clusters can be confined to the sample area or may leave the sample area becoming spanning clusters. The term spanning is applied generically to clusters which stretch across and connect different edges of a sample area (Aizenman, 1997).

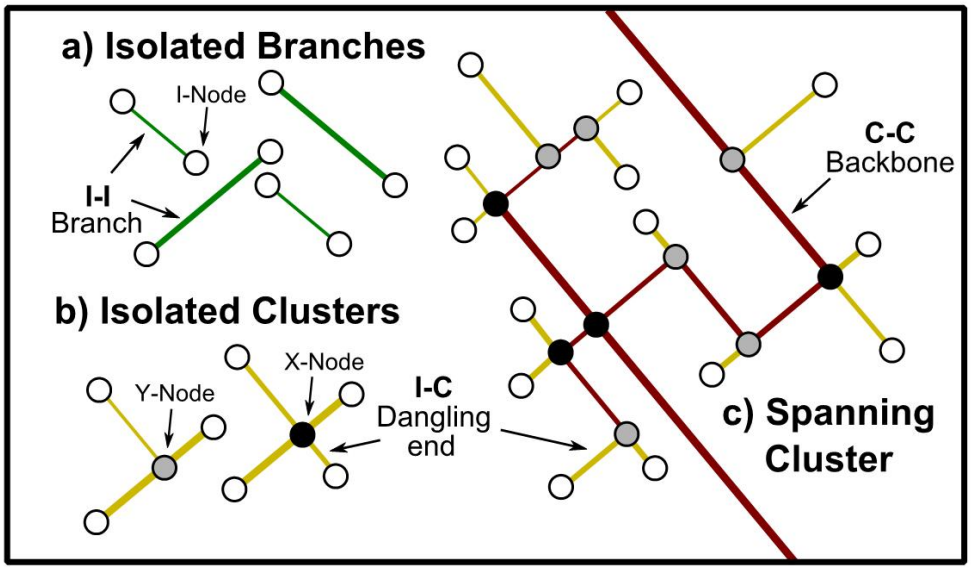

Figure 4.3 Schematic diagram illustrating different topological arrangements and clusters within a fault network. Topology nomenclature is also labelled (see discussion in text).

As the different nodes and branches within a fault network provide a description of the topology of the network, we use a node and branch analysis to assess and characterize the fault network. This involves analysing the spatial distribution, number and proportion of the different node and branch types throughout a network. We then discuss the role that this analysis plays in describing the connectivity of a fault network.

4.3. Methodology

4.3.1. Topological measures

In this study a number of topological measures were used to describe the topology of fault networks. The simplest topological measures are number counts of the different types of topological component (Jing and Stephansson, 1997) such as each node type (N_I, N_Y, N_X) and each branch type (N_{II}, N_{IC}, N_{CC}), which can then be used to calculate the relative proportions (P_I, P_Y, P_X and P_{II}, P_{IC}, P_{CC}). These are important parameters as further information can be derived from these number counts.

4.3.1.1. *Ternary Diagrams*

The proportions of each topological component (nodes and branches) provide information about the organization of faults within a fault network. Manzocchi (2002) plots the proportions of I-, Y-, and X-nodes in a ternary diagram (Figure 4.4a and 4.4b). Where the network plots within the ternary diagram represents the networks connectivity with networks becoming better connected the further they plot away from the I-node corner (Manzocchi, 2002). Nixon et al. (2012) also use an IYX ternary diagram to show the connectivity of fault networks and, hence, this is used for the nodal analysis in this study as well.

Micarelli et al. (2006a; 2006b) use a ternary diagram to illustrate the connectivity of fracture lines. This is based on a method by Ortega and Marrett (2000) and involves classifying fractures as isolated, singly connected or multiply connected. This describes each fracture line by the number of connections per line and the terms ‘singly connected’ and ‘multiply connected’ represent fractures with one connection and fractures with two or more

connections, respectively. We adapt this ternary diagram for the branch analysis, by simplifying the classification to three distinct groups of branches: I-I branches, I-C branches and C-C branches (Figure 4.4c). In general, networks that plot in the I-I corner of the triangle have a low level of connectivity and networks that plot in the C-C corner of the triangle have a high level of connectivity. This also indicates the proportion of the faults within a fault network that contribute to the backbone (C-C) and dangling ends (I-C) of clusters within a network.

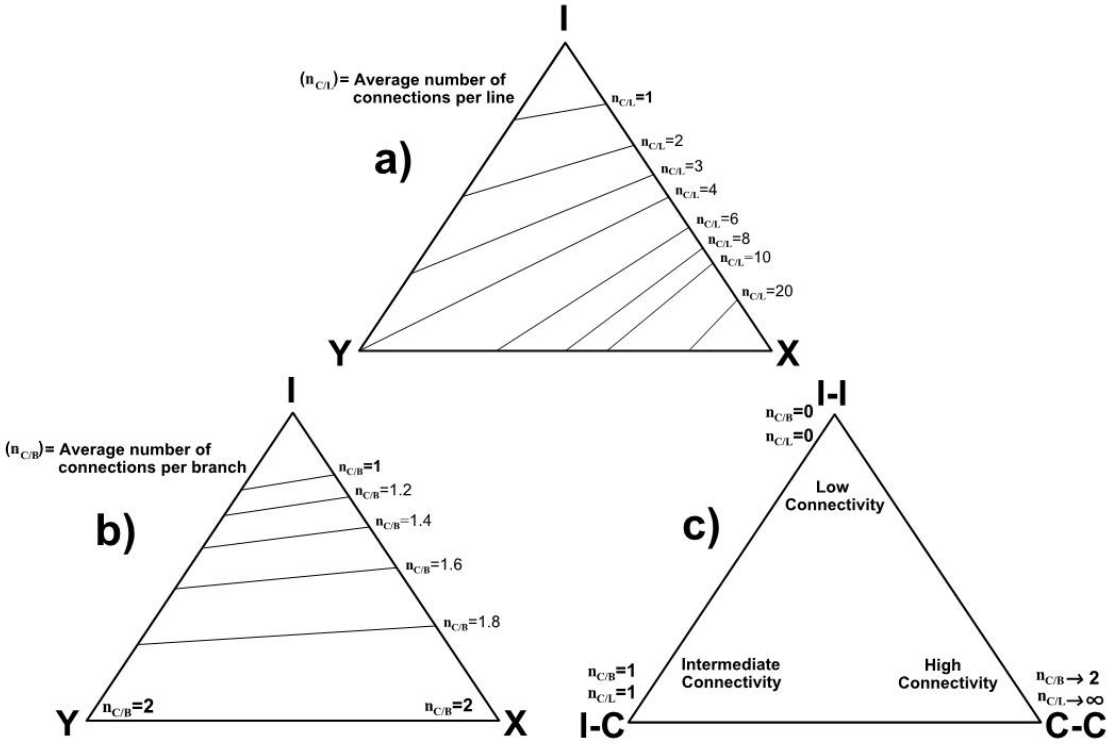

Figure 4.4 a) A ternary node triangle which plots the I:Y:X ratio of a fault network. The number of connections per line ($n_{C/L}$) are contoured onto the node triangle. b) A ternary node diagram with contours of the number of connections per branch ($n_{C/B}$). c) A ternary branch triangle which plots the proportion of trace-length that forms I-I branches, I-C branches and C-C branches with broad regions of connectivity. The values of $n_{C/L}$ and $n_{C/B}$ are extrapolated to each corner of the branch triangle.

4.3.1.2. *Dimensionless parameters derived from number counts*

Number counts of nodes (N_I, N_Y, N_X) are particularly useful as these can be used to count other topological components. For example the number of connections (N_C) is the sum of the number of Y-nodes (N_Y) and X-nodes (N_X):

$$N_C = N_Y + N_X \tag{4.1}$$

As each I-node and Y-node represents the tip of a line (fault trace) the number of lines (N_L) within a network is given by:

$$N_L = \frac{(N_I + N_Y)}{2} \tag{4.2}$$

Since each I-node contributes to one branch, each Y-node contributes to 3 branches and each X-node contributes to 4 branches, then the number of branches (N_B) within a network is given by:

$$N_B = \frac{(N_I + 3N_Y + 4N_X)}{2} \tag{4.3}$$

Equations 4.1 to 4.3 allow us to calculate the number of connections, lines and branches within a network by simply counting nodes. The relationship between these parameters can also be used to produce a 'local' measure of connectivity.

The connectivity of a network can be described in terms of the average number of connections per line ($n_{C/L}$). As each connecting node provides a connection on two lines then:

$$n_{C/L} = \frac{2N_C}{N_L} = \frac{2(N_Y + N_X)}{N_L} \tag{4.4}$$

Connectivity can also be represented by the number of connections per branch ($n_{C/B}$). As each Y-node connects 3 branches and each X-node connects 4 branches then:

$$n_{C/B} = \frac{(3N_Y + 4N_X)}{N_B} \tag{4.5}$$

N_I, N_Y and N_X in equations 4.4 and 4.5 can be replaced by P_I, P_Y and P_X, which represent the proportions of each node type. Hence, values of $n_{C/L}$ or $n_{C/B}$ can be represented on the IYX ternary diagram (Figure 4.4a and 4.4b). Both the number of connections per line and the number of connections per branch have a value of 0 at the I-node corner of the node ternary triangle. They also share the same contour for values of 1 connection per line and branch. However, the

number of connections per line tends to infinity as $P_X \rightarrow 1$, whereas the number of connections per branch reaches a maximum of 2 when $P_I = 0$.

The values of $n_{C/L}$ or $n_{C/B}$ can also be extrapolated to the three corners of the branch ternary triangle (Figure 4.4c). Again both have values of 0 and 1 at the I-I and I-C corners of the triangle, respectively. However, for networks that are dominated by C-C branches $n_{C/L} \rightarrow \infty$ whereas $n_{C/B} \rightarrow 2$. This means that the proportion of I-C and C-C branches can have a large impact on the connectivity of the network.

4.3.1.3. *Branches vs lines*

Number counts of topological components has led to the derivation of many parameters that can describe the topology of fault networks and these have included the use of both branches and lines. However, due to problems when characterizing fault trace-lengths in networks, we favour the use of branches over lines because:

1. ***Branches are easily identified*** – due to the heterogeneity in fault character within fault networks it is difficult to define the tips of a fault line because of processes such as splaying. However, as branches are defined by their nodes at each end, which are either tips or intersections, they are easily identified making them more consistent for sampling.
2. ***Sampling*** – due to the length of fault lines generally being greater than branches it is more likely that the full length of a line will be censored within a sample area (e.g. Pickering et al., 1995). Branches have smaller lengths, which provide a greater chance of sampling a whole branch length within a sample area.
3. ***Branch length distribution*** – fault lengths within a network have been shown to follow a power-law or negative exponential distribution (Soliva and Schultz, 2008). Therefore, they can exhibit a wide range of lengths making the individual lines lengths hard to characterize or represent and in the case of power law distributions there is no mean length. However, since each line is segmented into branches by connecting nodes and longer faults are more likely to connect with other faults, the resulting

branches have a narrower range of lengths and probably conform to a log-normal or negative exponential distribution.

4. ***Assessing connectivity*** – using $n_{C/L}$ can be misleading when assessing the connectivity of a network as networks with a $P_X \rightarrow 1$ produce a significantly greater number of connections per line than networks with a $P_Y \rightarrow 1$ (Figure 4.4a). This suggests that networks with only Y-node intersections cannot form a network where $P_{CC} \rightarrow 1$ as $n_{C/L} \rightarrow \infty$ (Figure 4.4c). However, in reality this is not the case as a network with only Y-nodes will form a network dominated by C-C branches. Therefore $n_{C/B}$ is a better assessment of the connectivity as this provides an equal maximum value of connecting nodes per branch ($n_{C/B} = 2$) for networks where P_X and $P_Y = 1$ (Figure 4.4b), indicating that both can form a network that has only C-C branches (Figure 4.4c).

4.3.1.4. *Sampling of nodes and branches*

The sampling of nodes is straight forward as you simply count the number of nodes that lie within the boundaries of the sample area (Figure 4.5). However, a branch may go beyond the boundary of a sample area, which means that a) the length of such a branch is unknown or censored and b) the topological classification of the branch is unknown. As these parameters are unknown these branches cannot be used in the branch analysis. Therefore, any branch that crosses the boundary of a sample area is omitted from the sample (Figure 4.5).

When sampling subareas within a fault network we use a circular sampling technique. Circles are used as they do not provide an orientation bias. Subareas were chosen to compare the effects of fault density on topology, therefore the radius of each circle may be varied depending on the sample area (Figure 4.6a and 4.6b). For example, high density subareas are often small zones of intense deformation that are surrounded by regions of low density, hence only circles that were small enough to sample the area of high fault density were used. Furthermore, areas with low fault densities and long faults often produce low volumes of data, as there are fewer intersections and

branches, so we use larger circles for these subareas in order to maximize the amount of data for the topological analysis.

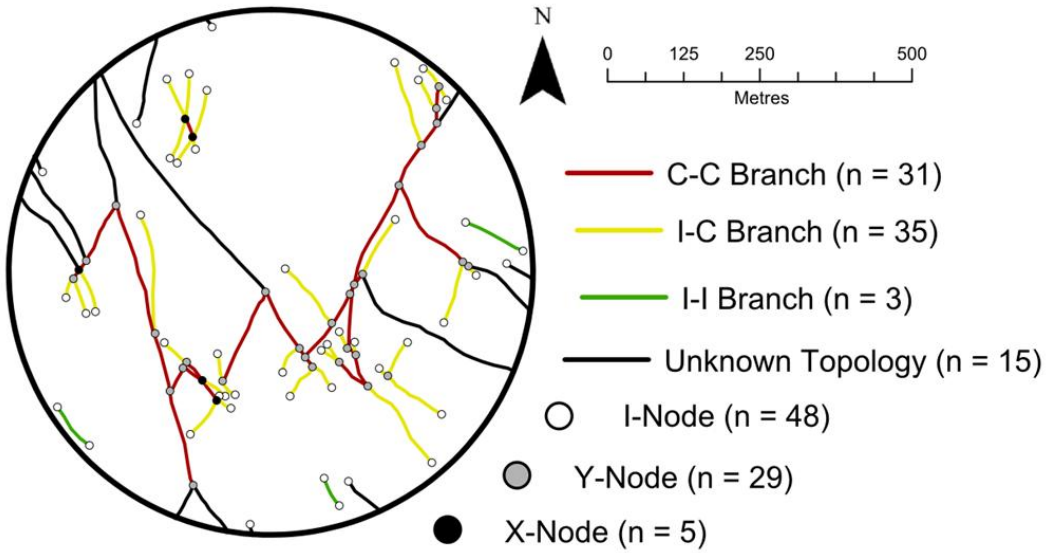

Figure 4.5 An example of sampling the nodes and branches from subarea 3 (see Figure 4.6). Note that branches with unknown topologies are omitted from the analysis.

4.3.2. Maps and contour plots

The spatial distribution of geometrical and topological attributes were analysed through a combination of maps and contour plots. Fault maps were used to illustrate the geometry of faulting and distribution of different branch and node types within the fault networks, whereas contour plots were used to show the spatial variation in fault density (km/km^2) and connecting node frequency (N_C/km^2) within a network.

We use line and point contour plots which show the spatial variation in the total line length or the total number of points per square kilometre, respectively. However, due to the potential for certain attributes (e.g. connecting nodes) to be scattered and/or at low frequency we use a kernel function, which reduces the effect of artefacts that might occur within a contour plot. The kernel function produces a surface for each line/point that uses a quadratic relationship, as described in Silverman (1986, pg. 76, equation 4.5), to apply a weighting factor related to the surface's proximity to its given line/point. The maximum weighting

to each surface is 1 at the given line or point and decreases to zero at a specified radius. The values of each overlapping surface that lie within a grid cell are then summed together to produce a contour value for the grid cell itself. The contour plots use a 10 m X 10 m grid and a 450 m surface radius around each feature for Hartland and a 3 m x 3 m grid and a 100 m surface radius around each feature for Westward Ho!.

The resulting kernel contour plots have smooth contours that allow the comparison of the spatial distribution of different attributes. This means that the links between different attributes (e.g. fault density and connecting node frequency) can be investigated and illustrated.

4.4. Case studies – Hartland Point and Westward Ho!

The two natural fault networks used to explore the topology of fault networks are from Hartland Point and Westward Ho!, north Devon (Figure 4.6d). The fault networks were mapped by Nixon et al. (2011, 2012) using multibeam bathymetry imagery offshore Hartland Point and a combination of aerial photography and field observations onshore at Westward Ho!. Both networks comprise a conjugate set of strike-slip faults, with NW-trending right-lateral faults and NE-trending left-lateral faults, forming geometrically simple fault networks, which are ideal for this study.

At Westward Ho! there is a higher density of fault traces, which accommodate much higher strains than the fault network offshore Hartland Point (Table 4.1). Furthermore, Nixon et al. (2011) observe a large degree of heterogeneity at Westward Ho! with fault dominance changing between areas, whereas the fault network offshore Hartland Point is less heterogeneous deforming in a right-lateral domino fashion (Nixon et al., 2012). Nixon et al. (2012) also established that the network from Hartland Point appears to be relatively unconnected, whereas the network at Westward Ho! is well connected. Thus the two fault networks comparison of topology and the extensive areas of faulting allow any spatial changes within each network to be analysed.

Table 4.1 Different physical attributes for both fault networks. The subareas (located in Figure 4.6) for each fault network are in ascending order of fault density with dark grey representing subareas that have >80% of one fault set.

Area Subarea	Fault Trace-length (km)	Fault Density (km/km^2)	Proportion of L-L Faults	Proportion of R-L Faults	Average Displacement (m)	%Extension	Orientation of Extension
Hartland	**100.8**	**6.4**	**19.5%**	**80.5%**	**11.2**	**4.4**	**N112°E**
1	6.5	5.2	3.6%	96.4%	-	-	-
4	5.2	6.3	4.9%	95.1%	-	-	-
5	4.4	8.3	42.8%	57.2%	-	-	-
3	7.7	9.5	31.3%	68.7%	-	-	-
2	5.3	10	17.1%	82.9%	-	-	-
7	5.6	10.4	23.7%	76.3%	-	-	-
6	5.8	10.9	8.0%	92.0%	-	-	-
Westward Ho!	**21.1**	**40**	**45.7%**	**54.3%**	**7.6**	**14.0**	**N083°E**
9	0.8	25.8	90.0%	10.0%	-	-	-
13	1.3	42.8	17.0%	83.0%	-	-	-
8	1.1	56.6	57.7%	42.3%	-	-	-
14	1.2	62.1	40.9%	59.1%	-	-	-
12	1.3	64.5	58.2%	41.8%	-	-	-
11	1.4	69.1	30.0%	70.0%	-	-	-
10	2.2	71.5	46.5%	53.5%	-	-	-

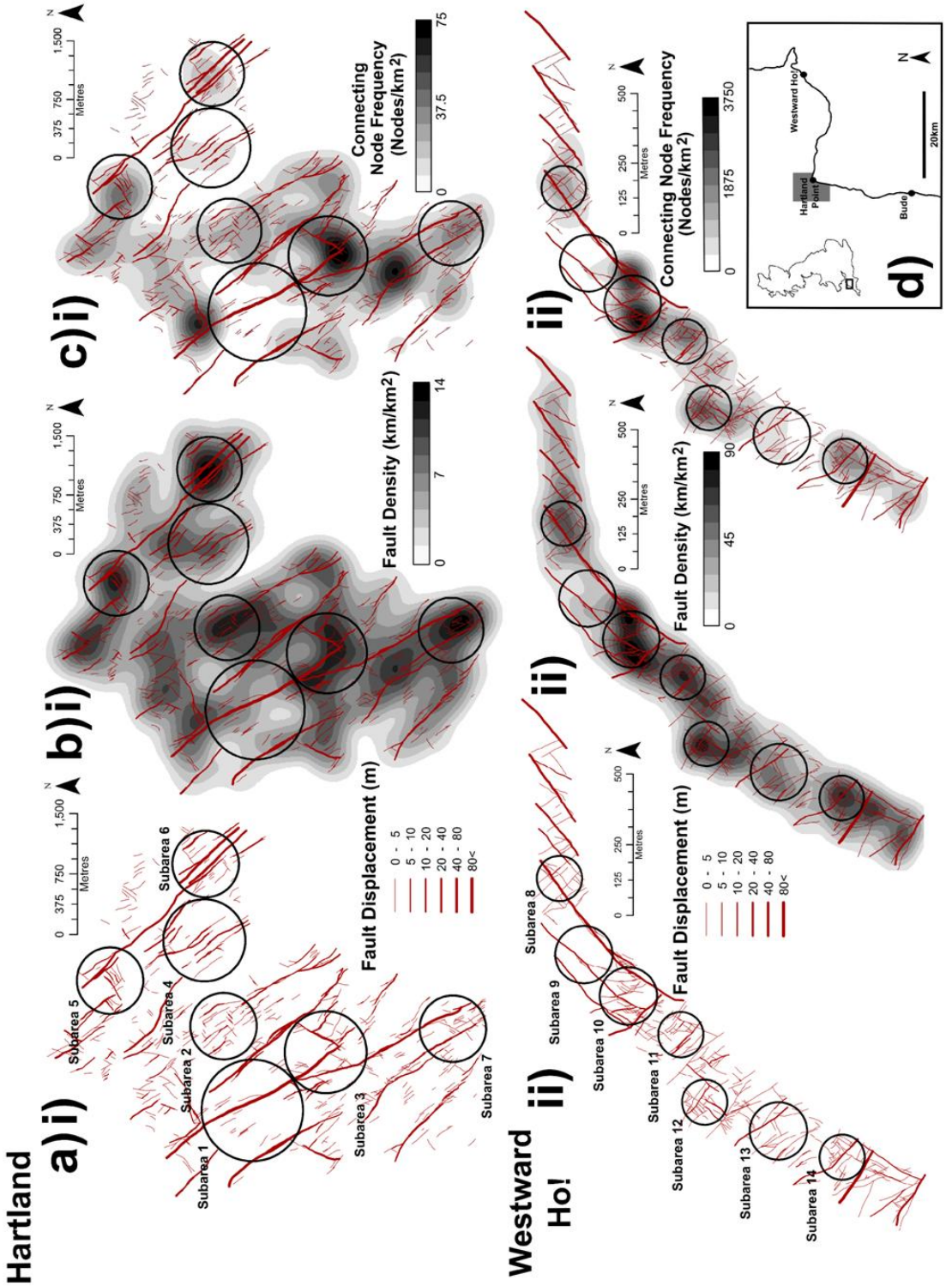

Figure 4.6 a) A fault trace map of displacement for i) Hartland and ii) Westward Ho! indicating the location of each subarea; b) Contour plots of fault trace-length density showing the distribution of fault trace-length; c) Contour plots of connecting node frequency (Y- and X-nodes), illustrating the spatial distribution of connectivity; d) inset location map of the two fault networks. Each density contour plot uses a 10 m X 10 m grid and a 450 m radius around each feature for Hartland and a 3 m x 3 m grid with a 100 m radius around features at Westward Ho!.

4.4.1. Spatial distribution of trace-length and displacement

Seven sub areas have been picked from each network (Figure 4.6a) to sample variations in fault density (km/km^2) and fault set dominance (Table 4.1). Subareas 1 to 7 are from offshore Hartland and have fault densities which range from 5.2-10.9 km/km^2, whereas subareas 8-14 are from Westward Ho! and have fault densities which range from 25.8-71.5 km/km^2 (Table 4.1). These variations in fault density within each subarea indicate spatial heterogeneity with areas of greater fault density (i.e. subareas 3 and 10) separated by areas of lower density (i.e. subareas 1 and 9) (Figure 4.6b).

Localized areas with high densities are associated with areas of damage due to interaction and linkage between large faults (i.e. subareas 3 and 10) and include numerous short faults with low displacements (Nixon et al., 2012). Areas of low density are dominated by a few faults with long trace-lengths and larger displacements. Furthermore, when looking at the distribution of right- and left-lateral faults within each subarea, the areas of low density are often dominated by one fault set taking up at least 80% of the trace-length (Table 4.1), whereas the high density areas generally include more equal proportions of both left- and right-lateral faults (Table 4.1). There are two exceptions, subareas 2 and 6, which have high fault densities and are dominated by one fault set.

These trends are also seen on a larger scale when comparing the two networks. The Westward Ho! area has a much higher fault density and also has approximately even proportions of right- and left-lateral faults. Whereas, at Hartland the fault density is low and the whole network is dominated by long right-lateral faults making up ~80% of the fault trace-length (Table 4.1).

4.5. Topological analysis

4.5.1. Node analysis

4.5.1.1. *Spatial distribution of connecting nodes*

The average connecting node frequency for Westward Ho! (741 N_C/km^2) is much greater than Hartland (15 N_C/km^2; Table 4.2). The majority of the

connecting nodes within both networks form localized clusters (Figure 4.6c) that coincide with the bulls eyes of high trace-length density (Figure 4.6b), indicating that the connecting node distribution is strongly related to fault density (e.g. subareas 3 and 10). In general, the number of connecting nodes increases with fault density producing a positive correlation, which is particularly obvious for subareas at Westward Ho! (Figure 4.7a). This is because with increasing fault density the probability of two faults intersecting or abutting increases. Therefore, areas of damage (subarea 10) and linkage (subarea 3), which are generally areas with high trace-length densities, will produce a greater number of connecting nodes.

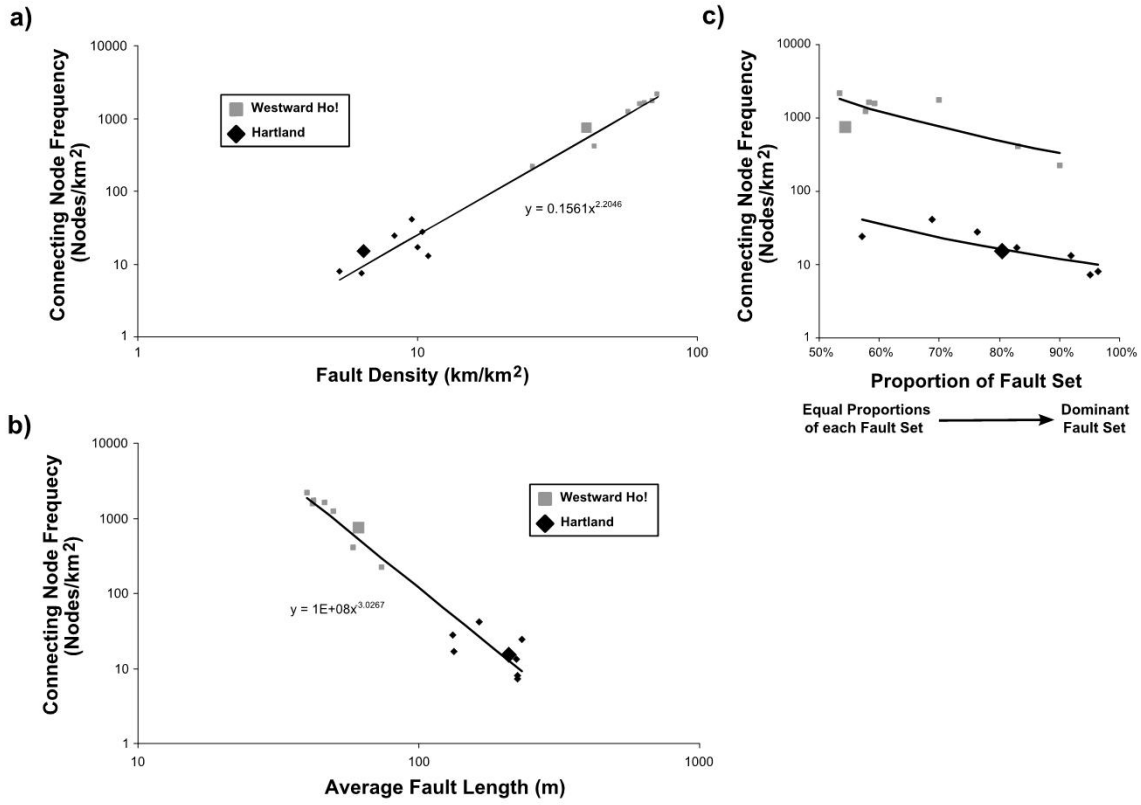

Figure 4.7 a) log-log plot of connecting node frequency vs fault density. b) log-log plot of connecting node frequency vs fault length. c) log-normal plot of connecting node frequency vs fault set proportion where 50% represents equal proportions of each fault set.

The average fault length also influences the connecting node frequency. This has the opposite effect to fault density with increasing fault length forming a negative correlation with connecting node frequency (Figure 4.7b). This is because if you increase the length of each fault in a network you inherently keep the same number of nodes but increase the area to accommodate the longer fault lengths, hence decreasing the connecting node frequency. This

Table 4.2 Proportions of each node type within the fault networks at Hartland and Westward Ho!. The subareas (located in Figure 4.6) for each fault network are in ascending order of fault density and the dark grey represents subareas that have >80% of one fault set.

Area / Subarea	I-Nodes (%)	Y-Nodes (%)			X-Nodes (%)	Connecting Node Frequency (Nodes/km^2)	No. of Branches (N_B)	Connections per Line ($n_{C/L}$)	Connections per Branch ($n_{C/B}$)	I-I Branch (%)	I-C Branch (%)	C-C Branch (%)
		Total	Ya	Ys								
Hartland	**74.7**	**21.7**	**13.4**	**8.3**	**3.6**	**15**	**721.5**	**1.05**	**1.03**	**26**	**46.5**	**27.5**
1	76.2	23.8	7.1	16.7	0	8	31	0.95	0.97	47.8	17.4	34.8
4	80.6	16.1	6.5	9.7	3.2	7	22	0.8	0.86	21.4	64.3	14.3
5	59.4	37.5	28.1	9.4	3.1	24	29.5	1.68	1.36	7.7	61.5	30.8
3	58.5	35.4	26.8	8.5	6.1	42	77.5	1.77	1.38	4.3	50.7	44.9
2	87	10.1	4.3	5.8	2.9	17	44.5	0.54	0.65	43.9	46.3	9.8
7	77.9	17.6	10.3	7.4	4.4	28	50.5	0.92	0.95	31	38.1	31
6	82.9	14.6	7.3	7.3	2.4	13	28	0.7	0.79	45.8	37.5	16.7
Westward Ho!	**42.2**	**48.5**	**31.4**	**17.2**	**9.3**	**741**	**760.5**	**2.55**	**1.63**	**4.4**	**30**	**65.7**
9	41.7	58.3	8.3	50	0	223	13	2.33	1.62	0	44.4	55.6
13	56.7	43.3	13.3	30	0	414	28	1.73	1.39	10	40	50
8	24.2	63.6	54.5	9.1	12.1	1243	43.5	3.45	1.82	0	20.6	79.4
14	42.9	46.4	37.5	8.9	10.7	1592	63	2.56	1.62	5.2	31	63.8
12	35.3	49	37.3	11.8	15.7	1641	62.5	3.07	1.71	3.5	21.1	75.4
11	31.4	62.7	37.3	25.5	5.9	1741	62	2.92	1.74	0	21.4	78.6
10	30.3	58.6	41.4	17.2	11.1	2196	124	3.14	1.76	0.9	25	74.1

suggests that large-scale fault networks will produce less connecting nodes as fault lengths are much longer and fault densities are much lower (i.e. Hartland).

Subareas 2 and 6 for offshore Hartland do not display as high a connecting node frequency as would be expected, considering their fault densities in comparison to other subareas at Hartland (Table 4.2). This is due to a dominance of one fault set within these subareas (Table 4.1). In general, subareas with equal proportions of both fault sets (i.e. 50%; Figure 4.7c) have a greater connecting node frequency than subareas that are dominated by one fault set (i.e. 100%; Figure 4.7c).

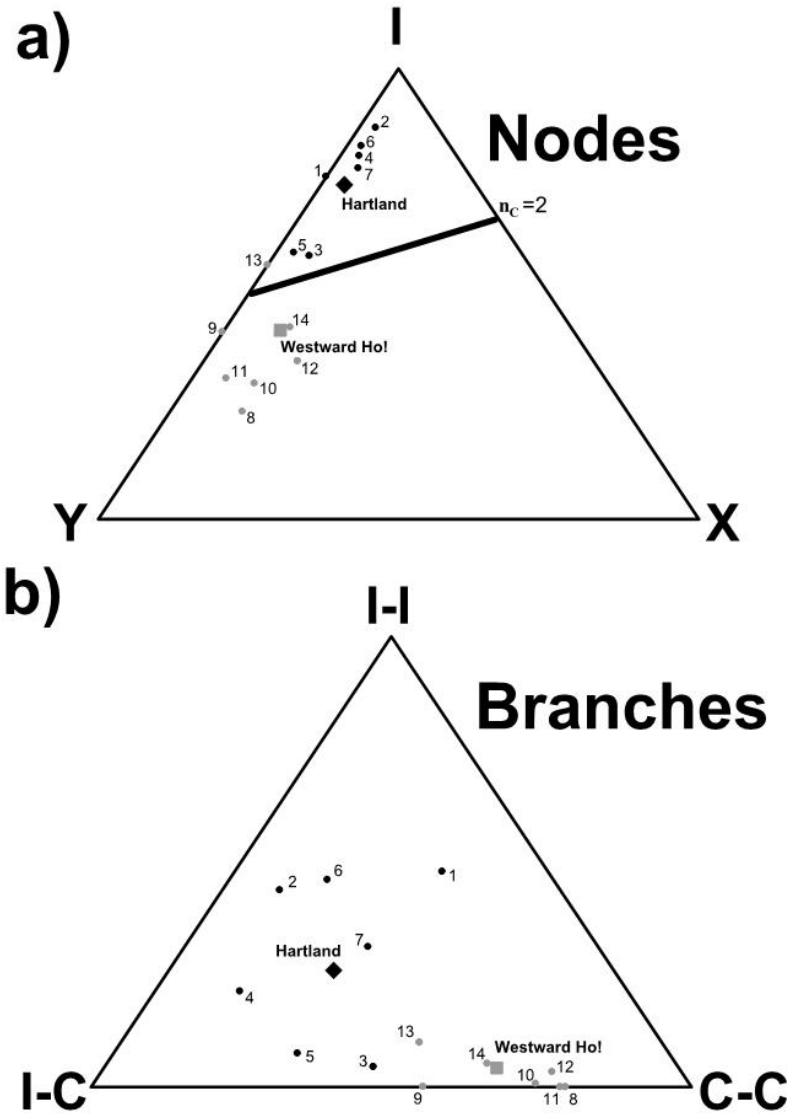

Figure 4.8 a) A ternary plot of the proportions of I-, Y- and X- nodes. b) A ternary plot of the proportions of I-I, I-C and C-C branches. Data from the fault networks at Westward Ho! and Hartland are in grey and black, respectively. Subareas are indicated by the number next to each dot.

Overall the frequency of connecting nodes is largely influenced by fault density and fault length producing a correlation across both datasets, suggesting scale dependence (Figure 4.7a and 4.7b). However, the proportion of each fault set affects both fault networks independently and only has a small influence on the connecting node frequency (Figure 4.7c).

4.5.1.2. *Node proportions*

The proportions of I- Y- and X-nodes for each network are plotted in a ternary diagram in Figure 4.8a. All of the subareas cluster around the points where their respected networks plot in the ternary triangle. Both fault networks plot in the IY half of the ternary diagram, however, the fault network at Westward Ho! plots further away from the I-node corner of the ternary triangle than the fault network offshore Hartland (Figure 4.8a). Therefore, Westward Ho! has a greater proportion of connecting nodes (~58%) than Hartland (~25%; Table 4.2).

The difference in node topology is further reflected in the number of connections per line ($n_{C/L}$) and per branch ($n_{C/B}$) with Hartland producing lower values than at Westward Ho! (Table 4.2). Subareas at Hartland produce $n_{C/L}$ values of 0.54 to 1.77 (i.e. $n_{C/L} < 2$), whereas subareas at Westward Ho! have $n_{C/L}$ values of 1.73 to 3.45. Most of the subareas at Westward Ho! have an $n_{C/L} > 2$. The values of $n_{C/B}$ show the same trend as values of $n_{C/L}$ with subareas offshore Hartland producing values of $n_{C/B}$ from 0.65-1.36, whereas subareas at Westward Ho! have values of $n_{C/B}$ from 1.39-1.82. In general, values of $n_{C/B}$ produce a much narrower range but are very similar to values of $n_{C/L}$ for subareas that plot near the $n_{C/B} = 1$ contour.

4.5.2. Branch analysis

4.5.2.1. *Spatial distribution of branches*

In Figure 4.9 the fault trace-lengths are displayed by branch type: I-I (isolated) branches, connected I-C (dangling ends) and connected C-C (backbone) branches. Overall, the network at Hartland has many more I-I branches and I-C branches in comparison with Westward Ho!, which has mainly C-C branches.

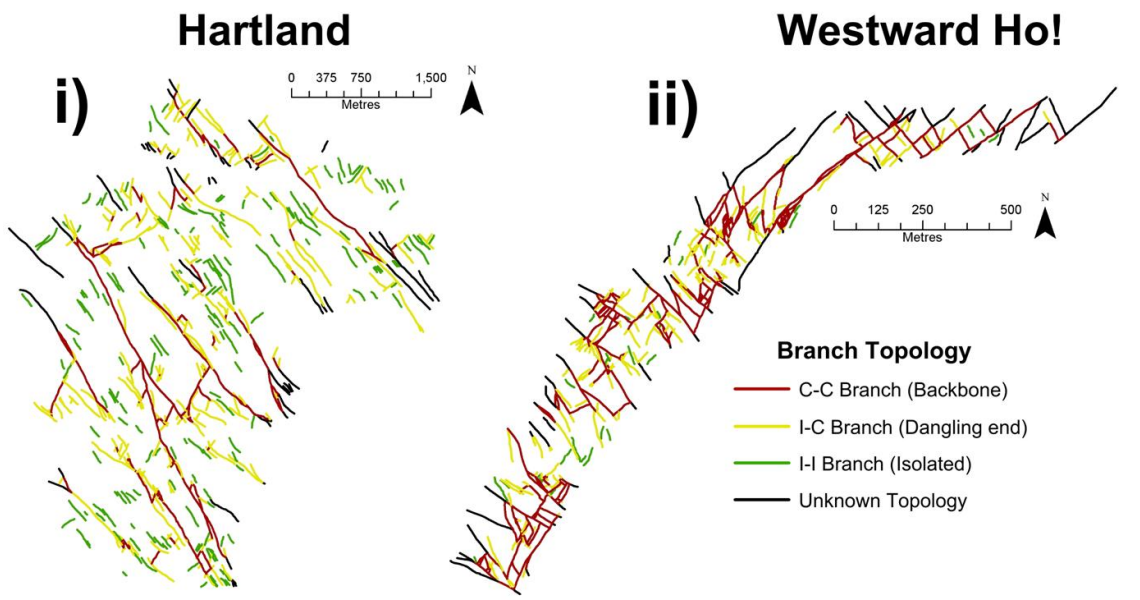

Figure 4.9 Fault maps of each network displaying the distribution of each branch type (I-I, I-C and C-C) within the fault networks at i) Hartland and ii) Westward Ho!.

Although there are many isolated faults in the fault network at Hartland, the long right-lateral fault traces within the network are made up of numerous C-C branches forming the backbone of several large elongated clusters. C-C branches also make up some of the long fault traces at Westward Ho!, however, they mainly form dense clusters with numerous small interconnected C-C branches from both fault sets. These produce localized areas of high connectivity (for example subarea 12) and coincide with areas of high connecting node frequencies and high trace-length densities (Table 4.2; Figure 4.6b and 4.6c). In general, the character of the clusters in each network reflects the overall fault density and fault trend of the network itself.

4.5.2.2. *Branch proportions*

The ternary diagram showing the proportions of each branch type indicates that both fault networks and all of the sub areas have a greater number of connecting branches (I-C and C-C) than isolated (I-I) branches. (Table 4.2; Figure 4.8b). Westward Ho! has a much smaller proportion of I-I branches (~4%) than Hartland (26%) with all of the subareas from Westward Ho! plotting at the base and in the C-C corner of the triangle (Figure 4.8b). Therefore, the majority of the branches at Westward Ho! are C-C branches, which form the backbone of large clusters.

The subareas at Hartland are very scattered when plotted in Figure 4.8b showing a much greater heterogeneity in branch topology in comparison to Westward Ho!. The majority of the subareas at Hartland have more I-C branches than C-C branches, which indicates that there are more dangling ends and small isolated clusters within the network (Table 4.2).

4.6. Characteristic properties of topological components

4.6.1. Synthetic Y-nodes vs antithetic Y-nodes

Synthetic Y-nodes produce more acute angles (~27°) of intersection between faults than antithetic Y-nodes (~67°; Figure 4.10a). This is because, synthetic Y-nodes occur between faults with the same motion sense that are at low angles to one another (<45°) forming splays and lenses. Whereas, antithetic Y-nodes involve two faults with opposing motion senses that are at high angle to one another (>45°) forming fault abutments and intersections.

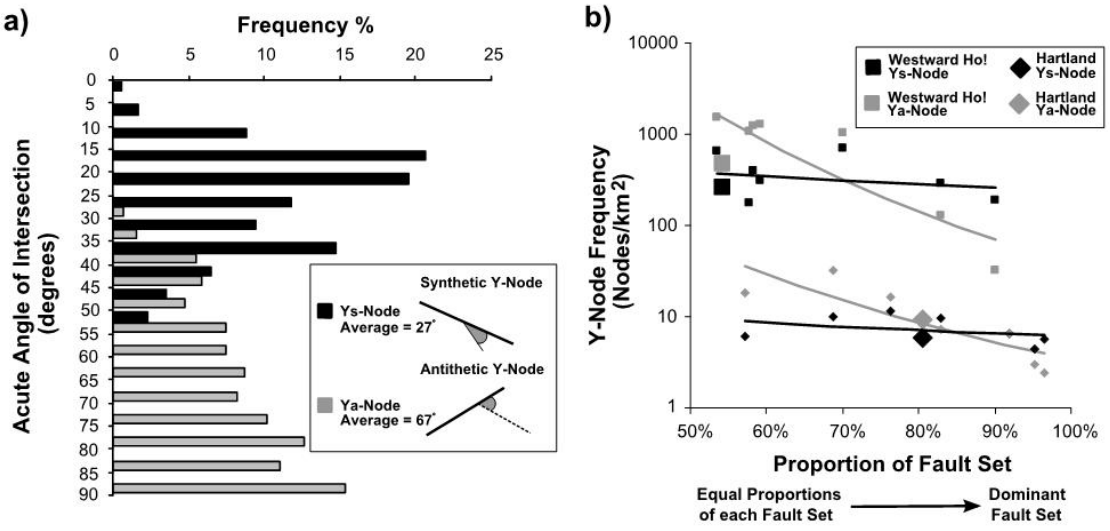

Figure 4.10 a) Histogram illustrating the acute angles of intersection for synthetic and antithetic Y-node interactions. b) Log-normal plot of connecting node frequency vs fault set proportion for synthetic Y(s)-nodes and antithetic Y(a)-nodes in black and grey, respectively.

Both fault networks have more antithetic than synthetic Y-nodes, however this varies between subareas. In general, subareas that are dominated by one fault set (i.e. >80% of one fault set) have a greater proportion of synthetic Y-nodes (Table 4.2). Whereas subareas with opposing fault sets produce more

antithetic Y-nodes (Table 4.2). Although the proportion of antithetic and synthetic Y-nodes appears to be related to the fault set dominance, only the number of antithetic Y-nodes varies between subareas as indicated by the relationship between Y-node frequency and fault dominance (Figure 4.10b). Overall the number of synthetic Y(s)-nodes in a network is constant despite changes in fault set dominance between subareas, whereas the number of antithetic Y(a)-nodes decreases with an increased dominance of one fault set (i.e. fault set dominance tends to 100%; Figure 4.10b).

4.6.2. Branch length distribution

Branch length is an important characteristic as it is linked to the number of connecting nodes per line, which are used to calculate the number of branches (N_B), and the length of each fault (l). The average branch length (L_B) can be calculated by the following relationship:

$$L_B = \frac{\sum l}{N_B} = \frac{2 \times \sum l}{N_I + 3N_Y + 4N_X} \tag{4.6}$$

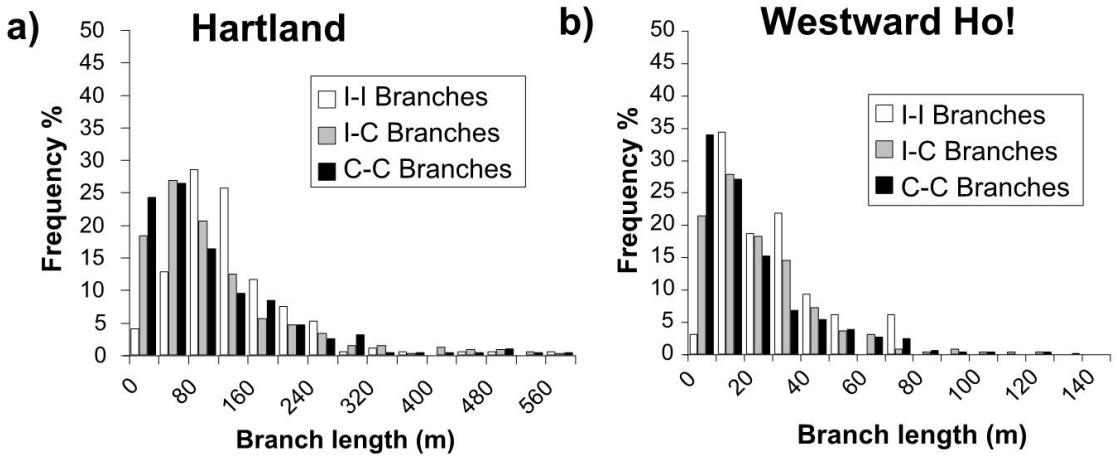

Figure 4.11 Histograms showing the frequency of different branch lengths for a) Hartland and b) Westward Ho!.

The average branch lengths range from 100 - 234 m and 18 - 62 m for subareas from Hartland and Westward Ho!, respectively. In comparison to fault lines the branches have much lower mean and median lengths in both fault networks (Table 4.3). Both the branch and line lengths have median lengths that are much smaller than the mean lengths indicating a skewness in their

distribution (Table 4.3). However, calculated values for skewness show that the branch length distributions are much less skewed than the line length distributions (Table 4.3). Furthermore, the coefficient of variance (CV) is generally lower for branches (i.e. ~ CV ≤ 1) than for lines (i.e. CV > 1) indicating that there is less variability in the branch length (Table 4.3).

Table 4.3 Statistical analysis of branch and line lengths

	I-I Branches	I-C Branches	C-C Branches	Fault traces
Hartland				
Mean length (m)	137.5	126.1	116.9	208.9
Median length (m)	121.4	89.0	79.4	139.3
Standard Deviation (m)	82.0	126.7	125.9	272.6
Coefficient of Variation (CV)	0.6	1.0	1.1	1.3
Skewness	2.1	2.6	3.3	5.6
Westward Ho!				
Mean length (m)	29.5	26.1	22.5	60.9
Median length (m)	25.4	20.2	14.9	40.7
Standard Deviation (m)	17.0	20.7	22.8	67.5
Coefficient of Variation (CV)	0.6	0.8	1.0	1.1
Skewness	1.3	1.8	2.2	4.5

The different branch types (I-I, I-C and C-C) have similar length distributions in each network with peaks in frequency around ~100 m at Hartland and ~20 m at Westward Ho! (Figure 4.11). There are slight variations for each branch type with the peak frequencies for more connected branches (i.e. C-C) occurring at shorter branch lengths. In general, the branch length distributions show either a log-normal distribution or a negative exponential distribution (Figure 4.11).

4.6.3. Isolated branches vs connected branches

A fault network can be considered as two separate systems: a connected system of branches, which are connected to other branches by connecting nodes, and an isolated system, which consists of isolated branches and isolated nodes. The branch analysis established that the fault network at Westward Ho!

has very few isolated branches, whereas Hartland has a considerable proportion of I-nodes and isolated branches. Therefore, we use the network offshore Hartland to further investigate the different characteristics of isolated and connected branches:

a) *Isolated Branches* – The isolated branches make up ~28% of the fault trace-length within the fault network offshore from Hartland. The fault density contour plot in Figure 4.12a shows that the isolated branches are evenly distributed throughout the fault network. The faults that are made up of isolated branches have an average trace-length of 144 m but the right-lateral faults produce the longer trace-lengths of up to ~800 m (Figure 4.13a) which reflects the overall right-lateral dominance of the fault network. Although there are numerous isolated branches throughout the fault network they have small displacements with an average displacement of 3.4 m (Figures 4.12a). As a result the isolated system does not accommodate much of the overall strain producing a maximum extension of ~0.4% at an orientation of N111°E (Figure 4.12a).

b) *Connected Branches* – The majority of fault trace-length (~72%) within the fault network forms the connecting branches and nodes. The NW-trending dominance of the fault trend of the network is also seen in connected branches, which have a dominance of NW-trending right-lateral faults (Figure 4.12b). The connected branches produce large clusters that form the main fault pattern of the network including long fault traces that form elongated fault bound blocks (Figure 4.12b). These long fault traces can have lengths up to 2700 m. Smaller faults appear to be concentrated in high density areas of damage and linkage connecting the longer fault traces. The faults within the connected system have an average displacement of 14.2 m, which is much greater than the faults in the isolated system. This is reflected in the amount of strain accommodated by the connected system, which produces a maximum extension of ~4% orientated at N112°E (i.e. >90% of the total strain produced by the fault network; Figure 4.12b).

Although the overall fault trends for both the isolated and connected branches are similar there are some key differences. Most long fault traces within the

network are made up of connected branches, whereas the isolated branches have smaller fault lengths. This is due to an increase in the probability of one fault abutting/intersecting another fault as the fault traces become longer.

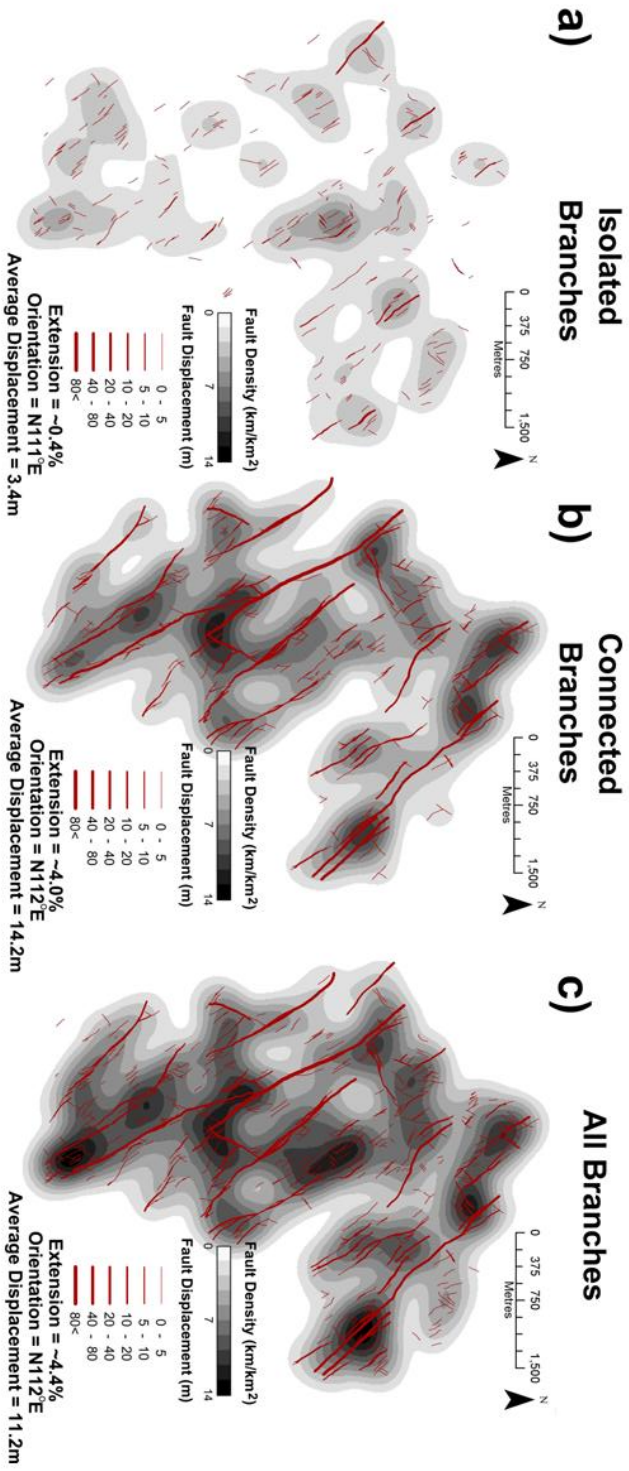

Figure 4.12 Fault maps and contour plots of fault trace-length for the fault network offshore Hartland. These show the distribution of a) the isolated branches; b) the connected branches within the fault network and c) the entire fault network. The density contour plots used a 10 m X 10 m grid and a 450 m radius around each feature.

Even though the longer fault traces are made up of connected branches, the connected branches themselves can be as short as 5 m in length. This is very different to the isolated branches which have very few branches with lengths that are <50 m (Figure 4.13). This is because isolated branches have space to grow in length without abutting another fault, whereas many connected branches are produced by intersecting faults and can be cut smaller by other connecting branches.

The long fault traces that are produced within the fault network also accumulate the largest displacements (Figure 4.12c) as strain is localized onto them. This is why the connected branches accommodate the majority of the strain indicating that strain is localized to the connected faults within a fault network. Strain can be localized onto individual faults, which may then grow by segment linkage, or be localized to an area producing a damage zone with a high fault density, both of these processes favour connectivity.

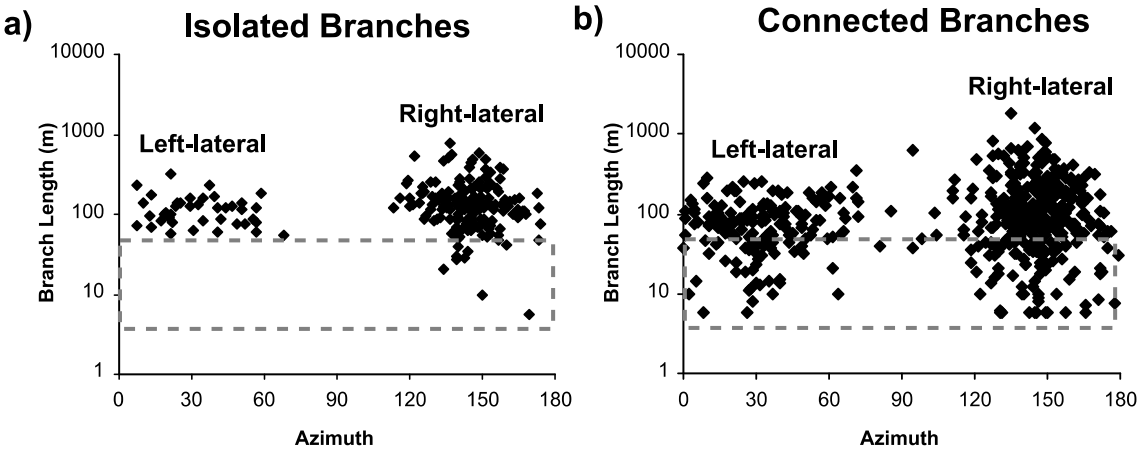

Figure 4.13 Plot of branch length (log) against azimuth for a) isolated branches from Hartland and b) connected branches from Hartland. Note the scarcity of isolated branches within the grey box in comparison to the connected branches.

4.7. Discussion – Assessing connectivity

This chapter has concentrated on exploring the topology of fault networks by developing and applying a node and branch analysis to two natural fault networks from north Devon, UK. The node and branch analysis allows us to describe and characterize each fault network and the sub areas within them.

The topology is intrinsically linked to the pattern of connectivity within a network and has been often used for assessing the connectivity of fracture networks and their ability to percolate (Robinson, 1983; Huseby et al., 1997; Jing and Stephansson, 1997; Manzocchi, 2002). Therefore, in this section we discuss the application of the topological analysis for describing the connectivity of fault networks from offshore Hartland and onshore at Westward Ho!.

4.7.1. Characterizing connectivity in fault networks

The nodal analysis allows a quantitative assessment of the connecting nodes within each fault network by using the connecting node frequency, the number of connections per line ($n_{C/L}$) and the number of connections per branch ($n_{C/B}$). These parameters quantify the connections within a fault network and therefore describe the connectivity. Hence, contour plots of these different parameters allow the spatial distribution of connectivity to be assessed. The $n_{C/L}$ and $n_{C/B}$ values are particularly useful as they are dimensionless measures of connectivity and can also be contoured onto the ternary node diagram, which is very useful for visualizing and assessing the connectivity (e.g. Manzocchi, 2002).

The fault network at Westward Ho! plots further away from the I-node corner of the ternary node diagram and has higher values of $n_{C/L}$ and $n_{C/B}$ than the network offshore Hartland. Therefore, the node analysis indicates that the fault network at Westward Ho! is better connected than the fault network offshore Hartland. We show that the connecting nodes within the two fault networks are dominated by Y-nodes, which is consistent with examples presented by Manzocchi (2002). This is because the displacements on faults make it difficult to preserve X-nodes (cf. Nixon et al., 2012) suggesting that fault network connectivity is strongly reliant on the development of Y-nodes.

We furthered this analysis by dividing Y-nodes into antithetic and synthetic Y-nodes. The results show that synthetic Y-nodes (i.e. fault splays and lenses) form from branches that are at low angles (<45°) to each other, whereas, antithetic Y-nodes (i.e. abutments and cross-cutting faults) form from branches that are a higher angles (>45°) to one another and vary depending on the fault set proportions. This agrees with the work by Robinson (1983) who showed

that more fractures are needed to form a connected network when the angle of intersection between fractures is very acute.

The contour plots show a spatial heterogeneity in connecting frequency within both fault networks with clusters of connecting nodes forming mainly in areas of high fault density suggesting that these regions are better connected. These are often regions of fault linkage and damage which is consistent with results from Nixon et al. (2012) and Micarelli et al. (2006a, 2006b) who also show that areas of damage are better connected. High values of $n_{C/L}$ and $n_{C/B}$ also develop and correlate with areas of high connecting node frequencies showing that these three parameters are a consistent measure of relative connectivity.

The branch analysis identifies I-I, I-C and C-C branch types which have $n_{C/B}$ values of 0, 1 and 2, respectively (Figure 4.14a). Each branch type has a different degree of connectivity as indicated by the estimated path of increasing connectivity in Figure 4.14a, which is estimated from the values of $n_{C/B}$ for each subarea. Therefore the proportions of each branch type can be used to describe the proportion of fault trace-length that is locally connected within each network. The spatial distribution of the different branch types is also useful as it shows the position of large clusters and gives an indication of the geometric character of the clusters (i.e. the spatial extent of the backbone and dangling ends etc).

Westward Ho! has a higher proportion of connected branches (particularly C-C branches) than the network offshore Hartland indicating that Westward Ho! is better connected, which agrees with the node analysis. The maps of branch type identify two different geometries of large cluster within the two fault networks, which are related to the proportions of each fault set. In areas that have equal proportions of each fault set, the clusters are dominated by antithetic Y-nodes and have a core of many small C-C branches forming highly connected clusters. However, areas with a dominant fault set (>80%) form elongate clusters, with long C-C branches, and a higher proportion of synthetic Y-nodes. These different cluster geometries correlate with the density and orientation clusters described by Manzocchi (2002) forming clusters that involve both fault sets and one fault set, respectively.

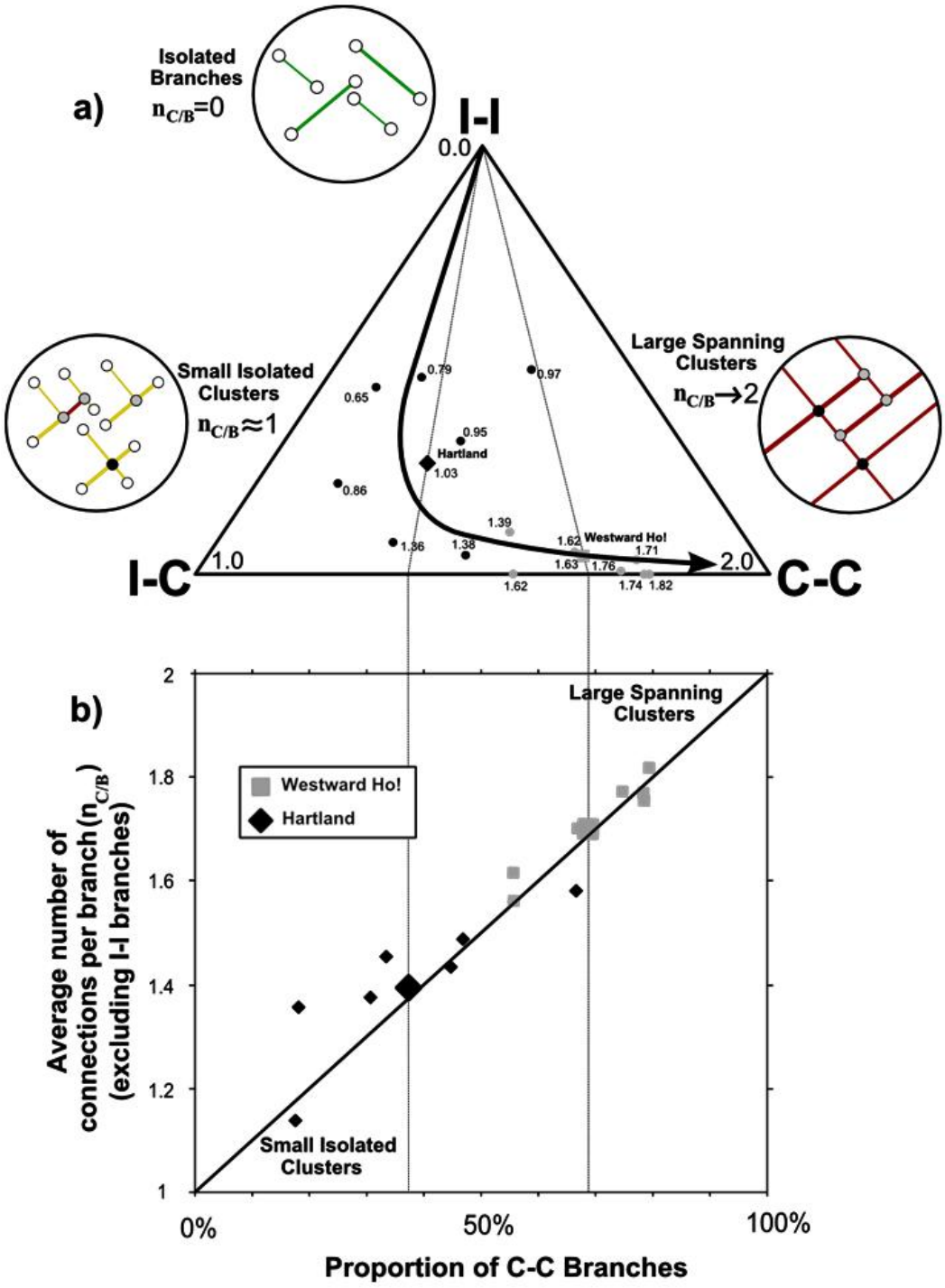

Figure 4.14. a) A ternary branch diagram showing the estimated path of increasing connectivity broadly matched to values of the number of connections per branch ($n_{C/B}$), which are labelled for each subarea from Hartland in black and Westward Ho! in grey. Illustrations show the different topological arrangements and cluster types if a network was dominated by I-I branches, I-C branches or C-C branches. Values for $n_{C/B}$ are shown for each end member indicating that networks with only I-I and I-C branches cannot form spanning clusters. b) A plot showing the linear relationship between the proportion of I-C and C-C branches and values of $n_{C/B}$ after the I-I branches have been removed from the system. This can be used to predict the cluster behaviour of the connected branches.

Overall, there is much heterogeneity in the local connectivity within each fault network. This heterogeneity can be seen in the spatial distribution of parameters that describe the connectivity and also in the clustering behaviour. This is important because it shows that connectivity and therefore the fluid transport properties of a fault network can change spatially within the network.

4.7.2. Clustering

As well as describing the connectivity of the trace-length within each fault network, the branch analysis also gives an estimate of the size of clusters within each network. This is important as although a network may be well connected forming large clusters, it is the spanning extent of these large clusters that controls the networks ability to percolate across a sample area. Manzocchi (2002) introduced a quantitative measure of clustering for fracture networks by looking at the coefficient of variance of fracture spacing. This indicates whether a network is randomly or uniformly clustered. The branch analysis develops this by describing if the clusters within the fault network are small isolated clusters (dominated by I-C branches) that do not percolate or whether they are large clusters (dominated by C-C branches) that span the sample area (spanning clusters) and could percolate (cf. Figure 4.3).

A network that plots in the I-I corner of the branch ternary diagram (Figure 4.14a) will have no connecting nodes within the network and therefore no clusters. If a network plots in the I-C corner of the ternary diagram all branches will have a tip (I-node) and will form small isolated clusters that only have one connecting node per cluster and therefore an $n_{C/B}$ of 1. For percolation, spanning clusters are needed, which have an extensive backbone of C-C branches providing a connected pathway for fluid flow across a sample area (Jing and Stephanson, 1997). Hence, any network that plots in the I-C corner will consist mainly of small clusters that will not be sufficiently connected to form a spanning cluster. Networks that consist of only C-C branches plot in the C-C corner of the ternary diagram, forming a spanning cluster that percolates and these have a $n_{C/B}$ of 2 (Figure 4.14a).

The relationship between values of $n_{C/B}$ and I-C and C-C branches is significant as this provides a link between the node and the branch proportions. If $n_{C/B}$ is

calculated after removing all the I-I branches from the network then $n_{C/B}$ can be used as a quantitative assessment of the degree and character of clustering. This is shown in Figure 4.14b, which shows that $n_{C/B}$ increases in a linear relationship with increasing proportions of C-C branches to I-C branches. Therefore, the connected branches have more chance of forming a significant spanning cluster as $n_{C/B} \rightarrow 2$.

4.7.3. Influences on connectivity

The influence of network properties on connectivity has been well studied including properties such as fault density, fault length, topology and angle of intersection between faults (e.g. Robinson, 1983; Balberg, 1986; Bour and Davy, 1997; Manzocchi et al., 1998; Zhang and Sanderson, 1998; Berkowitz et al., 2000; Manzocchi, 2002; Yazdi et al., 2011). We have also identified that fault set dominance also has an influence on connectivity. Increasing the proportion of one fault within a fault network decreases the number of connections within an area. This is due to the reduced chance of forming an antithetic Y-node (Robinson, 1983, 1984). However, this control affects each fault network independently (Figures 4.7c and 4.10b).

Investigating the characteristics of the isolated branches and the connected branches within the fault network offshore Hartland, also highlighted a link between strain localization and connectivity. The majority of the strain is accommodated by the connected branches indicating strain localization onto the faults and spanning clusters within the connected system. This supports a variety of studies that show that fault systems evolve into longer and simpler systems with faults increasing in fault length and becoming better connected as strain is localized onto the (e.g. Cowie et al., 1995; Dawers and Anders, 1995; Cowie, 1998; Gupta et al., 1998; Ferrill et al., 1999; Gupta and Scholz, 2000; Walsh et al., 2001; Soliva and Schultz, 2008). This is also a positive feedback because strain localizes onto the longer more connected parts of the system as a fault network grows (Meyer et al., 2002; Walsh et al., 2003; Taylor, 2004). It is important to understand the link between strain and connectivity as areas of localized deformation often coincide with localized fluid flow (e.g. Sanderson and Zhang, 1999, 2004).

4.8. Conclusions

The topological analysis developed in this study considers a fault network to be formed from two components: nodes and branches. Nodes are divided into I-nodes (fault tips), Y-nodes (abutments and splays) and X-nodes (cross-cutting faults). Branches are divided into I-I branches (isolated faults), I-C branches (dangling ends of clusters) and C-C branches (backbone of clusters).

The number counts and proportions of each component can be used to assess the topology of fault networks. They can also be used to calculate further descriptive parameters such as the number of connections per line ($n_{C/L}$) and the number of connections per branch ($n_{C/B}$). These parameters are dimensionless and can be plotted in contour plots and ternary diagrams to help characterize the topology of a fault network. This study showed that:

1. Fault networks form more Y-nodes than X-nodes, and therefore fault abutments and fault splays are more common than cross-cutting intersections.
2. There is much heterogeneity in spatial distribution of connecting nodes within fault networks. Clusters of connecting nodes form in areas of damage and linkage between faults producing high values of $n_{C/L}$ and $n_{C/B}$ in these regions.
3. Connecting node frequency increases with increasing fault density but decreases with increasing fault length.
4. The proportion of antithetic Y-nodes that form within a network decreases when one fault set becomes predominant.
5. Long fault traces within fault networks are made up of numerous C-C branches. These form the backbone of large clusters.
6. The branch analysis is a new method for characterizing the cluster behaviour of the connected branches within a fault network. Once I-I branches are removed values of $n_{C/B}$ range from 1 to 2. When $n_{C/B} \approx 1$ the clusters are made up of mainly I-C branches producing isolated clusters, whereas, as $n_{C/B} \rightarrow 2$ the clusters are made up of mainly C-C branches forming spanning clusters.

7. A fault network with a dominant fault set forms elongate clusters, whereas, a fault network with equal proportions of two fault sets forms highly connected clusters with a central core of C-C branches.

Topological components are useful for assessing and investigating the connectivity of a fault network. Parameters such as the number of connections per line ($n_{C/L}$) or per branch ($n_{C/B}$) and the proportions of different branch types provide dimensionless measures that relate to connectivity. Mapping and sampling the spatial distribution of these parameters within a fault network shows that:

8. There is much spatial heterogeneity in the character and degree of connectivity within fault networks.
9. The majority of strain is localized onto the connected faults within a fault network.

Overall, this study shows that topological analysis is an important tool for characterizing and describing fault networks. It produces parameters that are largely independent of the specific geometry of the faults (i.e. size, orientation etc), that relate to the connectivity within the fault network and can be used to characterize connectivity such as the clustering behaviour of the network.

4.9. References

Adler, P.M., Thovert, J.F., 1999. Fractures and fracture networks. Kluwer Academic Publishers, Dordrecht.

Aizenman, M., 1997. On the number of incipient spanning clusters. Nuclear Physics B 485, 551–582.

Balberg, I., 1986. Connectivity and conductivity in 2D and 3D fracture systems. Annals of the Israel Physical Society 8, 89–101.

Berkowitz, B., Bour, O., Davy, P., Odling, N., 2000. Scaling of fracture connectivity in geological formations. Geophysical research letters 27, 2061–2064.

Boccaletti, S., Latora, V., Moreno, Y., Chavez, M., Hwang, D., 2006. Complex networks: Structure and dynamics. Physics Reports 424, 175–308.

Bour, O., Davy, P., 1997. Connectivity of random fault networks following a power law fault length distribution. Water Resources Research 33, 1567–1583.

Childs, C., Nicol, A., Walsh, J.J., Watterson, J., 2003. The growth and propagation of synsedimentary faults. Journal of Structural Geology 25, 633–648.

Cowie, P., Underhill, J., Behn, M., Lin, J., Gill, C., 2005. Spatio-temporal evolution of strain accumulation derived from multi-scale observations of Late Jurassic rifting in the northern North Sea: A critical test of models for lithospheric extension. Earth and Planetary Science Letters 234, 401–419.

Cowie, P. A., Sornette, D., Vanneste, C., 1995. Multifractal scaling properties of a growing fault population. Geophysical Journal International 122, 457–469.

Cowie, P.A., 1998. A healing – reloading feedback control on the growth of seismogenic faults. Journal of Structural Geology 20, 1075–1087.

Dawers, N.H., Anders, M.H., 1995. Displacement – length scaling and fault linkage. Journal of Structural Geology 17, 607–614.

Faulkner, D.R., Mitchell, T.M., Jensen, E., Cembrano, J., 2011. Scaling of fault damage zones with displacement and the implications for fault growth processes. Journal of Geophysical Research 116, 1–11.

Ferrill, D.A., Stamatakos, J.A., Sims, D., 1999. Normal fault corrugation: implications for growth and seismicity of active normal faults. Journal of Structural Geology 21, 1107–1110.

Giba, M., Nicol, A., Walsh, J.J., 2010. Evolution of faulting and volcanism in a back-arc basin and its implications for subduction processes. Tectonics 29, 1–18.

Gupta, A., Scholz, C.H., 2000. A model of normal fault interaction based on observations and theory. Journal of Structural Geology 22, 865–879.

Gupta, S., Cowie, P., Dawers, N., Underhill, J., 1998. A mechanism to explain rift-basin subsidence and stratigraphic patterns through fault-array evolution. Geology 26, 595–598.

Huseby, O., Thovert, J.-F., Adler, P.M., 1997. Geometry and topology of fracture systems. Journal of Physics A: Mathematical and General 30, 1415–1444.

Jing, L., Stephansson, O., 1997. Network topology and homogenization of fractured rocks, in: Jamtveit, B., Yardley, B.W. (Eds.), Fluid Flow and Transport in Rocks. Mechanisms and Effects. Chapman & Hall, Oxford, pp. 191–202.

Kim, Y-S., Andrews, J., Sanderson, D., 2000. Damage zones around strike-slip fault systems and strike-slip fault evolution, Crackington Haven, southwest England. Geosciences Journal 4, 53–72.

Latora, V., Marchiori, M., 2002. Is the Boston subway a small-world network? Physica A: Statistical Mechanics and its Applications 314, 109–113.

Manzocchi, T., 2002. The connectivity of two-dimensional networks of spatially correlated fractures. Water Resources Research 38, 1162.

Manzocchi, T., Ringrose, P.S., Underhill, J.R., 1998. Flow through fault systems in high-porosity sandstones. Geological Society, London, Special Publications 127, 65–82.

McClay, K., Dooley, T., Whitehouse, P., Mills, M., 2002. 4-D evolution of rift systems: Insights from scaled physical models. AAPG Bulletin 86, 935–959.

Meyer, V., Nicol, A., Childs, C., Walsh, J.J., Watterson, J., 2002. Progressive localisation of strain during the evolution of a normal fault population. Journal of Structural Geology 24, 1215–1231.

Micarelli, L., Benedicto, A., Wibberley, C. A. J., 2006a. Structural evolution and permeability of normal fault zones in highly porous carbonate rocks. Journal of Structural Geology 28, 1214–1227.

Micarelli, L., Moretti, I., Jaubert, M., Moulouel, H., 2006b. Fracture analysis in the south-western Corinth rift (Greece) and implications on fault hydraulic behavior. Tectonophysics 426, 31–59.

Mouslopoulou, V., Walsh, J.J., Nicol, A., 2009. Fault displacement rates on a range of timescales. Earth and Planetary Science Letters 278, 186–197.

Nicol, A., Walsh, J.J., Villamor, P., Seebeck, H., Berryman, K.R., 2010. Normal fault interactions, paleoearthquakes and growth in an active rift. Journal of Structural Geology 32, 1101–1113.

Nicol, A., Walsh, J., Berryman, K., Villamor, P., 2006. Interdependence of fault displacement rates and paleoearthquakes in an active rift. Geology 34, 865.

Nixon, C.W., Sanderson, D.J., Bull, J.M., 2011. Deformation within a strike-slip fault network at Westward Ho!, Devon U.K.: Domino vs conjugate faulting. Journal of Structural Geology 33, 833–843.

Nixon, C.W., Sanderson, D.J., Bull, J.M., 2012. Analysis of a strike-slip fault network using high resolution multibeam bathymetry, offshore NW Devon U.K. Tectonophysics 541-543, 69–80.

Ortega, O., Marrett, R., 2000. Prediction of macrofracture properties using microfracture information, Mesaverde Group sandstones, San Juan basin, New Mexico. Journal of Structural Geology 22, 571–588.

Peacock, D.C.P., Sanderson, D.J., 1996. Effects of propagation rate on displacement variations along faults. Journal of Structural Geology 18, 311–320.

Pickering, G., Bull, J.M., Sanderson, D.J., 1995. Sampling power-law distributions. Tectonophysics 248, 1–20.

Putz-Perrier, M.W., Sanderson, D.J., 2008. The distribution of faults and fractures and their importance in accommodating extensional strain at Kimmeridge Bay, Dorset, UK. Geological Society, London, Special Publications 299, 97–111.

Putz-Perrier, M.W., Sanderson, D.J., 2010. Distribution of faults and extensional strain in fractured carbonates of the North Malta Graben. AAPG Bulletin 94, 435–456.

Ravasz, E., Barabási, A.-L., 2003. Hierarchical organization in complex networks. Physical Review E 67, 1–7.

Robinson, P., 1983. Connectivity of fracture systems-a percolation theory approach. Journal of Physics A: Mathematical and General 16, 605–614.

Robinson, P., 1984. Numerical calculations of critical densities for lines and planes. Journal of Physics A: Mathematical and General 17, 2823–2830.

Sanderson, D.J., Zhang, X., 1999. Critical stress localization of flow associated with deformation of well-fractured rock masses, with implications for mineral deposits. Geological Society, London, Special Publications 155, 69–81.

Sanderson, D.J., Zhang, X., 2004. Stress-controlled localization of deformation and fluid flow in fractured rocks. Geological Society, London, Special Publications 231, 299–314.

Schlische, R., Young, S., Ackermann, R., Gupta, A., 1996. Geometry and scaling relations of a population of very small rift-related normal faults. Geology 24, 683–686.

Silverman, B.W., 1986. Density estimation for statistics and data analysis. Chapman & Hall/CRC, New York.

Soliva, R., Schultz, R. A., 2008. Distributed and localized faulting in extensional settings: Insight from the North Ethiopian Rift–Afar transition area. Tectonics 27, TC2003.

Taylor, S.K., Bull, J.M., Lamarche, G., Barnes, P.M., 2004. Normal fault growth and linkage in the Whakatane Graben, New Zealand, during the last 1.3 Myr. Journal of Geophysical Research 109, B02408.

Valentini, L., Perugini, D., Poli, G., 2007a. The “small-world” topology of rock fracture networks. Physica A: Statistical Mechanics and its Applications 377, 323–328.

Valentini, L., Perugini, D., Poli, G., 2007b. The “small-world” nature of fracture/conduit networks: Possible implications for disequilibrium transport of magmas beneath mid-ocean ridges. Journal of Volcanology and Geothermal Research 159, 355–365.

Walsh, J.J., Childs, C., Imber, J., Manzocchi, T., Watterson, J., Nell, P. A. R., 2003. Strain localisation and population changes during fault system growth within the Inner Moray Firth, Northern North Sea. Journal of Structural Geology 25, 307–315.

Walsh, J.J., Childs, C., Manzocchi, T., Imber, J., Nicol, A., Meyer, V., Tuckwell, G., Bailey, W.R., Bonson, C.G., Watterson, J., Nell, P.A.R., Strand, J., 2001. Geometrical controls on the evolution of normal fault systems. Geological Society, London, Special Publications 186, 157–170.

Walsh, J.J., Watterson, J., 1988. Analysis of the relationship between displacements and dimensions of faults. Journal of Structural Geology 10, 239–247.

Yazdi, A., Hamzehpour, H., Sahimi, M., 2011. Permeability, porosity, and percolation properties of two-dimensional disordered fracture networks. Physical Review E 84, 1–10.

Zhang, X., Sanderson, D.J., 1998. Numerical study of critical behaviour of deformation and permeability of fractured rock masses. Marine and Petroleum Geology 15, 535–548.

Zhang, X., Sanderson, D., 2001. Evaluation of instability in fractured rock masses using numerical analysis methods: Effects of fracture geometry and loading direction. Journal of Geophysical Research 106, 26671–26687.

5. Mesoscale faulting on the Kaikoura Peninsula, South Island, NZ

Casey W. Nixon, David J. Sanderson, Jonathan M. Bull

5.1. Abstract

A strike-slip fault network on the Kaikoura Peninsula is described and mapped from field observations. The kinematic history of faulting is unravelled to add to our understanding of deformation associated with the regional tectonics of the Marlborough Fault Zone. The behaviour of the fault network is locally variable due to changes in lithology, damage zones and fault reactivation. The observations have revealed a complex reactivation history over the past 4 Ma with two main phases of deformation: **1.** NW-SE compression forming two conjugate fault sets consisting of N-trending left-lateral faults and WNW-trending right-lateral faults with extension fractures that form parallel to the principal stress direction; **2.** E-W compression resulting in left-lateral reactivation of NW-trending faults and extension fractures. It is suggested that the NW-SE compression accommodates clockwise rotations of the Northern Marlborough Domain whereas E-W compression reflects relative plate motion and the ENE right-lateral shear of the Southern Marlborough Domain.

5.2. Introduction

This study aims to describe a mesoscale fault network and other deformation structures seen on the Kaikoura Peninsula to unravel the kinematic history of the faults and discuss their relevance to the regional tectonics of the area. It will also investigate variations in fault geometry and different physical attributes within the fault network to illustrate localized effects on fault network behaviour.

The Kaikoura Peninsula is located in a highly dynamic setting on the NE coast of South Island, New Zealand (Figure 5.1). Offshore to the east is the southern most part of the NE-trending Hikurangi Margin where the Australian plate converges obliquely on the Pacific plate at a rate of 38 mm/yr at an azimuth of 079° (DeMets et al., 1994). The majority of the plate motion is taken up by right-lateral strike-slip faults in the transpressive Marlborough Fault Zone that forms part of a diffuse transform boundary between the Pacific and Australian plates (Van Dissen and Yeats, 1991; Barnes and Audru, 1999; Wannamaker et al., 2009). The most active and southern part of the Marlborough Fault Zone is the ENE-trending right-lateral Hope Fault, which is ~10 km north of the Kaikoura Peninsula and produces horizontal slip rates of between 18-32 mm/yr (Langridge et al., 2003). The remainder of the plate motion is accommodated by NE-trending folds and reverse faults that occur offshore and along the coastline of North Canterbury and Marlborough (e.g. Van Dissen and Yeats, 1991; Barnes, 1996; Barnes and Audru, 1999).

The tectonic evolution of the plate boundary zone has been well studied with subduction thought to have started in the early Miocene along with inception of the right-lateral strike-slip faulting in the Marlborough Fault Zone (Lamb and Bibby, 1989; Rait et al., 1991; Audru and Delteil, 1998). Palaeomagnetic studies indicate clockwise rotations of up to ~130° for faults and fault blocks with the Hikurangi Margin rotating from ~W to ~NE since the early Miocene (Lamb and Bibby, 1989; Vickery and Lamb, 1995; Little and Roberts, 1997; Furlong and Kamp, 2009; Lamb, 2011; Randall et al., 2011). Large rotations are thought to be accommodated from 20 Ma – 8 Ma and the remainder from 4 Ma – present day (Vickery and Lamb, 1995). Rotation was driven by right-lateral shear accommodated by the Marlborough Fault Zone and the extent of

rotation decreases to the south with Kaikoura Peninsula expressing rotations of only 40.5° +/- 17° (Hall, 2004; Randall et al., 2011).

Lamb and Bibby (1989) describe two deformation phases (D_1 and D_2) related to these two periods of rotation. Early Miocene low angle thrust faults and steeply plunging folds make up D_1 which are deformed by Plio-Pleistocene faulting and folding which make up D_2 (Lamb and Bibby, 1989; Vickery and Lamb, 1995). This study will focus on describing a mesoscale fault network seen on the Kaikoura Peninsula associated with D_2 and hypothesise the chronology of sub-phases of deformation within the last 4 Ma.

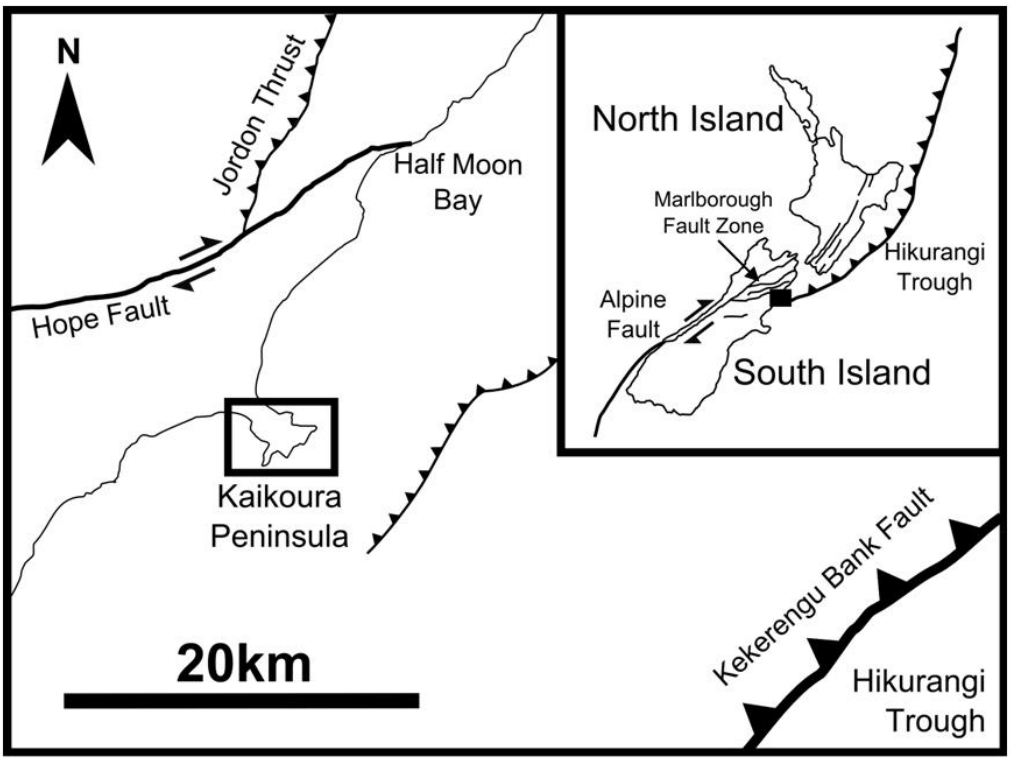

Figure 5.1 Location map of Kaikoura Peninsula showing the main structures that surround the peninsula.

5.2.1. Stratigraphy and Structure

The stratigraphy of the Kaikoura Peninsula consists of marine limestones, mudstones and siltstones dating from late Cretaceous to middle Miocene. These include the carbonates of the Eocene Amuri Limestone and Oligocene Spyglass Formation, and the mudstones of the Miocene Waima Formation (Browne et al., 2005; Lever, 2007) which all outcrop on the wave-cut platforms around the peninsula (Figure 5.2).

Large-scale folds (wave-lengths >2 km) can be seen across the peninsula, folding stratigraphy into kilometre scale NE-trending anticlines and synclines (Figure 5.2) (Ota et al., 1996; Cambell et al., 2005; Rattenbury et al., 2006). These are thought to be related to NW-dipping thrust structures that can be seen offshore ~5 km south east of the peninsula, causing continuing deformation and a north-westerly tilt of marine platforms on the peninsula (Ota et al., 1996). Further deformation associated with this NW-SE compression includes small-scale folding (wave-lengths <20 m), parasitic to the large-scale folds, which intensely deforms the carbonates of the Amuri Limestone and Spyglass Formation (Figure 5.3). The Waima Formation on the other hand is not so intensely folded, instead deforming by layer-parallel slip and producing more open mesoscale folds that envelope the small scale folding in the underlying limestone units.

A mesoscale network of faults cuts the rocks across the Kaikoura Peninsula. The pattern of faulting is complex but there are two main fault orientations: N-trending and WNW-trending (Figure 5.4). The faults laterally offset bedding and fold hinges of parasitic folds indicating they post-date the folding.

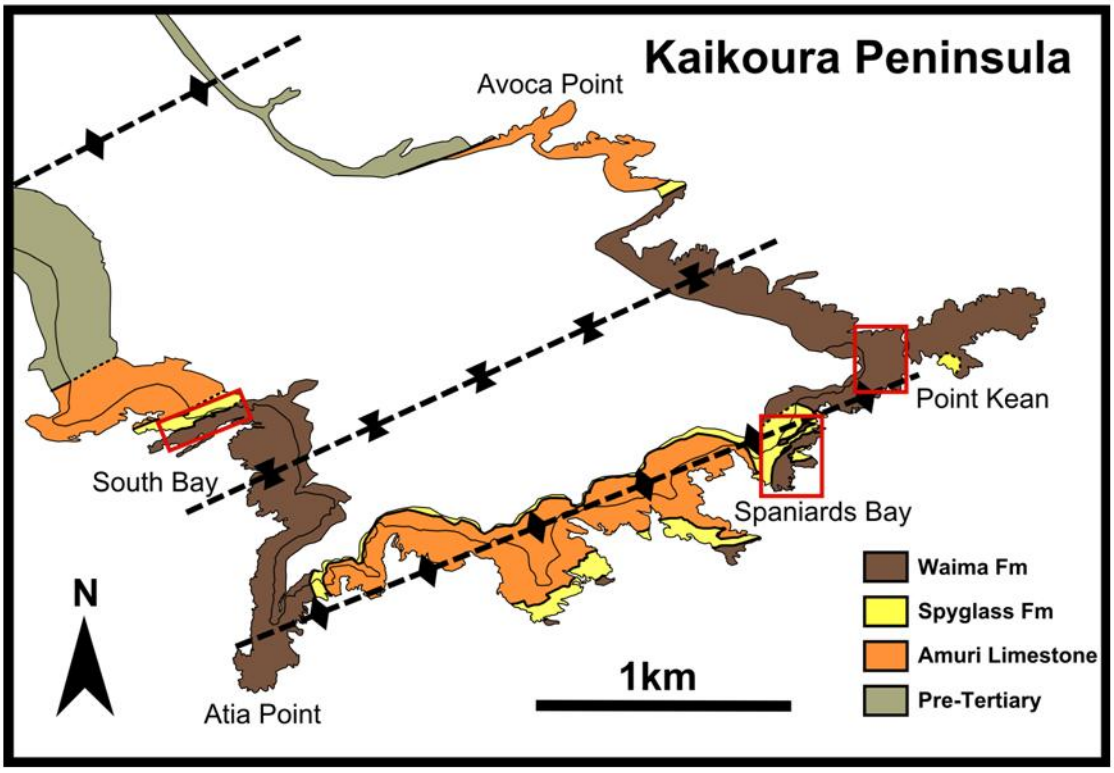

Figure 5.2 Geological map of Kaikoura Peninsula showing the main lithologies of the wave-cut platforms, NE-trending fold structures and the three study areas.

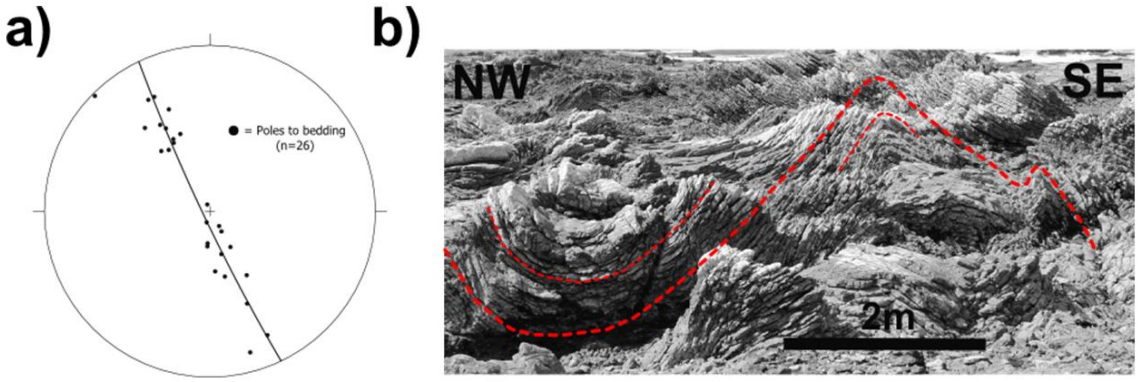

Figure 5.3 a) Equal angle stereographic projection of bedding showing the main trend of folding; b) field photograph of parasitic folding within the Spyglass Formation at Spaniards Bay.

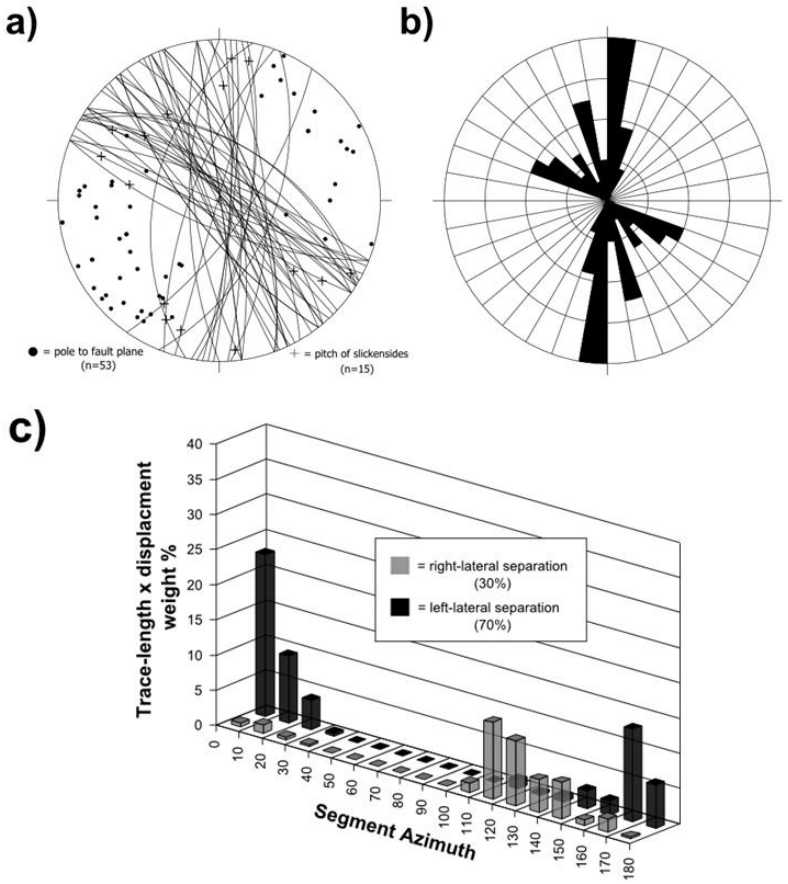

Figure 5.4 a) Equal angle stereographic projection of fault planes and associated slickensides taken from fault and fractures across the three study areas; b) Length x displacement weighted rose diagram of faults from all three study areas; c) Length x displacement weighted histogram showing the distribution of faults with right-lateral and left-lateral separations.

5.3. Methodology

5.3.1. Mapping

Fault mapping was focused to three key areas (Point Kean, Spaniards Bay and South Bay; Figure 5.2) that were used to describe and analyse the fault network. They consist of wave-cut platforms in the Waima Formation, where the faults are well exposed and marker beds allow mapping and measuring of lateral separations. Faults were mapped in the field using aerial photographs as base maps and 3D structural data were collected across the areas, including bedding and fault orientations as well as slickenside measurements where possible.

The mapped faults, interpreted marker beds and associated displacement data were all digitized and imported into ArcGIS. Fault traces were segmented by lateral separation points of marker beds and an average displacement was attributed to each fault segment (see Appendix for more detail). The data for each segment were extracted from ArcGIS into spreadsheets for further analysis and display (i.e. rose diagrams, strain determination etc.).

5.3.2. Line sampling

Line sampling involved following and measuring the lengths of an identified marker bed along strike and recording the separations and orientations of each faulted offset. By inputing the data into spreadsheets, attributes of the faults can be calculated such as fault density, two dimensional strain vectors, average displacements etc. This is useful for comparing the spatial distribution of these attributes across structural features or boundaries (e.g. damage zones and lithilogical boundaries). The technique works particularly well at Kaikoura as the strike of bedding (ENE-WSW) is at a high angle to the orientations of both fault sets.

5.3.3. Strain determination

The two-dimensional strain of each line sample was calculated using a method by Peacock and Sanderson (1993). This uses the eigenvectors and eigenvalues of a Lagrangian strain tensor to estimate the orientation and

magnitude of the principal strains. The Langrangian strain tensor, $\boldsymbol{E_{ij}}$, is given by:

$$\boldsymbol{E_{ij}} = N/L \sum [(\boldsymbol{D_{ij}} + \boldsymbol{D_{ji}})/2] \quad (5.1)$$

where $\boldsymbol{D_{ij}}$ is a displacement tensor and N is the number faults sampled across a sample line of length L.

The displacement tensor, $\boldsymbol{D_{ij}}$, is calculated from the cross-product of the unit vector normal to the fault plane, (n), and the displacement direction within the fault plane, (s u), where s is the displacement on the fault and u is the unit vector in the slip direction. Due to the orientation of the sample line, Peacock and Sanderson (1993) add a weighting factor $w = 1/\cos \gamma$, where γ is the angle between the sample line and the normal to the fault trace. Hence, for a fault trace that strikes at an angle θ to north then:

$$n = (-\sin \theta, \cos \theta) \quad \text{and} \quad u = (\cos \theta, \sin \theta) \quad (5.2)$$

and,

$$\boldsymbol{D_{ij}} = \sum ws \begin{pmatrix} n_1u_1 & n_1u_2 \\ n_2u_1 & n_2u_2 \end{pmatrix} = \sum ws \begin{pmatrix} -\sin\theta\cos\theta & -\sin^2\theta \\ \cos^2\theta & \cos\theta\sin\theta \end{pmatrix} \quad (5.3)$$

where w is the weighting factor and s is +ve for left-lateral faults and –ve for right-lateral faults.

Nixon et al. (2011) apply this method for sampling fault traces within a plane. When sampling on a plane the weighting factor (w) is calculated using the angle between the exposure surface and fault normal. This can be ignored for strike-slip faults as they are sub-vertical, hence, both the fault normal and the displacement vector are sub-horizontal. When calculating the Lagrangian strain tensor in equation (5.1), N/L represents the fault density, however, this needs to be replaced by the planar equivalent of $\Sigma t/A$, where t is the trace-length and A is the sample area. Hence, for a plane, the Lagrangian strain tensor is given by:

$$\boldsymbol{E_{ij}} = 1/A \sum [t (\boldsymbol{D_{ij}} + \boldsymbol{D_{ji}})/2] \quad (5.4)$$

5.4. Fault systems on the Kaikoura Peninsula

5.4.1. Evidence of strike-slip deformation

The complex nature of the faults on Kaikoura Peninsula make their history of deformation difficult to constrain. The faults display lateral separations offsetting stratigraphy. Due to the dip of the beds these lateral separations could be caused by vertical movements in which case the lateral separations do not represent displacements. However, observations and field relationships attest a strike-slip motion for many of the faults.

5.4.1.1. *Slickensides*

3D structural data collected from exposed fault planes and fracture surfaces in cliff sections and on wave-cut platforms show that the majority of dips range from 60° to sub-vertical (Figure 5.4a). Shallowly (< 30°) plunging slickensides indicate a dominant movement in the horizontal plane and that the lateral separations of marker beds approximate the displacement on the faults. The fault plane data show a range of orientations within the fault network. However, when weighted by length and displacement two conjugate sets of fault are distinguishable consisting of N-trending faults and WNW-trending faults, which dominantly express left-lateral and right-lateral separations, respectively (Figure 5.4).

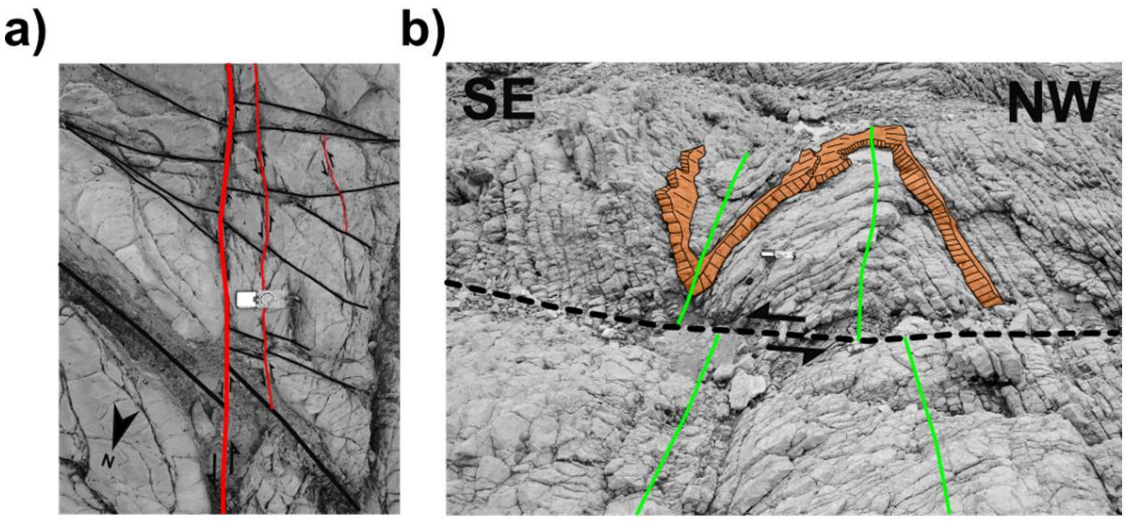

Figure 5.5 a) Field photograph from Spaniards Bay of steeply dipping fractures being offset laterally by left-lateral faults; b) field photograph from South Bay showing the axial trace of a parasitic fold being offset laterally offset by a fault.

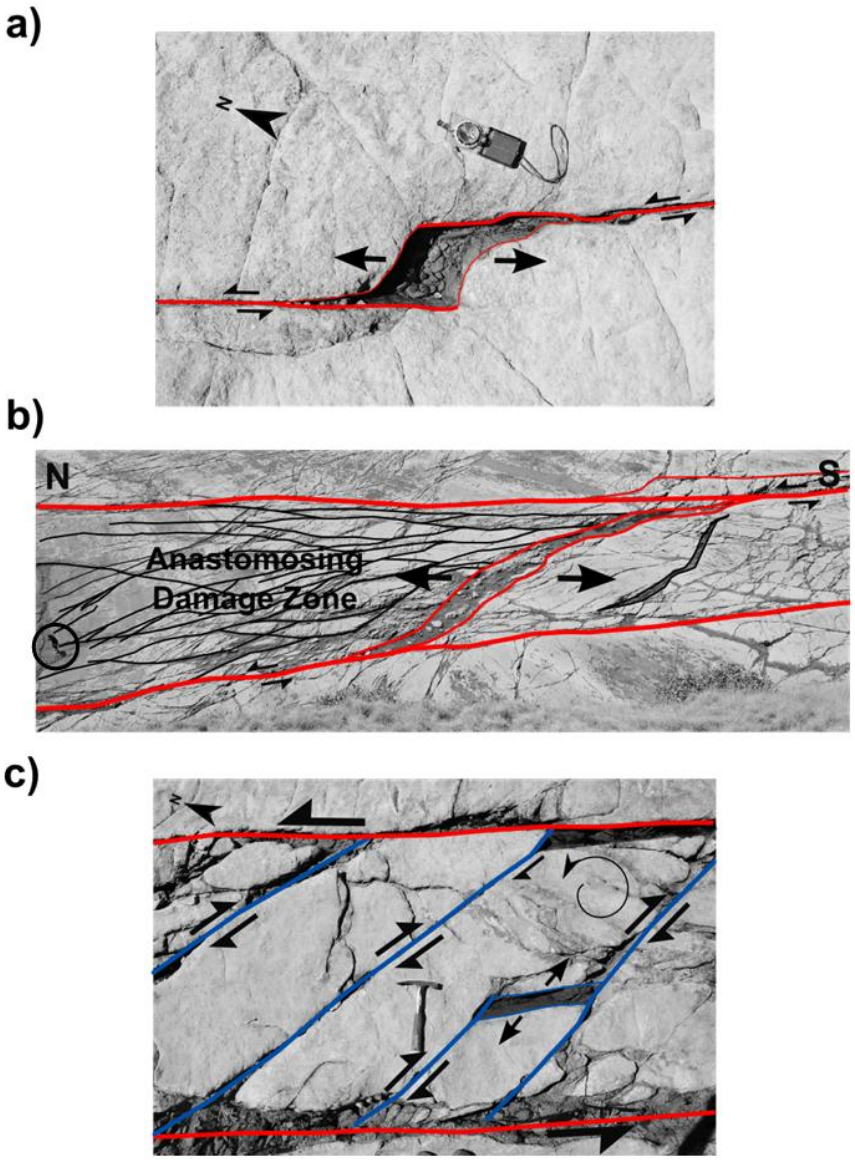

Figure 5.6. a) Small scale pull apart associated with a step-over between two small left-lateral faults; b) a releasing bend with an anastomosing damage zone between to left-lateral faults. Note the person circled on the left hand side for scale; c) field photograph from Point Kean showing a dilational jog between right-lateral shear fractures (blue lines) within a lens structure.

5.4.1.2. *Cross-cutting relationships*

Strike-slip movement is supported by small-scale structures and cross-cutting relationships. In many places sub-vertical fractures and fault sets are offset laterally, for example, in Figure 5.5a a N-trending fault offsets several WNW-trending faults with consistent left-lateral separations. As the fault planes are steeply dipping this means that the main slip component must be strike-slip on this fault. This is further supported by Figure 5.5b where a N-trending fault cuts

a parasitic fold within the Spyglass Formation at South Bay. The fault offsets both the limbs and hinge line of the fold in a left-lateral motion indicating a dominant strike-slip movement.

5.4.1.3. *Step-over structures*

There are often damage zones related to step-overs between fractures and faults with openings at releasing step-overs along small-scale faults. For example, the fault in Figure 5.6a illustrates an opening related to a left step-over indicating left-lateral movement on the fault. These structures are also seen on a larger scale, producing damage zones of faults and fractures that splay in an anastomosing pattern away from the releasing bends (Figure 5.6b). Lens structures often form with antithetic faults producing wedge shaped openings at the edges of lenses. For example, the lens structure in Figure 5.6c formed between two NNE-trending left-lateral faults and has antithetic WNW-trending right-lateral shear fractures that are producing tensile openings both within the lens and at the edges.

All of these structures along with the slickenside data agree with a lateral movement along these fault planes. This indicates at least one phase of strike-slip deformation. Therefore, by using the lateral separations as approximate displacements, orientation data for left-lateral and right-lateral faults can be analysed for each of the studied areas.

5.4.2. South Bay

South Bay is the farthest west of the three study areas and consists of a 50 x 350 m wave-cut platform. The faults cut a stratigraphic succession that dips approximately 50° to the south and consists mainly of the Waima Formation with the Spyglass Formation only outcropping at the northern limits of the mapped area (Figure 5.7a). The fault trace-lengths are dominated by faults that trend 005° with a few that trend 305°. The N-S faults all display apparent left-lateral separations, some up to 21 m. The 305°-trending faults are more localized and have right-lateral separations with a somewhat greater average separation in comparison to faults with left-lateral separations (Figure 5.7c).

Assuming that these are strike-slip faults, the lateral separations can be used in a strain analysis of the area showing the principal strain directions within the

horizontal plane. These indicate a maximum extension of 7.5% with an orientation of N057°E (Table 5.1). This indicates that these faults formed by NW-SE compression which is the same orientation as the compression that caused the main fold structures that deform the peninsula.

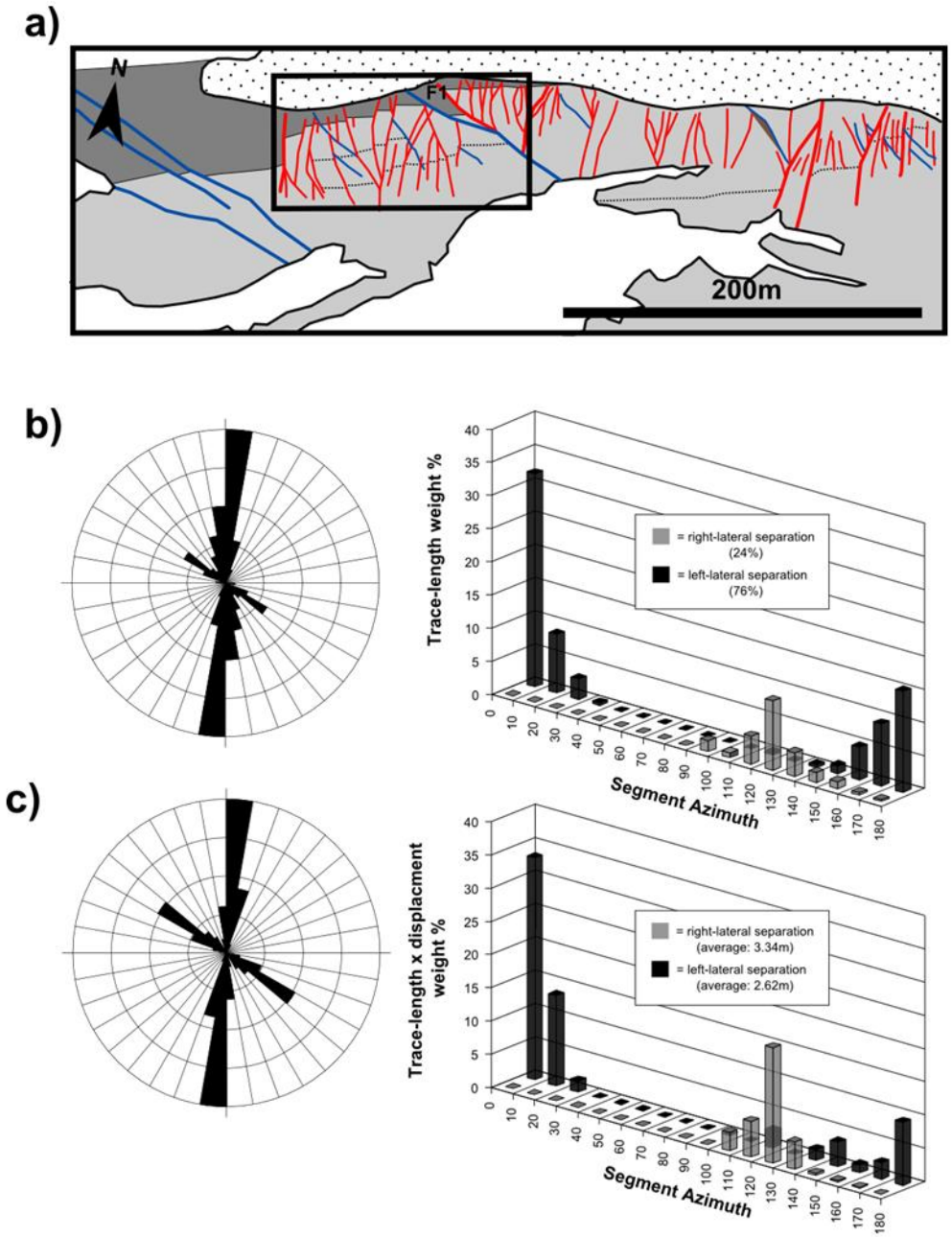

Figure 5.7 a) Fault map of the South Bay study area with right-lateral faults in blue and left-lateral faults in red. The Spyglass and Waima Formations are in dark grey and light grey, respectively. The boxed area is the location of the line samples in Figure 5.13; b) trace-length weighted rose diagram and histogram for the mapped South Bay fault network; c) trace-length x displacement weighted rose diagram and histogram for the mapped South Bay area. Note the histograms show the distribution of right- and left- lateral faults.

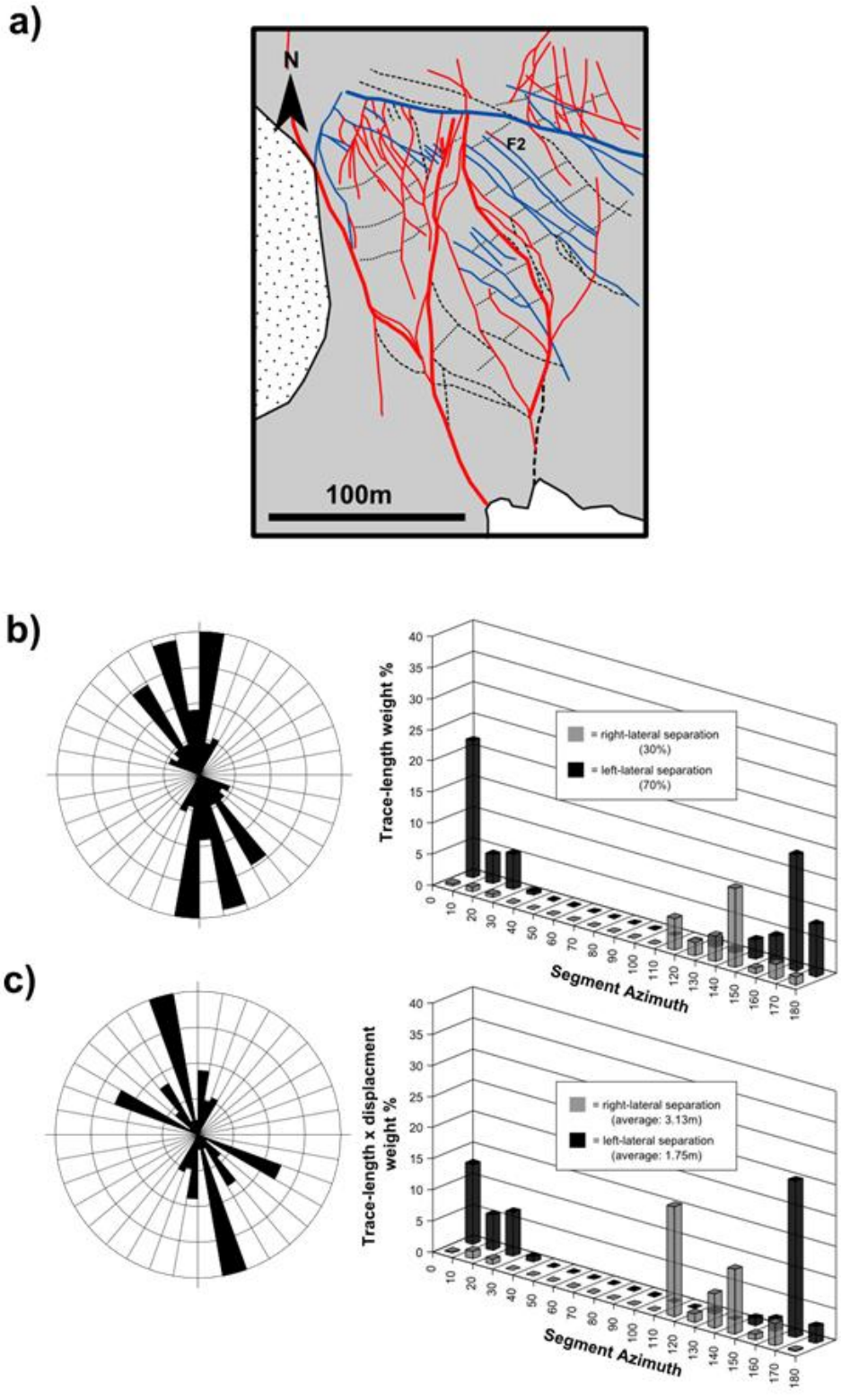

Figure 5.8 a) Fault map of the Point Kean study area with right-lateral faults in blue and left-lateral faults in red. Dashed lines represent faults with unknown motion senses and dotted lines are marker beds. Note the anastomosing fault patterns. b) Trace-length weighted rose diagram and histogram for the mapped Point Kean fault network; c) trace-length x displacement weighted rose diagram and histogram for the mapped Point Kean area. Note the histograms show the distribution of right- and left- lateral faults.

Table 5.1 Strain values and orientations within the horizontal plane for each mapped fault network.

	South Bay	Point Kean	Spaniards Bay
% Extension	7.5	5.6	1.8
Orientation	N057°E	N068°E	N026°E

Although there are two dominant orientations for the majority of fault segments, some fault segments vary quite significantly from these. For the most part these are only minor faults that display small lateral separations, however, there is one large left-lateral fault (F1) that has a similar trend to the right-lateral fault segments (c. 305°) (Figure 5.7a). This could be due to a number of reasons including a dip slip component to some of these faults, reactivation of a pre-existing structure or even a separate phase of strike-slip faulting. Overall the dominant orientations both length weighted and length x displacement weighted indicate a conjugate set of faults with WNW-trending right-lateral faults and N-trending left-lateral faults agreeing with the hypothesis that these are strike-slip faults formed by NW-SE compression.

5.4.3. Point Kean

Point Kean is the eastern most point of Kaikoura Peninsula. The area consists of a 200 x 300 m wave-cut platform with shallow dipping beds (<30°) of the Waima Formation. The fault trace arrays appear more complicated than the South Bay area, with anastomosing, lens shaped patterns and fault traces splaying and curving into other fault traces (Figure 5.8a). Like South Bay there are faults which express left-lateral and right-lateral separations with average displacements of 1.75 m and 3.13 m, respectively (Figure 5.8c).

The added complexity is reflected in the length weighted rose diagram showing three main orientations (005°, 345°, 325°) and two minor orientations (295° and 035°). The more N-trending orientations are dominated by left-lateral faults, whereas, the more WNW-trending orientations are dominated by right-lateral faults (Figure 5.8b). When weighted by displacement as well as length the orientation data show a more obvious pattern (Figure 5.8c). There are two main orientations at 345° and 295° for faults with left-lateral and right-lateral

separations, respectively. There are also two minor orientations at 005° and 325° which again are dominated by left-lateral and right-lateral separations, respectively. These minor orientations could indicate rotation of faults or the main compression direction. Overall the fault orientations indicate NW-SE compression.

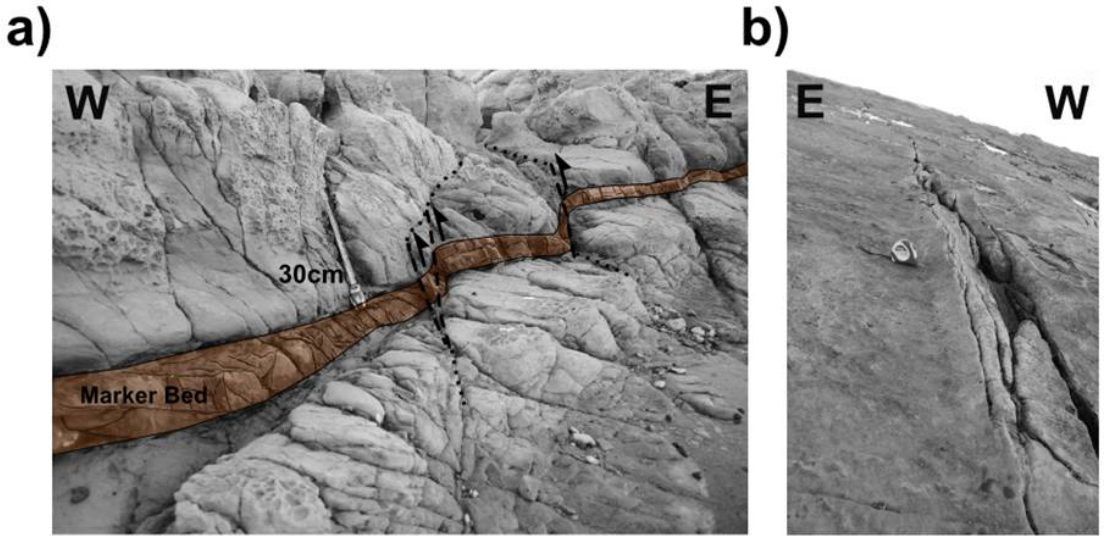

Figure 5.9 a) Field photograph illustrating vertical movement and drag of a siltstone bed at Point Kean indicating transpression; b) a more competent ridge along a fault line indicative of transpression.

The kinematic origin of these faults is complicated by some field evidence of vertical movement on faults. Separations and drag of bedding can be seen when the faults are viewed in cross section (Figure 5.9a). These faults dip steeply to the east and have a component of reverse fault movement. This indicates that these strike-slip faults are expressing some oblique-slip, possibly due to transpression. This is further supported by ridges forming along fault edges as seen in Figure 5.9b. Compression on these faults would have to be ~E-W to cause these structures which does not fit with the NW-SE compression suggested by the conjugate fault sets.

The fault in Figure 5.9b is fault F2 (Figure 5.8a), which trends ~320°, and expresses a right-lateral separation along its trace-length yet has a left-lateral separation at its NW tip. As the dip of bedding is consistent along its length, this suggests reactivation and propagation of the original structure indicating that there has been at least two phases of movement on this fault (Figure 5.10). The orientation of fault F2 is parallel to the maximum stress orientation that

bisects the two major fault trends. This matches the orientation of tensile fracture formation associated with NW-SE compression, which suggests it could be a reactivated joint/extension fracture. Reactivated joints and fractures are not uncommon and have been described many times in previous studies (cf. Segall and Pollard, 1983a, 1983b; Granier, 1985; Zhao and Johnson, 1992; Wilkins et al., 2001). This has very important implications for the deformation history and interpretation of these faults as reactivation could be caused by a phase of E-W compression. This would explain the vertical movement on faults and ridges at fault edges (Figure 5.9).

Although some vertical movement has been seen on these faults the consistent dominant orientations for right-lateral and left-lateral faults indicates a movement in the horizontal plane. The principal strain directions within the horizontal plane are similar to South Bay with an overall extension of 5.6% in an orientation of N068°E again indicating NW-SE compression, which is in agreement with the conjugate fault geometries (Table 5.1).

Overall, like South Bay, there is a dominant conjugate fault set with N-trending left-lateral faults and WNW-trending right-lateral faults associated with NW-SE compression. However, tensile fractures and joints that formed parallel to this maximum stress direction have been reactivated. This explains the range of fault planes plotted in Figure 5.4a and indicates a change in the maximum stress direction.

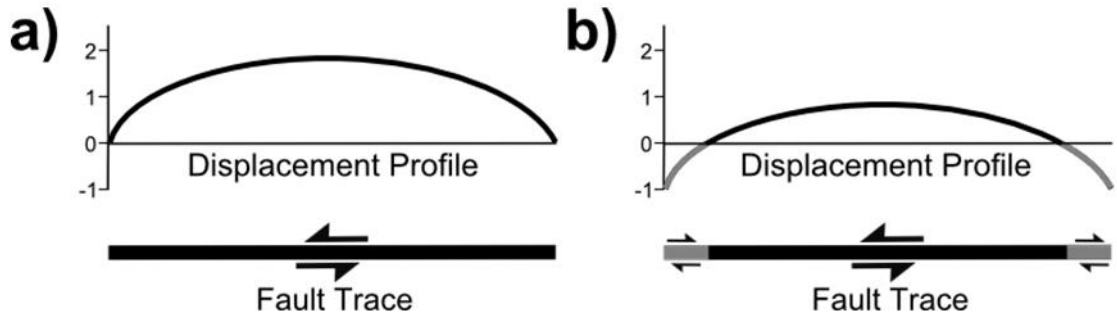

Figure 5.10 A schematic illustration of right-lateral reactivation of a left-lateral fault. Displacement profiles represent the fault before (a) and after (b) reactivation. Note the change in motion sense at the fault tips.

5.4.4. Spaniards Bay

The mapped fault network at Spaniards Bay is the smallest of the three study areas and is located on a wave-cut platform just south of Point Kean (Figure 5.11a). The west side of the wave-cut platform comprises heavily folded limestone of the Spyglass Formation, which are juxtaposed against mudstones and siltstones of the Waima Formation on the east side. The Spyglass Formation is heavily brecciated at the boundary as a large N-trending fault (F3) separates the two lithologies with the Waima Formation to the east being the down thrown side (Figure 5.11a). The vertical movement must only be a few metres as in many places the fold crests of the Spyglass Formation break through the Waima Formation and there are beds of the Waima Formation in mesoscale troughs of the folded limestone. These are seen best in the northern half of the area forming elongated lenses of siltstone and limestone (Figure 5.11a).

Although the Spyglass Formation appears brecciated and fractured, very few faults penetrate far into it. A N-trending cleavage is common throughout the limestone suggesting a component of E-W compression. This orientation is very different to the overall compression that formed the large-scale folds across the peninsula. Some of the N-trending cleavage planes have infilled with calcite indicating post-formation extension which could be caused by a later change in the stress field.

A dense population of faults and fractures deform a 75 x 75 m area of south dipping beds of the Waima Formation (Figure 5.11a). The fault segments form two main trends that are acutely angled to each other at 005° and 335° (Figure 5.11b and 5.11c). The N-trending faults form long traces that appear to splay off fault F3 and eventually tail off further south with fault tips curving to the SE, which is parallel to the NW-SE compression that caused the large-scale folding across the peninsula.

This pattern of faulting is very similar to descriptions of horsetail damage zones seen at the lateral tips of strike-slip faults (McGrath and Davison, 1995; Kim et al., 2000, 2004). Horsetail damage zones consist of extensional fractures that splay off the tip of a propagating strike-slip fault and curve towards the

maximum compression orientation as they move away from the localized stress field produced by the main fault (McGrath and Davison, 1995; Kim et al., 2000). There are also individual faults and fractures that trend 335° which is a similar orientation to the reactivated joints/extension fractures seen at Point Kean. The combination of individual fractures and a horsetail splay is very similar to the bifurcating tip damage described by McGrath and Davison (1995) suggesting this is also close to the shallow/upper tip of fault F3.

The fault pattern at Spaniards Bay is interpreted as forming in the extensional quadrant at the tip of a strike-slip fault (F3), which would indicate that fault F3 is left-lateral. This explains why there are no WNW-trending right-lateral faults in this area forming an acute angle between fault trends. Kim et al. (2000) observe similar acute angles between sets of strike-slip faults and hybrid shear fractures at Crackington Haven in southwest Britain further suggesting that these are reactivated extensional fractures and joints.

The faults express left-lateral and right-lateral separations for both orientations (Figure 5.11) which might suggest a component of vertical movement. However, considering there has been evidence of reactivation at Point Kean and there is a N-S cleavage trend indicating E-W compression, it is more likely that this pattern is caused by reactivation after a change in the principal compression direction. Kim et al. (2001) show similar trends for reactivated strike-slip faults at Crackington Haven in southwest Britain with tips and horsetail fractures expressing both left- and right-lateral separations. This combined with the acute angle between fault trends and the pattern of faulting, indicate that this area of faulting is a reactivated extensional quadrant of a propagating left-lateral fault tip.

Using the lateral separations to estimate the principal strain directions within the horizontal plane indicates that the area of faulting has an overall extension of 1.8% with an orientation of N026°E (Table 5.1). This is different to the principal strain directions of the South Bay and Point Kean areas and could be due to either the reactivation of the damage zone, the local strain effects of fault F3 or the lack of WNW-trending right-lateral faults.

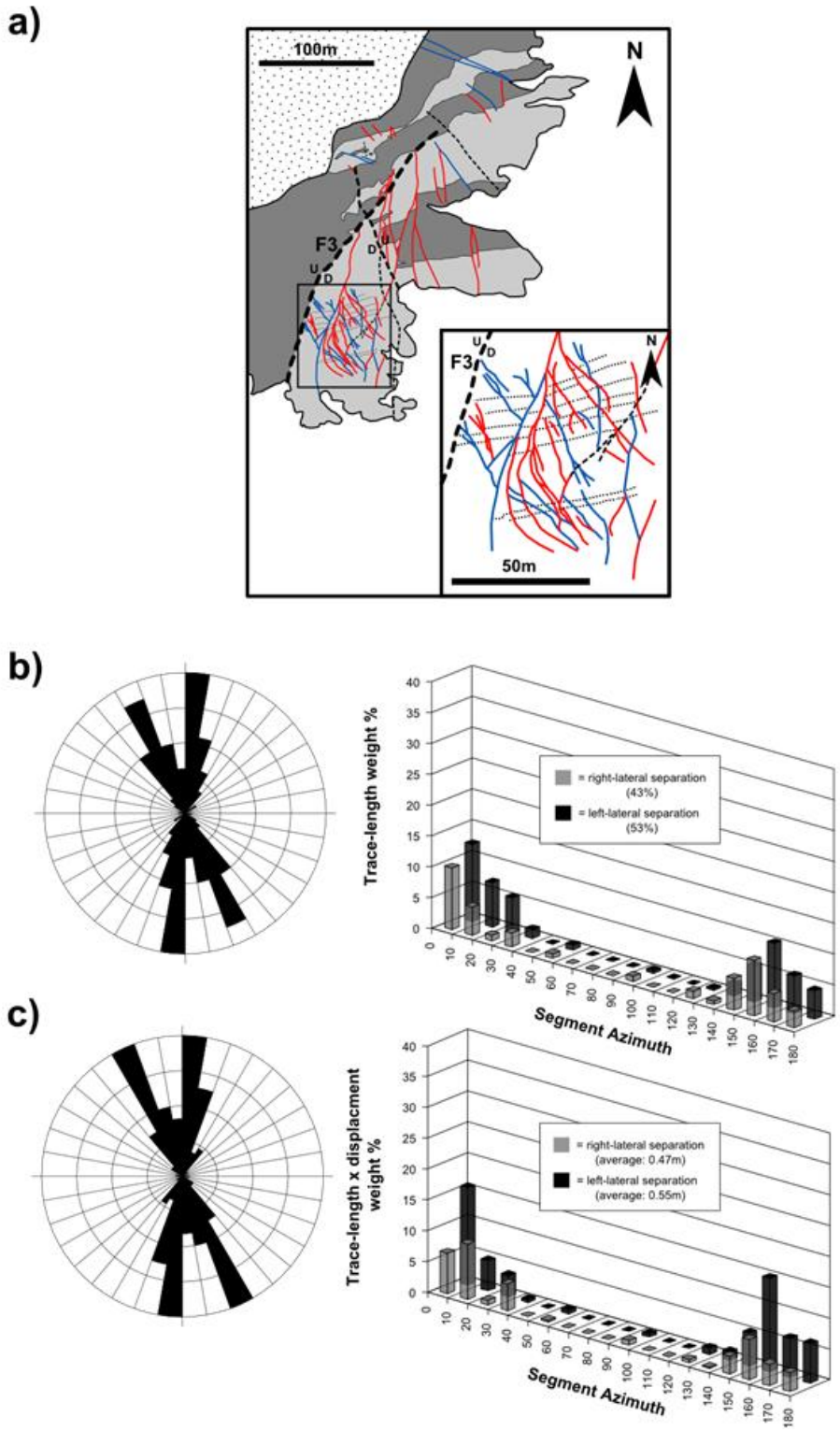

Figure 5.11 a) Fault map of the Spaniards Bay study area with right-lateral faults in blue and left-lateral faults in red. The Spyglass and Waima Formations are in dark grey and light grey, respectively. Note large fault structures follow similar trends to South Bay and Point Kean with WNW-trending right-lateral faults and N-trending left-lateral faults. Inset is an enlarged map of the anastomosing fault network that was mapped and analysed. b) Trace-length weighted rose diagram and histogram and c) trace-length x displacement weighted rose diagram and histogram for the mapped anastomosing fault network at Spaniards Bay. Note the histograms show the distribution of right- and left- lateral faults.

In summary, the mapped fault network at Spaniards Bay is characterized by its location within a fault tip damage zone, which has been reactivated by a change in the maximum stress field from NE-SW to E-W. This has influenced the fault geometries and principal strain directions forming an acute angled set of strike-slip faults and hybrid shear fractures.

5.5. Local variations in fault network behaviour

There is much heterogeneity within fault networks with local variations in the character and behaviour of the faulting (Zhang and Sanderson, 2001; Nixon et al., 2011). There are many causes for such variations and the observations of each area on the Kaikoura Peninsula have already highlighted the effect of reactivation and presence of large-scale structures, which have caused changes in the geometry and kinematic behaviour of faults within the fault network. Local variations also occur across structural features or boundaries such as damage zones and changes in lithology. By taking multiple line samples we calculate the fault density, average displacement, strain and the orientation of strain for each line sample to further investigate these localized effects on fault network behaviour across such structures and boundaries.

5.5.1. Damage zones

The mapped fault network at Spaniards Bay has already been identified as a damage zone in the extensional quadrant of the tip of fault F3. Fault tip damage zones are localized areas of strain that accommodate rapid decreases in displacement at the tips of a fault. A fault tip damage zone mapped at this scale allowed two line samples (Table 5.2) to be taken, illustrating the changes in strain and fault density across the damage zone, with Line 1 taken from the north of the area and Line 2 from the south (Figure 5.12).

As the fault network becomes more diffuse to the south there is an overall increase in fault density from 250 km^{-1} to 441 km^{-1} (faults per km) (Table 5.2). This is accompanied by a decrease in average displacement from 1 m to 0.2 m, a decrease of 80%. This indicates that the northern area has fewer faults but

with larger displacements. These faults splay and become more diffuse to the south where the network has more faults with smaller displacements.

The decrease in average displacement is reflected in the strain values which decrease from an extension of 5.3% to an extension of 3.6% for the north and south lines, respectively. The decrease in strain and displacement appears to be accommodated by a densely populated fracture zone that sits between the two line samples (Figure 5.12). The orientation of strain also differs, with the direction of maximum horizontal extension changing from N045°E to N110°E (Table 5.2). This variation in strain orientation reflects the change in fault dominance from left-lateral to right-lateral for the north and south line, respectively. This is caused by the change in fault orientation and the reactivation of fractures and fault tips.

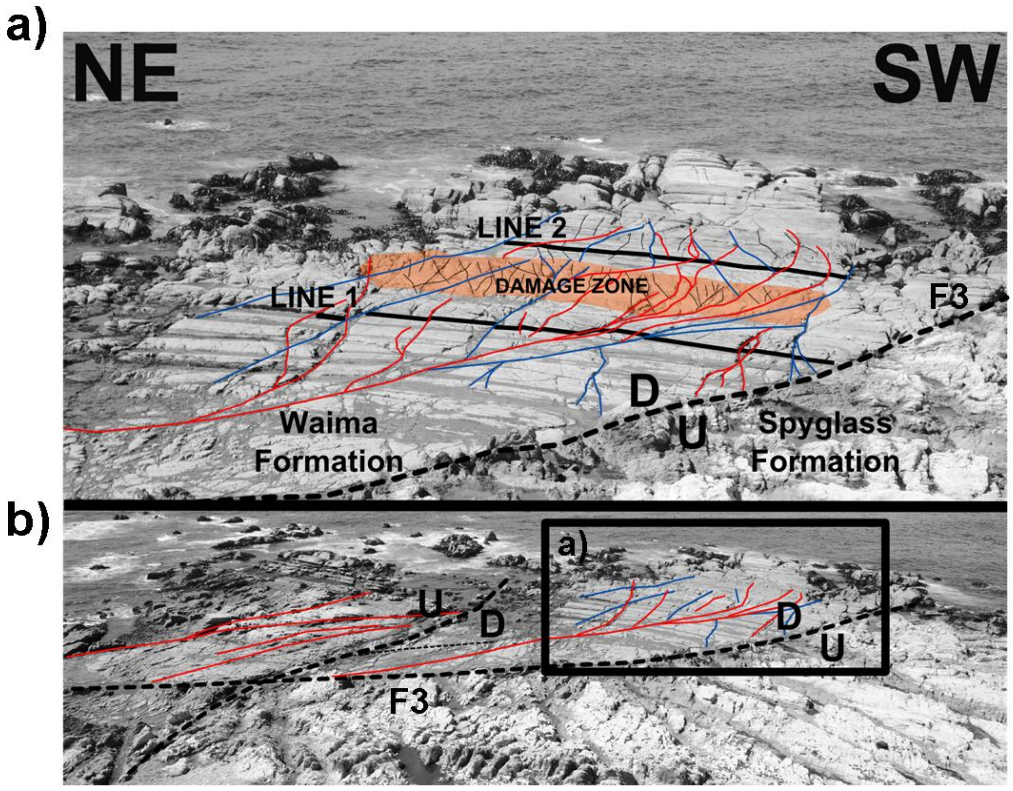

Figure 5.12 Cliff top photographs of the mapped wave-cut platform at Spaniards Bay. a) The location of two line samples and a damage zone between them. b) Shows the extent of fault F3 and the location of the mapped area in photograph 5.12a. Right- and left-lateral faults are in blue and red, respectively.

Overall the variations in physical attributes across the fault tip damage zone reflect the accommodation and dissipation of displacement changes on the main fault. Although damage zones are areas of strain localization it appears

that strain is localized onto a few faults that splay off the main fault (i.e. fault F3). Strain and displacement are then dissipated by further splays and small scale damage zones (Figure 5.12) increasing fault density and decreasing the overall deformation.

5.5.2. Lithology

The fault systems across the Kaikoura Peninsula are more extensively developed in the siltstones and mudstones of the Waima Formation. Only the large faults and a few minor faults appear in the limestone beds of the Amuri and Spyglass Formations.

Line samples 3, 4 and 5 (Table 5.2) are taken from bedding at South Bay illustrating this variation in faulting with proximity to the boundary between the Spyglass Formation and the Waima Formation (Figure 5.13). The line samples indicate that the strain accommodated by faulting decreases from 17.1% for a marker bed 20 m away from the boundary (Line 5) to 13.0% for a marker bed on the boundary (Line 3) (Table 5.2). This is a 24% decrease in strain, furthermore, over half of this strain loss happens within 4.2 m (Line 4) of the lithological boundary.

Table 5.2 Physical Attributes of Line samples taken from Spaniards Bay an South Bay.

	Line Location	Fault Density	Average Displacement	Extension	Orientation
Spaniards Bay – Damage Zone					
Line 1	North	250 km^{-1}	1.0 m	5.3%	N045°E
Line 2	South	441 km^{-1}	0.2 m	3.6%	N110°E
South Bay – Spyglass/Waima Boundary					
Line 3	0 m	310 km^{-1}	0.84 m	13.0%	N042°E
Line 4	4.2 m	370 km^{-1}	0.85 m	15.7%	N041°E
Line 5	20 m	280 km^{-1}	1.16 m	17.1%	N040°E

The density of faulting increases from 280 km^{-1} (faults per km) at 20 m away from the boundary to 370 km^{-1} at 4.2 m away from the boundary. This is accompanied by a decrease in average displacement from 1.16 m to 0.85 m and represents a damage region to accommodate the decrease in strain near

the boundary. The density of faulting decreases at the boundary to 310 km^{-1} as faults begin to terminate. The faults then continue to decrease in number and displacement as they travel further into the limestone units, so much so that only large faults make an impression on the boundary between the Amuri Limestone and the Spyglass Formation.

The limestone beds appear to deform differently to the siltstones and mudstones of the Waima Formation. This variation is not only seen in the brittle deformation but also in the ductile deformation of the rock mass. The limestone beds are dominated by metre scale parasitic folding associated with the large scale folds across the peninsula. This intense deformation is not seen in the Waima Formation which appears to deform by layer parallel slip, enveloping small scale fold structures within the limestone to form very open and shallow folds.

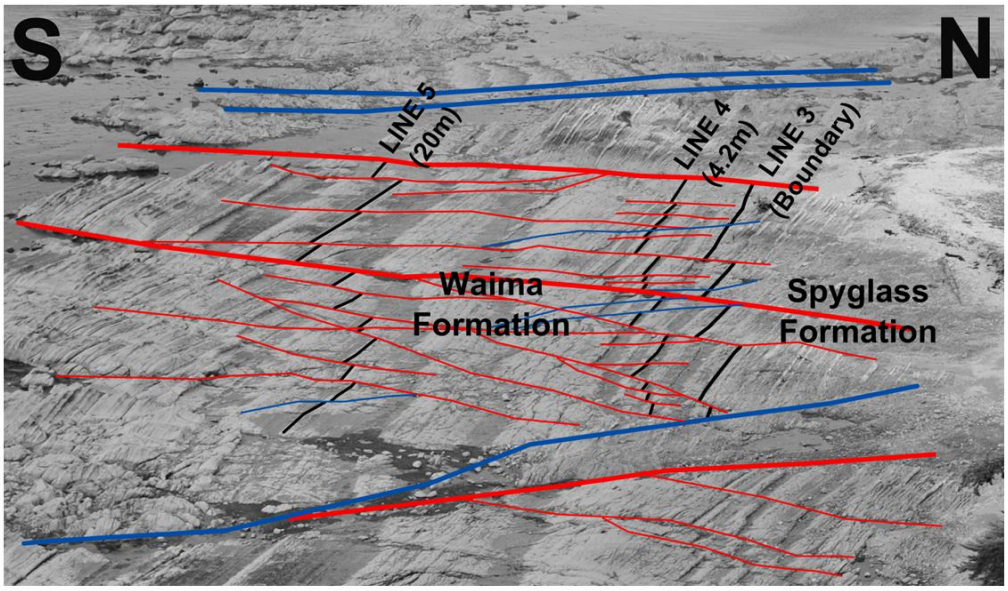

Figure 5.13 Cliff top photograph of the wave-cut platform at South Bay showing the location of line samples 3, 4 and 5 with proximity to the Spyglass/Waima boundary. Right- and left-lateral faults are blue and red, respectively.

5.6. Discussion

The NE-trending folds that deform the Kaikoura Peninsula match the description of early NNW-NE-trending folding associated with the D_2 deformation described by Lamb and Bibby (1989). As the phases of brittle deformation cut and offset

fold hinges they are part of a later phase of D_2 and have formed in the last 4 Ma (Lamb and Bibby, 1989; Vickery and Lamb, 1995).

The observations and descriptions of the fault systems around the Kaikoura Peninsula show evidence of dominant strike-slip deformation. Orientation data from across the peninsula show that the faults have segments that trend ~000° for faults with left-lateral separations and ~290° for faults with right-lateral separations (Figure 5.4). The consistency and dominance of each motion sense for these orientations indicate that these are a conjugate set of strike-slip faults formed by NW-SE compression. 3D structural data show that these faults have sub-vertical fault planes and gently plunging slickensides, attesting to lateral movement rather than vertical. These trends are seen particularly well at both South Bay and Point Kean, but not so clearly at Spaniards Bay. This is because Spaniards Bay is a horsetail damage zone that appears to have formed at the tip of a large left-lateral strike-slip fault (fault F3), hence, the absence of any large WNW-trending right-lateral faults within the mapped fault network at Spaniards Bay. In general the orientations suggest that many of these structures are related to NW-SE compression. This is approximately the same orientation of compression that formed the NE-trending fold and thrust structures suggesting the faults may have formed in relation to these structures.

Although there appears to be a conjugate set of faults there are many faults that are orientated between the two main trends (Figure 5.4a). These are interpreted as reactivated joints/extension fractures as they:

1. Bisect the angle between the two main fault trends (cf. Hancock, 1985);
2. Form parallel to the maximum compression direction that forms the main conjugate fault set (i.e. NW-SE) (cf. Wilkins et al., 2001);
3. Tend to show both left- and right-lateral separations.

Even though opposing lateral slip senses on faulted joints can be produced by vertically offsetting shallowly dipping beds, there is clear evidence for a strike-slip reactivation of some of these structures. However, the reactivation history for these brittle structures appears quite complicated. There was a phase of left-lateral reactivation as indicated by the tip of fault F2 at Point Kean but the rest of fault F2 expresses right-lateral separations, which indicates that these

joints/extension fractures were also affected by a phase of right-lateral reactivation. This is supported by the minor fault orientations seen at Point Kean as there appears to be a conjugate left-lateral fault set associated with this right-lateral phase.

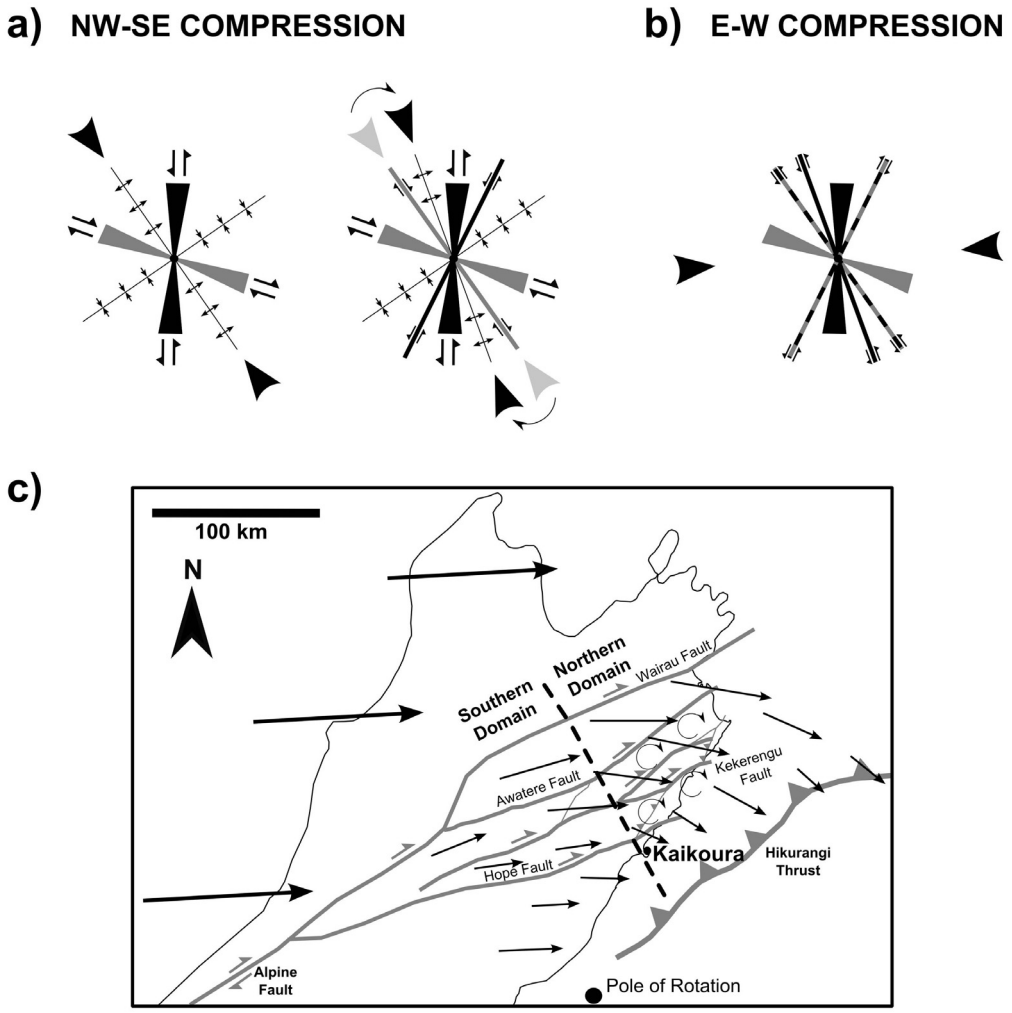

Figure 5.14 Schematic diagrams showing the main structures seen on the Kaikoura Peninsula and their associated regional stress directions: a) an initial phase of NW-SE compression forming NE-trending folds, a conjugate strike-slip fault set of N-trending left-lateral faults and WNW-trending right-lateral faults, and NW-trending joints/extension fractures. A small clockwise rotation of the regional stress field causes right-lateral reactivation of the NW-trending joints/extension fractures; b) E-W compression causing left-lateral reactivation of NW-trending right-lateral faults and extension fractures and right-lateral reactivation of NNW-trending left-lateral faults. Black arrow heads indicate the far field loading orientations. c) Regional map of the Marlborough fault zone illustrating the plate motions and the characteristics of the Northern Marlborough Domain and Southern Marlborough Domain, modified from Lamb and Bibby (1989) and Vickery and Lamb (1995). Note the position of Kaikoura Peninsula with respect to the two domains.

This minor conjugate fault set is orientated ~30° clockwise from the main conjugate fault set and would have formed in a similar regional stress field. Reactivation of the joints/extension fractures could have occurred by either a change in the orientation of the regional stress field or by rotation of the joints/extension fractures within the regional stress field (Wilkins et al., 2001). Palaeomagnetic data indicate that the Kaikoura Peninsula has experienced an overall clockwise rotation of 40.5° +/- 17° (Hall et al., 2004). However, a clockwise rotation of the faulted area would have caused a minor conjugate set to form anticlockwise to the main conjugate set, therefore, the reactivated joints/extension fractures are more likely to have formed by a local clockwise rotation of the regional stress field (Figure 5.14a).

The reactivated right-lateral fault at Point Kean (fault F2) indicates that local right-lateral reactivation of the joints/extension fractures happened before the main left-lateral phase of reactivation. The left-lateral reactivation of a NW-SE trending fault would have to be caused by ~E-W compression. This agrees with the ~N-trending cleavage observed at Spaniards Bay, which overprints the NE-trending folds. E-W Compression would also explain the presence of some ~NNE-NE-trending right-lateral faults, which could also be reactivated structures (Figure 5.14b). These orientations match the description of D_2 faulting by Lamb and Bibby (1989), which formed a conjugate set of NW-trending left-lateral faults and NE-trending right-lateral faults related to ~E-W compression.

Hence, we conclude that the Kaikoura Peninsula has been deformed by two main phases of brittle deformation. First NW-SE compression producing NE-trending folds and a conjugate set of strike-slip faults, which has been overprinted by ~E-W compression causing reactivation of faults and producing a ~N-trending cleavage. Lamb and Bibby (1989) illustrate similar variations in the orientation of the regional stress field with further phases of folding deforming the early NE-trending fold phase of D_2. The deformation is thought to accommodate rotation of crustal blocks with further rotation causing refolding of previous structures (Lamb and Bibby, 1989; Vickery and Lamb, 1995). This could be a plausible hypothesis for the deformation on the Kaikoura Peninsula, however, this would mean that the clockwise rotation measured by Hall et al.

(2004) would have to have happened in the last 4 Ma. This is not plausible considering the age of the magnetization was 43-54 Ma.

Vickery and Lamb (1995) identify two separate domains of D_2 deformation, the Northern Marlborough Domain and the Southern Marlborough Domain (Figure 5.14c). Regions in the Northern Marlborough Domain rotate clockwise relative to regions further south whereas the regions in the Southern Marlborough Domain appear to be effected purely by ENE right-lateral shear (Vickery and Lamb, 1995). The Kaikoura Peninsula appears to sit within the hinge zone that accommodates the rotation of the Northern Marlborough Domain but is very close to the boundary between the two different domains, therefore, we suggest that the peninsula is affected by a combination of the deformation associated with both domains (Figure 5.14c). The rotation of the Northern Marlborough Domain is accommodated by NE-trending folds and the conjugate set of strike-slip faults, associated with intrablock ~NW-SE compression, as crustal blocks rotate clockwise against the offshore southern segment of the Hikurangi Margin. The later ~E-W compression reflects the relative plate motion and ENE right-lateral shear that characterizes the Southern Marlborough Domain, which may become dominant when rotating crustal blocks lock and/or stop rotating.

The tensile reactivation of the N-trending cleavage seen in the Spyglass Formation and the ongoing north westerly tilt of the peninsula recorded by Ota et al. (1996) indicate that N-NW compression is still affecting the Kaikoura Peninsula causing uplift. This suggests that deformation is again accommodating rotation of the Northern Marlborough Domain and supports the fact that the phases of fault reactivation are due to changes in the regional stress field, rather than rotation of the faults within a consistent regional stress field.

5.7. Conclusions

A description of the fault systems across the Kaikoura Peninsula has revealed a complex strike-slip fault network with variable orientations. Unravelling the kinematic history of these faults has revealed a complex reactivation history over the past 4 Ma:

1. The fault network originally formed by NW-SE compression forming the distinguishable conjugate pair of fault sets consisting of N-trending left-lateral faults and WNW-trending right-lateral faults. A set of ~NW trending faults and fractures bisect these two main fault trends and are interpreted as originally forming as tensile fractures associated with NW-SE compression.
2. Clockwise rotation of the regional stress field caused local right-lateral reactivation of the NW-trending extension fractures and a conjugate left-lateral fault set.
3. A change in the regional stress field from ~NW-SE compression to ~E-W compression resulted in left-lateral reactivation of the NW-trending faults and extension fractures.

There is much variation in fault network behaviour across the Kaikoura Peninsula. Many of these variations are caused by localized structures such as changes in lithology and the formation of damage zones. These can cause changes in fault density and dissipation of strain and displacement adding to the heterogeneity of fault networks. Fault tip damage zones accommodate rapid decreases in displacement at fault tips and become more diffuse as they splay away from the main fault with a localized increase in fault density and a decrease in strain. On the other hand, a lithological boundary can cause a change in fault behaviour, with faults preferentially forming in the siltstones and mudstones of the Waima Formation and becoming more diffuse in the limestone beds of the Spyglass Formation.

Overall the study of faulting on the Kaikoura Peninsula has added to the complex history of deformation associated with the regional tectonics of the Marlborough Fault Zone. We suggest that the reorientations of the regional stress field are due to the combined affects of the mechanical behaviour of the Northern Marlborough Domain and the Southern Marlborough Domain. NW-SE compression accommodates clockwise rotations of the Northern Marlborough Domain, whereas E-W compression reflects the relative plate motion and dominant ENE right-lateral shear of the Southern Marlborough Domain.

5.8. References

Audru, J., Delteil, J., 1998. Evidence for early miocene wrench faulting in the Marlborough fault system, New Zealand: structural implications. Geodinamica Acta 11, 233–247.

Barnes, P., Audru, J., 1999. Recognition of active strike-slip faulting from high-resolution marine seismic reflection profiles: Eastern Marlborough fault system, New Zealand. Geological Society of America Bulletin 111, 538–559.

Barnes, P.M., 1996. Active folding of Pleistocene unconformities on the edge of the Australian-Pacific plate boundary zone, offshore North Canterbury, New Zealand. Tectonics 15, 623.

Browne, G.H., Laird, M.G., Field, B.F., 2005. Stratigraphic and Sedimentological Teasers, Kaikoura Peninsula, Marlborough, in: Pettinga, J., Wandres, R. (Eds.), Field Trip Guides, Geological Society of New Zealand 50th Annual Conference, Kaikoura, New Zealand. Geological Society of New Zealand Misc. Publ. 119B, pp. 129–140.

Cambell, J., Tonkin, P., Bradshaw, J., 2005. Structure and Tectonics of the Kaikoura Peninsula, in: Pettinga, J., Wandres, A.. (Eds.), Field Trip Guides, Geological Society of New Zealand 50th Annual Conference, Kaikoura, New Zealand. Geological Society of New Zealand Misc. Publ. 119B, pp. 111–128.

DeMets, C., Gordon, R.G., Argus, D.F., Stein, S., 1994. Effect of recent revisions to the geomagnetic reversal time scale on estimates of current plate motions. Geophysical Research Letters 21, 2191–2194.

Furlong, K.P., Kamp, P.J.J., 2009. The lithospheric geodynamics of plate boundary transpression in New Zealand: Initiating and emplacing subduction along the Hikurangi margin, and the tectonic evolution of the Alpine Fault system. Tectonophysics 474, 449–462.

Granier, T., 1985. Origin, damping, and pattern of development of faults in granite. Tectonics 4, 721–737.

Hall, L.S., 2004. Cenozoic distributed rotational deformation, South Island, New Zealand. Tectonics 23, 1–16.

Hancock, P.L., 1985. Brittle microtectonics: principles and practice. Journal of Structural Geology 7, 437–457.

Kim, Y-S., Andrews, J., Sanderson, D., 2000. Damage zones around strike-slip fault systems and strike-slip fault evolution, Crackington Haven, southwest England. Geosciences Journal 4, 53–72.

Kim, Y-S., Andrews, J.R., Sanderson, D.J., 2001. Reactivated strike–slip faults: examples from north Cornwall, UK. Tectonophysics 340, 173–194.

Kim, Y-S., Peacock, D.C.., Sanderson, D.J., 2004. Fault damage zones. Journal of Structural Geology 26, 503–517.

Lamb, S., 2011. Cenozoic tectonic evolution of the New Zealand plate-boundary zone: A paleomagnetic perspective. Tectonophysics 509, 135–164.

Lamb, S., Bibby, H., 1989. The last 25 Ma of rotational deformation in part of the New Zealand plate-boundary zone. Journal of Structural Geology 11, 473–492.

Langridge, R., Campbell, J., Hill, N., Pere, V., Pope, J., Pettinga, J., Estrada, B., Berryman, K., 2003. Paleoseismology and slip rate of the Conway Segment of the

Hope Faultat Greenburn Stream, South Island, New Zealand. Annals of Geophysics 46, 1119–1139.

Lever, H., 2007. Review of unconformities in the late Eocene to early Miocene successions of the South Island, New Zealand: Ages, correlations, and causes. New Zealand Journal of Geology and Geophysics 50, 245–261.

Little, T., Roberts, A., 1997. Distribution and mechanism of Neogene to present-day vertical axis rotations, Pacific-Australian plate boundary zone, South Island, New Zealand. Journal of Geophysical Research 102, 20447–20468.

McGrath, A., Davison, I., 1995. Damage zone geometry around fault tips. Journal of Structural Geology 17, 1011–1024.

Nixon, C.W., Sanderson, D.J., Bull, J.M., 2011. Deformation within a strike-slip fault network at Westward Ho!, Devon U.K.: Domino vs conjugate faulting. Journal of Structural Geology 33, 833–843.

Ota, Y., Pillans, B., Berryman, K., Beu, A., Fujimori, T., T, M., G, B., 1996. Pleistocene coastal terraces of Kaikoura Peninsula and the Marlborough coast, South Island, New Zealand. New Zealand Journal of Geology and Geophysics 39, 51–73.

Peacock, D.C.P., Sanderson, D.J., 1993. Estimating strain from fault slip using a line sample. Journal of Structural Geology 15, 1513–1516.

Rait, G., Chanier, F., Waters, D., 1991. Landward-and seaward-directed thrusting accompanying the onset of subduction beneath New Zealand. Geology 19, 230–233.

Randall, K., Lamb, S., Niocaill, C.M., 2011. Large tectonic rotations in a wide zone of Neogene distributed dextral shear, northeastern South Island, New Zealand. Tectonophysics 509, 165–180.

Rattenbury, M.S., Townsend, D.B., Johnston, M.R., 2006. Geology of the Kaikoura area. Institute of Geological and Nuclear Sciences.

Segall, P., Pollard, D., 1983a. Joint formation in granitic rock of the Sierra Nevada. Geological Society of America Bulletin 94, 563–575.

Segall, P., Pollard, D., 1983b. Nucleation and growth of strike slip faults in granite. Journal of Geophysical Research 88, 555–568.

Van Dissen, R., Yeats, R., 1991. Hope fault, Jordan thrust, and uplift of the seaward Kaikoura range, New Zealand. Geology 19, 393–396.

Vickery, S., Lamb, S., 1995. Large tectonic rotations since the Early Miocene in a convergent plate-boundary zone, South Island, New Zealand. Earth and Planetary Science Letters 136, 43–59.

Wannamaker, P.E., Caldwell, T.G., Jiracek, G.R., Maris, V., Hill, G.J., Ogawa, Y., Bibby, H.M., Bennie, S.L., Heise, W., 2009. Fluid and deformation regime of an advancing subduction system at Marlborough, New Zealand. Nature 460, 733–6.

Wilkins, S., Gross, M., Wacker, M., Eyal, Y., Engelder, T., 2001. Faulted joints: kinematics, displacement–length scaling relations and criteria for their identification. Journal of Structural Geology 23, 315–327.

Zhang, X., Sanderson, D., 2001. Evaluation of instability in fractured rock masses using numerical analysis methods: Effects of fracture geometry and loading direction. Journal of Geophysical Research 106, 26671–26687.

Zhao, G., Johnson, A., 1992. Sequence of deformations recorded in joints and faults, Arches National Park, Utah. Journal of Structural Geology 14, 225–236.

6. The organization of faulting and distribution of strain around a large magnitude fault in the Whakatane Graben, New Zealand

Casey W. Nixon, David J. Sanderson, Jonathan M. Bull

6.1. Abstract

The along strike organization of deformation around the Rangitaiki Fault in the Whakatane Graben is characterized and described with particular focus on the accumulation of displacement and distribution of strain. The rifting fault network is divided into three main groups: the Rangitaiki Fault; its hanging wall faults to the NW; and its footwall faults to the SE.

Over the past 17 kyr the strain has been consistent along strike of the fault network, however, there is a change from distributed faulting to localized faulting forming two distinct domains. Distributed faulting is characterized by strain and displacement being distributed across numerous faults in the hanging wall and footwall blocks of the Rangitaiki Fault. Whereas for localized faulting there are fewer but larger displacement faults and the majority of strain (>80%) is localized onto the Rangitaiki Fault.

Syn-depositional sedimentation indicates that since 17 ka there has been progressive localization of deformation onto the Rangitaiki Fault. Hence, the transition from distributed to localized faulting is attributed to progressive strain localization and a change in the linkage maturity along strike of the Rangitaiki Fault. The pattern of deformation within the fault network is seen for all time intervals, as small as 2-3 kyr, preserving a kinematic coherency.

6.2. Introduction

The aim of this chapter is to investigate the spatial and temporal pattern of deformation around a large magnitude fault within a fault network. Fault networks often have few large magnitude faults that dominate the system, localize strain (e.g. Walsh et al., 2003; Nixon et al., 2012) and rarely form without associated deformation. They often grow by the interaction of fault segments that eventually link (Cartwright et al., 1995; Childs et al., 1996; Peacock, 2002) developing a range of structures (i.e. relay ramps; Long and Imber, 2011) and damage (i.e. tip damage; Kim et al., 2003) as the system evolves. Therefore, understanding the organization of deformation around such large magnitude faults is important for seismic hazard analysis and understanding fault network growth and development.

A variety of techniques can be used to study the short term distribution of both inter-seismic and co-seismic deformation associated with fault systems such as satellite radar interferometry, GPS monitoring and the use of abundant seismic data catalogues (e.g. Wright et al., 2004; Fialko, 2006; Doubre and Peltzer, 2007; Biggs et al., 2010; Nobile et al., 2012). These techniques are limited to the past few decades and can only be used for studying present day deformation processes, for example earthquake rupture events (Quigley et al., 2012). Since such rupture events maybe separated by 1000 yr recurrence intervals, there is little scope for understanding repeated deformation events on the same fault system. As fault networks develop and grow over much larger timescales, 10^4-10^6 years, it is therefore essential to investigate their longer term accumulation of deformation.

Normal faults that form with syn-sedimentary deposits allow the temporal evolution of fault systems over longer time periods, 10^4-10^6 years, to be defined by studying patterns of sediment infill (e.g. Contreras et al., 2000). This is a fundamental technique for investigating the evolution of fault geometries and fault displacements, identifying kinematic growth processes such as strain localization within fault systems (e.g. Meyer et al., 2002; Walsh et al., 2003), as well as describing larger scale tectonic processes including mechanisms of lithospheric extension (e.g. Cowie et al., 2005; Bell et al., 2008). Such data sets also record the accumulation of different slip events on individual faults,

allowing rates of co-seismic deformation to be compared at different time periods, furthering our knowledge of earthquake recurrence cycles and slip rate variability (Taylor, 2004; Mouslopoulou et al., 2009; Cowie et al., 2012).

In this study we investigate a normal fault network associated with the highly active Rangitaiki Fault, which is a large magnitude fault within the Whakatane Graben, New Zealand. This currently active fault network displaces near surface syn-sedimentary stratigraphy with continuous sedimentation and fault slip rates of the same order and known dated stratigraphic horizons (Lamarche et al., 2000; Taylor, 2004; Bull et al., 2006). This produces a high fidelity record of normal fault activity over the past 17 kyr and a high resolution data set that images small faults within the network. Hence, a more complete fault network can be investigated and analysed than in previous studies, which have been limited by the resolution of their seismic data (e.g. Walsh et al., 2003).

Bull et al. (2006) and Taylor et al. (2004) describe the linkage and displacement rate history of the Rangitaiki Fault. We aim to further this work by characterizing the along strike organization of faulting around the Rangitaiki Fault and investigate the temporal evolution of co-seismic deformation throughout the fault network. We also focus on the along strike distribution of strain and the accumulation of displacement accommodated by the fault network and compare the contributions of the main Rangitaiki Fault and its associated hanging wall and footwall faults.

6.3. Tectonic Setting

The study area is the most active part of the Whakatane Graben, which is located in the Bay of Plenty (Figure 6.1a). The graben is within the Taupo Fault Belt and is the youngest part of the Taupo Volcanic Zone (TVZ), a zone of Quaternary back-arc rifting and volcanism associated with the oblique westward subduction of the Pacific plate beneath the Australian plate at the Hikurangi Margin (Figure 6.1a) (Walcott, 1978). The Whakatane Graben lies beneath the Rangitaiki Plain and extends approximately 50 km offshore, at 200 m water depth, up to the White Island Volcano (Nairn and Beanland, 1989; Wright, 1990; Bull et al., 2006). The graben itself is bound by the White Island Fault (WIF) to

the east and the Rurima Ridge to the west. The WIF has a complicated history and separates the dip-slip dominated graben from the North Island Dextral Shear Belt, whereas the Rurima Ridge is a topographic high separating the Whakatane Graben to the east from the Motiti Graben to the west (Bull et al., 2006; Lamarche et al., 2006).

Seismic reflection data and multibeam bathymetry indicate that the Whakatane Graben is dominated by large NW-dipping active normal faults, which cut through the top 3 km of sediment including the post last glacial (<20 ka) sediments (Lamarche et al., 2000; Taylor, 2004). These are spaced at 1-3 km and produce large fault bound blocks that are back-tilted by 12-16° and cut by smaller synthetic and antithetic faults (Lamarche et al., 2006). Analysis of the post-last glacial transgressive surface, dated at 17 ka, indicates that the Whakatane Graben has an average subsidence rate of 2mm/yr (Wright, 1990) and a surface extension rate of 2.9 +/- 0.7 mm/yr (Lamarche et al., 2006).

The Rangitaiki Fault has been the most active structural element of the Whakatane Graben over the past 17 kyr. It is a typical normal fault with dip values no lower than 59° in the top 2 km of sediment (Taylor, 2003) and has growth sediments in the hanging wall, which indicate the fault has accumulated up to 830 m of dip slip displacement since ~1.3 Ma (Taylor et al., 2004). Over the past 1.3 +/- 0.5 Myrs the Rangitaiki Fault has grown by the linkage of five isolated fault segments. Taylor et al. (2004) demonstrated that each segment initially grew by tip propagation in the early stages of the faults growth history, with low displacement rates of 0.72 +/- 0.23 mm/yr. The fault system became fully linked between 300 ka and 17 ka with marked increases in displacement rate up to a maximum of 3.4 +/- 0.2 mm/yr (Taylor et al., 2004).

Using a high resolution fault displacement data set, Bull et al. (2006) investigated the post-linkage accumulation of displacement on the Rangitaiki Fault since 17 ka. In general, displacement rate patterns were highly irregular over smaller time intervals (2-3 kyr), with larger segments sometimes producing values of zero displacement, whereas longer time intervals of at least 9 kyr produced more regular displacement rate patterns similar to those for time periods of 300 kyr (Bull et al., 2006).

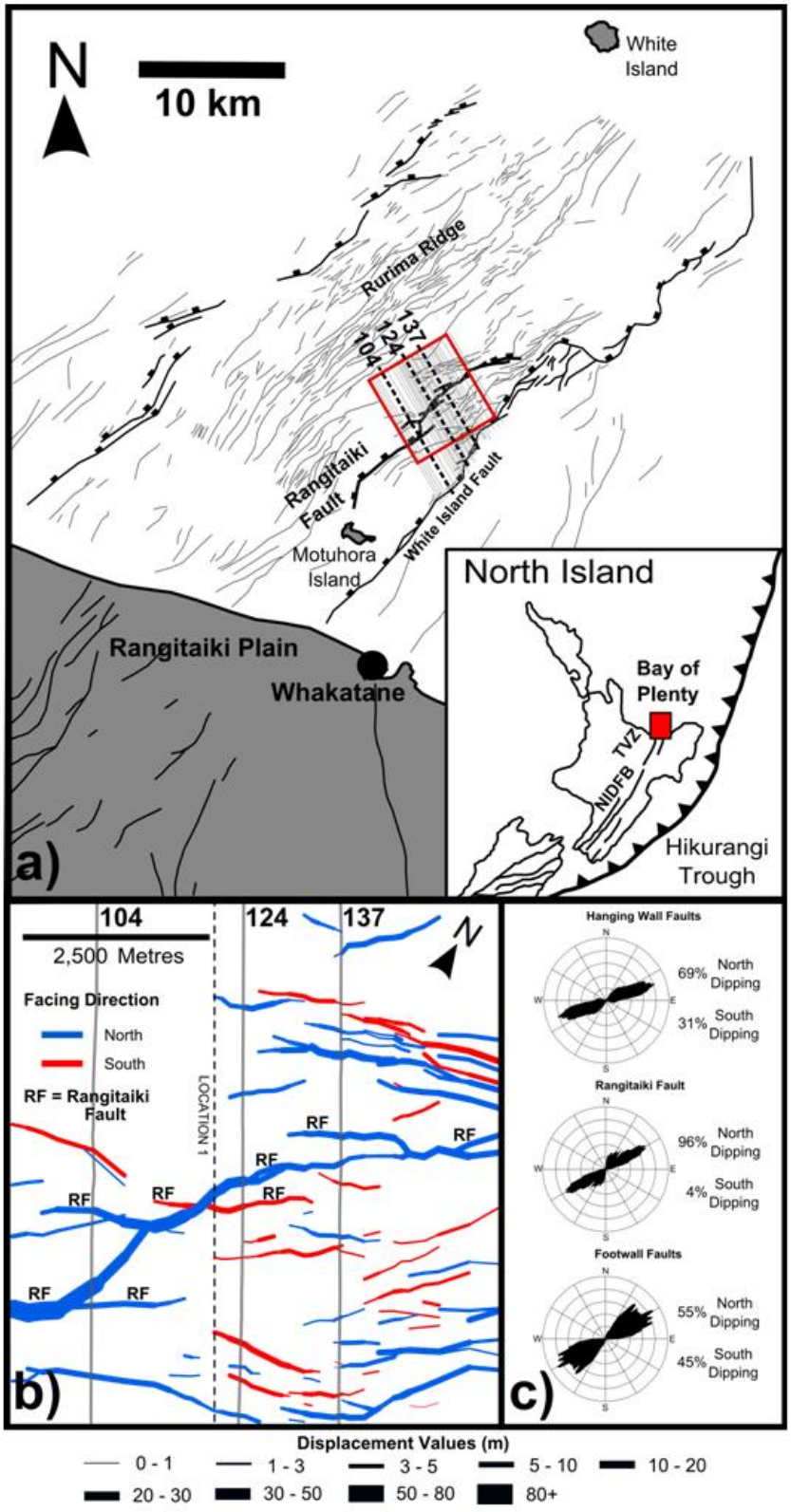

Figure 6.1 a) Location map of the Whakatane Graben showing the position of the Rangitaiki Fault and the study area. The position of boomer lines 104, 124 and 137 are also shown. b) A fault map of the study area showing the segments of the Rangitaiki Fault. The hanging wall and footwall fault groups are NW and SE of the Rangitaiki Fault, respectively. c) Length-weighted rose diagrams showing the fault trends within each fault group.

Overall the Rangitaiki Fault and its surrounding deformation are ideal for investigating the distribution and accumulation of displacement and strain through time. Hence, we add to the work by Bull et al. (2006) and investigate the post-linkage accumulation of displacement and strain in the areas of deformation surrounding the Rangitaiki Fault for different time scales over the past 17 kyr.

6.4. Methodology

6.4.1. Seismic data and interpretation

The high resolution seismic reflection data comprises 46 boomer profiles that were taken perpendicular to strike of the main Rangitaiki Fault, as summarized in Bull et al. (2006). The boomer profiles were spaced between 100-200 m covering an area of approximately 7.5 x 7.5 km (Figure 6.1a), imaging the last 17 +/- 1 kyr of sediment across the central part of the Rangitaiki Fault providing information on the top ~60 m of stratigraphy with a vertical resolution of ~0.5 m.

Table 6.1 A table showing the estimated ages of horizons H1- H4, from Bull et al. (2006).

Horizon	Age
H1	9+/-1 ka
H2	11.4+/-1 ka
H3	13.9+/-1 ka
H4	17+/-1 ka

The seismic profiles were interpreted using 3D seismic interpretation software to pick faults and horizons. Faults were correlated across profiles using geographic positioning of each fault pick and identifying realistic patterns of vertical separations of interpreted horizons, which represent the throw of the fault. Four strongly reflecting horizons (H1-H4) were identified and easily correlated across each boomer profile (Figure 6.2). These are laterally continuous and were used to constrain the evolution of the fault network over the last 17 +/- 1 kyr. The ages of each horizon are given in Table 6.1, which were constrained in Taylor et al. (2004) and are summarized by Bull et al. (2006).

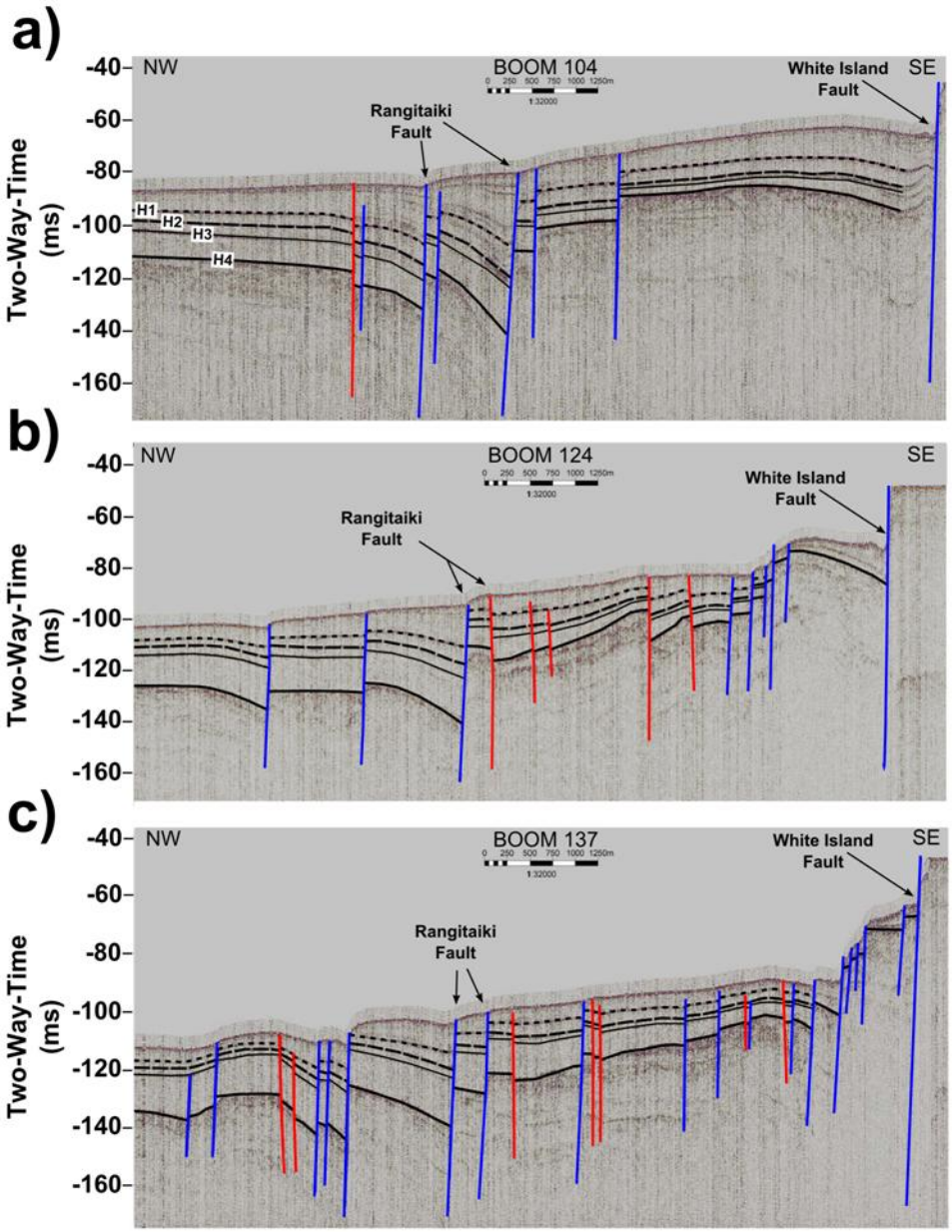

Figure 6.2 Interpreted seismic profiles for boomer lines 104, 124 and 137 (positions shown in Figure 6.1b) indicating the positions of four horizons H1-H4. The fault segments which make up the Rangitaiki Fault system and the White Island Fault are also shown. Blue and red represent faults which down throw to the north and south, respectively. Note the increase in fault frequency from line 104 to line 137.

6.4.2. Displacement measurements and analysis

Where horizons are cut by a fault, they are projected towards the fault plane to correct for localized deformation processes around the fault planes, such as fault drag. This is the same technique applied by Mansfield and Cartwright (1996) and Bull et al. (2006). The vertical separation (throw) at each fault was calculated for all four horizons from manual picks of the hanging wall and

footwall cut-offs of each horizon. We used an average interval velocity of 1550 +/- 25 ms^{-1} for the uncompacted near surface sediments, which was constrained by geophysical logging of 43 piston cores (Taylor et al., 2004). As the faults are normal in nature and have very steep dips (>70°) in the uncompacted sediments, the vertical separation approximates the fault displacement. For information on relative errors of displacement measurements and horizon ages see Bull et al. (2006).

The measured displacements are used to analyse the deformation across the fault network by calculating displacement rates and strain values for each horizon and different areas of the fault network. Displacement rates are calculated for each fault at different time periods using the displacements for differently aged horizons (Table 6.1). Strain was analysed by calculating the heave and dip separation for all the faults using fault dips derived by Taylor (2003) from multichannel seismic reflection data. The average dips for the fault network was 61° for the Rangitaiki Fault, 65° for the hanging wall faults and 68° for the footwall faults. The total extension of each boomer profile was then calculated from their cumulative heave.

3D Strain values were determined using a methodology defined by Nixon et al. (2011) who calculate the eigenvalues and eigenvectors of a Lagrangian strain tensor (E_{ij}) when sampling strike-slip faults from a plane:

$$E_{ij} = \frac{1}{\mathrm{A}} \times \sum \left(t \times \frac{D_{ij} + D_{ji}}{2} \right) \tag{6.1}$$

where A is the sample area, t is the fault trace-length and D_{ij} is the displacement tensor. As these are normal faults we apply a weighting factor (w) defined by Peacock and Sanderson (1993) to the displacement tensor, which corrects for the orientation bias between the sample plane and the dip angle of the faults, hence:

$$D_{ij} = ws \begin{pmatrix} n_1u_1 & n_1u_2 & n_1u_3 \\ n_2u_1 & n_2u_2 & n_2u_3 \\ n_3u_1 & n_3u_2 & n_3u_3 \end{pmatrix} \tag{6.2}$$

Where *s* is the displacement and unit vectors *n* and *u* are normal to the fault plane and parallel to the slip direction, respectively. We assume pure dip slip movement on these faults, therefore where faults dip θ towards Φ, then:

$\boldsymbol{n}$ = (-cosΦ sinθ, -sinΦ sinθ, cosθ) and $\boldsymbol{u}$ = (cosΦcosθ, sinΦcosθ, sinθ)

The displacement rates and strain values are used to analyse the spatial variation in deformation across the fault network. We use fault maps weighted by displacement rate as well as along strike profiles of strain and cumulative displacement rate, for different time intervals.

6.5. Results

6.5.1. Geometry and spatial variation in faulting

The fault network imaged by the high resolution seismic reflection data is illustrated in Figure 6.2 and shows the faults associated with the Rangitaiki Fault system (Figure 6.1b). We divide the faults into three groups based on their spatial and geometric characteristics: the Rangitaiki Fault, its hanging wall faults and its footwall faults. The Rangitaiki Fault consists of fault segments that link and form its main trace-length as defined by Bull et al. (2006) (Figure 6.1b). The hanging wall and footwall faults are the faults that form in the hanging wall fault block to the NW and footwall fault block to the SE of the Rangitaiki Fault, respectively (Figure 6.1b).

Rose diagrams of the fault trends indicate that each fault group is dominated by approximately ENE-trending faults (Figure 6.1c). The Rangitaiki Fault and the Footwall (FW) faults trend ~N058°E and ~N059°E, respectively, whereas the Hanging wall (HW) faults show a slightly rotated fault trend of ~N071°E. In general, the fault network is dominated by N-dipping normal faults with the longest and largest being the Rangitaiki Fault. This dominance is also reflected in HW fault group but not in the FW fault group, which has almost equal proportions of both N-dipping and S-dipping faults (Figure 6.1c).

The number of faults within the fault network increases along strike towards the NE side of the study area as is illustrated by boomer profiles 104, 124 and 137

(Figure 6.2). This is due to increased numbers of faults in the HW and FW blocks increasing the fault frequency from 8 faults at boomer profile 104 (Figure 6.2a) to 26 faults at boomer profile 137 (Figure 6.2c). As the character of the fault network changes from SW-NE, we investigate this further by comparing the distribution of displacement and strain within these two regions.

6.5.2. Distribution and accumulation of displacement

Although the fault frequency increases from boomer profile 104 to 137, the cumulative throws of each profile at H4 are very similar with values of 120 m, 111 m and 116 m for profiles 104, 124 and 137, respectively (Figure 6.2). This indicates that the displacement is localized onto fewer faults for profile 104 and becomes distributed across more faults for profiles 124 and 137. Furthermore, the displacement map in Figure 6.3d illustrates that to the NE of Location 1 displacement is distributed throughout the Hanging wall and Footwall blocks with less displacement on the Rangitaiki Fault, whereas to the SW of Location 1 the displacement appears to be mainly localized onto the Rangitaiki Fault.

Figure 6.3 also shows an accumulation of displacement through time for the entire fault network (Figure 6.3a) as well as showing the contribution of the Rangitaiki Fault and its HW and FW faults (Figure 6.3b and 6.3c). The cumulative displacement profiles are broadly similar for each horizon. Furthermore, the total cumulative displacement profile reflects the smooth profile of the Rangitaiki Fault up until location 1 (i.e. 0-2800 m strike distance), however, after location 1 (i.e. 2800-6500 m strike distance) the total cumulative displacement profile is similar to the profile of the HW and FW faults.

At H4 (17 ka) the Rangitaiki Fault steadily decreases in displacement from ~90 m to ~20 m from SW-NE, which is consistent with results from Bull et al. (2006). In contrast to the Rangitaiki Fault, the cumulative displacement contributed by the HW and FW faults abruptly changes at location 1. SW of location 1 the displacement profile is smooth with low displacements of ~20 m at H4, however, the displacement profile then increases abruptly in steps at locations 1, 2, 3, 4 and 5. These jumps in displacement decrease from ~40 m at location 1 to ~20 m at location 5 and are attributed to the introduction of fault segments in the HW and FW blocks as indicated in Figure 6.3d. Figure 6.4 shows the contribution of

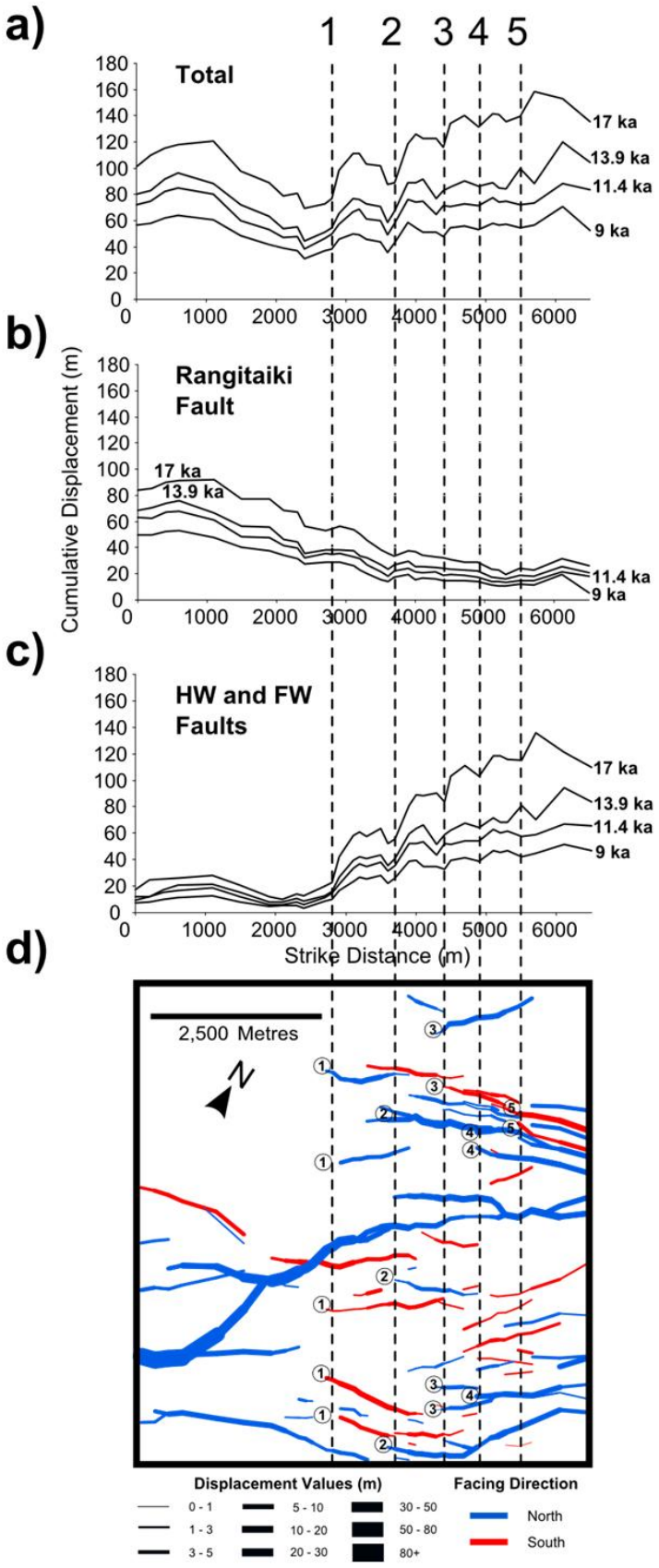

Figure 6.3 Fault displacement profiles of cumulative displacement along strike of the fault network for horizons H1- H4 of: a) the entire fault network; b) the Rangitaiki Fault and c) the Hanging wall and Footwall faults. d) A fault map weighted by displacement shows the positions of locations 1- 5.

these fault segments to the displacement profile of HW and FW faults for H4. In general, the faults introduced at locations 1, 2 and 3 influence the cumulative displacement profile and match the steps in displacement. However, the faults introduced at locations 4 and 5 do not match up as well due to the increased number of faults contributing to the displacement profile (Figure 6.4).

Overall, the fault network can be divided into two domains that show different kinematic behaviours. The change in behaviour occurs at location 1 where the fault network changes from localized faulting with displacement taken up by the Rangitaiki Fault to distributed faulting with numerous HW and FW faults contributing to the cumulative displacement of the network.

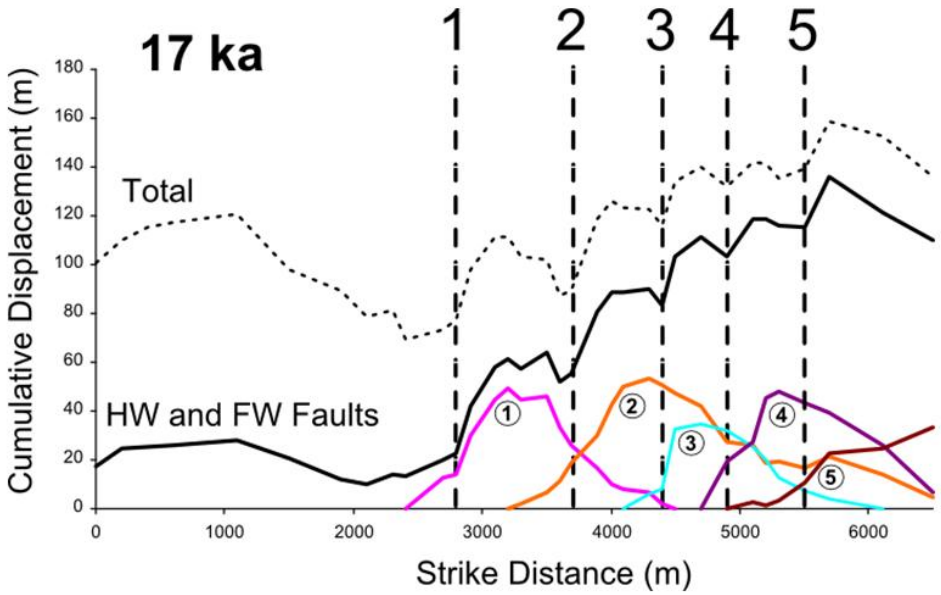

Figure 6.4 Fault displacement profiles of cumulative displacement along strike of the fault network for H4 showing the contribution to the overall displacement of individual groups of faults, introduced at locations 1- 5, within the hanging wall and footwall fault blocks of the Rangitaiki Fault. The location of the faults introduced at each location is indicated in Figure 6.3d.

6.5.3. Displacement rates

Average displacement rates for the entire fault network, the Rangitaiki Fault and the HW and FW faults are shown in Table 6.2 for different time intervals over the last 17 kyr. The average displacement rate of the network ranges from a maximum of 11.1 mm/yr between 17 ka – 13.9 ka to a minimum of 4.9 mm/yr between 13.9 ka – 11.4 ka. This is true for all parts of the network with the displacement rates of the Rangitaiki Fault and the HW and FW faults both producing maximum and minimum values for the same time intervals. The

average displacement rates and the displacement rate maps in Figure 6.5 clearly show that between 17 ka -13.9 ka the fault network was most active, including the Rangitaiki Fault as well as the HW faults and FW faults. However, the displacement rates for all the other time intervals appear to have been relatively constant with an overall average displacement rate of 6.7 mm/yr over the last 17 kyr (Table 6.2).

Table 6.2 A table of displacement rates for different time intervals over the last 17 kyr calculated from the throws each fault at each and the estimated ages of each horizon.

Time Interval	Average Displacement Rate (mm/yr)				
	Total	*Rangitaiki Fault*		*HW and FW faults*	
17 ka - Present	6.7	2.8	42.6%	3.8	57.4%
17 - 13.9 ka	11.1	4.0	36.0%	7.1	64.0%
13.9 - 11.4 ka	4.9	1.8	37.5%	3.0	62.5%
11.4 - 9 ka	6.9	2.8	41.3%	4.0	58.7%
9 ka - Present	5.6	2.7	48.4%	2.9	51.6%

The contribution of the HW and FW faults to the total displacement rate of the fault network is consistently greater than the contribution of the Rangitaiki Fault for all time intervals (Table 6.2). However, the proportion of the total average displacement rate contributed by the Rangitaiki Fault does increase from 36.0% to 48.4% through time. This suggests that the activity of the fault network has been steadily localizing onto the Rangitaiki Fault and that the HW and FW faults have proportionally become less active over the last 17 kyr. This can also be seen in the displacement rate maps, which show fairly consistent activity for the Rangitaiki Fault but steadily decreasing displacement rates on many of the individual HW and FW faults with time, in particular the FW faults of the network (Figure 6.5).

Figure 6.6 shows the displacement rate profiles of the Rangitaiki Fault and the HW and FW faults across location 1, which separates the area of localized faulting from the area of distributed faulting. Overall the total displacement rate profile is fairly consistent along strike of the fault network particularly for the longer time intervals (i.e. 17 ka and 9 ka; Figures 6.6a and 6.6e). In general, the Rangitaiki Fault decreases from SW-NE along strike producing a smooth decreasing profile for each time interval. However, the HW and FW faults displacement rate profile is more variable especially for shorter time intervals

(i.e. Figure 6.6b and 6.6c). Where there is localized faulting to the SW of location 1 all the displacement rate profiles are relatively smooth and show a constant displacement rate. However, at the transition from localized faulting to distributed faulting, location 1, there is a marked jump in the displacement rate within the HW and FW faults (Figure 6.6). This is seen across all of the time intervals and indicates that the transition is quite abrupt and persistent.

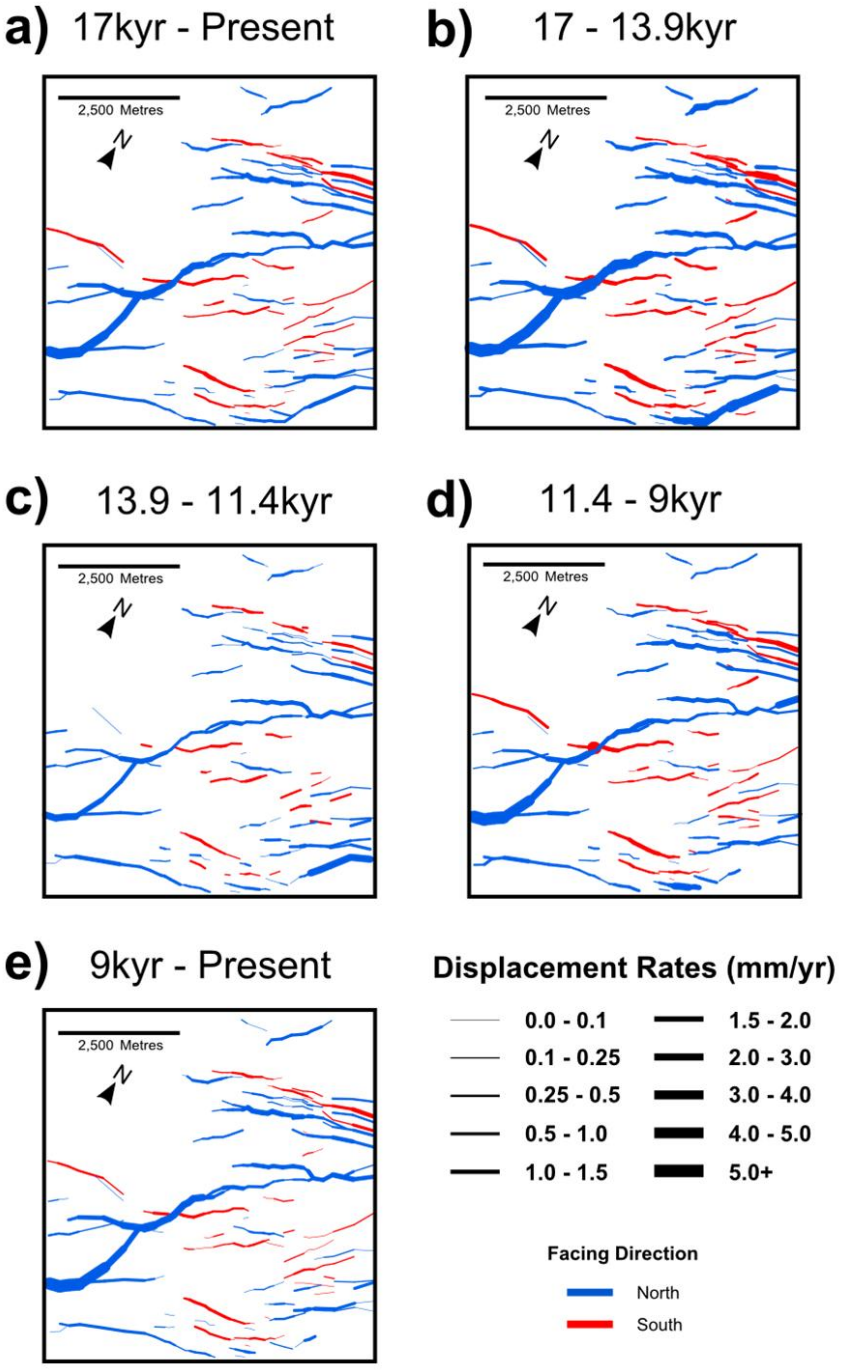

Figure 6.5 Fault maps showing the displacement rates of each fault within the fault network for different time intervals over the last 17 kyr.

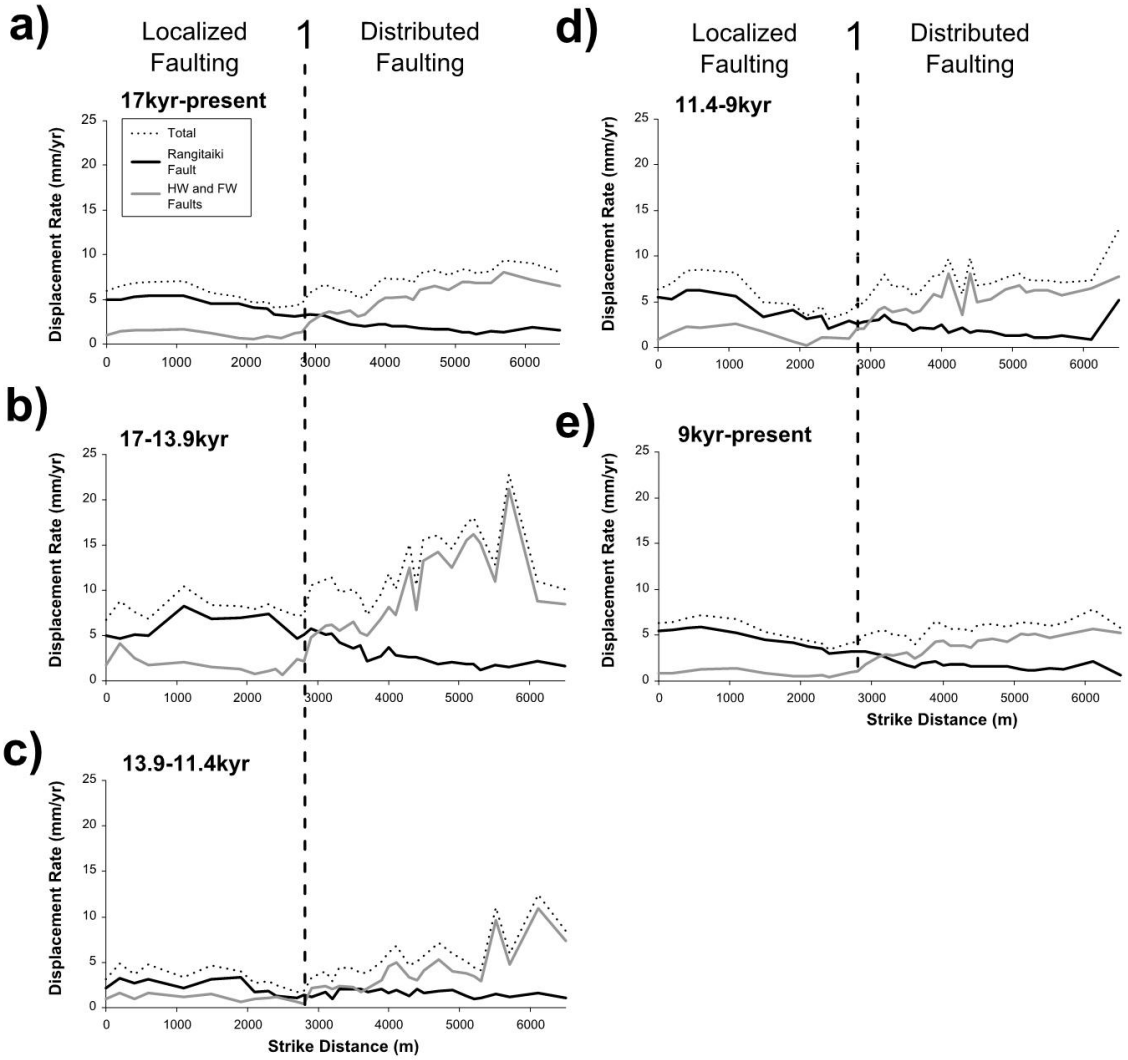

Figure 6.6 Displacement Rate variations along strike of the fault network for different time intervals, comparing the displacement rates of the Rangitaiki Fault (black) to the hanging wall and footwall faults (grey). Location 1 marks the change from localized faulting to distributed faulting.

6.5.4. Strain analysis

The overall total percentage extension of the fault network at H4 is 0.78% orientated approximately NW-SE. This was calculated by summing the individual extension values of each boomer line and then dividing by the number of lines. The overall percentage extensions of each boomer line at H4 are plotted in an along strike strain profile in Figure 6.7a. This also shows the strain profiles of the Rangitaiki Fault and the HW and FW faults. The strain profiles are similar to the cumulative displacement profiles (Figure 6.3), showing a steady decrease in strain for the Rangitaiki Fault and abrupt step like

increases in strain accommodated by the HW and FW faults. At location 1 the overall strain profile across the fault network reaches a minimum, which marks the transition from localized faulting to distributed faulting (Figure 6.7a).

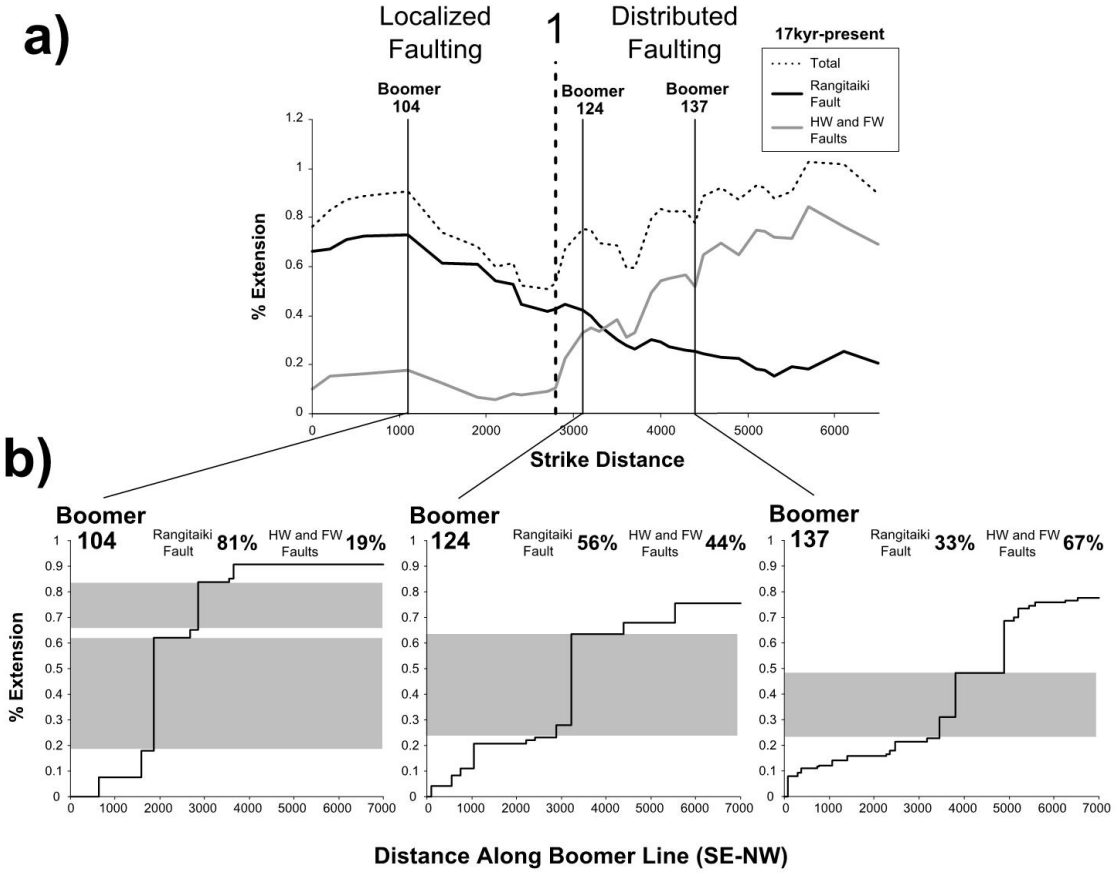

Figure 6.7 a) Strain Profile for H4 indicating the variations in the % extension of each boom line along strike of the fault network showing the strain accommodated by the Rangitaiki Fault (black) and the hanging wall and footwall faults (grey). b) Shows the contribution of each fault to the overall extension of boomer lines 104, 124 and 137 (positions are indicated in Figure 6.7a). These also show the changing proportions of strain accommodated by the Rangitaiki Fault highlighted in grey.

Figure 6.7b shows the contribution to strain by each individual fault along the boomer lines 104, 124 and 137. Boomer line 104 goes through the area of localized faulting and has very few faults which accommodate the strain. In general, two fault segments of the Rangitaiki Fault accommodate ~86% of the overall strain for boomer line 104 (Figure 6.7b). Therefore, the majority of strain is localized onto the Rangitaiki Fault within the area of localized faulting.

Boomer lines 124 and 137 are within the area of distributed faulting. These both have many more faults than boomer line 104, which all contribute to the overall strain of each boomer line. However, there are still some fault segments

Table 6.3 3D strain values of the fault network at H4. Comparing the strain distribution within the area of localized faulting and the area of distributed faulting.

	Localized Area					Distributed Area					Entire Area				
	Overall	Rangitaiki Fault	HW and FW faults			Overall	Rangitaiki Fault	HW and FW faults			Overall	Rangitaiki Fault	HW and FW faults		
			Total	FW faults	HW faults			Total	FW faults	HW faults			Total	FW faults	HW faults
% Extension	0.83	0.72	0.13	0.09	0.05	0.85	0.3	0.56	0.23	0.33	0.83	0.47	0.38	0.17	0.21
Dip/Azimuth	15/315	15/311	14/337	23/338	03/161	12/327	14/321	11/331	09/325	12/335	13/324	15/315	11/332	12/327	11/335
RF:HW/FW	**85%:15%**					**35%:65%**					**55%:45%**				

of the Rangitaiki Fault that individually accommodate more strain than the others (Figure 6.7b). Even so, the Rangitaiki Fault does not accommodate as much of the overall strain in the area of distributed faulting as it does within the area localized faulting, accommodating only 56% and 33% of the overall extension for boomer lines 124 and 137, respectively (Figure 6.7b). This shows a progressive increase in strain accommodated by the HW and FW faults within the area of distributed faulting as the strain transfers from the Rangitaiki Fault onto the surrounding structures. It also indicates that the degree of strain localization onto the Rangitaiki Fault decreases along strike of the fault network from SW-NE.

The 3D strain analysis allows us to calculate the strain for the entire study area as well the localized and distributed area using the fault trace-lengths and their dip azimuths. As the strain of the network over the last 17 kyr is quite low we only calculate strain values for H4. In general, the maximum extension of the entire fault network is 0.83% dipping at approximately 13° towards N324°E with negligible extension in the intermediate plane of deformation (Table 6.3). This is consistent with the average overall extension calculated from the 2D boomer lines. Furthermore, the ratio of strain contributed by the Rangitaiki Fault and HW and FW faults within the entire fault network is approximately equal (Table 6.3).

The values of maximum extension for the areas of localized and distributed faulting are also similar with maximum extensions of 0.83% and 0.85% indicating that the overall strain is constant along strike of the fault network. Although the overall extension values are consistent, their orientations differ slightly between the two areas with a maximum extension orientation of 15°/N315°E for the localized area and 12°/N327°E for the distributed area. These orientations are controlled by the Rangitaiki Fault in the localized area and the HW and FW faults in the distributed area (Table 6.3), indicating that the overall strain of a fault network is not always accommodated by the large fault and can vary locally along strike of the fault system. This is supported by the ratios of strain contributed by the Rangitaiki Fault and the HW and FW faults (Table 6.3). The HW and FW faults contribute ~65% of the maximum extension in the distributed area but only ~15% of the maximum extension in the localized

area. This agrees with the strain analysis from the 2D boomer profiles indicating the majority of strain is accommodated by the Rangitaiki Fault within the area of localized faulting, whereas strain is accommodated by the surrounding HW and FW faults in the area of distributed faulting.

6.6. Discussion

The results show that the amount of deformation is consistent throughout the Rangitaiki Fault network with values of cumulative displacement, displacement rate and strain remaining relatively constant along strike of the network over the last 17 kyr (Figures 6.3a, 6.6a and 6.7; Table 6.3). Furthermore, the strain analysis produced a maximum extension orientation of N324°E, which is consistent with the oblique rifting orientation of N331°E deduced by Lamarche et al. (2006), agreeing with their model of a transtensional rift system.

The amount of deformation accommodated by the different parts of the fault network varies and we argue that this is due to the progressive process of strain localization. We observe two clear domains within the fault network that behave differently and are characterized by:

a) *Localized Faulting* – deformation is accommodated by few faults with individual large faults taking up the majority of the strain i.e. >80% of the strain is localized onto the Rangitaiki Fault (Table 6.3). Within this domain there are very few faults in the hanging wall and footwall blocks of the main Rangitaiki Fault. Hence, the displacement and strain profiles for this domain reflect the profiles of the Rangitaiki Fault and are relatively smooth for each time interval (Figures 6.3, 6.6, 6.7). Overall the Rangitaiki fault contributes most of the deformation within the domain of localized faulting.

b) *Distributed Faulting* – numerous small faults contribute to the overall deformation with only ~35% of the strain localized onto the main Rangitaiki Fault. There are many faults in the hanging wall and footwall blocks of the Rangitaiki Fault and the overall displacement on the Rangitatiki Fault is much lower than the domain of localized faulting. As more faults are introduced to the network the strain and displacement

increase with a step-like profile reflecting the profile of the HW and FW faults. Overall the HW and FW faults contribute most of the deformation within the domain of distributed faulting.

The transition between these two domains shows a steady decrease in the displacement and the proportion of strain localized onto the main Rangitaiki Fault (Figure 6.7). The transition within the HW and FW faults occurs more abruptly with a jump in displacement rate and the proportion of strain increases in a series of steps (Figure 6.6 and 6.7). These occur as more faults are introduced to the network to accommodate the decrease in displacement on the Rangitaiki Fault (Figure 6.4). Overall, this indicates interaction between the two domains and the different parts of the fault network. Nixon et al. (2011) show similar interactions between domains within a fault network in north Devon (U.K.), where changes in fault polarity produce variations in the strain profile across the fault network. They show lows in the strain profile at the transition between the two domains, which is similar to the strain profile across the Rangitaiki Fault network where a low in the strain profile is seen at the transition between the area of localized faulting and distributed faulting (Figure 6.7a).

The domains of localized faulting and distributed faulting are observed at different time intervals over the last 17 kyr including intervals as small as 2-3 kyr. These time intervals only reflect a few earthquake events on each individual fault and it is known that displacement rates and accumulation on individual faults are highly variable over small time intervals (i.e. Bull et al., 2006; Mouslopoulou et al., 2009). However, the distribution of these events over many faults throughout the entire fault network appears to be ordered and preserves the overall pattern of displacement distribution across the network for all time intervals (Figure 6.3 and 6.6). This agrees with Nicol et al. (2010) who show that variability in displacement decreases with increasing fault numbers, indicating that the pattern of faulting and displacement rates of a fault population are more ordered than the individual faults within the fault population.

The decrease in strain localization onto the Rangitaiki Fault, between the two domains, can be attributed to the linkage history of the fault. Bull et al. (2006) establish the linkage behaviour of the Rangitaiki Fault in the subsurface

sediments over the last 17 kyr. We note that within the domain of localized faulting the linkage of the fault is well established both in a geometrical and kinematic sense. However, within the domain of distributed faulting the Rangitaiki Fault is well linked geometrically but not so well linked in a kinematic sense (c.f. Bull et al., 2006), indicating that linkage of the Rangitaiki Fault is less established in this domain. This indicates that the change in domain is related to the maturity and linkage evolution of the Rangitaiki Fault. Therefore, as fault linkage becomes more established the deformation associated with the fault evolves from a distributed fault network to a localized fault network. This process is still ongoing as the Rangitaiki Fault has progressively contributed more to the overall displacement rate of the fault network over the last 17 kyr by ~12% (Table 6.2).

Progressive strain localization from distributed faulting to localized faulting has been recognised in a number of fault networks at a range of scales. For example, Walsh et al. (2003) identify strain localization onto large individual large faults within a growth fault population in the inner Moray Firth, Northern North Sea. Furthermore, Soliva and Schultz (2008) show that fault populations within the Main Ethiopian Rift evolve from areas of distributed faulting within the basalt plains of the rift to localized border fault systems. This study is of particular importance as we show that these processes occur at the scale of an individual fault system, therefore, progressive strain localization occurs over a range of scales affecting the overall architecture of a rift as well as the organization of faulting around individual large magnitude faults within the rift.

6.7. Conclusions

We have investigated the organization of faulting, the accumulation of displacement and the distribution of strain around the large magnitude Rangitaiki Fault in the Whakatane Graben, NZ. We used offshore high resolution seismic reflection imagery of the post last-glacial syn-sedimentary growth deposits, dating back to ~17+/-1 ka, to pick a high quality fault population, which includes the Rangitaiki Fault and its hanging wall and footwall faults. The fault network changes in character along strike and can be

separated into two domains, which have different kinematic characteristics and different patterns of faulting but preserve the strain compatibility between the two domains. We describe these domains as an area of localized faulting to the SW and an area of distributed faulting to the NE. The area of localized faulting has:

a) Very few faults in the hanging wall and footwall blocks of the Rangitaiki Fault.

b) The majority of the strain (>80%) localized onto the main Rangitaiki Fault, which controls the orientation of maximum extension within the domain.

c) Smooth displacement and strain profiles which are similar to the main Rangitaiki Fault.

In contrast, the area of distributed faulting has:

a) Many faults in the hanging wall and footwall blocks of the Rangitaiki Fault that contribute to the overall deformation.

b) The majority of the strain (>65%) accommodated by the numerous hanging wall and footwall faults with only ~35% localized onto the Rangitaiki Fault. The hanging wall and footwall faults also influence the orientation of maximum extension.

c) Displacement and strain profiles influenced by the hanging wall and footwall faults creating increasing step-like increments as more faults are introduced to the network.

The change in character of the fault network reflects the process of progressive strain localization onto the Rangitaiki Fault and is influenced by the changing maturity and evolution of linkage along strike of the fault. The transition between the two domains produces a low in the strain profile across the fault network as strain is transferred between the Rangtaiki Fault and its hanging wall and footwall faults. This transition is marked by a steady decrease in displacement on the Rangitaiki Fault but produces an abrupt jump in the displacement rate of the hanging wall and footwall faults creating step-like increases in their cumulative displacement profiles.

The distribution of displacement within the fault network is seen for all time intervals over the last 17 kyr. This indicates that although there is much variability in the distribution of earthquake events on individual faults over such time intervals, their distribution across numerous faults throughout a fault network is still ordered and preserves a kinematic coherency.

Furthermore, faults in the hanging wall and footwall blocks have been becoming less active as activity localizes onto the Rangitaiki Fault indicating continuous progressive strain localization over the last 17 kyr. Therefore, the organization of faulting around a large magnitude fault changes as the system evolves with deformation becoming more localized.

6.8. References

Bell, R.E., McNeill, L.C., Bull, J.M., Henstock, T.J., 2008. Evolution of the offshore western Gulf of Corinth. Geological Society of America Bulletin 120, 156–178.

Biggs, J., Nissen, E., Craig, T., Jackson, J., Robinson, D.P., 2010. Breaking up the hanging wall of a rift-border fault: The 2009 Karonga earthquakes, Malawi. Geophysical Research Letters 37, 1–5.

Bull, J.M., Barnes, P.M., Lamarche, G., Sanderson, D.J., Cowie, P. a., Taylor, S.K., Dix, J.K., 2006. High-resolution record of displacement accumulation on an active normal fault: implications for models of slip accumulation during repeated earthquakes. Journal of Structural Geology 28, 1146–1166.

Cartwright, J., Trudgill, B., Mansfield, C., 1995. Fault growth by segment linkage: an explanation for scatter in maximum displacement and trace length data from the Canyonlands Grabens of SE Utah. Journal of Structural Geology 17, 1319–1326.

Childs, C., Nicol, A., Walsh, J., Watterson, J., 1996. Growth of vertically segmented normal faults. Journal of Structural Geology 18, 1389–1397.

Contreras, J., Anders, M.H., Scholz, C.H., 2000. Growth of a normal fault system: observations from the Lake Malawi basin of the east African rift. Journal of Structural Geology 22, 159–168.

Cowie, P., Underhill, J., Behn, M., Lin, J., Gill, C., 2005. Spatio-temporal evolution of strain accumulation derived from multi-scale observations of Late Jurassic rifting in the northern North Sea: A critical test of models for lithospheric extension. Earth and Planetary Science Letters 234, 401–419.

Cowie, P. A., Roberts, G.P., Bull, J.M., Visini, F., 2012. Relationships between fault geometry, slip rate variability and earthquake recurrence in extensional settings. Geophysical Journal International 189, 143–160.

Doubre, C., Peltzer, G., 2007. Fluid-controlled faulting process in the Asal Rift, Djibouti, from 8 yr of radar interferometry observations. Geology 35, 69.

Fialko, Y., 2006. Interseismic strain accumulation and the earthquake potential on the southern San Andreas fault system. Nature 441, 968–71.

Kim, Y-S., Peacock, D.C.., Sanderson, D.J., 2003. Mesoscale strike-slip faults and damage zones at Marsalforn, Gozo Island, Malta. Journal of Structural Geology 25, 793–812.

Lamarche, G., Barnes, P.M., Bull, J.M., 2006. Faulting and extension rate over the last 20,000 years in the offshore Whakatane Graben, New Zealand continental shelf. Tectonics 25, 1–24.

Lamarche, G., Bull, J., Barnes, P., 2000. Constraining fault growth rates and fault evolution in New Zealand. Eos, Transactions, AGU 81, 481–496.

Long, J.J., Imber, J., 2011. Geological controls on fault relay zone scaling. Journal of Structural Geology 33, 1790–1800.

Mansfield, C.S., Cartwright, J. A., 1996. High resolution fault displacement mapping from three-dimensional seismic data: evidence for dip linkage during fault growth. Journal of Structural Geology 18, 249–263.

Meyer, V., Nicol, A., Childs, C., Walsh, J.J., Watterson, J., 2002. Progressive localisation of strain during the evolution of a normal fault population. Journal of Structural Geology 24, 1215–1231.

Mouslopoulou, V., Walsh, J.J., Nicol, A., 2009. Fault displacement rates on a range of timescales. Earth and Planetary Science Letters 278, 186–197.

Nairn, I., Beanland, S., 1989. Geological setting of the 1987 Edgecumbe earthquake, New Zealand. New Zealand Journal of Geology and Geophysics 32, 1–13.

Nicol, A., Walsh, J.J., Villamor, P., Seebeck, H., Berryman, K.R., 2010. Normal fault interactions, paleoearthquakes and growth in an active rift. Journal of Structural Geology 32, 1101–1113.

Nixon, C.W., Sanderson, D.J., Bull, J.M., 2011. Deformation within a strike-slip fault network at Westward Ho!, Devon U.K.: Domino vs conjugate faulting. Journal of Structural Geology 33, 833–843.

Nixon, C.W., Sanderson, D.J., Bull, J.M., 2012. Analysis of a strike-slip fault network using high resolution multibeam bathymetry, offshore NW Devon U.K. Tectonophysics 541-543, 69–80.

Nobile, A., Pagli, C., Keir, D., Wright, T.J., Ayele, A., Ruch, J., Acocella, V., 2012. Dike-fault interaction during the 2004 Dallol intrusion at the northern edge of the Erta Ale Ridge (Afar, Ethiopia). Geophysical Research Letters 39, 2–7.

Peacock, D.C.., 2002. Propagation, interaction and linkage in normal fault systems. Earth-Science Reviews 58, 121–142.

Peacock, D.C.P., Sanderson, D.J., 1993. Estimating strain from fault slip using a line sample. Journal of Structural Geology 15, 1513–1516.

Quigley, M., Van Dissen, R., Litchfield, N., Villamor, P., Duffy, B., Barrell, D., Furlong, K., Stahl, T., Bilderback, E., Noble, D., 2012. Surface rupture during the 2010 Mw 7.1 Darfield (Canterbury) earthquake: Implications for fault rupture dynamics and seismic-hazard analysis. Geology 40, 55–58.

Soliva, R., Schultz, R. A., 2008. Distributed and localized faulting in extensional settings: Insight from the North Ethiopian Rift–Afar transition area. Tectonics 27, TC2003.

Taylor, S.K., 2003. A long timescale high-resolution fault activity history of the Whakatane Graben, New Zealand. PhD Thesis, University of Southampton, UK.

Taylor, S.K., Bull, J.M., Lamarche, G., Barnes, P.M., 2004. Normal fault growth and linkage in the Whakatane Graben, New Zealand, during the last 1.3 Myr. Journal of Geophysical Research 109, B02408.

Walcott, R.I., 1978. Present tectonics and Late Cenozoic evolution of New Zealand. Geophysical Journal of the Royal Astronomical Society 52, 137–164.

Walsh, J.J., Childs, C., Imber, J., Manzocchi, T., Watterson, J., Nell, P. a. R., 2003. Strain localisation and population changes during fault system growth within the Inner Moray Firth, Northern North Sea. Journal of Structural Geology 25, 307–315.

Wright, I., 1990. Late Quaternary faulting of the offshore Whakatane Graben, Taupo Volcanic Zone, New Zealand. New Zealand Journal of Geology and Geophysics 33, 245–256.

Wright, T.J., Parsons, B., England, P.C., Fielding, E.J., 2004. InSAR observations of low slip rates on the major faults of western Tibet. Science (New York, N.Y.) 305, 236–9.

7. Analysis of a normal fault network with multiple fault sets at Milne Point, Alaska

Casey W. Nixon, David J. Sanderson, Stephen Dee, Jonathan M. Bull, Robert Humphreys

7.1. Abstract

A normal fault network from onshore Milne Point, Alaska is constrained from 3-D seismic reflection data. The network comprises a NNE-trending fault set and a WNW-trending fault set, which are analyzed at two stratigraphic horizons: the Kuparuk River Sandstone and the Sag River Sandstone. The analysis shows that the NNE-trending fault set is consistently developed in both horizons with similar densities and sizes. However, the WNW-trending fault set show variation in faulting both spatially and with depth. The WNW-trending fault set is influenced by a similarly orientated underlying structural grain. This influence is characterized by increases in displacement on several faults, strain localization, clockwise rotation of faults and an increase in linkage maturity.

NNE-trending faults post-date the WNW-trending faults causing fault reactivation and abutting interactions with displacement transferring onto the WNW-trending faults. The development of abutting faults is characterized from displacement profiles which can be divided into two main groups: early stage abutting faults with displacement minima at both the isolated and abutting tips; and developed abutting faults with a displacement maximum at the abutting tip.

The connectivity and compartmentalization of the network is also assessed using a topological analysis. This analyses the number, size and extent of compartments at each horizon. We show that modelling fault tips may identify new large compartments or show that previously identified large compartments are actually made up of smaller compartments.

7.2. Introduction

The major aim of this Chapter is to analyse the deformation of a normal fault network formed by more than one generation of faults. Many fault networks consist of more than one fault set, and these can either be conjugate fault sets (e.g. Zhao and Johnson, 1991; Nicol et al., 1995; Ferrill et al., 2009; Nixon et al., 2011) that formed in the same stress system, or multiple fault sets that form from the overprinting of two or more stress systems (Davatzes et al., 2003; Bailey et al., 2005). The latter can form new faults with different orientations and/or cause reactivation of pre-existing faults (e.g. Kim et al., 2001), which can also have a strong influence on the development of later fault sets (e.g. Segall and Pollard, 1983; Bailey et al., 2005). Hence, complex cross-cutting relationships and interactions can form between fault sets.

Understanding the relationships between different fault sets within a network is important as interconnected faults can provide pathways for fluids, allowing the migration and entrapment of hydrocarbons (Aydin, 2000), or they can act as fluid barriers compartmentalizing reservoirs (Bouvier et al., 1989; Leveille et al., 1997). Reservoir compartmentalization is a major uncertainty in the qualitative and quantitative assessment of a reservoir in the hydrocarbon industry (Jolley et al., 2010). Hence, there has been much work on the identification and assessment of compartmentalization (e.g. Bouvier et al., 1989; Gauthier and Lake, 1993; Smalley et al., 1994; Smalley and Hale., 1996; Permanyer et al., 2002; Manzocchi et al., 2010; Fokker et al., 2012; Go et al., 2012). As there is great potential for fault networks with more than one fault set to form compartments, it is important that such fault networks are analysed and characterized.

In this study we analyse a 3D seismic reflection data set that images a normal fault network at Milne Point, Alaska. Data from two horizon surfaces are used to investigate the geometry, kinematics, displacement distribution and fault interactions within the fault network. We aim to characterize the behaviour of the fault network and the relationships between different fault sets, investigating any variations both across the region and with depth. Furthermore, a topological analysis is applied to investigate the connectivity and compartmentalization within the network.

7.3. Geological setting

Milne Point is located on the northern edge of the Alaska North Slope (ANS) approximately 450 km north of the Arctic Circle and 40 km NW of Prudhoe Bay (Figure 7.1). The region is of particular interest due to the presence of numerous major gas and oil fields including the Prudhoe Bay, Milne Point and Kuparuk River oil fields (Carman and Hardwick, 1983; Collett, 1993; Bird, 1999; Boswell et al., 2011). Large quantities of oil have been produced, since the discovery of the first field in 1968, from complex structural/stratigraphic traps within Permian to Tertiary sand/carbonate reservoirs at production depths >2000 m (Boswell et al., 2011).

The principal structural features of the region (Figure 7.1) are the Barrow Arch just offshore to the north, and the Colville Basin and Brooks Range to the south (Carmen and Hardwick, 1983; Bird, 1999; Boswell et al., 2011). The Barrow Arch is an E-W trending rift shoulder and the Brooks Range is a fold and thrust mountain belt related to continent-continent collision (Bird, 1999). Together these structural highs provided source material that infilled the Colville (foreland) Basin, which has an E-W axial trend (Figure 7.1) (Carmen and Hardwick, 1983; Bird, 1999).

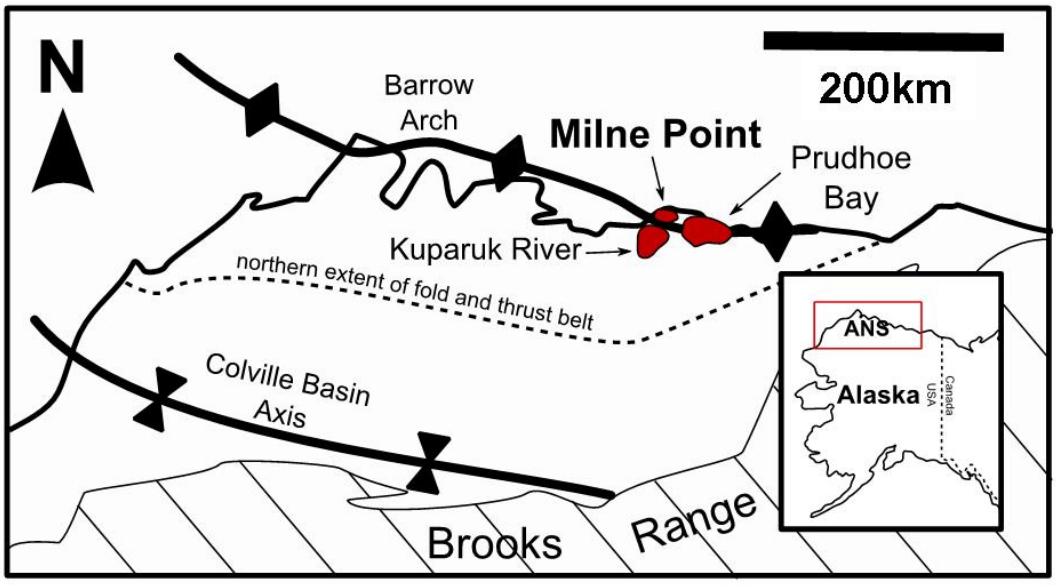

Figure 7.1 Location map showing the key structural features of the Alaska North Slope (ANS) and the position of Milne Point.

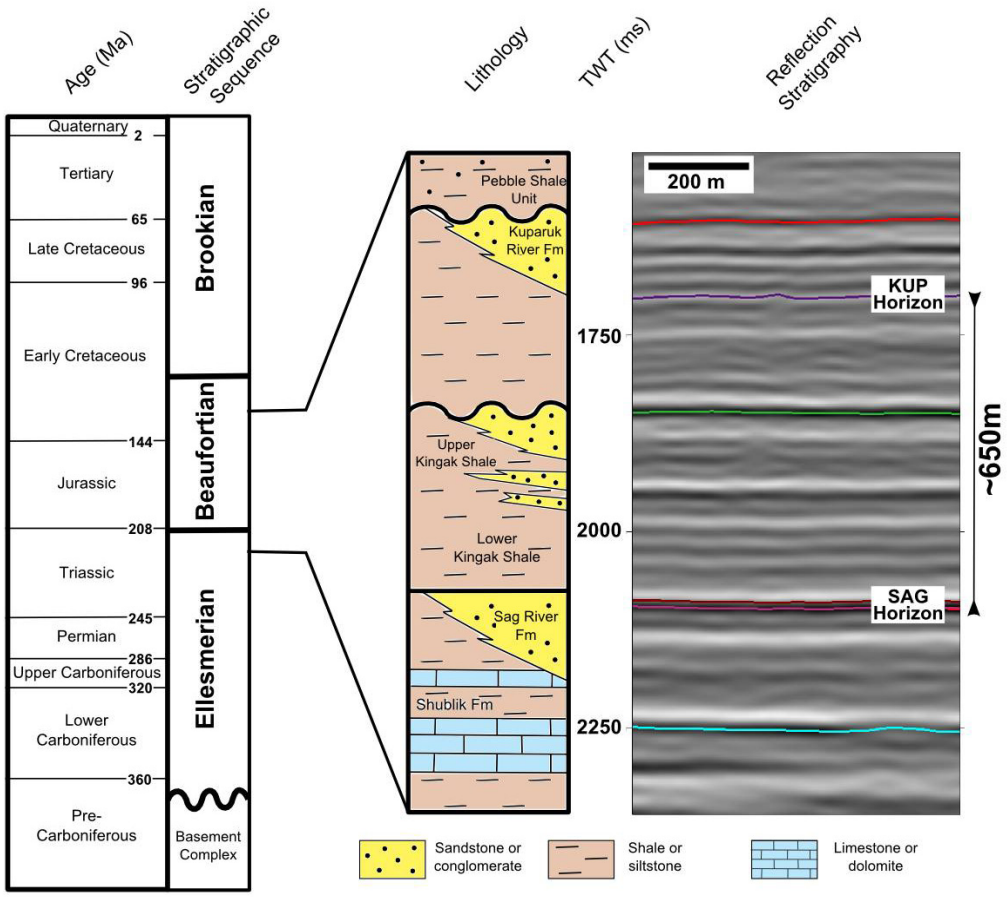

Figure 7.2 Summary of the ages of the stratigraphic sequences and the formation lithologies that were seismically imaged. The KUP and SAG horizons are also indicated.

The sedimentary rocks of the ANS consist of south-dipping passive continental margin deposits of Upper Palaeozoic and Mesozoic age, overlain by north-dipping foreland basin deposits in the Mesozoic and Cenozoic (Collett, 1993; Bird, 1999). These deposits have been divided into three main tectono-stratigraphic sequences (Figure 7.2) that are described in detail by Bird (1999). The earlier passive-margin deposits are termed the Ellesmerian sequence. These consist of clastic and carbonate strata of middle Devonian to Triassic age, that onlap onto a stable south-facing continental margin (Collett, 1993; Bird, 1999). The Ellesmerian was followed by the Beaufortian sequence which was deposited during a period of continental rifting in the Jurassic and Early Cretaceous (Bird, 1999). The rifting is characterized by a change in fault pattern from south-dipping normal faulting in the Jurassic followed by north-dipping normal faulting in the early Cretaceous (Hubbard et al., 1987). It was this rift that formed the palaeo-high of the Barrow Arch. Then during the

Cretaceous and Tertiary, continent-continent collision caused uplift to the south, i.e. the Brooks Range, and subsidence to the north producing the Colville Basin and the foreland basin deposits called the Brookian sequence (Carmen and Hardwick, 1983; Collett 1993; Bird, 1999). The Brookian sequence is extensively faulted in the Milne Point region by NNE-striking normal faults in units as young as the Eocene Sagavanirktok Formation (Boswell et al., 2011; Lorenson et al., 2011). These also reach down to the top of the Kuparuk River oil field (Masterson et al., 2001).

The fault network studied in this paper affects the Triassic to Early Cretaceous rocks (Figures 7.2 and 7.3). We concentrate on analysing the network at two stratigraphic horizons within the 3D seismic data. The youngest horizon is within the Beaufortian sequence and is called the Kuparuk River Sandstone (KUP horizon; Figure 7.2). This is an early Cretaceous sandstone that hosts several oil reservoirs in northern Alaska, including Kuparuk River and Milne Point fields (Bird, 1999). The oldest horizon is the Sag River Sandstone (SAG horizon; Figure 7.2), which is within the Ellesmerian sequence, and is a Late Triassic sandstone unit that is also a reservoir in the Prudhoe Bay area and contains gas in the Kavik field SE of Prudhoe Bay (Bird, 1999). The fault network cuts both of these reservoir horizons, hence it is vital to understand the behaviour and potential compartmentalization of such a network.

7.4. Methods

7.4.1. Data acquisition and interpretation

The 3D seismic reflection data was acquired using Vibroseis in early 2008. It covers an onshore area at Milne Point of ~200 km^2 (Figure 7.1), and is 120 fold containing frequencies between 6 and 96 Hz. The 3D volume comprises 1238 inlines bearing N045°E and 897 cross-lines bearing N135°E with a spacing of 16.8 m (Figure 7.3). Interval velocities of 3050 ms^{-1} and 4100 ms^{-1} were calculated for the KUP horizon and the SAG horizon, respectively, using True Vertical Depth Subsea (TVDSS) and Two-Way-Time (TWT) values taken from geophysical wire log well data.

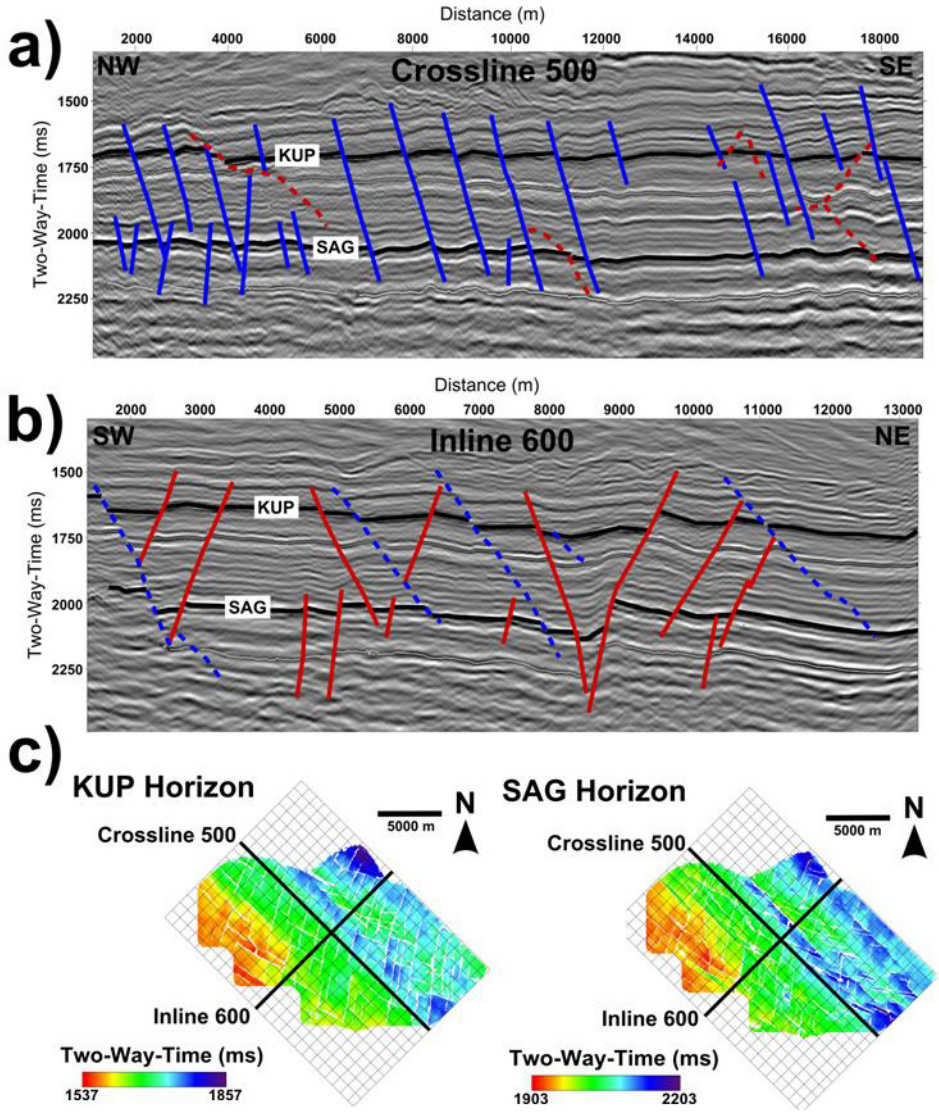

Figure 7.3 Seismic reflection images of a) a NW-SE trending crossline and b) a NE-SW trending inline. Red represents the WNW-trending fault set which were picked on the inlines and blue represents the NNE-trending fault set which were picked on the crosslines. Dashed lines are the faults that were not picked on the inline or crossline but have been projected onto the seismic section. c) is a location map showing the orientation of the inlines and crosslines.

The fault network was interpreted by employees of BP for a sequence of sedimentary rocks, ~650 m thick at a depth >2000 m, from just above the KUP horizon to just below the SAG horizon (Figure 7.3). Faults were identified and picked on every tenth inline section (N045°E) and cross-line section (N135°E) from offsets of multiple key seismic reflectors. We further checked the fault and horizon interpretations in TrapTester, a seismic interpretation and seismic modelling software (Figure 7.3). In general, the seismic data imaged faults with >10 m displacement. Within TrapTester an interconnected 3D fault model was

produced, which involved identifying fault intersections that were validated using the raw horizon data for multiple horizons and coherency time slices.

Hanging wall and footwall cut-offs of the KUP and SAG horizons were projected from raw horizon data onto the modelled fault surfaces. To correct for local effects, such as fault drag and noise around fault surfaces, the raw horizon data that was within 75 m of each fault was trimmed and a 100 m wide patch of horizon data was used to calculate and project each horizon surface onto the fault surface. The interval velocities and the TWT of each hanging wall and footwall cut-off were then used to measure numerous fault surface attributes (such as displacement, throw, heave, dip, azimuth and strike) at 100 m intervals along the plan view length of each interpreted fault surface.

7.4.2. Network analysis

The measured fault attributes were extracted from TrapTester as point data with associated *x* and *y* co-ordinates. The point data were imported into ArcGIS and fault traces were digitized to produce fault maps for both the KUP and SAG horizons. Each fault trace was segmented by the point data, and average throws and segment azimuths were calculated allowing the network to be displayed by fault trend and fault throw (cf. Appendix). The fault maps combined with length-weighted rose diagrams, fault length vs fault throw plots and fault throw profiles were used to investigate the geometry, kinematics and interactions within the fault network. In addition, 3-D strain was calculated, assuming dip-slip for each horizon, and using the fault orientation and dip separation to construct the Lagrangian strain tensor, as described by Peacock and Sanderson (1993) and Nixon et al. (2011). These calculations were made using an Excel-based tool - Dip-slip - developed for BP by Professor David Sanderson.

The topological analysis of the fault network follows the methodology developed in Chapter 4, which involves analysing the number and proportion of different nodes and branches between nodes. Nodes can be isolated fault tips (I-nodes) or connecting nodes between faults such as intersections, abutments or splays (X-nodes and Y-nodes). Branches are defined by the number of connecting nodes at each end. A branch can either be an isolated branch (I-I branch) with

no connecting nodes; a dangling end (I-C branch) of a cluster with one connecting node; or the backbone (C-C branch) of a cluster with two connecting nodes. In this study we also use the number and proportion of each node type to calculate parameters related to the connectivity of the fault network. These include the connecting node frequency, which is the number of connecting nodes per square km (N_C/km^2), and the number of connections per line ($N_{C/L}$) and per branch ($N_{C/B}$). See Chapter 4 for full description and derivation of topological parameters. The topological analysis is developed further in order to assess the compartmentalization of the network.

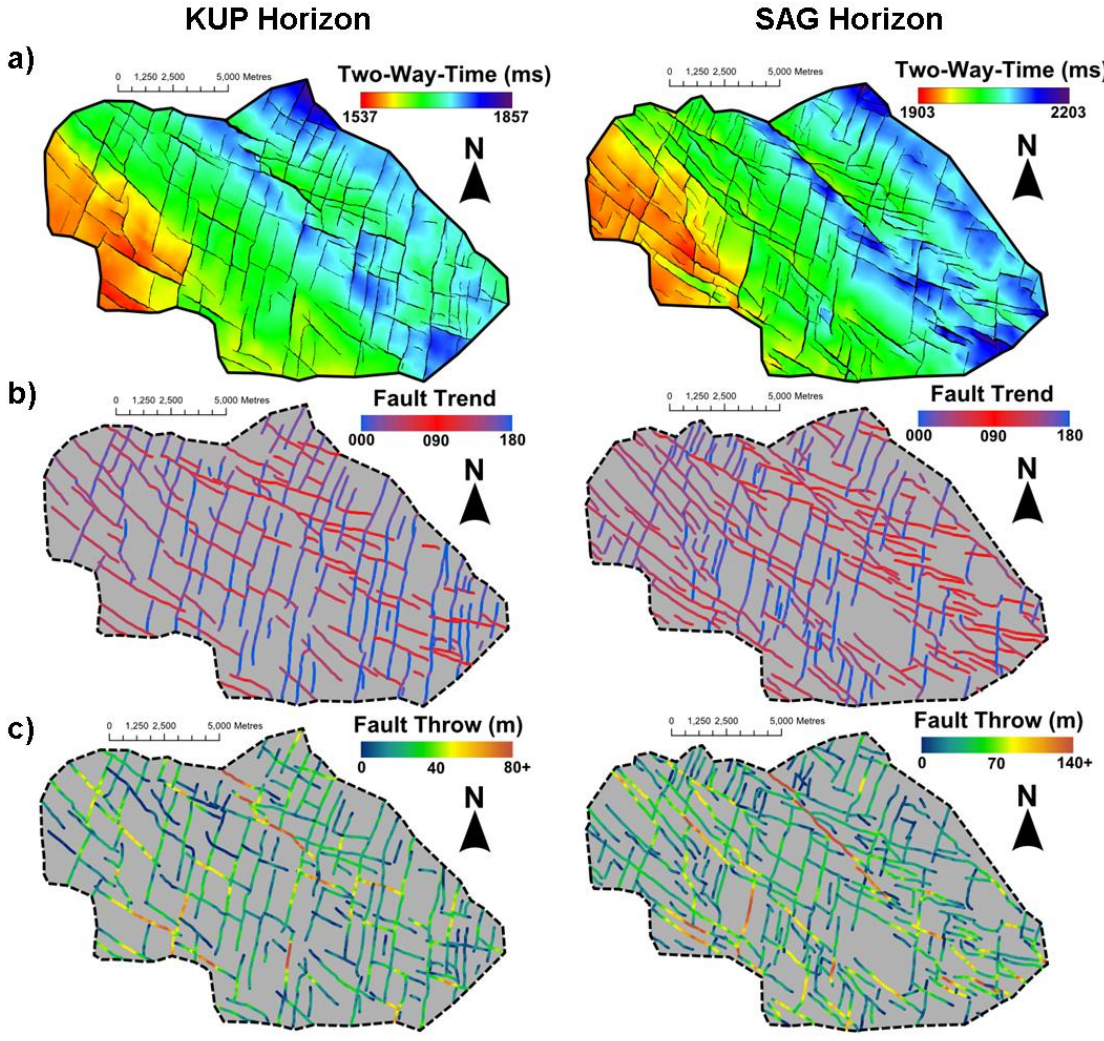

Figure 7.4 Fault maps of the KUP horizon on the left and the SAG horizon on the right: a) Surface horizon maps showing the topography of the horizons; b) Fault map colour-coded by azimuth with red generally representing WNW-faults and blue generally representing NNE-faults; c) Fault map colour-coded by throw with blue and orange representing low and high throw values, respectively.

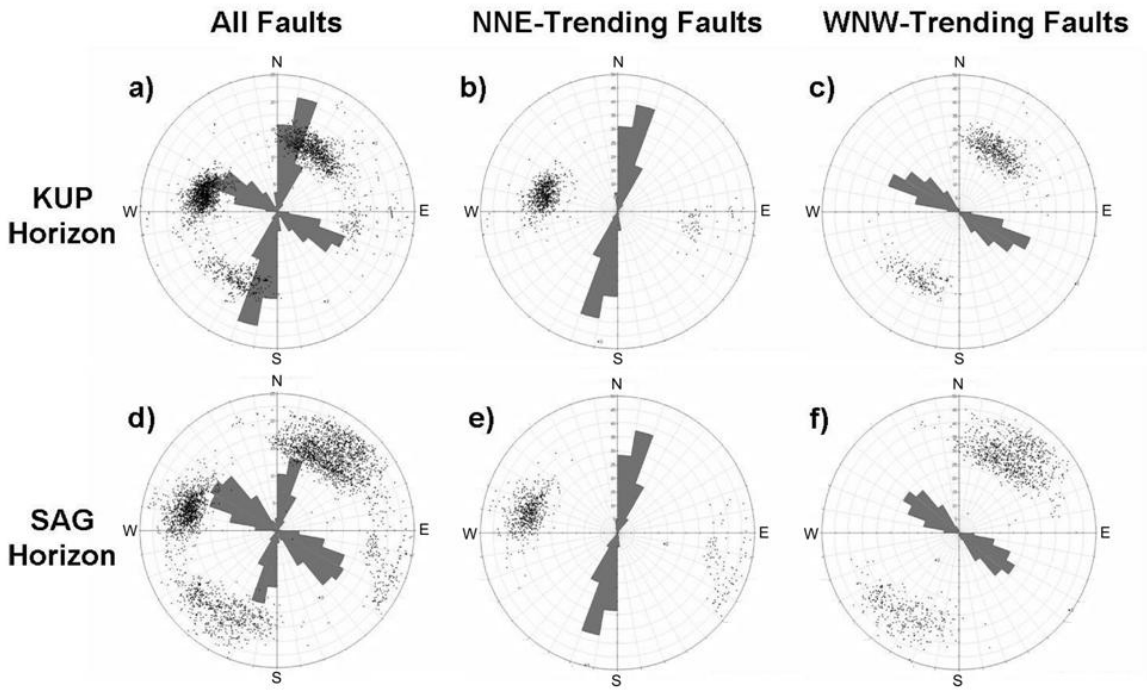

Figure 7.5 Length-weighted rose diagrams and an equal angle stereographic projection of poles to fault segments for each fault set in the KUP horizon (top) and SAG horizon (bottom).

7.5. Fault network characteristics

7.5.1. General structural trends and relationships

The study area has an underlying structural grain trending NW-SE which forms broad-scale graben and horst structures on both horizons (Figure 7.4a). These are particularly well defined in the deeper SAG horizon and coincide with an overall deepening to the ENE of ~490 m in the KUP horizon and ~615 m in the SAG horizon. The fault network overprints this structural grain and has two sets of normal faults – a NNE-trending set and a WNW-trending set (Figures 7.4b and 7.5).

The NNE-trending faults are regularly spaced (1-2 km) and most face SE (Figures 7.3a and 7.5) with constant dips of ~50°-60°. They displace both the KUP and SAG horizons by similar amounts (Figure 7.3a and 7.6a), therefore these are not growth faults and are post-depositional, as indicated by the constant thickness of stratigraphy across each fault (Figure 7.6a). The majority of the faults in the WNW-trending fault set dip to the SW (Figures 7.3b and 7.5).

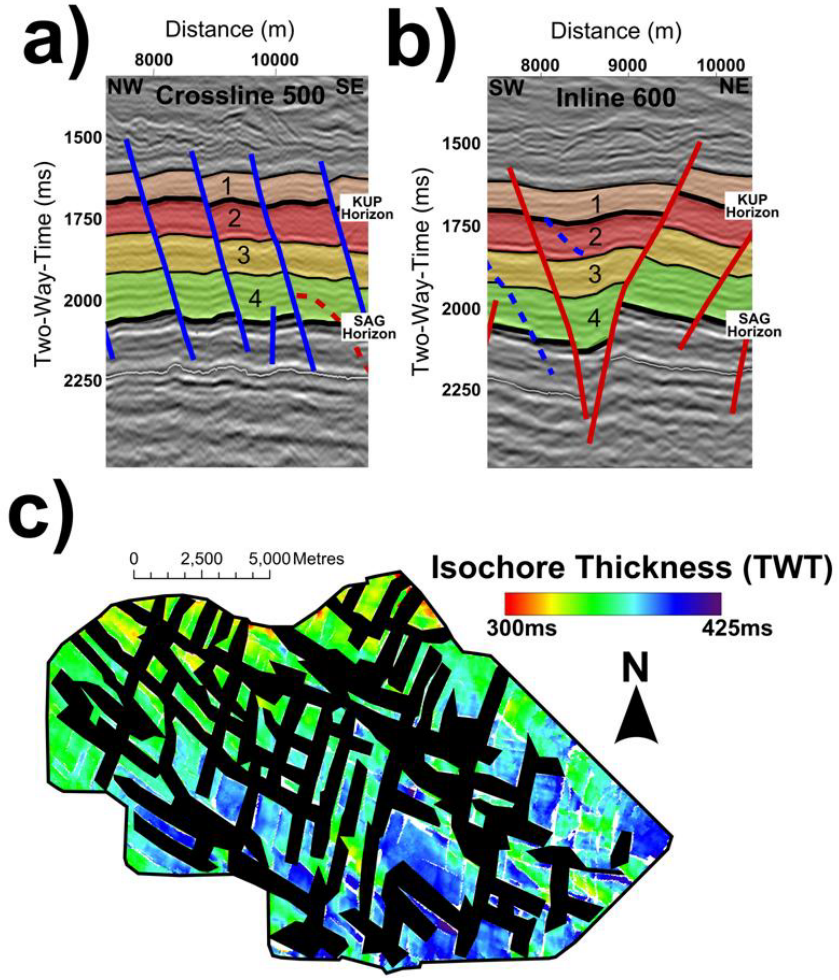

Figure 7.6 Interpreted seismic sections showing the stratigraphic thickness in relation to a) the NNE-trending faults and b) the WNW-trending faults. c) An isochore map showing the variation in stratigraphic thickness between the KUP and SAG horizon. The black patches cover the areas that have been tectonically thinned by through going faults.

Unlike the NNE-trending faults these are not regularly spaced and many of the larger faults steepen with depth from ~40°-50° to ~70°-80° (Figures 7.3b and 7.6b). Furthermore, the WNW-trending faults often displace the SAG horizon more than the KUP horizon (Figure 7.3b and 7.6b) and, hence, have a small amount of growth associated with them (i.e. stratigraphic sequence 4; Figure 7.6b).

Overall the stratigraphic thickness between the KUP and SAG horizons increases from a minimum of ~580 m in the north to a maximum of ~760 m in the south of the study area and is relatively independent of both fault sets (Figure 7.6c). However, the presence of some syn-rift sedimentation associated with the WNW-trending faults indicates that they pre-date the NNE-trending faults. As many of the WNW-trending faults are south-dipping it is

likely that they formed during the Jurassic rifting event (Hubbard et al., 1987), whereas the NNE-trending faults are likely to be related to the Tertiary faults that deform the overlying Brookian sequence (Masterson et al., 2001; Boswell et al., 2011).

7.5.2. Organization of faulting and displacement distribution

Many of the large WNW-trending faults are aligned with the underlying NW-SE structural grain and other smaller faults rotate into these structures (Figure 7.4c). This is more obvious in the deeper SAG horizon where faults from the WNW-trending fault set bound many of the graben structures (Figure 7.4a). Furthermore, the trend of the WNW-trending faults is rotated clockwise by ~10° in the SAG horizon, which can be seen clearly in the length-weighted rose diagrams (Figure 7.5c and 7.5f).

Table 7.1 Fault trace-length and throw statistics.

	Trace-length (km)	Density (km/km^2)	Proportion (%)	Max Throw (m)	Average Max Throw (m)
KUP horizon					
Total	317	1.67	-	138	43
NNE	170	0.89	54	103	41
WNW	147	0.77	46	138	45
SAG horizon					
Total	384	2.01	-	332	83
NNE	140	0.73	36	157	63
WNW	244	1.28	64	332	93

The WNW-trending faults also become more pervasive with depth, increasing in dip (Figures 7.6b) and density from 0.77 km^{-1} to 1.28 km^{-1} between the KUP and SAG horizons, respectively (Table 7.1). Whereas the NNE-trending faults have similar fault density values for each horizon (i.e. 0.89 km^{-1} at the KUP horizon and 0.73 km^{-1} at the SAG horizon; Table 7.1). As a result the KUP horizon has approximately equal proportions of NNE-trending and WNW-trending faults, whereas the SAG horizon has an increased proportion of WNW-trending faults (~64%; Table 7.1).

The largest faults in the network trend WNW with maximum throws of up to 138 m in the KUP horizon and 332 m in the SAG horizon (Table 7.1; Figure 7.4c).

However, both fault sets have similar length vs throw distributions (Figure 7.7). There is an increase in the maximum throw of faults from the shallower KUP horizon to the deeper SAG horizon (Figure 7.7a). This increase is seen mainly in the WNW-trending faults (Figure 7.7c) as indicated by the average max throw values for each fault set (Table 7.1).

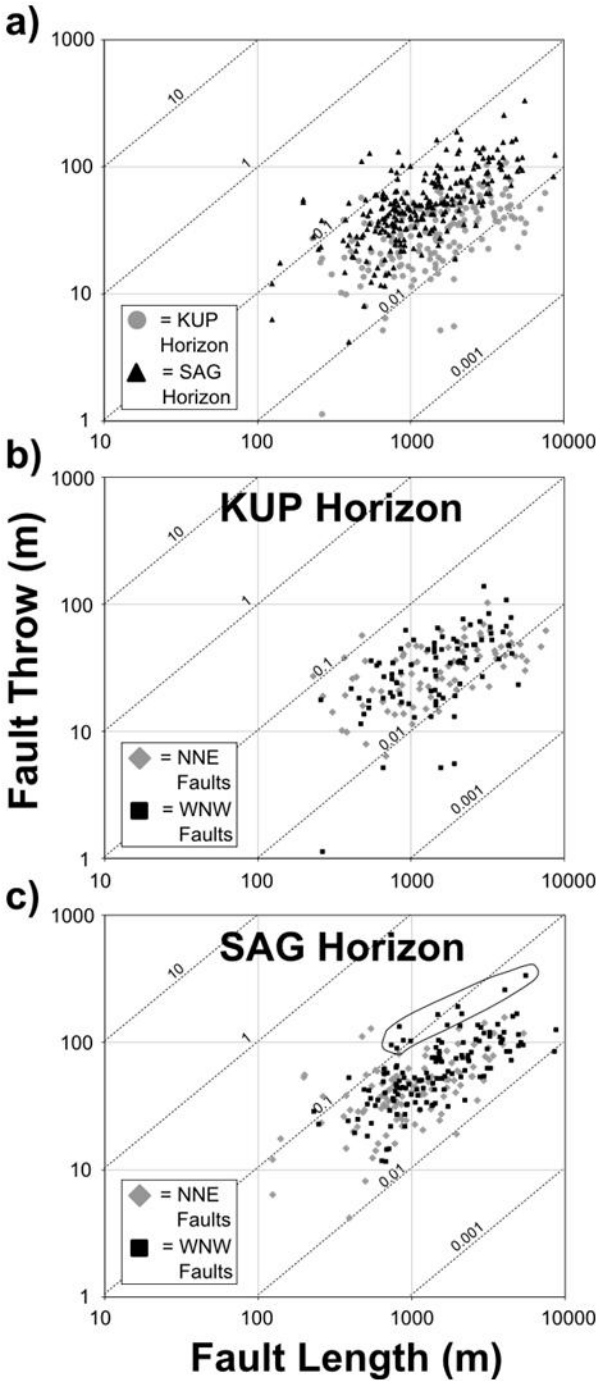

Figure 7.7 Logarithmic plots of fault length vs maximum throw for a) all the faults; b) the KUP Horizon and c) the SAG horizon. Note the significantly greater throws for some WNW-trending faults in the SAG horizon.

Overall the NNE-trending faults are evenly distributed both spatially and with depth showing similar orientations, fault densities and throws for each horizon. In contrast, the WNW-trending faults increase in both density and size with depth. The increase in displacement for the WNW-trending faults could be due to fault growth as indicated by the presence of small syn-sedimentary deposits, however these are too small to account for the total increase in displacement. As the orientation of the WNW-trending faults is affected by the underlying structural grain there is an obvious influence of deeper pre-existing structures. This also agrees with the steepening of the faults with depth.

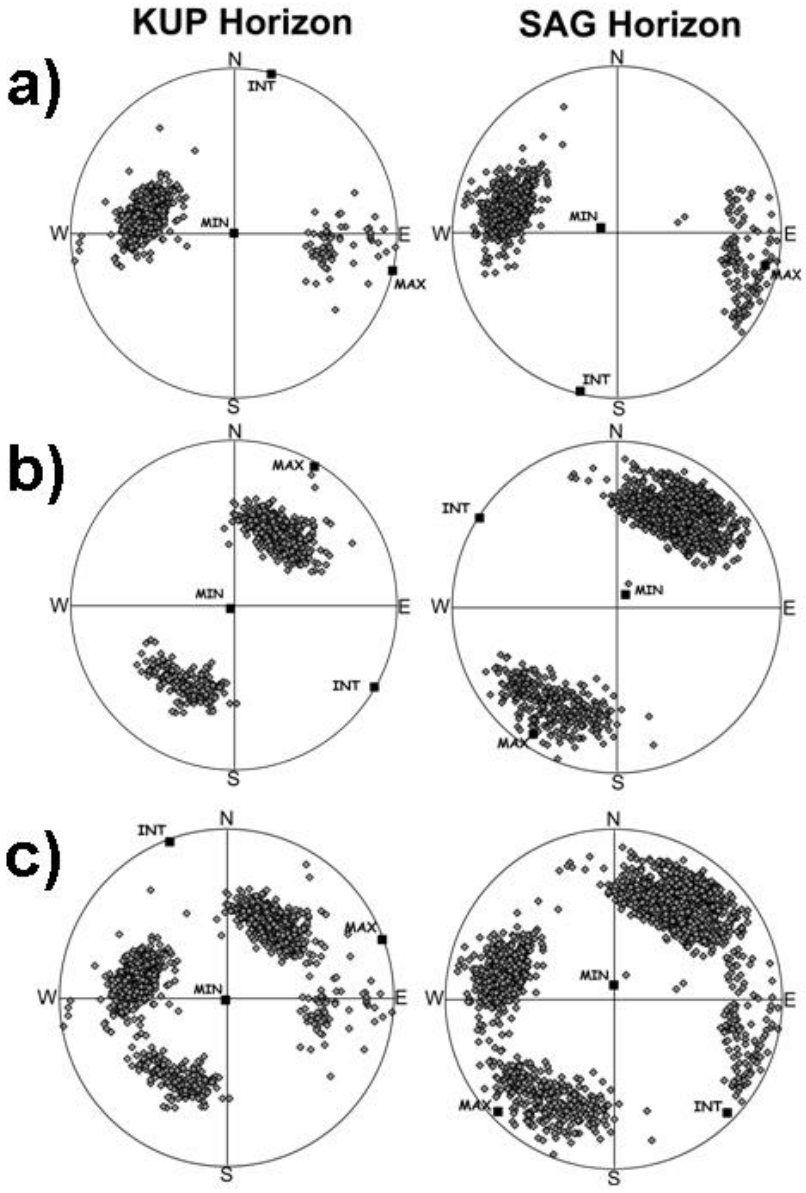

Figure 7.8 Equal angle stereographic projection of poles to fault segments showing the principal strain orientations for: a) the NNE-trending faults; b) the WNW-trending faults; and c) all faults.

7.5.3. Strain analysis

The strain accommodated on each individual fault set shows negligible amounts of extension for the intermediate strain component producing a pure plane strain perpendicular to the trend of each fault set (Figure 7.8a and 7.8b; Table 7.2). The NNE-trending faults accommodate similar amounts of extension in each horizon, whereas there is an increase in the maximum extension accommodated by the WNW-trending faults in the SAG horizon (Table 7.2). Hence, in the SAG horizon the majority of the strain (69%) is accommodated by the WNW-trending faults.

The overall strain accommodated by the faults indicates subhorizontal extension and subvertical shortening at each horizon (Figure 7.8; Table 7.2). The maximum extension accommodated by the fault network increases from 2.4% orientated at N070°E for the KUP horizon to 3.7% orientated at N225°E for the SAG horizon (Table 7.2), which is accommodated entirely by the WNW-trending faults. As the fault sets are orthogonal there is also an intermediate strain component with an extension of ~1.5% orientated at N340°E and N135°E for the KUP and SAG horizons, respectively. In the KUP horizon the total strain is accommodated equally between the two fault sets, as indicated by the minimum extension percentages (Table 7.2), resulting in the maximum extension direction of the network bisecting the angle of intersection between the two fault sets (ENE-WSW; Figure 7.8c). However, in the SAG horizon there is a 25° anticlockwise rotation of the networks maximum extension direction to ~NE-SW (Table 7.2; Figure 7.8c), as more of the total extension is weighted towards the WNW-trending fault set.

In general, the strain analysis shows an increase in strain with depth due to more strain being localized onto the WNW-trending faults in the deeper SAG horizon. This localization of strain onto the WNW-trending faults further suggests that these faults are being influenced by the pre-existing structures that form the NW-SE underlying structural grain. The contrast between the behaviour of the two fault sets indicates that they are independent fault sets as only the WNW-trending faults appear to interact with the underlying structural grain.

Table 7.2 3-Dimensional strain values and orientations for the KUP and SAG horizons.

	Maximum		Intermediate		Minimum		Proportion
	Extension %	Orientation	Extension %	Orientation	Extension %	Orientation	
KUP horizon							
Total	2.4	01/070	1.4	01/340	-3.8	88/209	-
NNE	1.9	00/103	0	00/013	-1.9	90/200	50%
WNW	1.8	02/030	0.1	00/120	-1.9	88/218	50%
SAG horizon							
Total	3.7	04/225	1.5	05/135	-5.2	84/358	-
NNE	1.6	08/103	0	00/193	-1.6	82/284	31%
WNW	3.4	08/213	0.2	01/303	-3.6	82/037	69%

7.6. Fault interactions

7.6.1. Isolated faults, abutments and splays

Faults can be divided into isolated, abutting and splaying faults. In general, abutments and cross-cutting faults involve faults from different fault sets whereas splays faults are from the same fault set. Nixon et al. (2011) describe

these interactions for strike-slip faults in plan view, which have comparable geometries to normal faults in cross-section. Here we describe these interactions for normal faults in plan view.

7.6.1.1. *Isolated faults*

There are very few isolated faults within the fault network at Milne Point, and these are mostly small faults with lengths ranging from approximately 400-1700 m accumulating maximum throws of <50 m. Throw profiles of the isolated faults can be divided into three main groups: Unrestricted, single tip restricted and double tip restricted (Figure 7.9) (cf. Nicol et al., 1996; Manighetti et al., 2001; Soliva and Benedicto, 2005).

The examples in Figure 7.9a are symmetrical profiles with the maximum throw located near the centre of the fault. These either match that of an ideal elastic profile, as modelled for fractures in a homogenous material by Pollard and Segall (1987), or a symmetrical cone shaped profile, as described by Muraoka and Kamata (1983) for faults that form in incompetent layers. Such profiles have been shown to be characteristic of faults with unrestricted tips (cf. Nicol et al., 1996, 2010; Manighetti et al., 2001) and are the smallest isolated faults within the network as indicated by their average maximum throw and average length (Figure 7.9a).

Other profiles are asymmetrical with the maximum throw located closer to one of the fault tips producing a tip with a steep throw-length gradient (Figure 7.9b). These profiles match the single tip and half restricted fault displacement profiles described in Manighetti et al. (2001). These are not caused by fault abutments but either by lithological barriers (such as changes in competency) or a nearby interacting fault that restricts the propagation rate of a fault tip indicating kinematic interaction between faults (Peacock and Sanderson, 1996; Schlagenhauf et al., 2008; Nicol et al., 2010).

The majority of isolated faults at Milne Point produce a symmetrical profile with a flat top and steep gradients at each fault tip (Figure 7.9c). Such a shape in fault displacement profiles has been described in numerous studies (Muraoka and Kamata, 1983; Peacock and Sanderson, 1991; Manighetti et al., 2001; Nicol et al., 2010). Muraoka and Kamata (1983) describe these as a mesa-

shaped profile for faults that form with tips that terminate in strain absorbing incompetent stratigraphic layering. Hence, these are double tip restricted fault profiles and have the largest average maximum throw and average length values of the isolated faults.

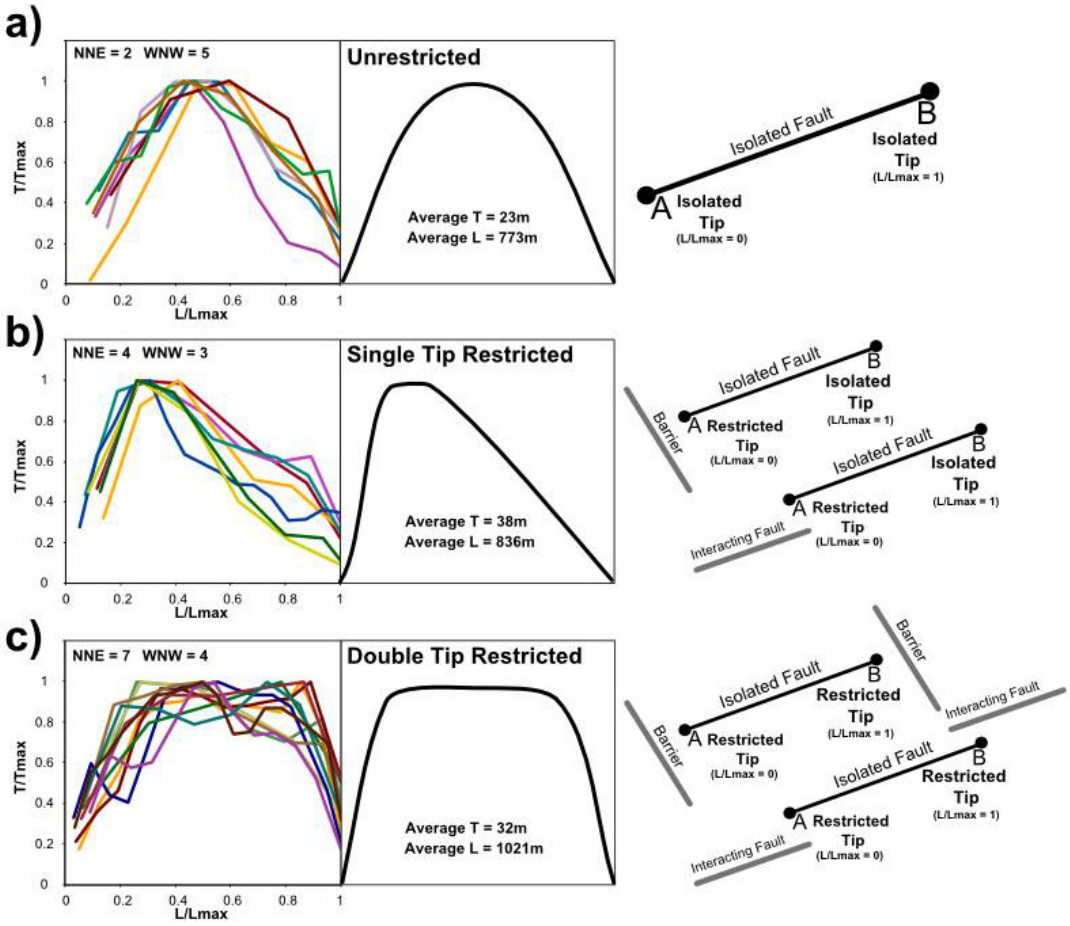

Figure 7.9 Normalized fault profiles for isolated faults from both the KUP and SAG horizons with length/maximum length (L/Lmax) along the x-axis vs throw/maximum throw (T/Tmax) on the y-axis. a) Isolated faults with unrestricted tips; b) isolated faults with a single tip restricted; c) isolated faults with both tips restricted. The graphs on the right hand side are cartoon examples of each profile.

7.6.1.2. *Abutting faults*

When a fault network has two or more fault sets, the tip of one fault often abuts and terminates against another, producing a Y- or T-shaped intersection (Figure 7.10). When a fault abuts another fault it becomes pinned and can only propagate away from its abutted tip. .Manighetti et al. (2001) describe these faults as 'single tip' restricted or 'half tip' restricted, however, we consider abutting faults to be separate from faults with restricted tips. This is based on

the fact that an abutting tip is actually pinned and cannot propagate any further, whereas a restricted fault tip can still propagate at low propagation rates.

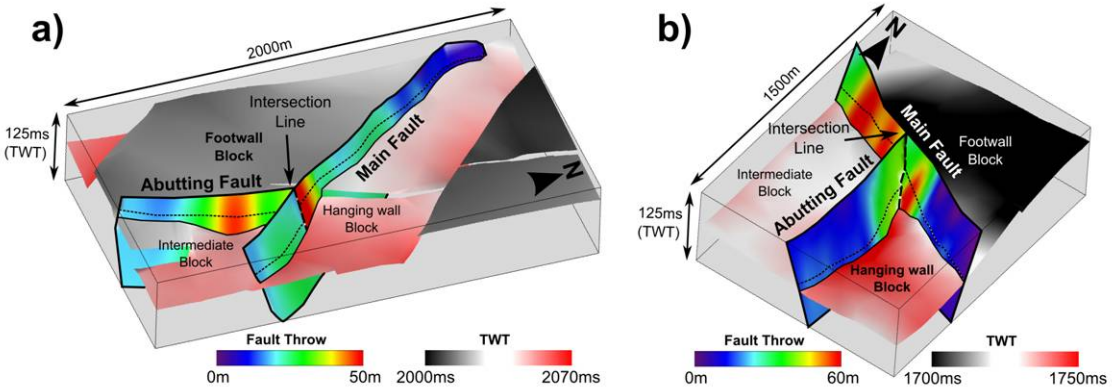

Figure 7.10 3D diagrams of fault planes that form abutting interactions: a) an example of an abutting fault that shares a footwall block with the main fault at the SAG horizon; b) an example of an abutting fault that shares a hanging wall block with the main fault at the KUP horizon. Throws are contoured onto each fault plane showing displacement transfer from the abutting fault to the main fault.

There are two geometrical relationships that abutting faults form with the earlier abutted fault (Figure 7.10). They can either form in the footwall block (Figure 7.10a) or the hanging wall block (Figure 7.10b) of the earlier fault and will therefore either share a footwall or hanging wall block, respectively. Abutting faults also have the possibility of interacting and transferring displacement onto the earlier fault, thus allowing displacement to build up at the abutting tip (e.g. Maerten, 2000; Maerten et al., 2001). This is accommodated by local reactivation of the earlier abutted fault and can cause local displacement variations adjacent to the intersection line (Figure 7.10). In general, the earlier fault will locally increase in displacement where it shares a fault block with the abutting fault (Figure 7.10).

The abutting faults can either be single tip abutting (Figure 7.11) or double tip abutting (Figure 7.11). Within the fault network at Milne Point these are small faults with lengths <2000 m. In general, single tip abutting faults can be divided into two groups, which are shown in Figure 7.11. Group 1 have minimum throws at their isolated and abutting tips suggesting that these faults abutted at a late stage of their development. This is supported by their average fault lengths, which are longer than other profile types for single tip abutting faults

(Figure 7.11). Therefore, profile types 1A and 1B are abutting faults that have preserved their isolated fault throw profiles for unrestricted and single tip restricted faults, respectively (Figure 7.11a and 7.11b).

Group 2 have shorter average lengths than Group 1 with maximum throws at their abutting tips, indicating that the faults have grown in size whilst being pinned by their abutments, thus interacting with the earlier fault. Profile type 2A is thought to represent a fault at an intermediate stage of development as it still inherits parts of a previous isolated fault profile (Figure 7.11c). However, types 2B and 2C are abutting faults that have grown and propagated whilst abutting another fault and have a restricted tip (flat top; Figure 7.11d) and unrestricted tip (linear; Figure 7.11e), respectively.

Double tip abutting faults also display two groups of fault throw profile (Figure 7.12). Group 1 preserves the throw profile of an isolated fault with both abutting

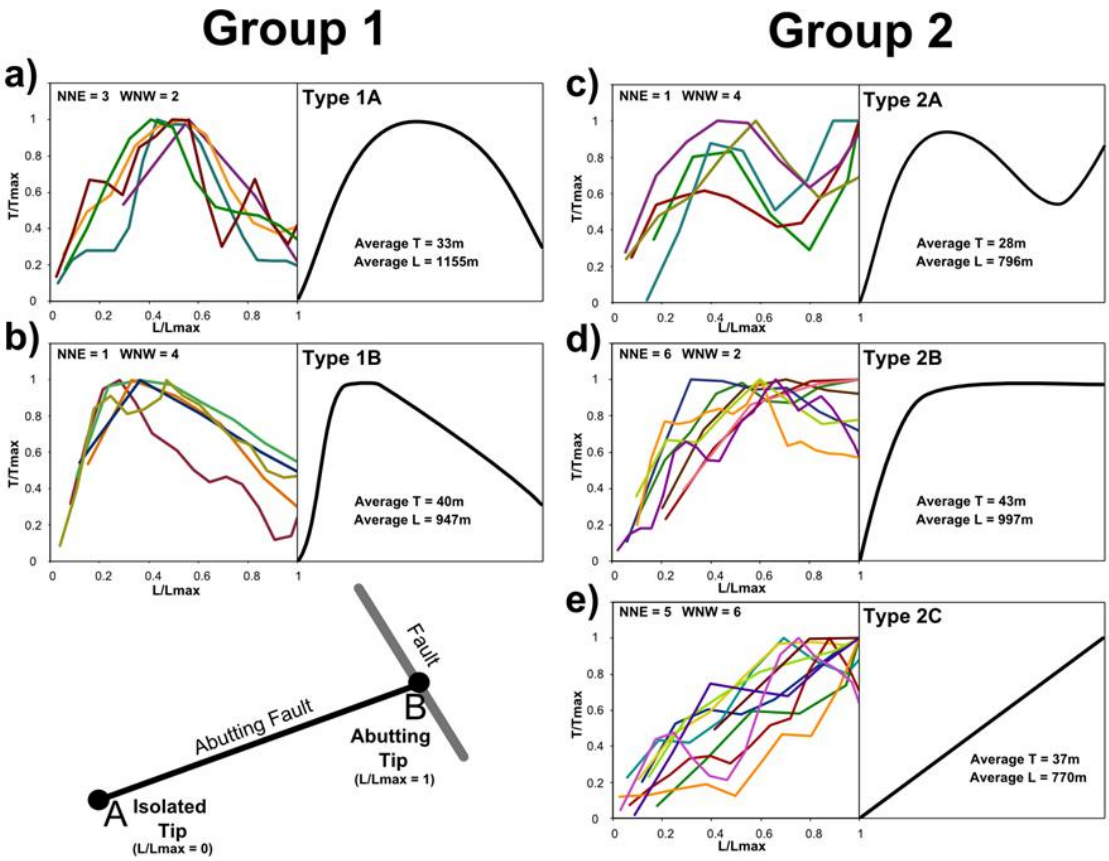

Figure 7.11 Normalized fault profiles of length/maximum length (L/Lmax) against throw/maximum throw (T/Tmax) for single tip abutting faults taken from both the KUP and SAG horizons with no other intersections with other faults. 5 profile types are identified and divided into two groups. The right hand graph for each profile type is a cartoon example. See text for discussion.

tips recording minimum throws (Figure 7.12a and 7.12b). This suggests that these faults abutted at late stages of the faults development. Group 2 represents a slightly more developed double tip abutting fault that has accumulated throws whilst being pinned at each abutting tip. Hence, these either show a maximum throw at one abutting tip (Figures 7.12c) or at both fault tips (Figure 7.12d). The asymmetry of the throw profiles could be due to the abutting tip with the largest throw value having abutted first.

In general, the profiles of abutting faults can indicate the relative time of abutment during the faults growth and development. Group 1 abutting fault profiles preserve an isolated fault profile and have minimum throws at abutting tips indicate that abutment occurred at a late stage of the faults development. Whereas Group 2 abutting faults have accumulated throws at the abutting tips indicating that the fault was still growing in size after it abutted another fault.

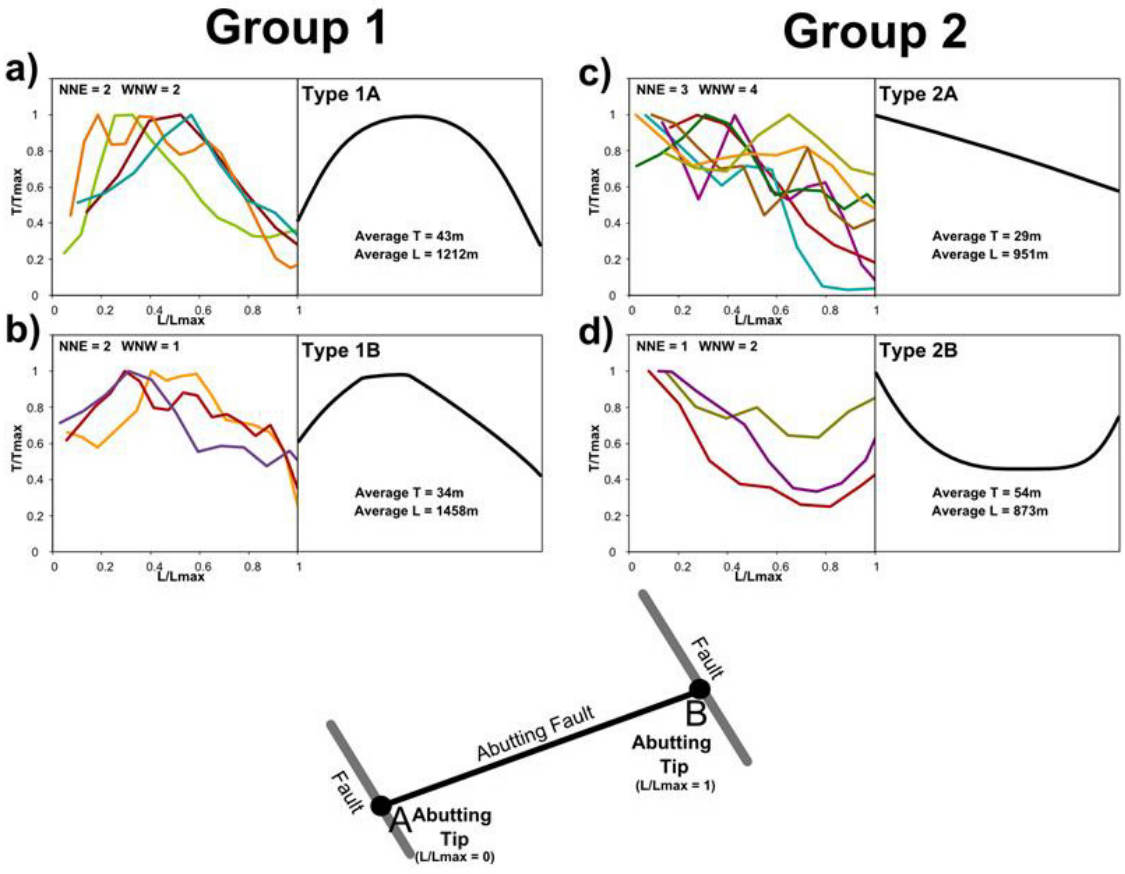

Figure 7.12 Normalized fault profiles of length/maximum length (L/Lmax) against throw/maximum throw (T/Tmax) for double tip abutting faults taken from both the KUP and SAG horizons with no other intersections with other faults. 4 profile types are identified and divided into two groups. The right hand graph for each profile type is a cartoon example. See text for discussion.

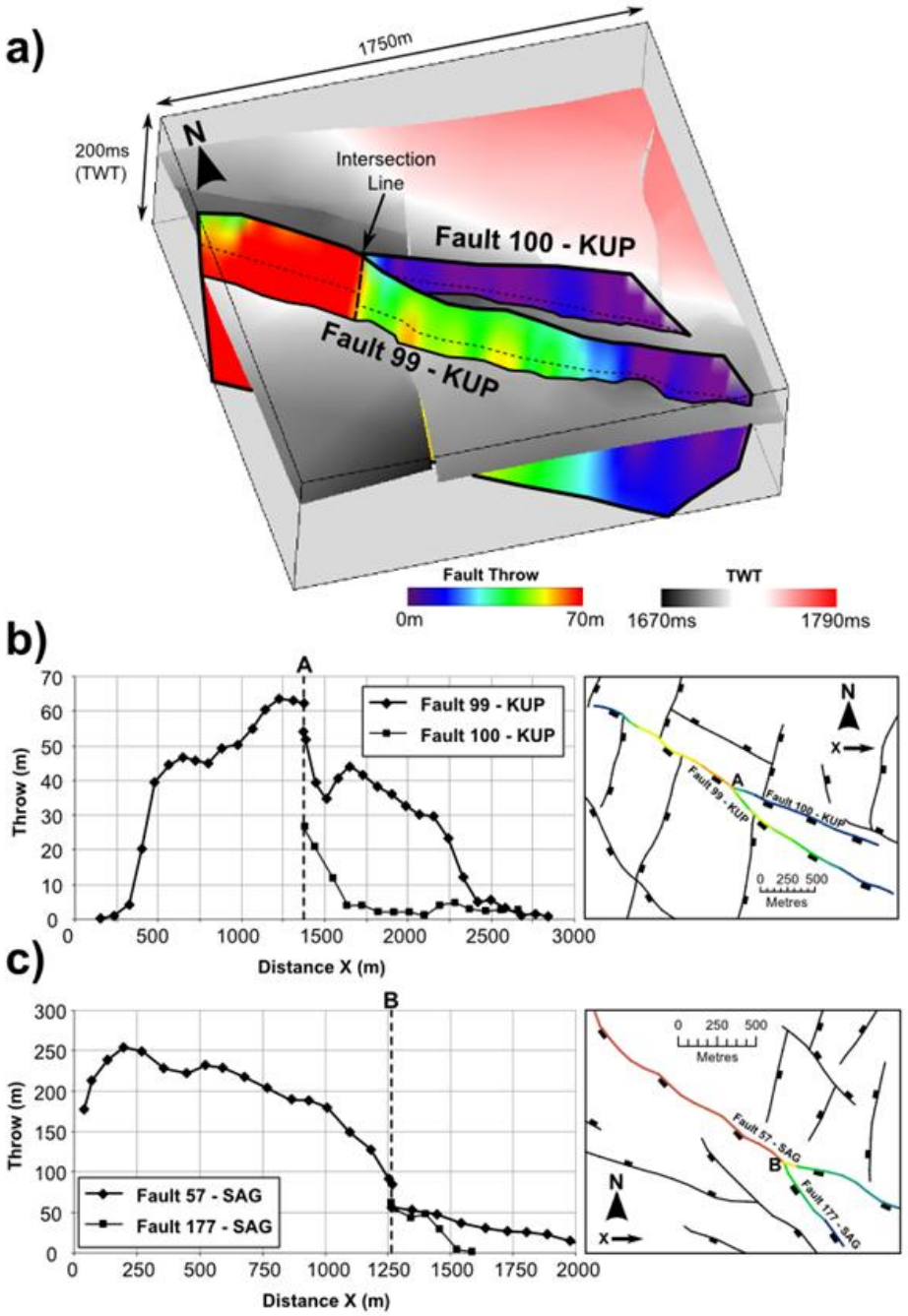

Figure 7.13 The fault profiles of a main fault and a splay fault showing their variations in throw along distance X, which increases to the east. a) 3D diagram of the fault planes geometries; b) an example from the KUP horizon; and c) an example from the SAG horizon. To the right of each graph are plan view fault maps of the interacting faults.

7.6.1.3. *Splays*

Fault splays often occur near the tips of faults. The smaller splay fault has a fault plane that is obliquely orientated to the larger main fault plane and has a displacement maximum along the line of intersection (Figure 7.13a). The displacement distribution on the fault plane of the main fault shows an abrupt

drop in displacement at the line of intersection with the splay fault (Figure 7.13a).

Fault throw profiles indicate that the decrease in displacement is accommodated by the splay fault. For example, Figure 7.13 shows the throw profiles of two main faults (Fault 99-KUP and Fault 57-SAG) which have corresponding splays (fault 100-KUP and Fault 177-SAG) at intersection points A and B. Both of the main faults show a step like decrease in throw at the intersection with the splay faults in the direction of the acute angle of intersection. This step down in throw approximately matches the throw of the respective splay faults near the point of intersection (Figure 7.13). After the point of intersection both the main fault and splay fault steadily decrease in throw before reaching null values at their isolated fault tips.

Nixon et al. (2011) describe fault splays in strike-slip faults as synthetic interactions that accommodate a decrease in displacement on a larger main fault. The fault splays identified in the normal fault network at Milne Point accommodate similar decreases in fault throw (Figure 7.13) and have the same motion sense (i.e. down thrown on the same side) as their corresponding main faults. Hence, they can also be called synthetic interactions.

7.6.1.4. *Individual faults*

The isolated faults and abutting faults within the network have short lengths (<2000 m), however, many of the faults within the network have longer fault lengths (up to 9000 m) and accumulate much larger throws (Figures 7.4 and 7.7). These longer faults are often segmented by cross-cutting faults or have numerous faults that abut them (Figure 7.4). Even though these long faults have many intersecting faults their throw profiles are often symmetrical with maximum throws near the centre of the faults length and minimum throws at their tips (Figure 7.14), which is similar to throw profiles of isolated faults.

As each segment has a displacement profile that is consistent with its adjacent segment these can be considered as coherent structures and not isolated fault segments that have aligned and linked (cf. Walsh et al., 2003). Therefore, despite interactions with other fault sets the larger and longer faults still act as individual isolated faults. This can be identified for both fault sets and indicates

that the faults in both sets originally developed as individual faults rather than simultaneously.

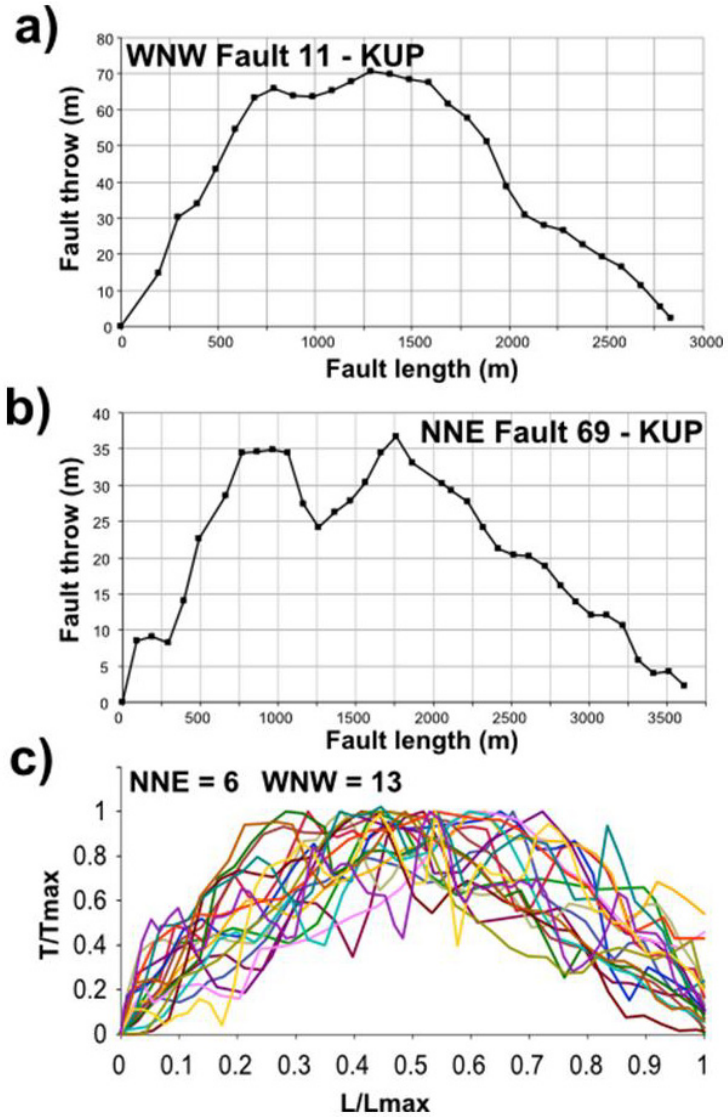

Figure 7.14 Fault throw profiles of long individual faults (>2000m length) which have intersecting and abutting faults for: a) an individual WNW-trending fault; b) an individual NNE-trending fault and c) normalized throw profiles of numerous long individual faults within the network. Examples are taken from both the KUP and SAG horizons. Note the similarity to isolated fault throw-length profiles.

7.6.2. Fault segments linked at depth

The WNW-trending faults are influenced by the underlying structural grain of the area. This affects the largest faults within the network, which are more developed in the SAG horizon and orientated NW-SE matching the underlying structural grain. Figure 7.15 shows the throw profiles for a group of four large WNW-trending faults (Faults i, ii, iii and iv) at the KUP and SAG horizons. All of these faults down throw to the SW and include smaller splay faults and relay

breach faults. In plan view only faults ii and iii are geometrically linked and these share relay ramps with fault i to the NW and fault iv to the SE (Figure 7.15). This suggests that these are interacting fault segments at different stages of linkage.

7.6.2.1. *SAG Horizon*

All of the faults have much larger throws in the deeper SAG horizon and fault iii (orange) is the largest fault, with a maximum throw of 325 m (Figure 7.15a), and the longest fault-trace (~4000 m). Fault iii shares relay ramps, which are ~250 m wide, with faults i (navy blue) and iv (turquoise) and all three faults are aligned with the NW-SE structural grain. The three faults are acting as interacting fault segments: Fault i has a splay fault at intersection point A that almost breaches the relay ramp with fault iii; whereas fault iv has an asymmetric throw profile that has a very steep throw gradient at its NW tip, indicating interaction with fault iii. Fault ii (pink) is connected to fault iii at point B but is independent of the linked system and is WNW-trending instead like the splay fault (Figure 7.15a).

7.6.2.2. *KUP Horizon*

In the shallower KUP horizon all of the long fault traces (faults i-iv) are WNW-trending indicating an anticlockwise rotation from their position in the SAG horizon. Furthermore, the width of the relays ramps between each fault has increased to ~750 m. Fault i (navy blue) is the largest fault with up to 128 m throw and it does not show any interaction with surrounding faults. Fault iv (turquoise) has an isolated fault profile that is symmetrical, therefore it is not interacting with fault iii (orange) like it does in the SAG horizon. Only faults ii (pink) and iii (orange) show any interaction and are linked by a relay breach between points D and E. Fault ii (pink) also has a very asymmetrical profile with a maximum throw near its western tip indicating a kinematic interaction (Figure 7.15b). The relay breach (black) and the splay fault (grey) are aligned with the NW-SE structural grain and are remnants of the fault pattern in the SAG horizon. They produce step like decreases in the throw profile of fault iii (orange) at intersection points D and E (Figure 7.15b), which matches the splay faults described in Figure 7.13.

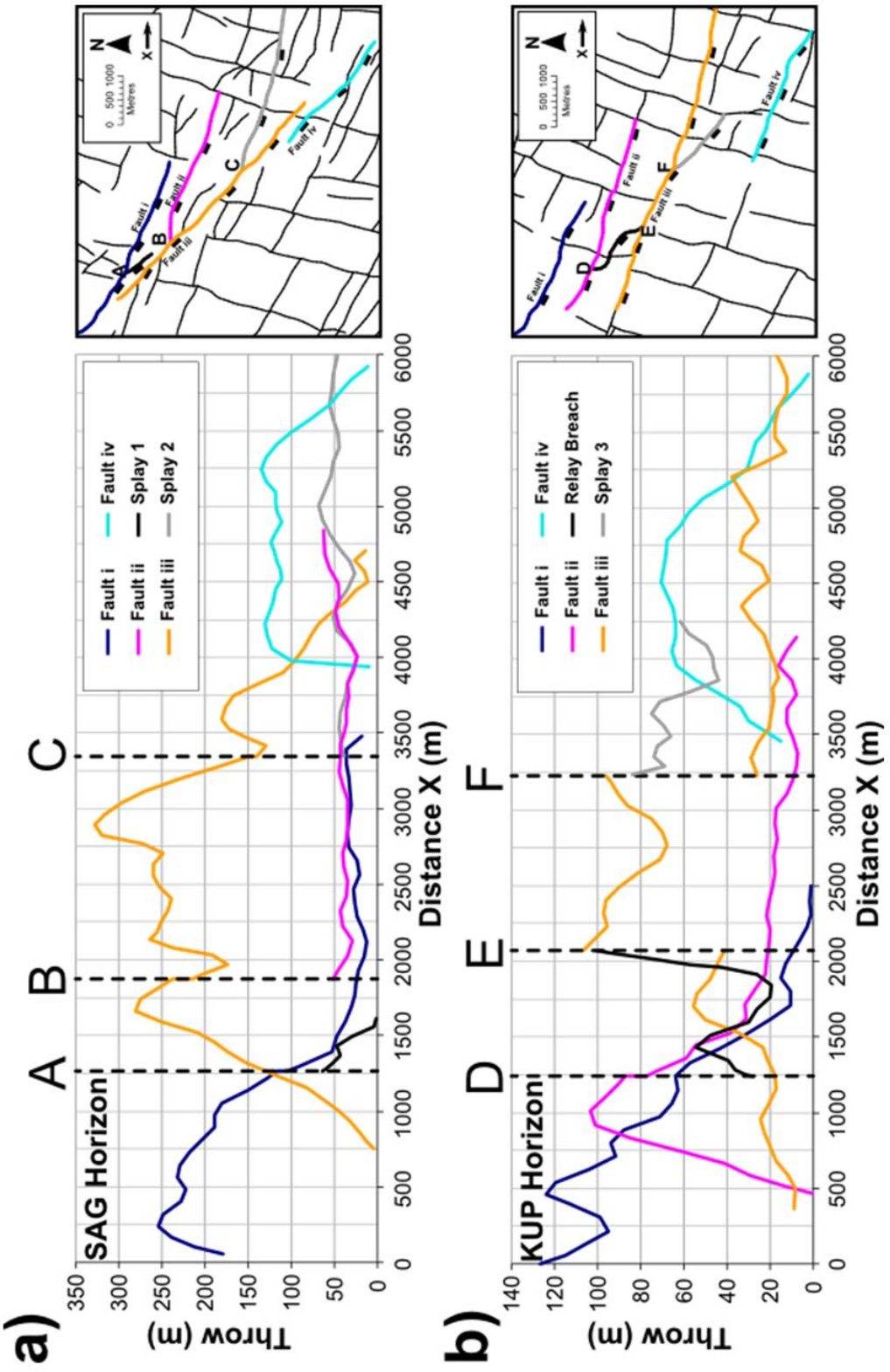

Figure 7.15 Fault throw profiles from a) the SAG horizon and b) the KUP horizon of four large WNW-trending faults (Faults i, ii, iii and iv) that share relay ramps and interact with each other with some associated splay faults. The plots show variations in throw for each fault along distance X, which increases to the east, indicating an increase in interaction, linkage and a clockwise rotation with depth. To the right are plan view maps of the interacting faults.

Overall the example in Figure 7.15 shows that the large WNW-trending faults are better linked at depth as the width of relay zones decreases and more of the faults interact in the SAG horizon. They also accumulate larger throws and are aligned with the underlying NW-SE structural trend. Therefore, they could either be an upward splay and segmentation of reactivated basement structures or new faults that are exploiting the pre-existing structures at depth.

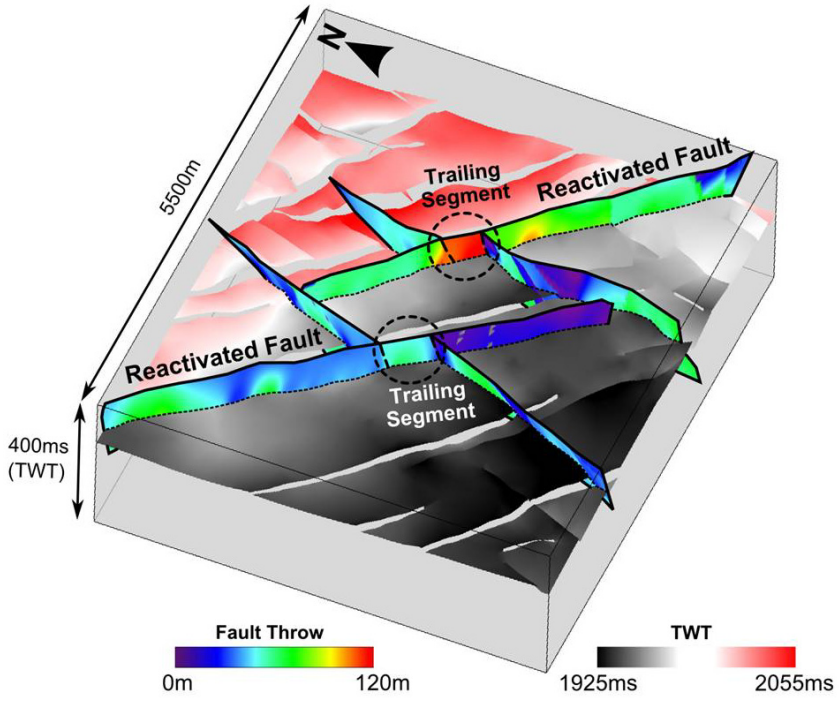

Figure 7.16 3D diagram of NNE trending fault planes that abut and locally reactivate WNW trending fault planes and form a trailing fault segment that links two abutting faults. The distribution of throw is contoured onto each fault plane and shows increases in throw at the trailing fault segments. This example is taken from the SAG horizon.

7.6.3. Trailing faults

Although Figure 7.14 indicates that many long faults in the fault network are acting as isolated individual faults, there are variable increases and decreases in some of their throw profiles. These often coincide with abutments and interactions with other faults of the opposite fault set causing 'local' reactivation of the pre-existing abutted fault plane (cf. Figure 7.10). Sometimes a section of a fault plane between two abutting faults is reactivated. This can be seen particularly well for longer WNW-trending faults whose fault planes show a change in displacement between the intersections with two abutting NNE-

trending faults (Figure 7.16). This indicates trailing of displacement from the abutting faults onto the original pre-existing abutted fault.

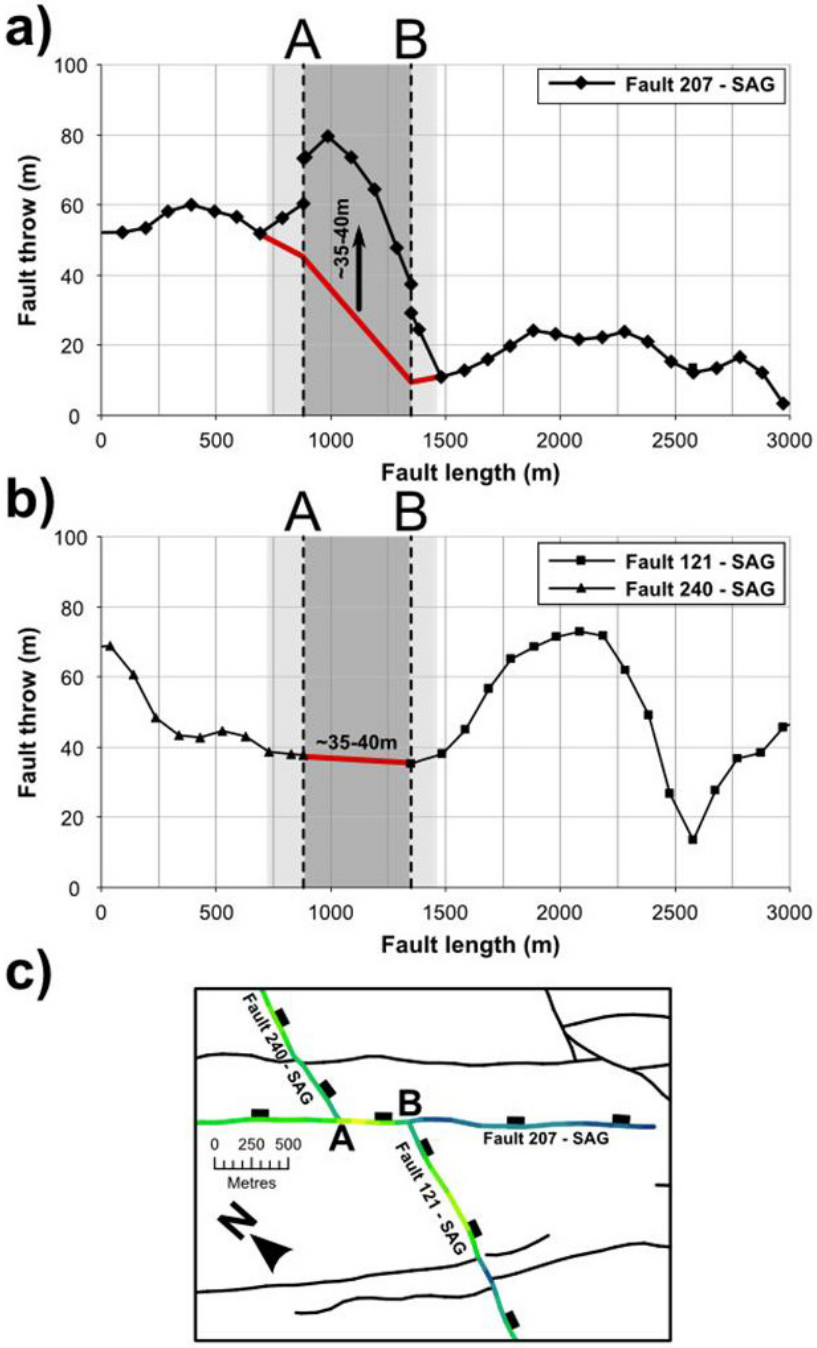

Figure 7.17 Fault throw profiles showing an example of a synthetic trailing fault interaction where two faults abut and reactivate a portion of another fault that shares the same motion sense. In this case fault 207 in a) is reactivated between intersection points A and B, increasing in throw, because of the abutting interactions of faults 121 and 240 shown in b). The red line is an estimated reconstruction of the original fault throw profile before interaction. c) Plan view map of the fault interactions.

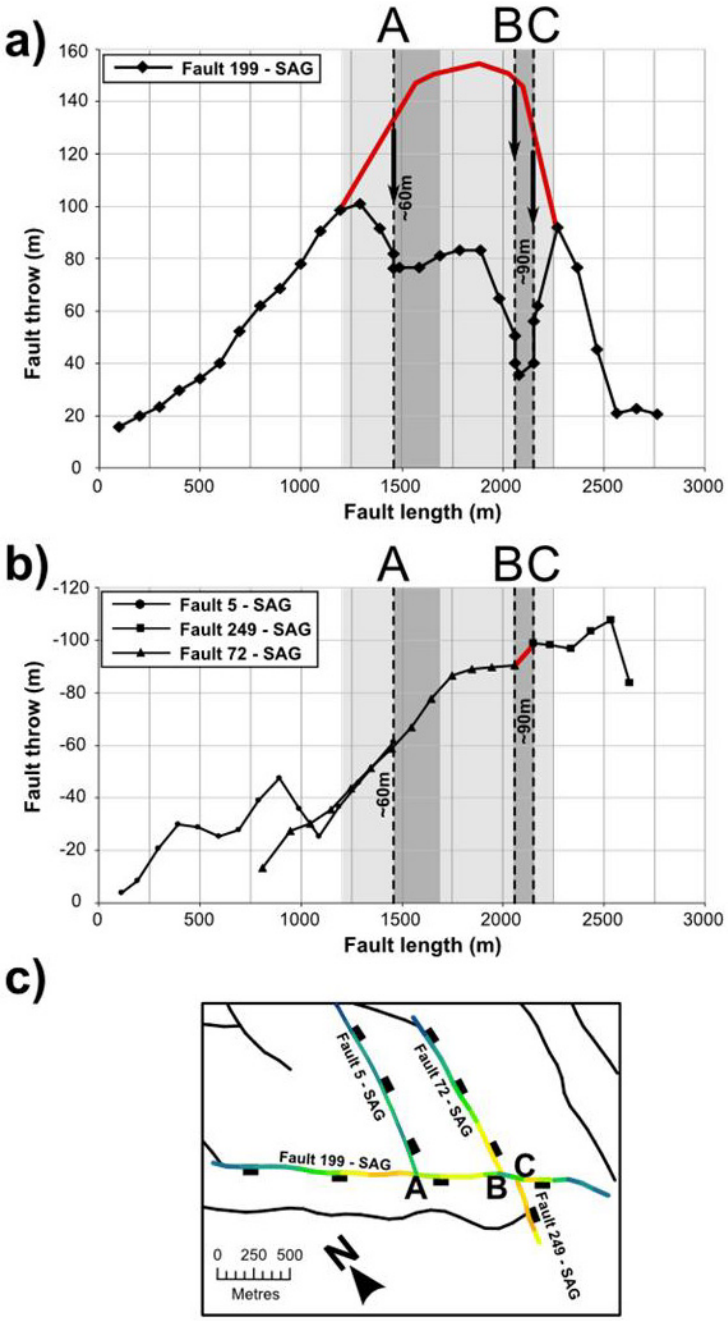

Figure 7.18 Fault throw profiles showing an example of an antithetic trailing fault where faults abut and reactivate a portion of another fault which has the opposite motion sense. In this case fault 109 in a) is reactivated between intersection points A and C, decreasing in throw, because of interactions with abutting faults 5, 249 and 72 shown in b). The red line is an estimated reconstruction of the original fault throw profile before interaction. c) Plan view map of the fault interactions.

For example, the WNW-trending fault 207-SAG, seen in Figure 7.17, is abutted by two NNE-trending faults at intersections A (Fault 240-SAG) and B (Fault 121-SAG). The two abutting faults have very similar throw values near the points of intersection (Figure 7.17b), whereas the segment AB of the WNW-trending fault

(Fault 207-SAG) that is between the two abutting faults and shows a marked increase in accumulated throw (Figure 7.17a). A reconstruction of the original throw profiles (Figure 7.17) indicates that the increase in throw along segment AB (35-40 m) is broadly similar to the throws values of the two abutting faults at their points of intersection (35-40 m). This suggests that the movement of the two abutting NNE-faults (Faults 240-SAG and 121-SAG) has reactivated segment AB producing a trailing fault segment. This links the two abutting faults to form a trailing fault. The increase in throw along the trailing fault segment AB is because it shares the same kinematic motion sense (i.e. downthrown to the east) as the two abutting faults. Therefore this may be regarded as a synthetic trailing interaction.

There are also examples of antithetic trailing interactions between the two fault sets (Figure 7.18). These are produced when the trailing segment does not share the same motion sense as the abutting faults. For example, Fault 199-SAG is a WNW-trending fault that is downthrown to the west, whereas the abutting faults (faults 240-SAG, 72-SAG, 5-SAG) are all downthrown to the east (Figure 7.18). As a result there are marked drops in the throw profile of fault 199-SAG at intersection point A and between intersection points B and C. The reconstructed throw profile of the fault 199-SAG (red; Figure 7.18a) indicates that these decreases in throw match the throw values of the three abutting faults at the points of intersection. Furthermore, the throw profiles of the abutting faults are broadly coherent on either side of fault 199-SAG (Figure 7.18b). This indicates that segment AC on fault 199-SAG inversely reactivated and interacted with the three abutting faults producing a kinematic and geometric link between them.

Overall, there are two types of trailing interactions between different fault sets. A synthetic trailing interaction produces a trailing fault with segments that have the same motion sense (Figure 7.17). These cause an increase in throw along the trailing segment. Whereas, an antithetic trailing interaction involves abutting faults that have the opposite motion sense to the trailing segment, therefore causing inversion of the reactivated trailing segment and a decrease in throw (Figure 7.18). In general, the pre-existing fault that reactivates is acting as a transfer fault between the abutting faults and the reactivated segment is

analogous to a linking fault that may breach a relay ramp between two parallel fault segments. As the NNE-trending faults trail and reactivate segments of the WNW-trending faults, these must originally post-date the WNW-trending faults.

7.7. Topology

Compartmentalization of reservoirs by faulting can be caused by the juxtaposition of sealing stratigraphic units against a reservoir unit, or by the faults themselves having good sealing properties. Both of these rely on the formation of compartments which means that faults need to be connected. Hence, in the following section we assess the topology of the fault network at the two reservoir horizons (KUP and SAG horizons) to investigate the relationship between topology, connectivity and the formation of compartments.

7.7.1. Nodes and branches

In general, the topology of the network is similar at each horizon (Figure 7.19) but there are some subtle differences. The KUP horizon has a slightly higher proportion of connecting nodes (57%) in comparison to the SAG horizon (49%). The KUP horizon also has a slightly greater number of connections per line ($N_{C/L}$) and number of connections per branch ($N_{C/B}$) than the SAG horizon (Table 7.3), suggesting that the KUP horizon is better connected than the SAG horizon (Table 7.3; Figure 7.19). Subareas (Figure 7.20) illustrate the variation within each horizon and indicate that there is much more variation in the KUP horizon than the SAG horizon (Table 7.3; Figure 7.19).

Overall, the majority of connecting nodes within the fault network are Y-nodes (i.e. splays and abutments) with very few crossing X-nodes (Figure 7.19a), which is consistent with results from Chapter 4. Furthermore, the fault network has very few isolated (I-I) branches and is dominated by C-C branches (Figure 7.19b; Table 7.3) meaning that the network has the potential to form large clusters (cf. Chapter 4).

7.7.2. Compartments

A closed compartment has a defined perimeter of C-C branches forming a finite area within the sampled network, whereas a compartment that is not closed

does not have a defined perimeter and goes beyond the area of the sampled network. In 2D, we analyse the number of closed compartments and their sizes within the fault network. Knowing the number and sizes of the compartments in each reservoir horizon is important as it can **1)** give an indication of how geometrically compartmentalized the reservoir is and **2)** allow identification economically viable compartments for drilling.

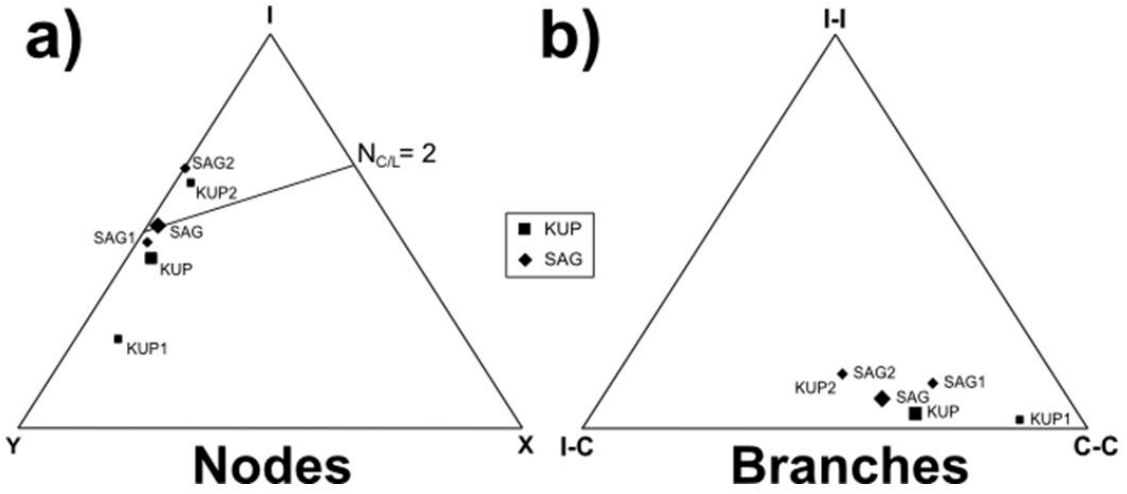

Figure 7.19 Ternary triangles showing the proportions of a) I, Y and X nodes and b) I-I, I-C and C-C branches within the network. KUP 1 and 2 and SAG 1 and 2 are subareas shown in Figure 7.20a and b, respectively, and discussed in the main text.

The proportion of area within the network that is enclosed by compartments is ~25% at each horizon (Table 7.4). However, the number and extent of closed compartments varies between horizons (Figure 7.20). There are more closed compartments at the KUP horizon than at the SAG horizon but the compartments are more dispersed in the KUP horizon (Figure 7.20a), whereas they are highly clustered in the SAG horizon (Figure 7.20b). The distribution of closed compartments coincides with clusters of C-C branches within the network (Figure 7.20), indicating that the formation of compartments is related to the proportion of C-C branches. Although the spatial distribution of compartments varies between the two horizons the size of the compartments is similar, with an average compartment size of 1.24 km^2 for the KUP horizon and 1.46 km^2 for the SAG horizon. The largest compartment is found at the KUP horizon with a size of 8.74 km^2 whereas the largest compartment at the SAG horizon is 5.33 km^2.

Table 7.3 Proportions of each topological component with the number of connections per line ($N_{C/L}$) and per branch ($N_{C/B}$) for both horizons and from selected subareas shown in Figure 7.20.

	Area (km^2)	I-Nodes (%)	Y-Nodes (%)	X-Nodes (%)	I-I Branches (%)	I-C Branches (%)	C-C Branches (%)	$N_{C/L}$	$N_{C/B}$
KUP Horizon									
KUP 1	189	43.1	52	4.9	3.8	32.2	63.9	2.40	1.61
KUP 2	19	22.2	68.9	8.9	2	12.2	85.7	3.41	1.83
SAG Horizon	19	62.1	34.5	3.4	10	55	35	1.57	1.31
SAG 1	191	51.4	46.5	2.1	7.5	36.9	55.6	1.99	1.48
SAG 2	19	47.1	51	2	11.4	25	63.6	2.16	1.55
	19	66	34	0	13.9	41.7	44.4	1.36	1.21

Subareas SAG 1 and KUP 1 are areas within the network that are fully compartmentalized, whereas subareas SAG 2 and KUP 2 are areas that have no closed compartments (Figure 7.20). In general, the compartmentalized subareas have a greater number of connections per line and per branch than the non-compartmentalized areas indicating that they are better connected (Table 7.3). It is apparent that there are more isolated (I-I) branches and

dangling ends (I-C branches) at the SAG horizon, which increases the internal deformation within compartments (Figure 7.20). The topological analysis indicates that the subareas that have no closed compartments are dominated by I-nodes and that the compartmentalized areas are dominated by Y-nodes (Table 7.3; Figure 7.19a). This is related to a change in the branch proportions as compartmentalized subareas (KUP 1 and SAG 1) are dominated by C-C branches (>60%), whereas the non-compartmentalized areas have a much greater proportion of I-C branches (Table 7.3; Figure 7.19b).

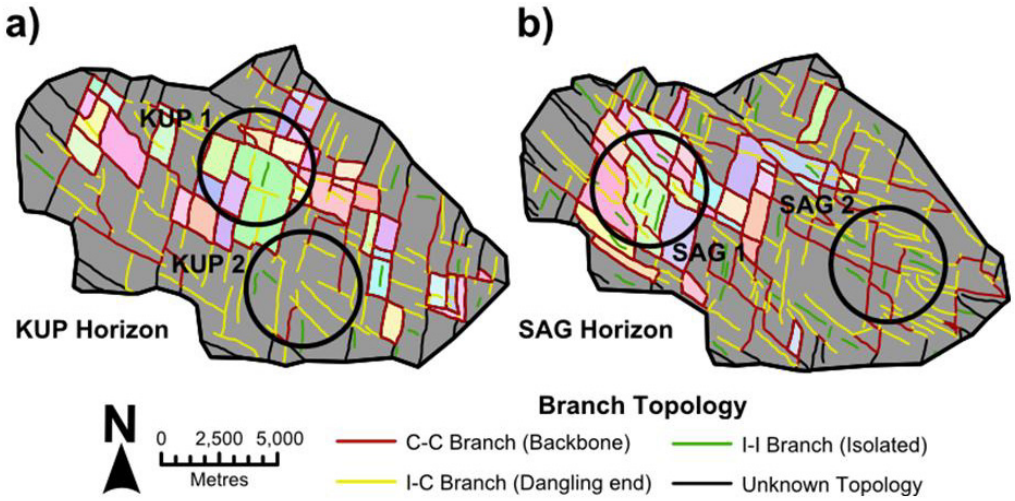

Figure 7.20 Fault map showing the topologies and spatial distribution of each branch type. The coloured areas represent the different closed compartments within the network at a) the KUP horizon and b) the SAG horizon.

7.7.2.1. *Effects of resolution*

The seismic data that images Milne Point can only resolve faults with greater than 10 m throw and therefore does not image the tips of many faults. Nixon et al. (2012) show that small faults and fault tips, which have less than 10 m displacement, contribute significantly to the connectivity and the proportion of connecting nodes within a fault network. Therefore being able to resolve whether the tips of a normal fault within the network connect with another fault is vital to assessing the number and extent of compartments within the network. To account for unresolved fault tips, Pickering et al. (1997) used a model for predicting and extending the length of tips of faults within a normal fault network in the North Sea. To model the effects of extending fault tip lengths on the formation of compartments at each horizon, we use a similar method that

extends the tips of faults by 50 m, 100 m, 200 m, 300 m, 400 m and 500 m until they intersect another fault (Figure 7.21).

Our results indicate that the number of compartments and extent of compartmentalization increases when each isolated fault tip is extended (Table 7.4; Figure 7.21). Furthermore, the average compartment size decreases indicating that larger compartments are being divided into smaller compartments (Table 7.4). Although the average compartment size decreases, the maximum compartment size increases in the SAG horizon (Table 7.4) as a larger compartment may also form within the network (Figure 7.21c).

Table 7.4 Compartment statistics showing their number and sizes at each horizon for different fault tip extensions.

Fault Tip Extension (m)	KUP Horizon					SAG Horizon				
	No.	Average (km^2)	Max (km^2)	Total (km^2)	Proportion %	No.	Average (km^2)	Max (km^2)	Total (km^2)	Proportion %
0	40	1.24	8.74	49.4	26	32	1.46	5.33	46.6	24.4
50	40	1.24	8.74	49.4	26.1	34	1.41	5.33	47.8	25
100	43	1.29	8.74	55.7	29.4	39	1.48	5.33	57.6	30.2
200	57	1.28	8.72	72.8	38.4	61	1.06	5.31	64.7	33.9
300	69	1.18	6.49	81.1	42.8	72	1.43	16.75	103.3	54.2
400	78	1.13	5.31	88.2	46.6	90	1.25	15.05	112.8	59.2
500	96	1.02	5.05	97.8	51.6	118	1.08	13.05	127.6	66.9

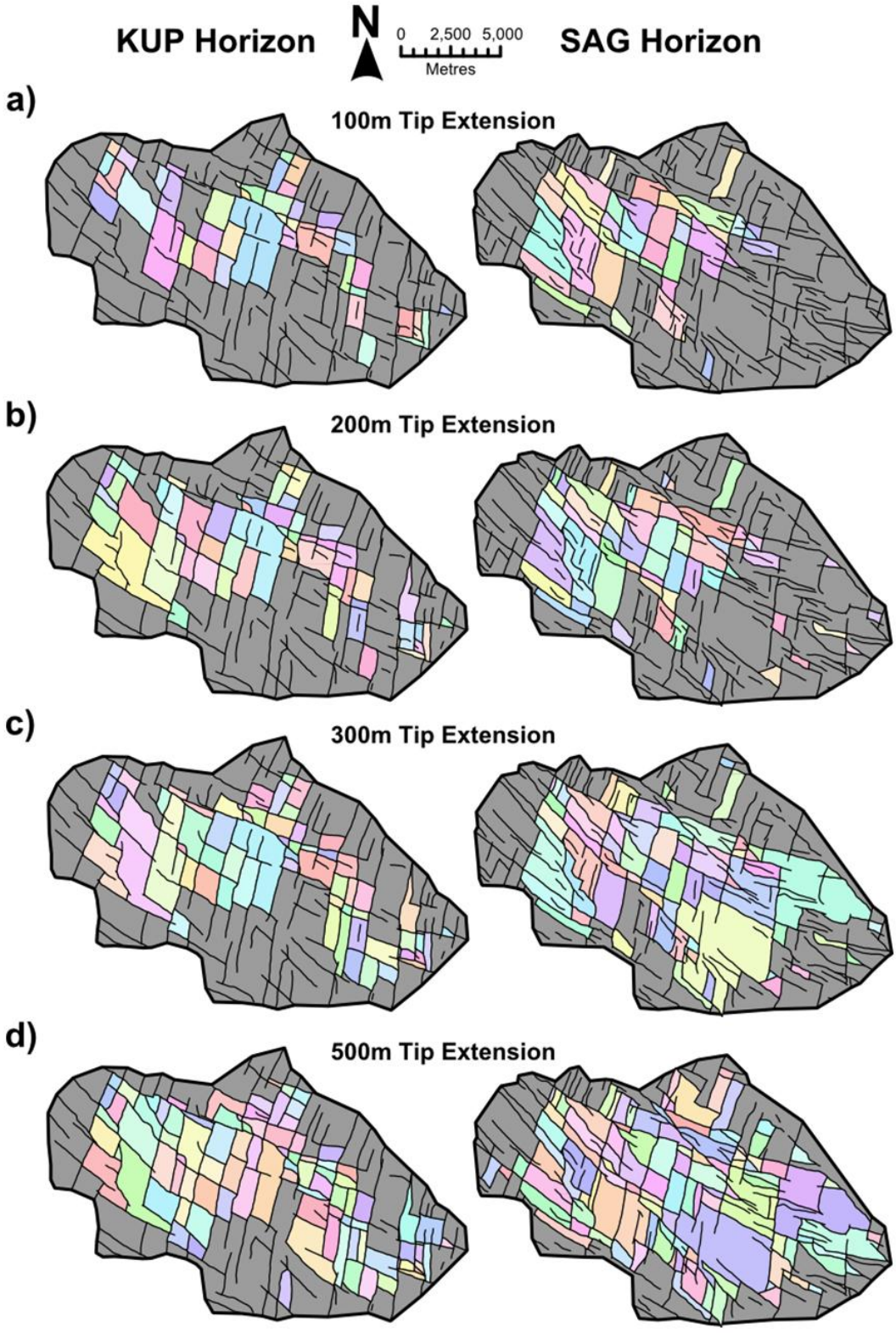

Figure 7.21 Fault maps (left; KUP horizon, right; SAG horizon) showing the compartments of the fault network after extending the tips of faults by a) 100 m, b) 200 m, c) 300 m and d) 500 m. The left side is for the KUP horizon and the right side is for the SAG horizon.

Using the displacement-length data plotted in Figure 7.7 and a linear relationship (i.e. Cowie and Scholz, 1992) we estimate that faults with 10 m throw have lengths of ~300 m in the KUP horizon and ~200 m in the SAG horizon. This is consistent with Pickering et al. (1997) who state that 500 m is a reasonable length extension to faults to account for the truncation effect, which is the equivalent of extending fault tips by 250 m. Therefore 200-300 m are more reasonable tip extension lengths for modelling the compartmentalization of the fault network.

7.8. Discussion

7.8.1. Fault chronology

Due to the presence of some syn-rift sedimentation associated with the WNW-trending faults we suggest that these are more likely to be associated with rifting during the deposition of the Beaufortian sequence (Jurassic to Lower Cretaceous). More specifically, as the majority of these are south dipping faults we can constrain them to the rifting period during the Jurassic when the polarity of rifting consisted of faults that down throw to the south (Hubbard et al., 1987; Bird, 1999). The NNE-trending faults are consistent with those that cut the Brookian sequence in the Tertiary (Boswell et al., 2011) which have been shown to cut the top of the Kuparuk River Sandstone (Masterson et al., 2001). Fault interactions and reactivation of structures within the fault network agree with this chronology of faulting. For example, the WNW-trending faults are strongly influenced by the underlying structural grain. Hence, they are probably related to reactivation of deeper pre-existing structures whereas the NNE-trending faults are not affected by such structures. The strain analysis of each individual fault set indicates that they have very differently oriented principal strains, thus both fault sets are individual deformation events. Furthermore, the NNE-trending faults trail and reactivate segments on the WNW-trending faults, therefore they must post-date the WNW-trending faults.

It is probable that there has been local reactivation of both fault sets due to changes in regional and local stress orientations, which is supported by the fact that many of the NNE-trending and WNW-trending small faults form abutting

relationships and cross-cut each other. This is also consistent with the presence of small faults and fault splays that trend ~NW-SE in the Eocene Sagavanirktok Formation (Boswell et al., 2011; Lorenson et al., 2011), which are thought to be genetically linked to the underlying faults (Collett et al., 2011). Furthermore, the present day stress regime of the area favours the reactivation of the WNW-trending faults (Zoback, 1992; Heidbach et al., 2010).

7.8.2. Network development

We analysed three main groups of small faults within the fault network – isolated faults, splay faults that involved one fault set, and abutting faults which involved two fault sets. The isolated faults within the network have isolated tips and produce common throw-length profiles whose shape depends on the restriction of the tips as is seen in numerous other studies (Muraoka and Kamata, 1983; Pollard and Segall, 1987; Nicol et al., 1996, 2010; Manighetti et al., 2001; Schlagenhauf et al., 2008).

Splay faults and abutting faults, however, intersect one another producing a branch line. Splay faults are characterised by a throw maxima at the point of intersection with the throw gradually decreasing towards their tips (Figure 7.13). They also cause steps in throw along the intersected fault with a decrease in the direction of splaying. This is consistent with results of Maerten et al. (1999) who observe and model similar throw profiles for synthetic splays along normal faults in both plan view and cross-section. Furthermore, similar variations in displacements are seen along strike of strike-slip faults in plan view by Nixon et al. (2011).

Abutting faults are faults that terminate against a pre-existing fault, producing a Y- or T-shaped intersection. When a fault abuts another fault it becomes pinned and can only propagate away from its abutted tip. If the fault continues to grow, displacement can accumulate and increase at the pinned tip transferring displacement and reactivating the abutted fault (Figure 7.22) (cf. Maerten et al., 2001). This is seen clearly in the numerous throw-distance profiles of individual abutting faults in Figures 7.11 and 7.12, which show abutments at different stages of development. Figure 7.22 shows the different stages of growth proposed for abutting faults with an unrestricted tip and a

restricted tip. In general, an abutting fault evolves from an isolated fault that has grown in length to abut and terminate at an earlier fault (stage 1). Early stage abutting faults have throw minima at both the abutting tip and isolated tip with a maximum throw near the middle of the fault (stage 2; Figure 7.22). They then increase in throw until a throw maximum is reached at the abutting tip and a throw minimum at the isolated tip (stages 3 and 4; Figure 7.22). Each stage is analogous to different stages of fault growth by segment linkage in the sense that the throw profile changes from an individual fault at stage 1 to a linking fault at stages 2 and 3 to a fully abutting fault at stage 4 (cf. Soliva and Benedicto, 2004).

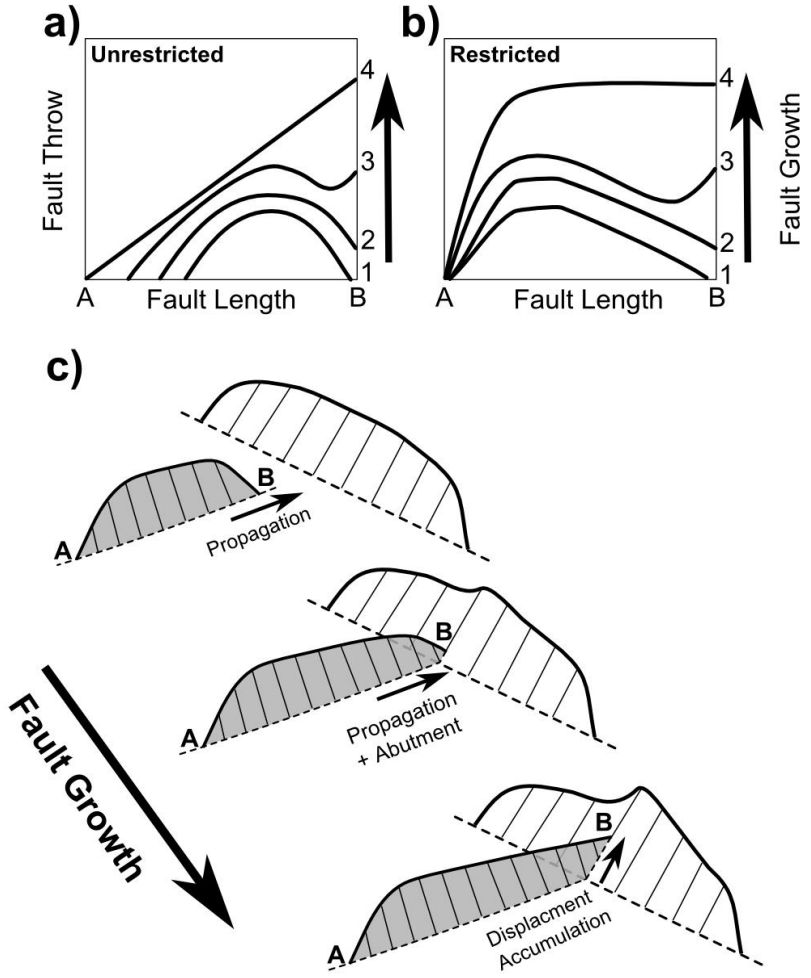

Figure 7.22 Schematic diagram of throw profiles for abutting faults at different stages of development. Stage 1 is an isolated fault profile. Stage 2 is an early stage abutment with throw minima at the tips of the faults; Stage 3 is an intermediate stage with throw increasing at the abutting tip; and Stage 4 is a fully developed abutting fault with a maximum throw at the abutting tip. a) and b) represents abutting faults with an unrestricted tip and a restricted tip, respectively. c) 3-D cartoon illustrating a developing abutting fault in grey.

7.8.2.1. *Effects and reactivation of pre-existing structures*

The fault network at Milne Point was analysed at two different stratigraphic horizons. The results show that the deeper SAG horizon has higher fault densities and accommodates larger strains in comparison with the KUP horizon. These changes are attributed to an increase in the number and size of the earlier WNW-trending faults as the later NNE-trending faults have similar density and strain values at each horizon (Table 7.1). We also suggest that the WNW-trending faults are influenced by the pre-existing underlying structural grain that trends NW-SE and bound broad-scale horst and graben structures. This effect of the underlying structures is characterized by several changes with depth:

1. Clockwise rotation of WNW-trending faults with depth as they align themselves with the underlying structural grain;
2. Increase in fault dip of larger WNW-trending faults;
3. Increase in displacement and strain localization onto WNW-trending faults;
4. Better linkage between large WNW-trending faults.

Reactivation of pre-existing structures can often produce and affect new fault sets in the overlying stratigraphy (Bailey et al., 2005; Frankowicz and McClay, 2010). For example, Bailey et al. (2005) see similar changes in the spatial development of two normal faults sets in the East Pennines Coalfield (UK) caused by reactivation of underlying basement faults causing strain localization onto one fault set.

As the WNW-trending faults are obliquely orientated to the NW-trending underlying structural grain, it is possible that these were driven by left-lateral transtension along the previous structures. This is supported by the strain orientation of the WNW-trending fault set, the steepening of the larger faults with depth and the splaying and rotation of faults into the NW-trending structural grain, which resembles the organization of faults in upward splaying flower structures and bifurcating up-tips above left-lateral strike-slip faults (cf. McGrath and Davison, 1995; Kim et al., 2004). Furthermore, Giba et al. (2012) show similar characteristics for an obliquely reactivated normal fault in the Taranaki

Basin, New Zealand, with fault splays propagating upward from the reactivated fault and rotating to align with the regional stress field.

The trailing faults (Figure 7.16) are also caused by the reactivation of pre-existing structures. However, unlike the effect of the underlying structural grain, which involves similar fault geometries and strain orientations, the trailing fault interactions involve faults sets that are at a high angle to one another. These involve two faults from one fault set abutting a fault from a pre-existing fault set. This then causes reactivation and trailing of the displacements from the abutting faults onto a segment of the pre-existing fault. The reactivation can be synthetic or antithetic to the pre-existing fault depending on the motion senses of the interacting faults. Maerten (2000) describes similar trailing interactions between faults from the Chimney Rock fault array in central Utah. These include the Bluebell fault which has an increase in displacement on a segment between two abutting faults. The segment also has slickensides with different pitch orientations to the rest of the fault, indicating reactivation (Maerten, 2000).

7.8.3. Compartmentalization

In this study the compartmentalization of the fault network is assessed by mapping the compartments and investigating their number and size at each horizon. The link between topology and compartmentalization is that the formation of a compartment requires a perimeter of C-C branches, hence compartmentalization is related to the proportion and distribution of C-C branches. This is supported by the topology of subareas that are compartmentalized and subareas that have no compartments.

In general, the spatial location and distribution of the compartments varies within the network. This can vary with depth and laterally within each horizon, changing the area of the network that is compartmentalized and the average number and size of compartments. Hence, indicating the importance of analysing and quantifying the compartmentalization of each reservoir horizon separately to identify the location of potentially economically viable compartments, or avoiding drilling into small uneconomic compartments.

Furthermore, using a sensible tip extension shows that each reservoir horizon might be more geometrically compartmentalized than the seismic data

suggests. Although this is not as important for stratigraphically sealed compartments, which typically need fault throws >> 10 m to offset a reservoir horizon, it is important to include tip extensions in models of fault networks if fault planes themselves are sealing. The model could identify a large compartment within the network not previously considered or it could indicate that a previously identified compartment consists of many smaller compartments. Hence, modelling realistic positions of fault tips could improve the quality of reservoir models.

7.9. Conclusions

A normal fault network from onshore Milne Point, Alaska has been analysed using 3D seismic reflection data. The network comprises NNE-trending and WNW-trending fault sets, which were analyzed at two stratigraphic horizons: the Kuparuk River Sandstone and the Sag River Sandstone. Analysis shows that:

1. The presence of small thickness changes within the Beaufortian sequence across the WNW-trending faults suggest syn-rift deposition indicating that these formed during rifting and originally pre-date the NNE-trending fault set. Hence, we suggest a Jurassic age for the WNW-trending faults and a Tertiary age for the NNE-trending faults. This is supported by the trailing faults where abutting NNE-trending faults reactivate segments of WNW-trending faults. As there are numerous abutting and cross-cutting relationships that involve small faults of both fault sets, it is probable that there has been reactivation of the WNW-trending fault set both during formation of the NNE-trending faults and subsequent stress.
2. The NNE-trending faults generally dip to the SE producing a plane strain with a maximum extension orientation of ~N103°E. These are consistently developed in both horizons with similar fault densities, fault sizes and strains.
3. The majority of WNW-trending faults dip to the SW and have a plane strain tensor, with a maximum extension orientation of ~N030°E. The

faults show variation, increasing in size, number and density with depth, hence accommodating greater strains.

4. The variation with depth of the WNW-trending faults is due to the interaction and reactivation of an underlying NW-SE structural grain. This influence is characterized by increases in dip and displacement on several faults, strain localization, clockwise rotation of faults and an increase in linkage maturity.

5. NNE-trending faults post-date the WNW-trending faults as they abut and reactivate segments of WNW-trending faults. This produces a trailing fault that links two abutting faults through the reactivated segment of the pre-existing fault. The motion sense of the trailing fault can either be synthetic or antithetic to the reactivated pre-existing fault producing an increase or decrease in throw, respectively.

6. Throw profiles of numerous faults within the network show that isolated faults and abutting faults form a range of throw profiles depending on the degree of restriction of fault tips and the timing of abutment during fault development. Trailing fault segments are usually short within the network (<2000 m). Longer faults (up to 8000 m) are usually cross-cut and abutted by numerous faults but show broad throw profiles that are similar to isolated faults.

As the fault network comprises two orthogonal fault sets there is great potential for compartmentalization of each reservoir horizon. Hence, we explored the relationship between topology and the compartmentalization of the fault network and assessed the size, number and spatial distribution of compartments at each horizon. The results show that:

7. Despite increases in density and strain with depth the topology of the network is consistent. There are more Y-nodes than X-nodes and there is a greater proportion of C-C branches at both horizons.

8. The spatial extent of compartments changes with depth but the number and average size remain similar, forming approximately 25% of the network area.

9. The better connected parts of the network form compartments. Furthermore, compartmentalized areas are dominated by C-C branches whereas as non-compartmentalized areas have more equal proportions of C-C branches and I-C branches.

10. The resolution of seismic data may lead to an underestimate of the number of compartments within the network. The effect of resolution can be accounted for by modelling fault tips extension. This can sometimes identify new large compartments or show that previously identified large compartments are actually made up of smaller compartments.

Overall, this study provides a robust network analysis that is important for understanding the behaviour of fault networks. It has identified numerous fault interactions and described the effects of pre-existing structures on network development. Furthermore, it develops a link between the topological analysis and compartmentalization that can be applied to predict/estimate whether or not the network may geometrically form closed compartments.

7.10. References

Aydin, A., 2000. Fractures, faults, and hydrocarbon entrapment, migration and flow. Marine and Petroleum Geology 17, 797–814.

Bailey, W.R., Walsh, J.J., Manzocchi, T., 2005. Fault populations, strain distribution and basement fault reactivation in the East Pennines Coalfield, UK. Journal of Structural Geology 27, 913–928.

Bird, K.J., 1999. Geographic and geologic setting, in: The Oil and Gas Resource Potential of the 1002 Area, Arctic National Wildlife Refuge, Alaska, by ANWR Assessment Team, U. S. Geological Survey Open File Report 98-34. U.S. Geological Survey.

Boswell, R., Rose, K., Collett, T.S., Lee, M., Winters, W., Lewis, K. A., Agena, W., 2011. Geologic controls on gas hydrate occurrence in the Mount Elbert prospect, Alaska North Slope. Marine and Petroleum Geology 28, 589–607.

Bouvier, J., Kaars-Sijpesteijn, C., Kluesner, D., Onyejekwe, C., van der Pal, R., 1989. Three-dimensional seismic interpretation and fault sealing investigations, Nun River Field, Nigeria. AAPG Bulletin 73, 1397–1414.

Carman, G., Hardwick, P., 1983. Geology and regional setting of Kuparuk oil field, Alaska. AAPG Bulletin 67, 1014–1031.

Collett, T.S., 1993. Natural gas hydrates of the Prudhoe Bay and Kuparuk River area, North Slope, Alaska. AAPG bulletin 77, 793–812.

Collett, T.S., Lee, M.W., Agena, W.F., Miller, J.J., Lewis, K. A., Zyrianova, M.V., Boswell, R., Inks, T.L., 2011. Permafrost-associated natural gas hydrate

occurrences on the Alaska North Slope. Marine and Petroleum Geology 28, 279–294.

Cowie, P.A., Scholz, C.H., 1992. Growth of faults by accumulation of seismic slip. Journal of Geophysical Research 97, 11085–11095.

Davatzes, N.C., Aydin, A., Eichhubl, P., 2003. Overprinting faulting mechanisms during the development of multiple fault sets in sandstone, Chimney Rock fault array, Utah, USA. Tectonophysics 363, 1–18.

Ferrill, D. A., Morris, A.P., McGinnis, R.N., 2009. Crossing conjugate normal faults in field exposures and seismic data. AAPG Bulletin 93, 1471–1488.

Fokker, P. A., Visser, K., Peters, E., Kunakbayeva, G., Muntendam-Bos, A. G., 2012. Inversion of surface subsidence data to quantify reservoir compartmentalization: A field study. Journal of Petroleum Science and Engineering 96-97, 10–21.

Gauthier, B., Lake, S., 1993. Probabilistic modeling of faults below the limit of seismic resolution in Pelican Field, North Sea, offshore United Kingdom. AAPG Bulletin 77, 761–777.

Giba, M., Walsh, J.J., Nicol, A., 2012. Segmentation and growth of an obliquely reactivated normal fault. Journal of Structural Geology 39, 253–267.

Go, J., Smalley, P.C., Muggeridge, A., 2012. Appraisal of reservoir compartmentalization using fluid mixing time-scales: Horn Mountain Field, Gulf of Mexico. Petroleum Geoscience 18, 305–314.

Heidbach, O., Tingay, M., Barth, A., Reinecker, J., Kurfeß, D., Müller, B., 2010. Global crustal stress pattern based on the World Stress Map database release 2008. Tectonophysics 482, 3–15.

Hubbard, R., Edrich, S., Rattey, R.P., 1987. Geologic evolution and hydrocarbon habitat of the “Arctic Alaska Microplate”. Marine and Petroleum Geology 4, 2–34.

Jolley, S.J., Fisher, Q.J., Ainsworth, R.B., 2010. Reservoir compartmentalization: an introduction. Geological Society, London, Special Publications 347, 1–8.

Kim, Y-S., Andrews, J.R., Sanderson, D.J., 2001. Reactivated strike–slip faults: examples from north Cornwall, UK. Tectonophysics 340, 173–194.

Kim, Y-S., Peacock, D.C.., Sanderson, D.J., 2004. Fault damage zones. Journal of Structural Geology 26, 503–517.

Leveille, G., Knipe, R., More, C., Ellis, D., Dudley, G., Jones, G., Fisher, Q.J., Allinson, G., 1997. Compartmentalization of Rotliegendes gas reservoirs by sealing faults, Jupiter Fields area, southern North Sea. Geological Society, London, Special Publications 123, 87–104.

Lorenson, T.D., Collett, T.S., Hunter, R.B., 2011. Gas geochemistry of the Mount Elbert Gas Hydrate Stratigraphic Test Well, Alaska North Slope: Implications for gas hydrate exploration in the Arctic. Marine and Petroleum Geology 28, 343–360.

Maerten, L., 2000. Variation in slip on intersecting normal faults- Implications for paleostress inversion. Journal of Geophysical Research 105, 25553–25565.

Maerten, L., Pollard, D.D., Maerten, F., 2001. Digital mapping of three-dimensional structures of the Chimney Rock fault system, central Utah. Journal of Structural Geology 23, 585–592.

Manighetti, I., King, G., Gaudemer, Y., Scholz, C., 2001. Slip accumulation and lateral propagation of active normal faults in Afar. Journal of Geophysical Research 106, 13667–13696.

Manzocchi, T., Childs, C., Walsh, J.J., 2010. Faults and fault properties in hydrocarbon flow models. Geofluids 10, 94–113.

Masterson, W., Dzou, L., Holba, A., 2001. Evidence for biodegradation and evaporative fractionation in West Sak, Kuparuk and Prudhoe Bay field areas, North Slope, Alaska. Organic Geochemistry 32, 411–441.

McGrath, A., Davison, I., 1995. Damage zone geometry around fault tips. Journal of Structural Geology 17, 1011–1024.

Muraoka, H., Kamata, H., 1983. Displacement distribution along minor fault traces. Journal of Structural Geology 5, 483–495.

Nicol, A., Walsh, J., Watterson, J., Bretan, P., 1995. Three-dimensional geometry and growth of conjugate normal faults. Journal of Structural Geology 17, 847–862.

Nicol, A., Watterson, J., Walsh, J., Childs, C., 1996. The shapes, major axis orientations and displacement patterns of fault surfaces. Journal of Structural Geology 18, 235–248.

Nicol, A., Walsh, J.J., Villamor, P., Seebeck, H., Berryman, K.R., 2010. Normal fault interactions, paleoearthquakes and growth in an active rift. Journal of Structural Geology 32, 1101–1113.

Nixon, C.W., Sanderson, D.J., Bull, J.M., 2011. Deformation within a strike-slip fault network at Westward Ho!, Devon U.K.: Domino vs conjugate faulting. Journal of Structural Geology 33, 833–843.

Nixon, C.W., Sanderson, D.J., Bull, J.M., 2012. Analysis of a strike-slip fault network using high resolution multibeam bathymetry, offshore NW Devon U.K. Tectonophysics 541-543, 69–80.

Peacock, D.C.P., Sanderson, D.J., 1993. Estimating strain from fault slip using a line sample. Journal of Structural Geology 15, 1513–1516.

Peacock, D.C.P., Sanderson, D.J., 1996. Effects of propagation rate on displacement variations along faults. Journal of Structural Geology 18, 311–320.

Permanyer, A., Douifi, L., Lahcini, A., Lamontagne, J., Kister, J., 2002. FTIR and SUVF spectroscopy applied to reservoir compartmentalization: a comparative study with gas chromatography fingerprints results. Fuel 81, 861–866.

Pickering, G., Peacock, D.C.P., Sanderson, D.J., Bull, J.M., 1997. Modeling Tip Zones to Predict the Throw and Length Characteristics of Faults. AAPG Bulletin 81, 82–99.

Pollard, D., Segall, P., 1987. Theoretical displacements and stresses near fractures in rock: with applications to faults, joints, veins, dikes, and solution surfaces, in: Atkinson, B.. (Ed.), Fracture Mechanics of Rock. Academic Press, New York, pp. 277–349.

Schlagenhauf, A., Manighetti, I., Malavieille, J., Dominguez, S., 2008. Incremental growth of normal faults: Insights from a laser-equipped analog experiment. Earth and Planetary Science Letters 273, 299–311.

Segall, P., Pollard, D., 1983. Nucleation and growth of strike slip faults in granite. Journal of Geophysical Research 88, 555–568.

Smalley, P., England, W., Rabaa, A.W.M., 1994. Reservoir compartmentalization assessed with fluid compositional data. SPE Reservoir Engineering 9, 175–180.

Smalley, P.C., Hale., N.A., 1996. Early identification of reservoir compartmentalization by combining a range of conventional and novel data types. SPE Formation Evaluation 11, 163–170.

Soliva, R., Benedicto, A., 2004. A linkage criterion for segmented normal faults. Journal of Structural Geology 26, 2251–2267.

Soliva, R., Benedicto, A., 2005. Geometry, scaling relations and spacing of vertically restricted normal faults. Journal of Structural Geology 27, 317–325.

Walsh, J., Bailey, W., Childs, C., Nicol, A., Bonson, C., 2003. Formation of segmented normal faults: a 3-D perspective. Journal of Structural Geology 25, 1251–1262.

Zhao, G., Johnson, A., 1991. Sequential and incremental formation of conjugate sets of faults. Journal of Structural Geology 13, 887–895.

Zoback, M.L., 1992. First- and second-order patterns of stress in the lithosphere: The World Stress Map Project. Journal of Geophysical Research 97, 11703–11728.

8. Summary and conclusions

This thesis has provided an extensive analysis of various strike-slip and normal fault networks from different tectonic settings and at a range of scales. An array of datasets from fieldwork, aerial photography, multibeam bathymetry, high resolution seismic profiles and 3-D seismic volumes were used and integrated with ArcGIS to produce a robust methodology for fault network analysis (see appendix). Each analysed fault network has individual characteristics, which are described in each chapter, however there were many coherent observations that could be applied and be representative of other fault networks. This chapter presents a summary of these main themes and concluding points that resulted from the material covered in the previous six chapters.

8.1. Fault organization, interaction and the role of pre-existing structures

In order to characterize fault networks as a whole this project investigated the behaviour within these fault networks, looking at different elements such as: individual fault interactions (Chapters 2 and 7); the organization of faulting/damage within a fault network (Chapter 2) and around large faults (Chapters 5 and 6); the role of small and large faults within a network (Chapters 3 and 6); the partitioning of deformation within a fault network (all Chapters); the reactivation and effect of pre-existing structures on fault development (Chapters 5 and 7). All of these add to the heterogeneity of deformation within a fault network and understanding these variations is essential for the characterization of fault networks.

1) There are numerous fault interactions that occur within both strike-slip and normal fault networks. In general, these can be divided into two main groups that relate to the kinematic behaviour of the faults involved in each interaction: synthetic fault interactions and antithetic fault interactions (Chapters 2 and 7).

2) Synthetic fault interactions involve faults that have the same motion sense. These usually include a large main fault with a smaller splay fault accommodating step like decreases in its displacement. The decrease in displacement occurs in the direction of the acute angle of intersection between the main fault and the splay fault. Splay faults decrease in displacement away from the intersection but sometimes rejoin the main fault forming a lens. Lenses are common at bends in the main fault or in areas of fault linkage (Chapters 2 and 7).

3) Antithetic fault interactions involve faults that have opposite motion senses. These include small faults that abut a larger main fault as well as crossing faults of similar size. Like synthetic splay fault interactions, abutments produce decreases in displacement along the main fault but in the direction of the obtuse angle of intersection. The displacement profile of an abutting fault depends on the time of abutment and how much the fault develops after abutment (Chapters 2 and 7).

4) Numerous small faults often organize themselves around larger magnitude faults within a network. These form areas of damage that accommodate variations in displacement along the larger magnitude fault. Deformation becomes more distributed within these areas with greater fault densities and smaller displacements. The horsetail splay at Spaniards Bay (Kaikoura Peninsula) is an excellent mesoscale strike-slip example (Chapter 5). Whereas the distributed area around the Rangitaiki Fault (Whakatane Graben) is a larger scale dip-slip example (Chapter 6).

5) Large damage domains can form within a fault network where numerous large faults decrease in displacement in the same area (e.g. the damage area at Westward Ho!; Chapter 2). This can be driven by changes in lithology or by interactions with other large faults.

6) The organization of faulting within fault networks can form distinct domains that interact with each other (Chapter 2). This is seen clearly at Westward Ho!, where changes in the size and proportion of fault sets produce domains that have domino geometries and domains that have conjugate geometries:

a. Domino domains are characterized by a dominant fault set with larger displacement, regularly spaced faults and antithetic faults forming in intervening blocks. These domains show systematic rotation of faults and bedding.

b. Conjugate domains have equal sizes and proportions of each fault set forming abutting and cross-cutting relationships. There is little or no rotation of bedding.

When domino domains with opposite dominant fault sets interact with each other, a conjugate domain forms in between (Chapter 2).

7) Pre-existing structures can influence the development of faults within a network including their geometry and arrangement. Faults that form sub-parallel to pre-existing structures will rotate into or splay from these structures often reactivating them. Whereas, faults that form orthogonal to pre-existing structures often produce abutting relationships and sometimes use and reactivate these structures as transfer faults (Chapter 7).

8.2. Distribution and localization of strain within fault

An important part of the fault network analysis was the collection of various fault attribute data such as displacement, length, orientation, motion sense, dip/azimuth etc. These were of particular use for calculating and demonstrating the distribution and localization of strain within fault networks. This was investigated at different levels within a fault network including: variations in strain around individual large faults from areas of distributed faulting to areas of localized faulting (Chapters 5 and 6); localization of strain onto individual faults within a network (Chapters 3 and 6); partitioning onto different fault sets (Chapters 2 and 7); and identification of spatial domains within networks that interact and behave differently (Chapters 2 and 6). In general, these cover a range of scales and highlight variations in kinematic behaviour adding to our understanding of strain localization within fault networks.

8) In Chapter 3 we demonstrate that strain is localized onto the large displacement fault segments within a fault network. These make up large

faults and the central parts of smaller faults. However, a significant proportion of strain is contributed by smaller fault segments, that form small faults and fault tips, and this should be accounted for when using low resolution datasets.

9) Strain progressively localizes onto larger faults within a network (e.g. the Rangitaiki Fault; Chapter 6), however, the distribution of strain along strike of large individual faults can be localized or distributed to many surrounding smaller faults. This is demonstrated for the Rangitaiki Fault, and is related to the linkage maturity of the fault. In general, areas of localized faulting form where linkage is well established and are characterized by strain localized onto a few large faults. Areas of distributed faulting form where linkage is not so well established and have many small faults that accommodate the majority of the strain (Chapter 6).

10) Strain can also be localized to domains of faulting within networks. The domino domains at Westward Ho! are a perfect example where rotation of fault blocks between the larger faults allows greater strains to develop. Whereas the interlinking conjugate domains accommodate lower strains as they are irrotational with many small faults (Chapter 2).

11) Although strain can be distributed or localized in different domains within fault networks and around large faults, the networks still preserve strain compatibility between these domains and along strike of large faults (Chapters 2 and 6).

12) In networks with more than one fault set strain is partitioned between the two fault sets. In networks with conjugate fault sets (e.g. Westward Ho! and Hartland; Chapters 2 and 3), domino domains are examples of areas where strain has been localized onto one fault set; whereas the conjugate domains are areas where strain is distributed evenly across both fault sets. In networks with independent fault sets (e.g. Milne Point; (Chapter 7) strain partitioning is reliant on the development of each fault set.

13) Pre-existing structures can also influence the strain distribution within a fault network. For example, at Milne Point greater strains are produced by one fault set in the deeper horizons due to the influence of sub-parallel pre-

existing basement structures. Whereas in the shallower horizons both fault sets accommodate equal proportions of strain (Chapter 7).

8.3. Topological variation in fault networks, connectivity and compartmentalization

The topological analysis, which is introduced in Chapter 3 and further developed in Chapters 4 and 7, is a novel approach aimed to be applicable to industry. It is important as it produces an array of parameters that: systematically characterize fault networks from their topological components (Nodes, Branches and Compartments); relate to the connectivity of a fault network; provide information about the clustering and compartmentalization within a network. Therefore, a topological analysis can be very useful as a basic assessment of the character and connectivity of a fault network, which can be insightful when considering the fluid flow/percolation potential of a fault network and the compartmentalization of a reservoir.

14) Fault networks have a greater number of Y-nodes than X-nodes, therefore fault abutments and fault splays are more common than crossing faults (Chapters 3, 4 and 7). This is due to the difficulty of preserving X-node geometries at greater fault displacements as shown in Chapter 2. This is in contrast to small scale fractures, joints and deformation bands which often preserve and preferentially form X-node geometries.

15) There is also much heterogeneity in the spatial distribution of connecting nodes (Y- and X-nodes) within fault networks (Chapter 4). Clusters of connecting nodes form in areas of damage and linkage between faults where fault densities are greater. In general, these areas have a higher number of connections per line ($n_{C/L}$) and per branch ($n_{C/B}$) than other parts of the fault network suggesting they are better connected. Therefore, these areas are of particular importance when considering fluid flow (Chapter 4).

16) The branch analysis is a new addition to the topological analysis of networks (Chapter 4). It segregates isolated faults within a network from the faults that connect to other faults. This is important as the branch

analysis can be related to the clustering and compartmentalization of networks:

a. The clustering nature of the connecting faults is related to the proportion of I-C to C-C branches. In general, connected faults with many I-C branches are more likely to form small isolated clusters, whereas faults with many C-C branches are more likely to form a large cluster that may span the network (Chapter 4).

b. C-C branches are a requirement for the formation of closed compartments within a fault network. Therefore, areas that have more C-C branches than I-C branches have the potential to form closed compartments, whereas areas with equal proportions of C-C and I-C branches are unlikely to form a closed compartment (Chapter 7).

The proportion of I-C to C-C branches within a network can be represented by the average number of connections per branch ($n_{C/B}$), after omitting the isolated (I-I) branches. This is easily calculated from the node proportions, producing a useful parameter that may be used to estimate the clustering of the network (Chapter 4).

17) The connectivity of a fault network is reliant on the low displacement fault segments that form the tips of faults (Chapter 3). This is important when considering the resolution of data used to constrain the fault network, and has implications when estimating the fluid flow potential of a fault network.

18) The resolution of fault tips also has implications when assessing the compartmentalization of a fault network (Chapter 7). Modelling fault tips shows that there could be a greater number of closed compartments within a network than the resolution of the dataset suggests. These may be larger compartments within a network or they could indicate that a large compartment is made up of smaller compartments. This is an important factor to account for as it could change the economic potential of a compartmentalized reservoir.

9. Appendix

This appendix contains additional information providing a summary of the workflows in ArcGIS that were used to analyse data from digital air photographs, high resolution multibeam bathymetry and seismic surveys. Also included in the appendix are examples of data extraction from ArcGIS for network analyses in Microsoft Excel, which produces rose diagrams, strain values, fault densities and various other attributes.

9.1. ArcGIS Workflow 1 – Analysis from field observation and digital air photographs at Westward Ho!

1. Digital air photographs of wave-cut platform at Westward Ho! downloaded from the Channel Coast Observatory at *www.channelcoast.org/*. Images can be downloaded as georectified image files (.ecw), and then imported directly into ArcMap.
2. Digital air photographs used as base maps for field mapping of key areas and for digitally mapping of wave-cut platforms.
3. ArcCatalog, geodatabase file (.gdb) created to save and organize feature classes created and used for interpreting and analysing the fault network.
4. Polyline feature classes used for digitizing faults, marker-beds and calculating lateral separations (approximate displacement for strike-slip faults). NB. It is important to tick the 'Measure' box when creating polylines as this automatically calculates their length. Point feature classes used to mark displacements that were measured in the field. All feature classes can be created using ArcToolbox.

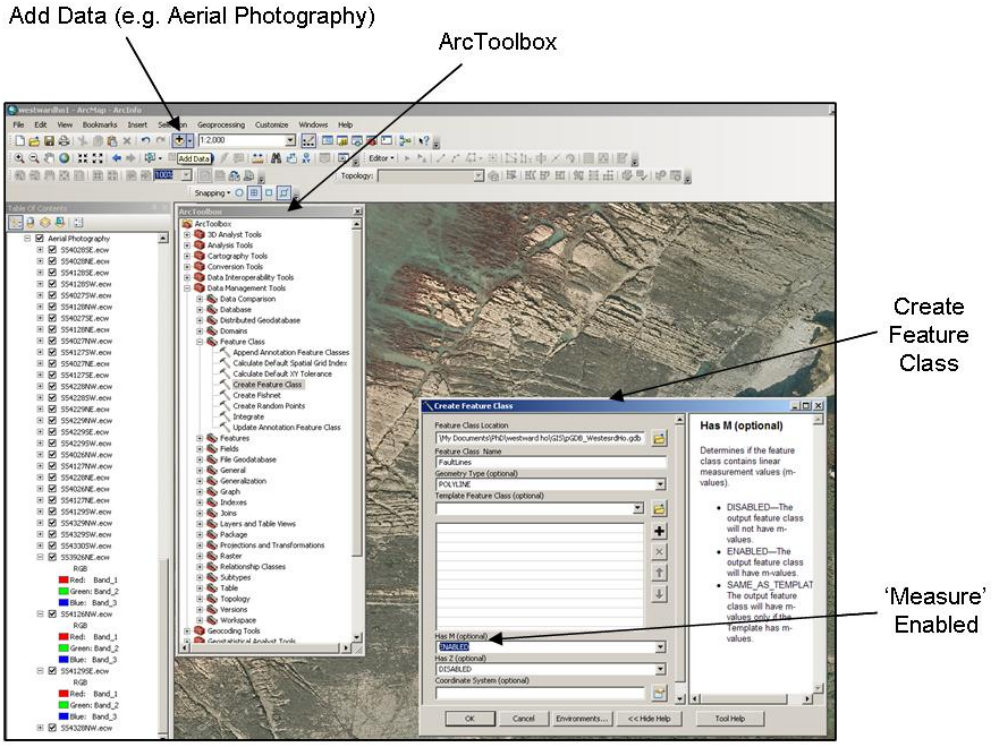

Fault map interpreted from aerial photography and field observation
(left-lateral faults displayed in red and right-lateral faults displayed in blue)

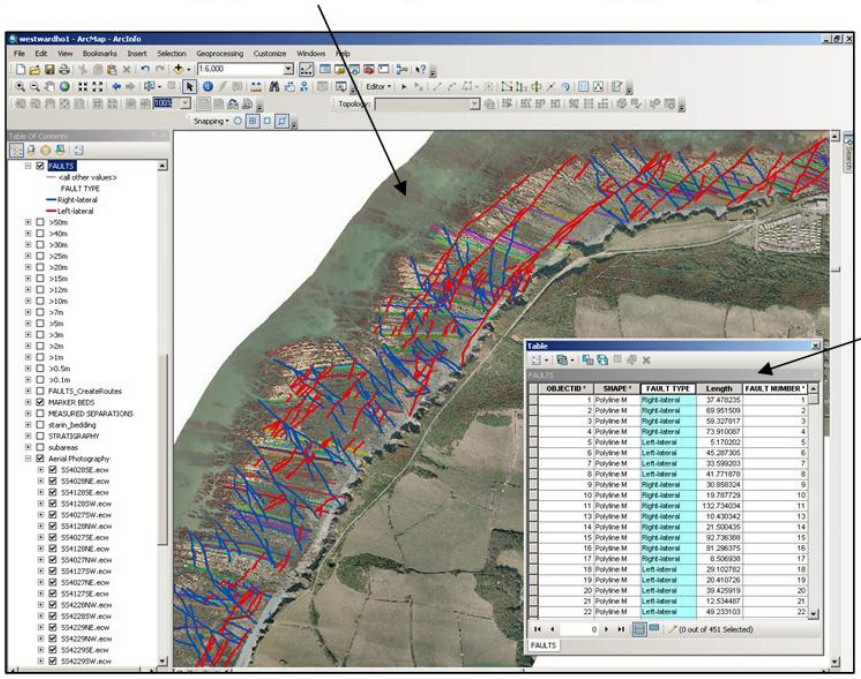

5. Faults interpreted from digital air photographs and offsets of marker beds identified (both in field and from imagery). Within the fault feature class attribute table, different fields were created such as fault number and fault-type (i.e. left-lateral or right-lateral). This is essential for collating and extracting information about the faults at later stages of the analysis. It also allows a visual analysis as faults can be displayed by different attributes, such as fault-type etc.

Length of line approximates displacement for the strike-slip faults

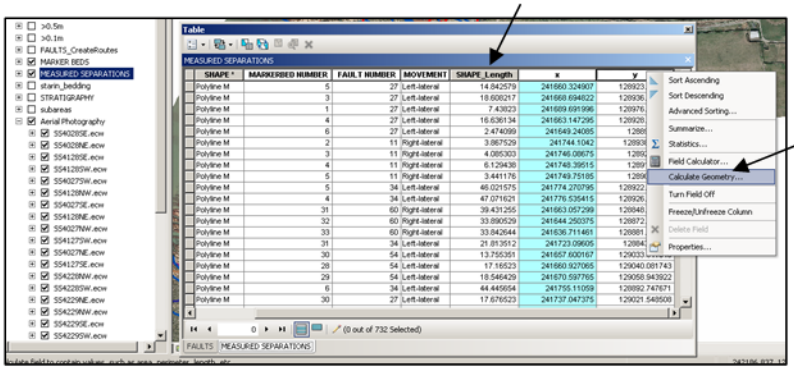

6. Displacements measured form the digital air photographs using a separate polyline feature class. Lines were then drawn between offset marker bed segments. Therefore, the length of a line is a measure of the displacement for the through going strike-slip fault. In the attribute table of measured displacements, fields for the *x* and *y* co-ordinates of the line mid-points were created and calculated using the 'calculate geometry' option. Data was exported in table format and using the *x,y* co-ordinates the measured displacement data was displayed as point features in ArcMap.
7. Each fault polyline split into smaller segments by their corresponding measured displacement point features using the 'Split Line at Point' tool in ArcToolbox.
8. Use 'calculate geometry' to calculate *x* and *y* co-ordinates for the start and end points of each fault polyline segment. Join the fault polyline table with the displacement point table allowing the average displacement for each polyline segment to be calculated. Therefore the fault polyline table has a series of attributes (*x,y* co-ordinates, length, displacement etc.) associated with each fault segment allowing the network to be displayed and analysed by displacement.

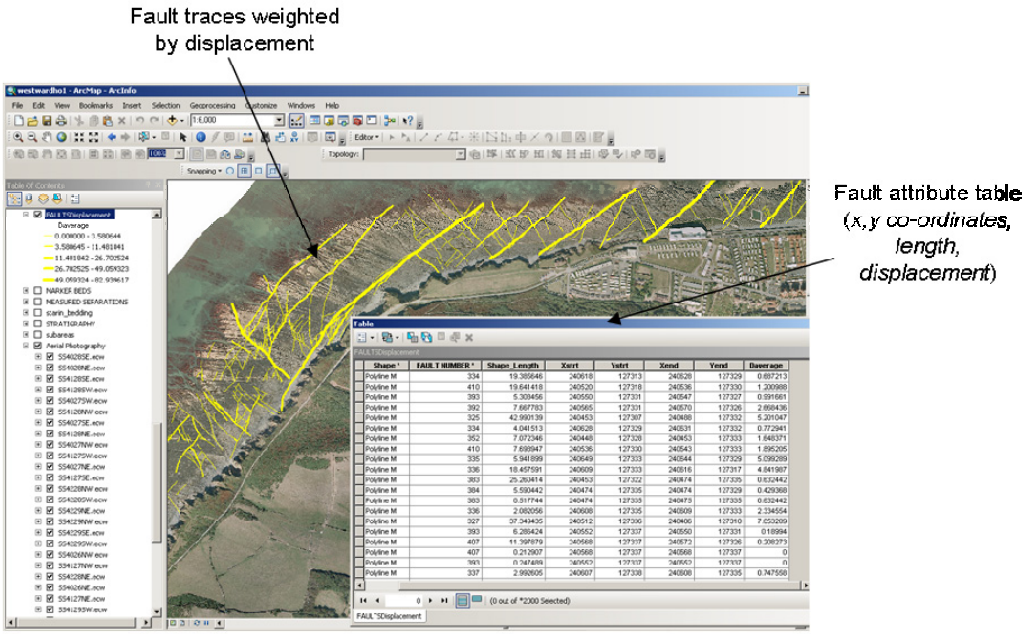

9.2. ArcGIS Workflow 2 – Structural analysis of multibeam bathymetry data offshore Hartland

1. Multibeam bathymetry data imported as ASCII file into ArcGIS by converting ASCII data into a point feature class using 'ASCII 3D to Feature Class' in ArcToolbox.
2. Point feature converted into a gridded Raster image with associated *x,y,z* data using 'Point to Raster' in ArcToolbox.
3. Hillshade applied to Raster image using 'Spatial Analyst Tools' in ArcToolbox. Produces a shades relief that enhances structural features (i.e. faults and bedding) allowing them to be mapped using the same workflow in 9.1 (steps 3-8).
4. Aspect and Slope applied to Raster image using 'Spatial Analyst Tools'. These produce raster images which show the calculated direction of maximum dip and the maximum dip on an identified surface, respectively.
5. Use the 'identify' icon on identified bedding planes to show the dip and dip direction values.

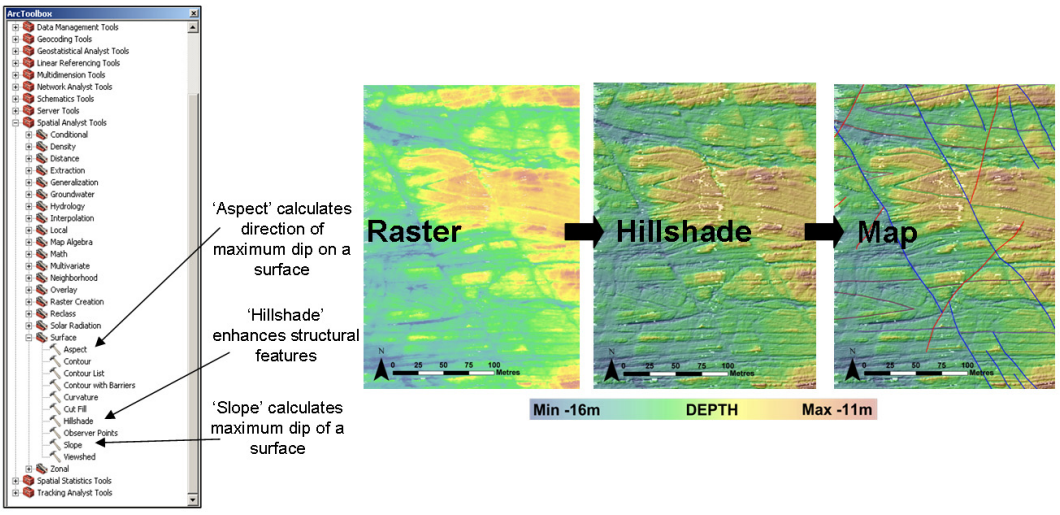

9.3. ArcGIS Workflow 3 – Analysis from high resolution seismic data and 3D seismic data

1. Microsoft Excel spreadsheets extracted from Petrel and Traptester are saved as database files (.dbf). These contain easting and northing co-ordinates of multiple measured sample points along each interpreted fault trace at each horizon. Associated with each sample point are fault identification field and calculated attributes such as throw, dip, azimuth etc.
2. Database files imported into ArcMap as tables.
3. Easting and northing co-ordinates used to plot data as point features. Right click on table and then 'Display XY Data'. Once the point data are displayed it is important to save as a feature class and convert to individual features using the 'Multipart to Singlepart' tool in ArcToolbox.
4. Use the 'Points to Line' tool in ArcToolbox to draw individual fault traces from the point features. The fault identification field separates the points into separate fault lines. This does not complete the intersections between faults which can be added manually using the 'Editor' toolbar.
5. Use 'Split Line at Vertices' in ArcToolbox to segments the faults by each sample point. Follow step 8 in workflow 9.1 and use 'calculate geometry' to calculate the *x* and *y* co-ordinates of the start and end point of each line as well as its length.

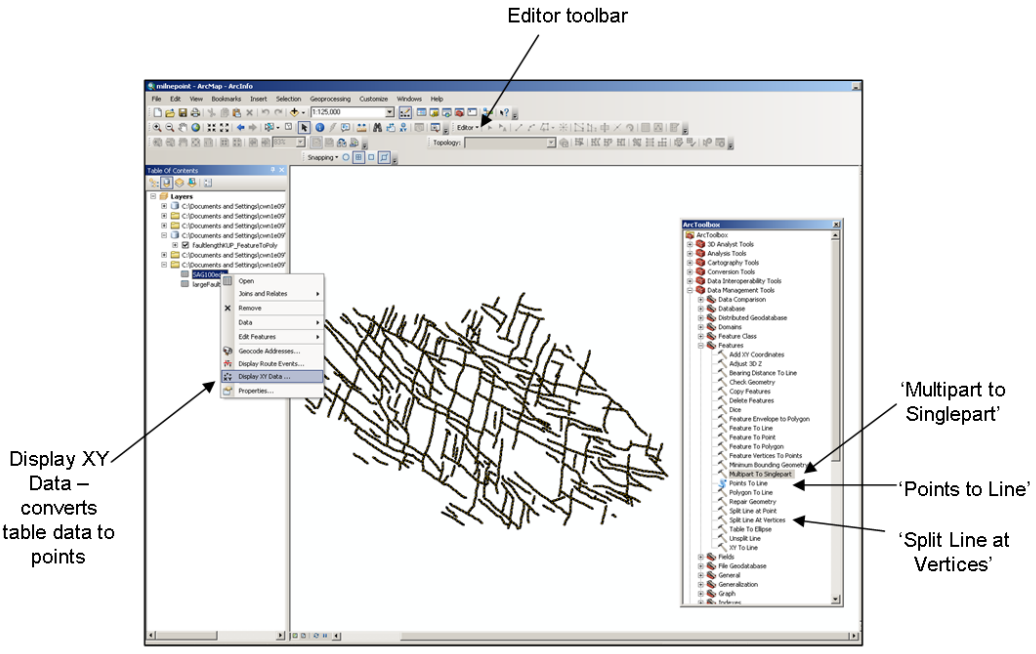

9.4. ArcGIS Workflow 4 – Extraction and analysis of data from ArcGIS

1. ‘Export’ records from the fault attribute table once the network has been interpreted and analysed in ArcMap (e.g. after following workflow 9.1). This exports the data in database format (.dbf) which can be viewed and edited in Microsoft Excel. The fault attribute table will contain useful information about each fault segment that can be manipulated in several ways using spreadsheets (i.e. fault ID, fault-type, *xy* start, *xy* end, length, displacement etc.).
2. To sample subares highlight the faults of interest in ‘Editor’ mode and select ‘Selected records’ when exporting the fault attribute table.

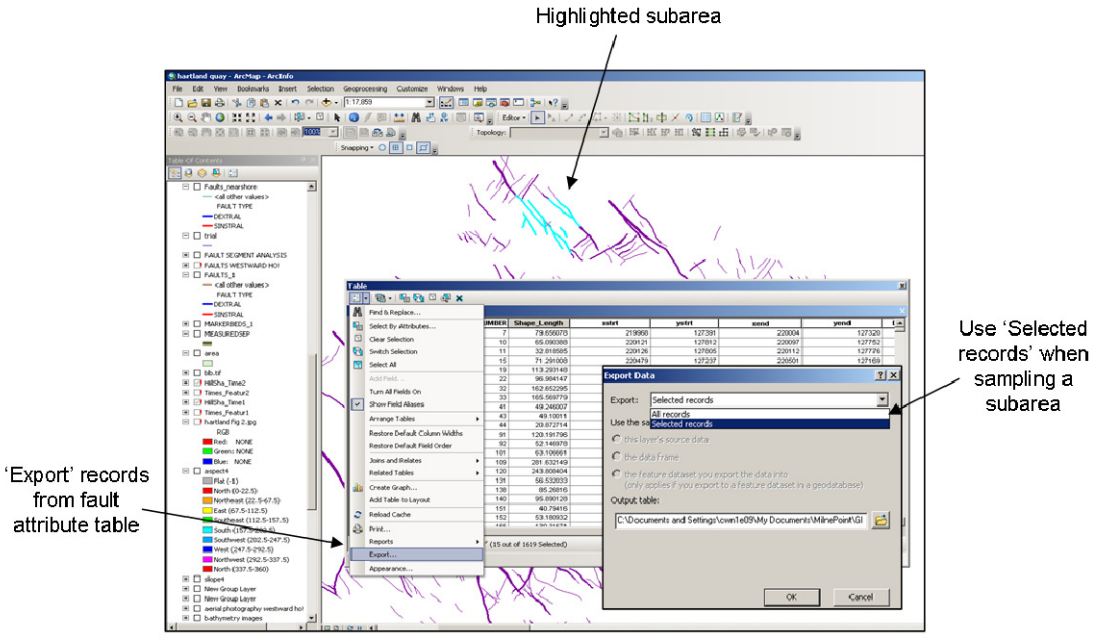

3. Formatted fault attribute data in Microsoft Excel and input into Strike-Slip-Network workbook. The Strike-Slip-Network workbook has been developed to analyse fault network data. It uses the length, displacement and co-ordinates of each fault segment to calculate the line azimuth and displacement tensor inputs 9i.e. unit vectors and displacement directions; see equation 2.3). This is used to calculate fault trend statistics (i.e. plot rose diagrams) and to calculate the eigenvalues and eigenvectors of the

lagrangian strain tensor. A similar Dip-Slip-Network workbook also exists that was developed for BP by Professor David Sanderson and was used for the strain analysis of normal faults.

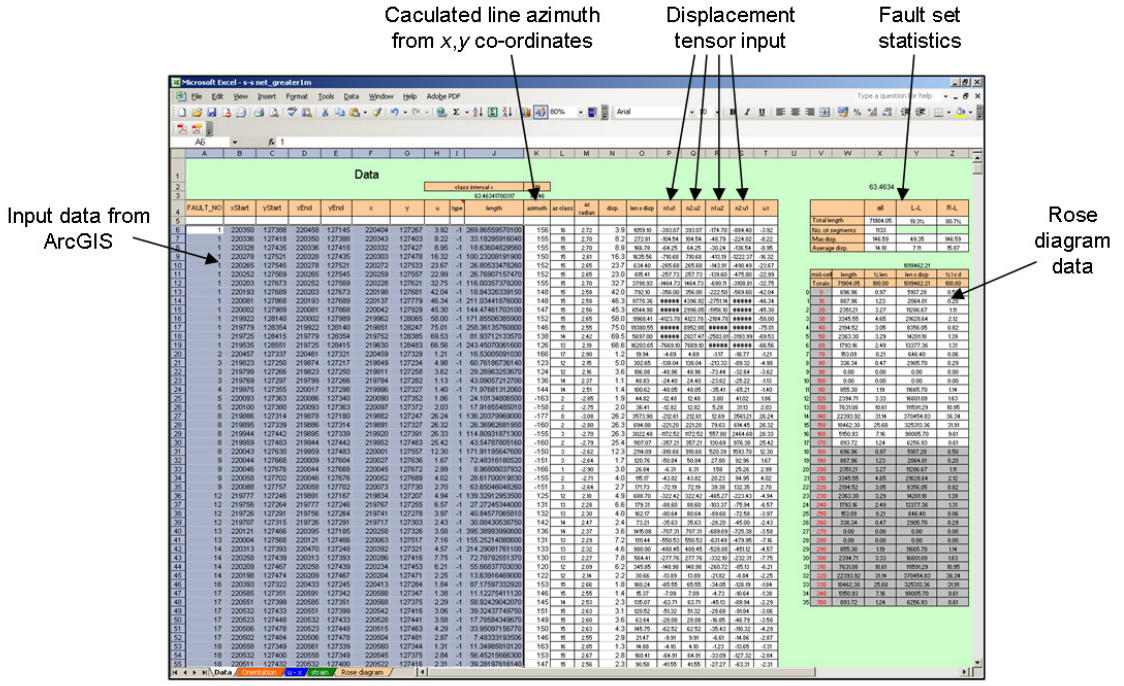

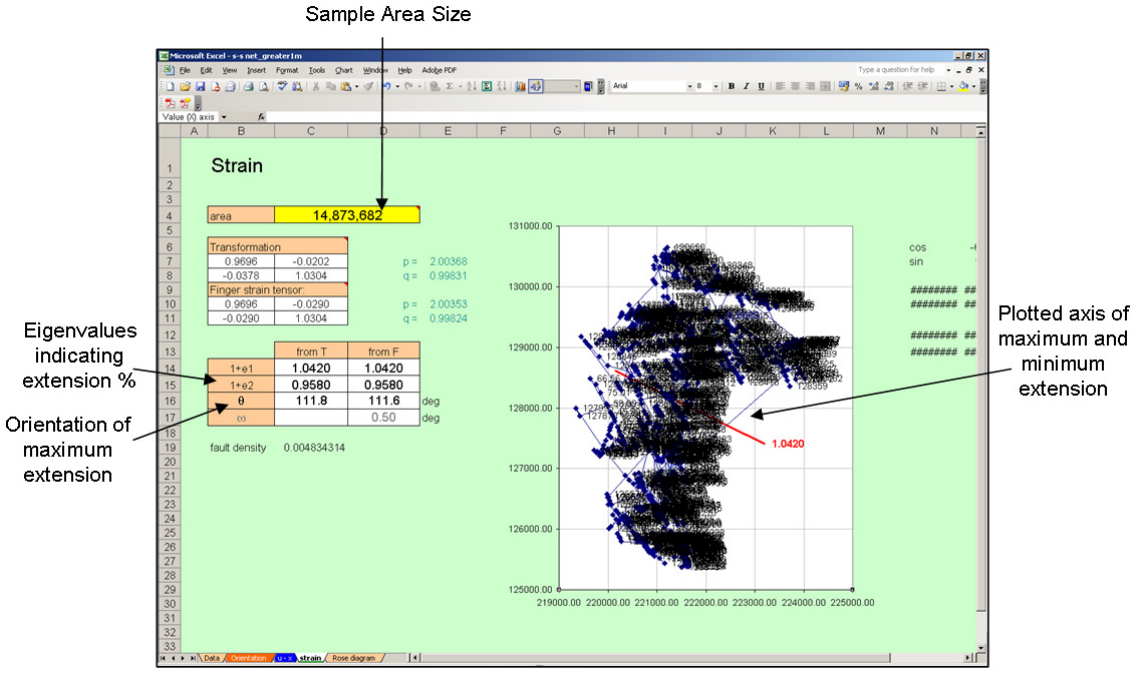

9.5. ArcGIS Workflow 5 – Analysis of network topology

1. Use a point feature class for the node analysis. A field in the attribute table should indicate the node type (i.e. I-, Y- or X-nodes), these need to be typed in manually.
2. Original fault lines are planarized using the 'Planarize Lines' icon on the 'Topology' toolbar in 'Editor' mode. This splits all of the faults at their intersections dividing the network into branches. The fault polylines need to be selected in order to 'Planarize' the network and should be done to a copy of the fault network at step 6 in workflow 9.1. A field in the attribute table should indicate the branch type (i.e. I-I, I-C or C-C branches), these need to be typed in manually.
3. Use the 'Feature to Polygon' tool in ArcToolbox and input the fault polyline feature class to automatically draw closed compartments within the fault network. Within the created polygon attribute table there is an area field that automatically calculates the area of each polygon.
4. All topological information is extracted using steps 1 and 2 of workflow 9.4 for further analysis in Microsoft Excel.